MACROSCOPIC MODELS AND EFFICIENT NUMERICAL SOLVERS FOR NONLINEAR REACTION-TRANSPORT PHENOMENA IN ELECTROCHEMICAL CELLS

By
Arunraj Balaji-Wright and Ali Mani

Prepared with support from
the Charles H. Kruger Stanford Graduate Fellowship,
the National Science Foundation,
the Office of Naval Research, and
the U.S. Department of Energy

Report No. TF-196

Flow Physics and Computational Engineering Group
Department of Mechanical Engineering
Stanford University
Stanford, CA 94305

August 2024

Macroscopic Models and Efficient Numerical Solvers for Nonlinear Reaction–Transport Phenomena in Electrochemical Cells

By

Arunraj Balaji–Wright and Ali Mani

Prepared with support from
the Charles H. Kruger Stanford Graduate Fellowship,
the National Science Foundation,
the Office of Naval Research, and
the U.S. Department of Energy

Report No. TF-196

Flow Physics and Computational Engineering Group
Department of Mechanical Engineering
Stanford University
Stanford, CA 94305

August 2024

Abstract

As electrochemical approaches for performing valuable syntheses, separations, and conversions gain prominence as components of strategies to address challenges in the energy and sustainability space, quantitative understanding of the underlying physicochemical phenomena becomes crucial for continued development of the technology and accurate evaluation of its potential. The assortment of features observed in electrochemical cells exhibits substantial richness and diversity, owing to non–linear coupling between numerous multiphysics processes. Concomitantly, the wide span of emergent spatiotemporal scales significantly increases the complexity and cost of numerical simulations. Through extensive analysis of examples in energy storage, CO_2 mitigation and water purification, this work conveys a research methodology for contending with the aforementioned difficulties and producing insight into factors that determine cell performance. The specific applications of interest are CO_2 electroreduction, capacitive deionization, and electrodialysis. We construct macroscopic models by supplementing well–known, continuum–scale models with novel, problem–specific model reduction techniques. Furthermore, we make use of physicochemical scaling arguments to select specialized numerical methods that enable efficient solution of the resulting equations. Our simulation results include detailed distributions of reactive species and electric potential throughout the cells in addition to cell–averaged performance parameters, allowing quantitative identification, analysis, and understanding of microscopic features that strongly influence the large–scale viability of electrochemical approaches in a variety of applications.

THIS PAGE DELIBERATELY LEFT BLANK

Acknowledgements

Generous funding from the Charles H. Kruger Stanford Graduate Fellowship allowed me to investigate numerous topics during the initial phase of my graduate studies. The project featured in Chapter 3 was supported by the Solar Photochemistry and Catalysis Programs of the Chemical Sciences, Geosciences, and Biosciences Division, Office of Basic Energy Sciences, U.S. Department of Energy, under Grant No. DE-SC0021633, and the project featured in Chapter 4 was supported by the National Science Foundation under Grant No. 1553275 and the Office of Naval Research. Finally, all simulations described in this dissertation were performed at the Stanford High Performance Computing Center.

THIS PAGE DELIBERATELY LEFT BLANK

Contents

List of Tables

List of Figures

THIS PAGE DELIBERATELY LEFT BLANK

List of Algorithms

THIS PAGE DELIBERATELY LEFT BLANK

Chapter 1

Introduction

1.1 Overview

The thematic bent of this dissertation is concisely conveyed by its title, which we discuss first before concrete summaries of problems studied and findings uncovered. We begin with the term '*macroscopic* models," which naturally implies a contrast against so–called "*microscopic* models." Due to the remarkably rich, multi–scale nature of physicochemical phenomena occurring within electrochemical cells, the point of division between microscopic and macroscopic is neither universally nor singularly defined. Rather, the sense in which a model is said to be macroscopic depends on context offered by the specific problem to be analyzed.

As a preliminary observation, we remark that all models presented in this dissertation are rooted in continuum mechanics, which may be considered macroscopic in contrast to molecular–scale approaches. We will proceed, however, to perform analyses in which the term macroscopic is used to describe a level of model reduction that surpasses simple continuum treatment of a single (typically aqueous) phase. For example, we encounter scenarios in which phenomena like interfacial microstructuring and chaotic fluid flow are treated using continuum methodologies at scales much larger than the associated feature sizes. Proceeding one level further, we explore cases in which even the spatial inhomogeneity of macroscopic structures may be modeled in such a way that the dimensionality of the problem is reduced while essential features and processes are retained.

The next part of the title involves efficient numerical solvers, which are necessitated by the complexity of the aforementioned models — models that generally take the form of

nonlinearly coupled partial differential equations. Though the development of macroscopic models is itself a means of reducing simulation cost compared to computationally–expensive microscopic models, even macroscopic models may entail substantial computational cost due to numerical stiffness. For each of the problems discussed in this work, we demonstrate that judicious selection of numerical methods permits low–cost solution of the governing equations, enabling practical use of macroscopic models as part of research, design, and optimization processes.

The third and last part of the title touches upon reaction–transport phenomena occurring in electrochemical cells. The previously–described models and solvers offer access to space–time–resolved distributions of ionic concentration and electric potential fields throughout electrochemical cells. Examination of these fields reveals richly coupled physicochemical dynamics that are extremely difficult to directly observe in experiments, if at all direct experimental observations are possible. Additionally, from a practical standpoint, we use this data to probe the connection between localized physicochemical phenomena (*e.g.,* shock–like pH fronts or localized reaction–diffusion layers) and cell–averaged performance metrics. This level of understanding opens new doors toward optimization of electrochemical cells for a variety of applications.

Though the methodology employed throughout this dissertation maps reasonably well to the three parts of its title, we emphasize that the components are not implemented step–by–step in the order of appearance. Perhaps unsurprisingly, aspects of each component are strongly and bidirectionally linked to each of the other components. For example, we make extensive use of intuitive scaling arguments and prior knowledge of reaction–transport phenomena to inform construction of the macroscopic models and selection of the numerical methods. Similarly, practical constraints associated with implementation of a numerical solver are used to motivate and guide model reduction efforts. Thus, though this tripartite description of our research methodology is a useful conceptual map, readers should anticipate (and perhaps even savor) the numerous ways in which aggregate interactions between the theoretical, computational, and physicochemical components of this work are central to the significant findings.

This dissertation contains three major technical chapters, each pertaining to a specific type of electrochemical cell. Chapter 2 discusses flow–through–electrode capacitive deionization, Chapter 3 discusses electroreduction of CO and CO_2 into C_{2+} products, and Chapter 4 discusses behavior commonly observed near ion exchange membranes in electrodialysis cells.

We round out this introduction by providing a broad summary of the motivation, research approach, and primary findings for each of the technical chapters. Note that this introduction is intended to serve as a concise summary for the dissertation as a whole; a focused literature review is provided in the "Background" section of each major chapter.

Capacitive deionization (CDI), discussed in Chapter 2, is notable for its ability to perform low–energy desalination of brackish water and selective separation/recovery of salt and metal ions. However, redox reactions at porous carbon electrodes, such as the formation of weakly–acidic, oxygen–containing surface groups, limit deionization performance and electrode lifespan. In this study, we employ porous electrode theory to investigate the coupled effects of transport, electrosorption, redox reactions, and acid/base surface chemistry in practical flow through electrode (FTE) CDI cells, and we develop an efficient numerical solver that allows us to perform full–cell simulations over numerous charging/discharging cycles. We verify that our high fidelity model's predictions agree with analytical solutions in the limit of small voltage perturbations, and we demonstrate the significance of accurately capturing interplay between pH dynamics and surface chemistry. Our simulations demonstrate that anodic oxidation in FTE CDI is substantially inhomogeneous in space and in time, exhibiting cyclic protonation/deprotonation of surface groups and traveling, shock–like pH fronts. Moreover, we uncover connections between microscopic behavior and macroscopic performance parameters, demonstrating that this theoretical and numerical approach may substantially benefit the practical design optimization of CDI cells.

Electroreduction of CO and CO_2, discussed in Chapter 3, offers a pathway toward renewable–powered synthesis of hydrocarbon chemicals and fuels. Both the composition and the structure of cathodic catalyst microenvironments in gas diffusion electrodes (GDEs) play dominant roles in determining the product distribution and energy efficiency metrics. Porous and hydrophilic copper environments are known to produce multi–carbon species and exhibit large active surface areas, but recent investigations have shown that the inclusion of sporadically–distributed porous hydrophobic regions creates additional pathways for the delivery of gaseous reactants, thereby mitigating transport limitations seen in pure Cu catalysts. As the design space for catalysts has grown to include a wide variety of material and geometric parameters, accurate PDE–based modeling and simulation of such systems has become necessary to understand and optimize the coupled reaction and transport processes that determine cell performance. In this work, we develop, numerically simulate, and validate a predictive model that efficiently incorporates a wide range of physical and

chemical processes occurring in catalysts with intermixed hydrophobic and hydrophilic regions. We employ homogenization as a means of model reduction, constructing a medium fidelity model that captures both microenvironment geometric scales and full device scales in 3D. Our model, coupled with the appropriate numerical methods for treatment of stiff and multi–dimensional problems, permits low–cost exploration of the high–dimensional parameter space associated with recently developed catalysts, offering quantitative insight into the optimal design of microenvironments for CO and CO_2 electroreduction.

For electroreduction of CO_2 in particular (as opposed to CO), carbon efficiency and energy efficiency are still inadequate for commercial use cases as a result of the ${CO_3}^{2-}$ problem: CO_2 and OH^- ions react rapidly in solution to eventually generate ${CO_3}^{2-}$, consuming the CO_2 feedstock while shifting the cell's pH and increasing energy requirements. We focus our attention here on designing a cathode GDE capable of performing CO_2 reduction at high throughput and carbon efficiency in basic electrolytes. We investigate the impact of a wide range of geometric configurations and operating conditions on the overall performance of the cathode.

We consider electrodialysis in Chapter 4. Near interfaces with charged structures like ion–exchange membranes, the coupling between ion transport, fluid flow, and electrostatics may give rise to electroconvection, a hydrodynamic instability that eventually transitions to a chaotic flow. In the chaotic regime, the flow is characterized by unsteady, three–dimensional vortices with a wide range of length scales and is accurately described by the Poisson–Nernst–Planck–Navier–Stokes (PNPNS) equations. However, 3D simulations of the PNPNS equations are extremely expensive due to inherent stiffness in the system. In practice, knowledge of the averaged ion concentration, velocity, and electric potential fields would be sufficient to predict essential performance benchmarks like the current–voltage curve. Unfortunately, the application of Reynolds–averaging to the PNPNS equations leads to a closure problem, thwarting direct computation of the averaged fields. In this work, we combine the macroscopic forcing method, a numerical technique for measurement of closure operators in Reynolds–averaged equations, with high–fidelity experimental data to close the Reynolds–averaged PNPNS equations. We show that the unclosed fluxes may be represented to the leading order as a gradient–diffusion term with a spatially varying eddy diffusivity, and we measure the eddy diffusivity from space–time–resolved experimental velocity fields. This finding allows direct computation of the averaged fields at a fraction of the cost of 3D PNPNS simulations by enabling use of the 1D Poisson–Nernst–Planck

equations with supplementary eddy diffusivity. The resulting current–voltage curve exhibits strong agreement with experiments.

Finally, we present concluding remarks in Chapter 5, focusing on valuable extensions of the studies presented in this dissertation. In some cases, we offer specific suggestions for additional characterization and validation experiments in order to further examine the model's predictive capabilities. In other cases, we comment on alternative approaches that might provide a worthwhile benchmark for comparison of results. The author wishes to return to these ideas in due time.

1.2 Authorship and publication statement

All work presented in this dissertation has been published or will be submitted for publication in academic journals. The author of this dissertation contributed substantively to each of the projects, as recognized by first or equally–contributing–first authorship on each of the respective publications. Additionally, the author of this dissertation played the primary role in drafting and editing each of the submitted manuscripts, with the incorporation of revisions based on feedback from co–authors and anonymous peer reviewers. Overlap between this dissertation and manuscripts that have been published or will be submitted for publication is summarized as follows:

Chapter 2: Electrode Corrosion in Capacitive Deionization

- Balaji–Wright, A. *et al.* "Understanding degradation of capacitive deionization cells: Full–cell simulations with anode corrosion". *Desalination* **587,** 117924 (2024)
  - Text and figures from this publication and its associated supplementary information file are reused with permission in Chapters 1 and 2.

Chapter 3: Intermixed Hydrophobic/Hydrophilic Catalysts

- A portion of the work presented in this chapter was undertaken as a collaboration with Kyle R. Disselkoen in the Department of Chemistry at Stanford University. For this portion of the work, both researchers jointly and equally developed the model and the simulation code, analyzed the results, generated the figures, and wrote the text.

  - Text and figures from two manuscripts in preparation appear in Chapters 1 and 3.
  - Portions of the text and figures in Sections 3.1, 3.4.3, 3.4.4 and 3.5 were jointly and equally developed by the author and Kyle R. Disselkoen. These portions also appear in the doctoral dissertation of Kyle R. Disselkoen [2].

Chapter 4: Eddy Diffusivity for Chaotic Electroconvection

- Balaji–Wright, A. *et al.* "Measurement of an eddy diffusivity for chaotic electroconvection using combined computational and experimental techniques". *Physical Review Fluids* **9,** 023701 (2024)
  - Text and figures from this publication are reused with permission in Chapters 1 and 4.

Chapter 2

Electrode Corrosion in Capacitive Deionization

2.1 Background

As the availability of fresh water, a vital resource in the contexts of health, sanitation, agriculture, and energy production, is projected to decline as a result of changes in global climate and population distribution [4–8], novel water treatment techniques have become a critical area of research [9]. While commonly utilized desalination methods such as reverse osmosis (RO) or multistage flash/multi–effect distillation (MFD/MED) employ mechanical or thermal driving forces to remove water molecules (the majority component) from a salty input solution, a variety of electrochemical methods have been developed to perform desalination by instead removing salt ions (the minority component) from the solution [10].

Among this class of desalination approaches, capacitive deionization (CDI) stands out as a promising technology for the energy–efficient deionization of brackish input streams [10–14]. Though the primary mechanism responsible for ion storage in CDI systems is typically electrosorption — the electrostatically driven accumulation of ions in the electric double layer (EDL) at the interface between aqueous and charged phases — a wide variety of cell geometries [15] and electrode materials [16, 17] have been studied. As seen in seminal experimental works, electrolyte flow may occur parallel to (flow–between) [18] or perpendicular to (flow–through) [19] porous electrodes. Later investigators showed that ion–selective membranes may be employed to mitigate parasitic co–ion transport [20], novel electrode materials may permit pseudo–capacitive storage of ions via intercalation reactions

[21, 22], or fixed electrodes may be omitted entirely in favor of carbon slurries that permit continuous desalination [23].

In addition to recent works attempting to standardize and improve a variety of general CDI performance metrics [13, 24–26], several recent investigations have expanded the functionality and applicability of CDI to include selective salt and heavy metal ion separation [27, 28]. Ion electrosorption selectivity is known to be a function of ion size, valence, and feed concentration, both with [29–33] and without [34–40] chemical functionalization of electrode surfaces. Additionally, the large internal pH gradients observed in a variety of CDI cell geometries [41–48] have recently been leveraged for the removal of amphoteric ions such as Boron, which is difficult to remove in membrane–based processes since it appears in a charge–neutral form (with relatively small solvated diameter) at neutral–pH conditions [47].

Flow–through electrode (FTE) CDI was originally developed by Johnson & Newman [19] and later revisited by Avraham *et al.* [49, 50], Cohen *et al.* [51], and Suss *et al.* [52]. The carbon electrodes used for FTE CDI typically exhibit a hierarchical structure comprising both macropores ($O(1\,\mu\text{m})$ diameter) and micropores ($O(1\,\text{nm})$ – $O(10\,\text{nm})$ diameter), as depicted in Fig. 2.1. The former permit electro–diffusion and advection of the ions and advection of the electrolyte through the electrodes with minimal hydraulic resistance, while the latter provide the electrodes' large specific capacitance. Previous work has shown that the FTE geometry permits a smaller device size and faster rate of electrosorption compared to flow–between geometries [52, 53], but substantial challenges impede commercial viability.

Recent reviews have highlighted long–term performance degradation of CDI cells due to electrochemical reactions at carbon electrode surfaces [13, 54]. We refer here not to the reactions responsible for pseudo–capacitive ion storage in hybrid–CDI cells [21, 22], but rather to the oxidation of carbon sites on the anode. Bouhadana *et al.* [55] and Cohen *et al.* [56, 57] found that repeated cycling of CDI cells (particularly in the FTE configuration) led to oxidation of activated carbon cloth anodes, which was exacerbated in the presence of dissolved oxygen reduction at the cathode. Numerous authors have reported that oxidation of carbon electrodes leads to the formation of charged, oxygen–containing chemical surface groups, as indicated by a shift in the potential of zero charge (PZC) [46, 48, 49, 56–58]. Further analysis revealed that though a number of groups with C–O and C=O bonds were present, such as lactonic, phenolic, and carbonyl groups [45, 48, 58, 59], the weakly acidic carboxylic group (–COOH) plays a dominant role [42, 58, 60, 61]. Strategies to mitigate

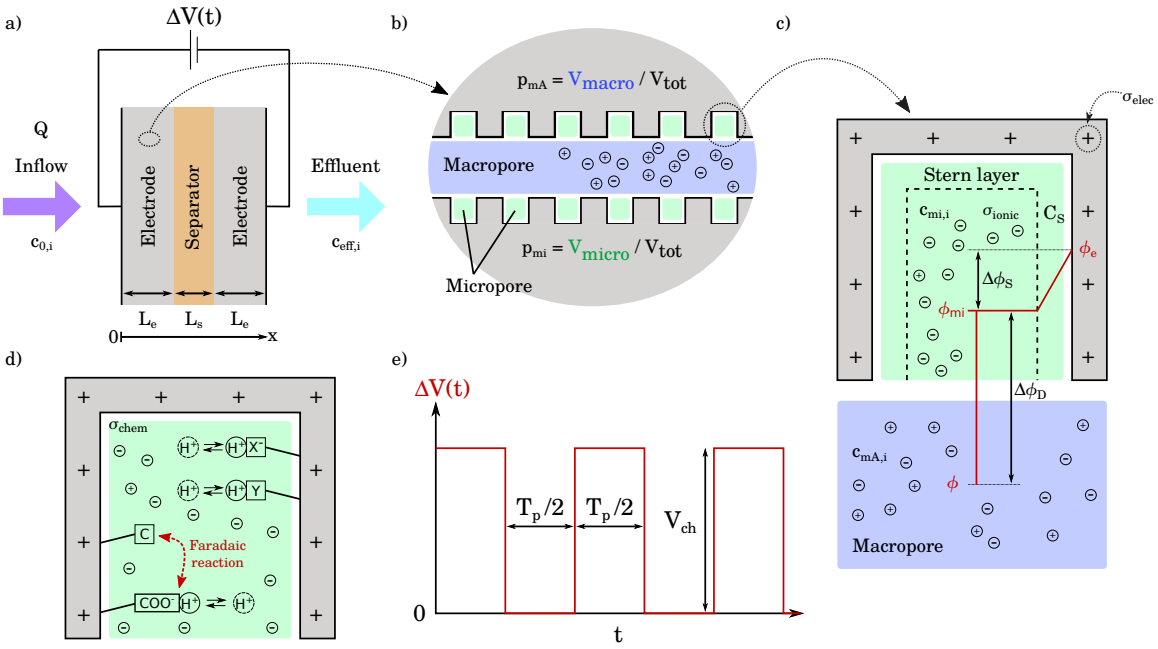

Figure 2.1: (a) Full FTE CDI cell, showing inflow, effluent, applied voltage, and relevant dimensions. Not drawn to scale. (b) Schematic of macropore (light blue) and micropore (light green) regions in hierarchically porous electrode. Shown without tortuosity only for demonstration purposes. (c) Inset of individual micropore depicting modified Donnan (mD) model. The Stern layer and corresponding capacitance are shown along the internal surface of the micropore. Micropore ionic charge density and electronic charge density are also shown. (d) Inset of micropore showing acidic/basic chemical surface groups (such as –COOH) in equilibrium with micropore pH. Chemical surface groups exhibit their own charge density. (e) A symmetric, square–wave driving potential is utilized in this study.

or exploit this phenomenon include careful selection of the working potential range [62, 63] and operation in the inverse–CDI (i–CDI) regime [61].

The pH dependence introduced by weakly acidic carboxylic groups (which can deprotonate into negatively charged carboxylate groups, $-COO^-$) enlarges the range of behavior that may be observed in CDI. Though many works have shown variation in effluent pH over the course of CDI operation, Holubowitch *et al.* [42] and Landon *et al.* [46] performed *in operando* measurements of local pH very close to the electrodes, finding that variations are large in magnitude (as much as eight units) and highly transient. Kang *et al.* [48] shed light on the interplay between redox reactions and the local pH, revealing two–way coupling. In all, the literature has shown that five nonlinearly coupled physio–chemical phenomena are pertinent in CDI degradation: i) electrodiffusive transport, ii) advective transport, iii) electrosorption, iv) electrochemical charge transfer, and v) weak acid/base surface chemistry.

The modeling of porous electrodes in CDI originally drew from the study of supercapacitors, wherein "transmission line" (TL) models were used to describe the charging and discharging dynamics by way of linear circuit elements [64, 65]. Such models have since been adapted and refined for electrodes with hierarchical pore structures, exhibiting good agreement with experiments [66–68]. The development of higher fidelity, nonlinear models was spurred by Johnson and Newman's application of macroscopic porous electrode theory to CDI cells, a continuum approach wherein averaging of ion concentration and electric potential fields is performed in control volumes that are small enough to resolve variation across an electrode but large enough to include a large number of pores. The modeling of electrosorption in EDLs is a critical component of this approach. Recent reviews [12, 13] trace the development of EDL modeling for porous electrodes, beginning with the simple Helmholtz model [19], progressing to the Gouy—Chapman–Stern (GCS) model [69–71] and finally arriving at the modified–Donnan (mD) model [71–75]. As will be discussed, the work we present here is grounded in the mD model, which is appropriate when micropores are small enough for the diffuse portion of contained EDLs to overlap with each other.

Recent developments in porous electrode theory have shown that the mD framework [72–75], which is appropriate when micropores are small enough for the diffuse portion of contained EDLs to strongly overlap with each other, is capable of capturing many of the unique phenomena observed in CDI cells. Though previous works have considered different subsets of the processes involved in electrode oxidation, we are not aware of any

investigations that have combined all five of the aforementioned physio–chemical phenomena into a single model and have used the resulting model to probe long–term, corrosion–induced degradation of CDI performance.

Biesheuvel *et al.* [76] and Guyes *et al.* [31, 32] have developed and employed models that include fixed concentrations of non–reactive chemical surface groups. Hemmatifar *et al.* [77] proceeded a step further, developing a model for weakly acidic or basic chemical surface groups in equilibrium with the local micropore pH. However, these four works do not include Faradaic reactions. Dykstra *et al.* [44], He *et al.* [78], and Biesheuvel *et al.* [75] presented models that include chemical surface groups *and* Faradaic reactions simultaneously, but within different contexts. Dykstra *et al.* [44] considered the pH dynamics induced by water reduction at the electrodes, but assumed fixed concentrations of non–reactive chemical surface groups. He *et al.* [78], on the other hand, considered redox reactions that form chemical surface groups, but the groups are not weakly acidic or basic. Biesheuvel *et al.* [75] specifically considered the influence of carboxylic groups in equilibrium with micropore pH, but the total concentration of the groups is not subject to Faradaic reaction kinetics — instead, the total number of functional group sites is held fixed while, separately, divalent aqueous cation are reduced into monovalent aqueous cations. Finally, note that Guyes *et al.* [79] have proposed a 1D model for FTE CDI using inert electrodes, and Shocron *et al.* [47] extended this model to include pH dynamics and fixed concentrations of weakly acidic/basic surface groups. These works serve as the basis for addition of electrochemical charge transfer.

In this study, we introduce a comprehensive model for long–term, oxidation–induced performance degradation in FTE CDI. Applying porous electrode theory through the lens of the mD approach for EDLs, we incorporate both the kinetics of carboxylic group formation in the anode and the weak acid equilibrium between the carboxylic groups and the local micropore pH. We also include dissolved oxygen reduction at the cathode. Given the level of mathematical complexity in the model and the transient variation of solution fields across the entire width of the FTE CDI cell, we find that full–cell numerical simulation is required to comprehensively investigate electrode oxidation in practical settings. Such simulations pose an immense challenge due to the wide discrepancy in length and time scales present in the problem, but we show that this challenge can be overcome by the judicious selection of numerical methods. We verify our solver's consistency against analytical results, and we compare our model's predictions against those of a similar model, highlighting the nuances

of interplay between pH dynamics and surface chemistry.

Our model and full–cell simulations of FTE CDI offer access to detailed concentration fields in macropores and micropores. The results reveal that oxidation and surface group protonation/deprotonation occur in a spatially and temporally inhomogeneous fashion as a result of coupled reaction–transport dynamics. Crucially, our methodology also connects the microscopic behavior of the system to macroscopic performance parameters, which are used to assess real–world viability of CDI. Thus, we anticipate that the combined power of accurate modeling and full–cell numerical simulation will substantially benefit the design optimization of CDI cells.

We begin in Section 2.2 with a theoretical discussion of the governing equations and physical constraints on free parameters in the model. A comprehensive description of the solver algorithm and numerical methods used to solve the governing equations is included in Section 2.3; a Matlab implementation was used to generate all data shown. In Section 2.4, we present numerical solutions to the governing equations under a variety of cell geometries and operating conditions, and we investigate the emergent physio–chemical phenomena.

2.2 Theory

In this section, we describe the full FTE CDI cell and introduce the model. First, we write the governing equations generally (i.e., agnostic to specific choice of composition and reaction mechanisms), such that they are valid for a variety of deionization, ion separation, and ion recovery applications. This approach is aligned with our numerical solver, which allows these details to be provided as input parameters. The specific chemistry of each demonstration case we present is included in Section 2.4. Second, we explain how free parameters in the kinetic model for the electrodes are related to measurable macroscopic properties of the electrodes and of the overall electrochemical cell. This discussion occurs within the context of anticipated future work in which we aim to quantitatively predict the behavior seen in FTE CDI experiments.

2.2.1 Governing Equations

As shown in Fig. 2.1(a), a pair of porous electrodes with thickness L_e sandwiches a separator membrane with thickness L_s. Though not shown in the schematic, the simulation domain also includes the reservoir regions before and after the electrodes, with length L_{res} on

either side. The electrodes have a hierarchical porous structure, quantified by macropore porosity p_{mA}, macropore tortuosity τ, and micropore porosity p_{mi}. Solution with known ionic concentrations $c_{0,i}$ flows into the cell with volumetric flow rate Q and leaves the cell as effluent with ionic concentrations $c_{\mathrm{eff},i}(t)$ (which are sampled precisely at the start of the downstream external region). A time trace of the applied voltage difference, $\Delta V(t)$, is shown in Fig. 2.1(e), depicting period T_p and amplitude V_{ch}. We proceed to develop a 1D mathematical description using porous electrode theory.

We take the local concentration of species i in the macropore region to be $c_{\mathrm{mA},i}(x,t)$, the concentration of species i in local micropores to be $c_{\mathrm{mi},i}(x,t)$, and the local electric potential in macropores (nondimensionalized by the thermal voltage, V_T) to be $\phi(x,t)$. Following convention, all macropore and micropore species concentrations are per unit volume of macropore or micropore respectively. As in the analysis of FTE CDI by Guyes *et al.* [79], the conservation equation for species i is

$$\begin{aligned}\frac{\partial}{\partial t}\left(p_{\mathrm{mA}}c_{\mathrm{mA},i}+p_{\mathrm{mi}}c_{\mathrm{mi},i}\right) =& \frac{\partial}{\partial x}\left[\frac{D_i p_{\mathrm{mA}}}{\tau}\left(\frac{\partial c_{\mathrm{mA},i}}{\partial x}+z_i c_{\mathrm{mA},i}\frac{\partial \phi}{\partial x}\right)\right] \\ &- \frac{\partial}{\partial x}\left(u_{\mathrm{sup}}c_{\mathrm{mA},i}\right)+R_i,\end{aligned} \tag{2.1}$$

where D_i is the mass diffusivity in bulk solution and z_i is the valence. Equation (2.1) represents the transport of ions in the macropores via diffusion, electromigration, and advection. The superficial velocity is computed as $u_{\mathrm{sup}} = Q/A_e$, where A_e is the total cross sectional area of the electrochemical cell. Equation (2.1) also includes R_i, which represents reaction source and sink terms in both macropores and micropores. Formulas for the individual terms contained in R_i are provided later in this section.

For chemical surface groups, which are immobile, Eq. (2.1) may be applied if the macropore concentration is set to zero for those species, leaving only the unsteady micropore term and the reaction term. This is appropriate because surface groups are not transported and largely occur in micropores.

The modified Donnan model [72–75] connecting the macropore and micropore concentrations for mobile ionic species is expressed as

$$c_{\mathrm{mi},i} = c_{\mathrm{mA},i}\exp\left(-z_i\Delta\phi_D+\mu_{\mathrm{att},i}\right), \tag{2.2}$$

where the electrochemical attraction potential is $\mu_{\mathrm{att},i}$ and $\Delta\phi_D \equiv \phi_{\mathrm{mi}} - \phi$ is the Donnan

potential. The nondimensional electric potential in local micropores is $\phi_{\mathrm{mi}}(x,t)$. Electric potential is taken to have a constant value inside each micropore due to the strong overlap of EDLs, but the local value of micropore potential is expected to vary across the electrode in space and in time. Several authors have noted that utilizing a concentration–dependent attraction potential with the form $\mu_{\mathrm{att}} \propto 1/\sum_i c_{\mathrm{mi},i}$ permits quantitative agreement with experimental data [79–81]. We do not employ such a model in this study, but we leave the possibility open for future works.

Electrolyte within the macropores is taken to be electroneutral, meaning

$$\sum_{i=\mathrm{mob.}} z_i c_{\mathrm{mA},i} = 0. \tag{2.3}$$

The sum in Eq. (2.3) is taken over mobile ionic species. The statement of electroneutrality for micropores, on the other hand, must include three components: i) mobile ions in the micropore solution, ii) chemical surface groups, and iii) electrons at the electrode's surface. The molar charge density of mobile ions per unit of micropore volume is given by

$$\sigma_{\mathrm{ionic}}(x,t) = \sum_{i=\mathrm{mob.}} z_i c_{\mathrm{mi},i}. \tag{2.4}$$

Chemical surface groups inside the micropores are represented using index j and concentration $c_{\mathrm{mi},j}$. Thus, the molar charge density of surface groups per unit of micropore volume may be written

$$\sigma_{\mathrm{chem}}(x,t) = \sum_{j=\mathrm{surf.}} z_j c_{\mathrm{mi},j}. \tag{2.5}$$

Incorporating all three components of micropore charge, the statement of electroneutrality for micropores,

$$\sigma_{\mathrm{ionic}} + \sigma_{\mathrm{chem}} + \sigma_{\mathrm{elec}} = 0, \tag{2.6}$$

may be used to determine the local electronic charge density $\sigma_{\mathrm{elec}}(x,t)$.

The potential drop over the Stern layer in micropores is modeled using volumetric capacitance C_S as

$$\Delta\phi_S = -\frac{F\sigma_{\mathrm{elec}}}{V_T C_S}, \tag{2.7}$$

where F is Faraday's constant, $\Delta\phi_S \equiv \phi_e - \phi_{\mathrm{mi}}$ is the Stern potential, and ϕ_e is the electrode potential. Though previous authors have considered the Stern layer capacitance to be an

empirically determined quadratic function of $\Delta\phi_S$ [73, 80, 81], a constant capacitance is sufficient for qualitative demonstration of CDI degradation.

We now discuss the different chemical reactions represented by R_i in Eq. (2.1), starting with homogeneous reactions and non–Faradaic surface reactions. Consider a general reversible first order or second order elementary reaction exemplified by

$$\sum_{k=\text{reac.}} s_k S_k \rightleftharpoons \sum_{l=\text{prod.}} s_l S_l, \tag{2.8}$$

where capital S represents the participating species and lower case s represents the stoichiometric coefficients. Furthermore, the subscript k represents the reactants and the subscript l represents the products (considering the forward direction). As a simple demonstration, we consider some species with index ξ, which is taken to be one of the products in the forward direction of Eq. (2.8). The reaction terms are written as

$$\begin{aligned} R_\xi =& s_\xi p_{\text{mA}} \left(k_f \prod_{k=\text{reac.}} c_{\text{mA},k}^{s_k} - k_b \prod_{l=\text{prod.}} c_{\text{mA},l}^{s_l} \right) \\ &+ s_\xi p_{\text{mi}} \left(k_f \prod_{k=\text{reac.}} c_{\text{mi},k}^{s_k} - k_b \prod_{l=\text{prod.}} c_{\text{mi},l}^{s_l} \right) \end{aligned} \tag{2.9}$$

for forward reaction rate coefficient k_f and backward reaction rate coefficient k_b, which are related via the equilibrium constant $K = k_f/k_b$. If the reaction involves a chemical surface group, only the micropore terms in Eq. (2.9) will be active. If multiple reactions produce or consume species ξ, the total R_ξ is the sum of the individual reaction terms.

Finally, we consider charge–transferring reactions occurring at the electrode surface inside the micropores. Consider a general redox reaction with the form

$$\sum_{k=\text{ox.}} s_k \text{Ox}_k + ne^- \rightleftharpoons \sum_{l=\text{re.}} s_l \text{Re}_l, \tag{2.10}$$

where coefficients s_k and s_l are stoichiometric coefficients for the oxidants (Ox_k) and reductants (Re_l) respectively, and n is the number of electrons involved in the reaction. The rate of production of species ξ (a reductant in Eq. (2.10) for demonstration purposes) is written

using generalized Frumkin–Butler–Volmer kinetics [82] as

$$R_\xi = -2 s_\xi p_{\mathrm{mi}} \sqrt{K_R K_O} \sqrt{\prod_{k=\mathrm{ox.}} \hat{c}_{\mathrm{mi},k}^{s_k} \prod_{l=\mathrm{re.}} \hat{c}_{\mathrm{mi},l}^{s_l}} \sinh\left(n\frac{\eta}{2}\right), \tag{2.11}$$

where we have assumed a transfer coefficient of 1/2. K_R is the reduction reaction rate coefficient, K_O is the oxidation reaction rate coefficient, and the $\hat{c}_{\mathrm{mi},k}$ terms are micropore activities computed using a reference concentration of $1\,\mathrm{mol\,L^{-1}}$. The overpotential is identified as $\eta \equiv \Delta\phi_S - \Delta\phi_{S,\mathrm{eq}}$, and the equilibrium Stern potential is given by the Nernst equation,

$$\Delta\phi_{S,\mathrm{eq}} = \frac{1}{n}\ln\left(\frac{K_R}{K_O}\right) + \frac{1}{n}\ln\left(\frac{\prod_{k=\mathrm{ox.}} \hat{c}_{\mathrm{mi},k}^{s_k}}{\prod_{l=\mathrm{re.}} \hat{c}_{\mathrm{mi},l}^{s_l}}\right). \tag{2.12}$$

As discussed next in Section 2.2.2, K_R and K_O for the anode and cathode are connected to the standard cell potential and the effective ion exchange current density for each electrode.

At this point, we summarize the model in its entirety. Consider an aqueous solution with N_M mobile ionic species and microporous electrodes with N_S chemical surface groups. Equations (2.1) to (2.3), (2.6) and (2.7) form a system of $2N_M + N_S + 3$ equations that may be solved for the variables $c_{\mathrm{mA},i=\mathrm{mob.}}$, $c_{\mathrm{mi},i=\mathrm{mob.}}$, $c_{\mathrm{mi},j=\mathrm{surf.}}$, ϕ, ϕ_{mi}, and σ_{elec}, with the appropriate reaction terms specified according to Eqs. (2.9), (2.11) and (2.12). These equations may be used for all regions of the electrochemical cell if the following modification are used: i) All micropore concentrations are set to zero in the separator, which has a purely macro–porous structure. ii) All micropore concentrations are set to zero and the macropore porosity/tortuosity are set to 1 in the upstream and downstream external bulk regions. iii) Chemical surface group macropore concentrations are set to zero in all regions.

2.2.2 Faradaic Reaction Kinetic Parameters

In this section, we explain how free parameters in the kinetic model for the electrodes — namely, reduction and oxidation rate coefficients (K_R and K_O) in the Frumkin–Butler–Volmer equation for each electrode — are related to measurable macroscopic properties of the electrodes and of the overall electrochemical cell. Anticipating that our model (or similar models) may find use in a variety of contexts involving electrochemical cells with hierarchically porous electrodes, we retain generality throughout this section, such that the results are agnostic to the specific reaction mechanism occurring in each electrode. We continue in Section 2.4.3, however, to tailor this analysis toward the specific case of FTE

CDI discussed in the main body of this work.

First, we discuss the cell voltage at open–circuit and standard conditions, which is related to the standard cell potential, E°_{cell}. Since E°_{cell} is known from chemical thermodynamics of the overall reaction, we demonstrate how the rate coefficients should be constrained to guarantee thermodynamic consistency. Second, we examine the volumetric exchange current density, i_0, for each electrode. Anticipating future work in which users may wish to calibrate model parameters via comparison of simulated and experimental polarization curves for a single electrode at standard conditions, we offer preliminary comments on how the Faradaic reaction rate coefficients for an electrode should be constrained to yield a specified effective exchange current density for that electrode.

Cell voltage at open–circuit and standard conditions

Consider a general electrochemical cell with one Faradaic reaction occurring in each porous electrode. The standard cell potential is given by $E^\circ_{\text{cell}} \equiv E^\circ_c - E^\circ_a$, where we have also indicated the standard half–cell potentials (SHE reference) of the cathode and anode, respectively. Thermodynamically, $E^\circ_{\text{cell}} = \frac{\Delta G^\circ}{nRT}$, where ΔG° is the change in molar Gibbs energy for the overall reaction at standard conditions, n is the number of electrons transferred in the overall reaction, R is the ideal gas constant, and T is the temperature. E°_{cell} is presented here as nondimensionalized by the thermal voltage, V_T, as is the case for electric potential throughout this work.

For the Frumkin–Butler–Volmer kinetics presented in Eq. (2.11), the non–dimensionalized equilibrium Stern potential (which is the Stern potential for which there is zero net reaction current, as is the case at open–circuit) for the anode and for the cathode is given by Eq. (2.12) as

$$\Delta\phi^a_{S,\text{eq}} = \frac{1}{n^a}\ln\left(\frac{K^a_R}{K^a_O}\right) + \frac{1}{n^a}\ln\left(\frac{\prod_{k=\text{an. ox.}}\hat{c}^{s_k}_{\text{mi},k}}{\prod_{l=\text{an. re.}}\hat{c}^{s_l}_{\text{mi},l}}\right) \tag{2.13}$$

and

$$\Delta\phi^c_{S,\text{eq}} = \frac{1}{n^c}\ln\left(\frac{K^c_R}{K^c_O}\right) + \frac{1}{n^c}\ln\left(\frac{\prod_{k=\text{cat. ox.}}\hat{c}^{s_k}_{\text{mi},k}}{\prod_{l=\text{cat. re.}}\hat{c}^{s_l}_{\text{mi},l}}\right), \tag{2.14}$$

respectively. Invoking the modified Donnan model (see Eq. (2.2)) and recognizing that the balance of charge for Faradaic reactions requires $\sum_{k=\text{ox.}} s_k z_k - \sum_{l=\text{re.}} s_l z_l = n^{a/c}$ at each electrode (see Eq. (2.10), and note that the '$n^{a/c}$' here refers to the electrons transferred in

each electrode's half reaction), Eqs. (2.13) and (2.14) may be rewritten as

$$\Delta\phi^{a}_{\mathrm{tot,eq}} = \frac{1}{n^a}\ln\left(\frac{K^a_R}{K^a_O}\right) + \frac{1}{n^a}\ln\left(\frac{\prod_{k=\text{an. ox.}}\hat{c}^{s_k}_{\mathrm{mA},k}}{\prod_{l=\text{an. re.}}\hat{c}^{s_l}_{\mathrm{mA},l}}\right) - \frac{\tilde{\mu}^a}{n^a} \tag{2.15}$$

and

$$\Delta\phi^{c}_{\mathrm{tot,eq}} = \frac{1}{n^c}\ln\left(\frac{K^c_R}{K^c_O}\right) + \frac{1}{n^c}\ln\left(\frac{\prod_{k=\text{cat. ox.}}\hat{c}^{s_k}_{\mathrm{mA},k}}{\prod_{l=\text{cat. re.}}\hat{c}^{s_l}_{\mathrm{mA},l}}\right) - \frac{\tilde{\mu}^c}{n^c}, \tag{2.16}$$

where the total potential difference between the electrode and the macropores at open–circuit is defined as $\Delta\phi_{\mathrm{tot,eq}} \equiv \Delta\phi_{S,\mathrm{eq}} + \Delta\phi_{D,\mathrm{eq}}$ for each electrode, and we have introduced

$$\tilde{\mu} \equiv \sum_{l=\mathrm{re.}} s_l\mu_{\mathrm{att},l} - \sum_{k=\mathrm{ox.}} s_k\mu_{\mathrm{att},k} \tag{2.17}$$

for convenience. The activity terms in Eqs. (2.15) and (2.16) now feature macropore activities ($\hat{c}_{\mathrm{mA},i}$) as opposed to the micropore activities ($\hat{c}_{\mathrm{mi},i}$) in Eqs. (2.13) and (2.14). Note, however, that the attraction potentials in Eqs. (2.15) and (2.16) may, generally speaking, have some prescribed functional dependence on the micropore activities, depending on the specific attraction potential model employed.

The standard state, denoted by the '$^\circ$' superscript, is taken to be one in which all $\hat{c}_{\mathrm{mA}}$ terms in Eqs. (2.15) and (2.16) are unity, meaning that all reactive species have concentration of 1 M throughout the macropore electrolyte. Furthermore, since no current is passed through the cell at open–circuit, the macropore potential is constant across the electrodes. The open–circuit potential across the entire cell at standard conditions is given, then, by

$$\Delta V^\circ_{\mathrm{eq}} = \Delta\phi^{c,\circ}_{\mathrm{tot,eq}} - \Delta\phi^{a,\circ}_{\mathrm{tot,eq}} = \ln\left[\left(\frac{K^c_R}{K^c_O}\right)^{1/n^c}\left(\frac{K^a_O}{K^a_R}\right)^{1/n^a}\right] + \left(\frac{\tilde{\mu}^{a,\circ}_{\mathrm{eq}}}{n^a} - \frac{\tilde{\mu}^{c,\circ}_{\mathrm{eq}}}{n^c}\right). \tag{2.18}$$

If the attraction potentials exhibit functional dependence on the micropore activities (as opposed to being specified as constants, as is the case in some studies), the use of the '$^\circ$' superscript and the 'eq' subscript in the attraction potential terms in Eq. (2.18) indicates that we are referring here to the values of the attraction potentials at standard conditions and open–circuit.

Recall that the attraction potential (introduced in Eq. (2.2)) has previously been used to capture effects such as size–based ion selectivity [39] and attraction between ions and image charges in the electrode [80]. We postulate that the cell voltage, $\Delta V^\circ_{\mathrm{eq}}$, should match

E°_{cell} in an idealized cell with $\mu_{\text{att},i} = 0$ for all ions (*i.e.*, in the hypothetical absence of the extraneous effects mentioned above). Therefore, the reaction rate coefficients should satisfy

$$\left(\frac{K^c_R}{K^c_O}\right)^{1/n^c}\left(\frac{K^a_O}{K^a_R}\right)^{1/n^a} = \exp\left(E^{\circ}_{\text{cell}}\right), \tag{2.19}$$

and the cell voltage at open circuit and standard conditions is given by

$$\Delta V^{\circ}_{\text{eq}} = E^{\circ}_{\text{cell}} + \left(\frac{\tilde{\mu}^{a,\circ}_{\text{eq}}}{n^a} - \frac{\tilde{\mu}^{c,\circ}_{\text{eq}}}{n^c}\right). \tag{2.20}$$

We find that the influence of attraction potentials in Eq. (2.20) agrees with intuitive expectations. Consider, for demonstration purposes, an electrolytic cell, which has $E^{\circ}_{\text{cell}} < 0$. At the anode, Eq. (2.17) indicates that $\tilde{\mu}^{a,\circ}_{\text{eq}}$ is driven to be more negative when oxidants are favorably electrosorbed (meaning $\mu^a_{\text{att},i=\text{ox.}} > 0$) and reductants are unfavorably electrosorbed (meaning $\mu^a_{\text{att},i=\text{re.}} < 0$) in the anode micropores. As $\tilde{\mu}^{a,\circ}_{\text{eq}}$ is driven to be more negative, Eq. (2.20) indicates that $\Delta V^{\circ}_{\text{eq}}$ will be shifted in the negative direction (further away from zero), signifying an increase in the magnitude of cell voltage required for electrolysis to occur compared to E°_{cell} on its own. To describe this effect most generally, we may say the following: decreased selectivity toward reactants and increased selectivity toward products in each electrode produces a situation in which $\Delta V^{\circ}_{\text{eq}} < E^{\circ}_{\text{cell}}$, and vice versa.

Note, however, that using Eq. (2.20) to quantitatively predict the cell voltage at open–circuit and standard conditions becomes difficult if the attraction potential terms have functional dependence on the micropore activities (as was the case in the works by [39] and [80]). Though Eq. (2.20) is still valid, the micropore activities at open–circuit and standard conditions (which are necessary to compute $\tilde{\mu}^{\circ}_{\text{eq}}$ in each electrode) may be difficult or impossible to write as closed–form expressions that depend only on the input parameters. In such cases, numerical solution of the full nonlinear system is required to reveal $\Delta V^{\circ}_{\text{eq}}$, the micropore activities, and $\tilde{\mu}^{\circ}_{\text{eq}}$ for each electrode at open–circuit and standard conditions.

Exchange current density at standard conditions

We are now interested in uncovering the relationship between the Faradaic reaction rate coefficients and the exchange current density for a given electrode at standard conditions. We aim to express the relationship in terms of experimentally accessible quantities, laying a path toward setting the kinetic parameters for each electrode based on comparison to an

experimentally–measured polarization curve at standard conditions.

The Frumkin–Butler–Volmer equation in Eq. (2.11) may be rewritten to give the volumetric current, i, in terms of the overpotential, $\eta \equiv \Delta\phi_S - \Delta\phi_{S,\mathrm{eq}}$, as

$$i = -2nFp_{\mathrm{mi}}\sqrt{K_R K_O}\sqrt{\prod_{k=\mathrm{ox.}} \hat{c}_{\mathrm{mi},k}^{s_k} \prod_{l=\mathrm{re.}} \hat{c}_{\mathrm{mi},l}^{s_l}}\,\sinh\left(n\frac{\eta}{2}\right), \tag{2.21}$$

where $\Delta\phi_{S,\mathrm{eq}}$ is defined in Eq. (2.12). Note that in this section, n refers to the number of electrons involved in the electrode half reaction, not the overall cell reaction. Though a transfer coefficient of 1/2 has been assumed, the analysis shown here may easily be generalized for different transfer coefficients. The definition of overpotential used in Eq. (2.21) signifies that electron transfer across the Stern layer drives Faradaic reactions. However, this driving overpotential (which occurs over a very thin zone adjacent to the micropore walls) is not directly measurable in experiments. Additionally, the appearance of micropore activities in Eq. (2.21) poses a problem, since the micropore concentrations vary with the cell voltage and and are not directly measurable either. As a result, Eq. (2.21) cannot be used to fit experimental polarization curves in its present state.

In order to remedy this dilemma, we begin by considering the total potential drop $\Delta\phi_{\mathrm{tot}} \equiv \Delta\phi_S + \Delta\phi_D$, which represents the difference in electric potential between the electrode and the macropore electrolyte. We also introduce the total overpotential as $\eta' \equiv \Delta\phi_{\mathrm{tot}} - \Delta\phi_{\mathrm{tot,eq}}$. Consider an experiment performed using a working porous electrode and a well–characterized counter–electrode (reference electrode) immersed in a known electrolyte (which we will take to have unity activity for all reactive species, *i.e.*, standard conditions). Unlike η, η' may be computed from experimentally measured profiles of current and cell voltage with relative ease (by applying analytical corrections to remove counter–electrode overpotential and bulk–electrolyte Ohmic overpotential).

Moving forward, we seek to write Eq. (2.21) in terms of the total overpotential η' instead of the driving overpotential η. Furthermore, we endeavour to replace the micropore activities with macropore activities wherever possible. For our preliminary analysis, we will assume that macropore activities remain equal to unity as the polarization curve is measured. This corresponds to a regime in which transport is rapid enough compared to reactions to assume that reactants are instantaneously resupplied into the macropores and products are instantaneously expelled. We anticipate that this assumption may be revisited in future work. Our aim in this section, however, is to present a simple starting point for setting the

reaction rate coefficients based on comparison to experimental measurements.

We begin by inserting the definition of the equilibrium Stern potential (Eq. (2.12)) into η in Eq. (2.21) and rewriting all micropore activities using the modified Donnan model as $\hat{c}_{\mathrm{mi},i} = \exp(-z_i \Delta\phi_D + \mu_{\mathrm{att},i})$, where macropore activities for reactive species have been set to unity in accordance with the preceding discussion. Recognizing that the balance of charge for Faradaic reactions requires $\sum_{k=\mathrm{ox.}} s_k z_k - \sum_{l=\mathrm{re.}} s_l z_l = n$ (Eq. (2.10)), the resulting equation reads

$$\begin{aligned} i = &- nF p_{\mathrm{mi}} \exp\left(-\frac{\tilde{z}}{2}\Delta\phi_D\right)\left[K_O \exp\left(\frac{n}{2}\Delta\phi_{\mathrm{tot}} + \sum_{l=\mathrm{re.}} s_l \mu_{\mathrm{att},l}\right)\right. \\ &\left. - K_R \exp\left(-\frac{n}{2}\Delta\phi_{\mathrm{tot}} + \sum_{k=\mathrm{ox.}} s_k \mu_{\mathrm{att},k}\right)\right], \end{aligned} \tag{2.22}$$

where we have introduced

$$\tilde{z} \equiv \sum_{k=\mathrm{ox.}} s_k z_k + \sum_{l=\mathrm{re.}} s_l z_l \tag{2.23}$$

for convenience.

We find the expression for $\Delta\phi_{\mathrm{tot,eq}}$ by setting Eq. (2.22) equal to zero, revealing

$$\Delta\phi_{\mathrm{tot,eq}} = \frac{1}{n}\left[\ln\left(\frac{K_R}{K_O}\right) + \tilde{\mu}_{\mathrm{eq}}\right], \tag{2.24}$$

where $\tilde{\mu}$ is defined in Eq. (2.17). Recall that the attraction potentials are, generally speaking, prescribed functions of the micropore activities, which may exhibit variation as the cell voltage (or current) is swept during measurement of the polarization curve. Thus, the attraction potentials in Eq. (2.24) should be evaluated using the micropore activities at open–circuit and standard conditions. Determining these values for a given set of electrode reaction rate coefficients may require numerical solution of the full nonlinear governing equations for a single electrode.

Incorporating the total overpotential, $\eta' \equiv \Delta\phi_{\mathrm{tot}} - \Delta\phi_{\mathrm{tot,eq}}$, and Eq. (2.24) into Eq. (2.22),

we find that Eq. (2.22) may be written as

$$\begin{aligned} i = &- 2nFp_{\mathrm{mi}}\sqrt{K_R K_O}\exp\left[\frac{1}{2}\left(\sum_{k=\mathrm{ox.}} s_k\mu_{\mathrm{att},k} + \sum_{l=\mathrm{re.}} s_l\mu_{\mathrm{att},l}\right)\right] \\ &\times \exp\left(-\frac{\tilde{z}}{2}\Delta\phi_D\right)\sinh\left[\frac{n\eta' + (\tilde{\mu}-\tilde{\mu}_{\mathrm{eq}})}{2}\right]. \end{aligned} \tag{2.25}$$

Equation (2.25) reveals that even under the assumption of unity activity for all reactive species in the macropores, the complexity introduced by the modified Donnan model makes it impossible to describe the electrode kinetics purely in terms of the total overpotential η'. We isolate some of the terms in front of the hyperbolic sine in Eq. (2.25) and draw an analogy to the classical Butler–Volmer equation, identifying the effective ion exchange current density for the porous electrode as

$$i_0 \equiv nFp_{\mathrm{mi}}\sqrt{K_R K_O}\exp\left[\frac{1}{2}\left(\sum_{k=\mathrm{ox.}} s_k\mu_{\mathrm{att},k} + \sum_{l=\mathrm{re.}} s_l\mu_{\mathrm{att},l}\right)\right]\exp\left(-\frac{\tilde{z}}{2}\Delta\phi_D\right). \tag{2.26}$$

We find that the effective ion exchange current density is enhanced when reactants or products exhibit increased selectivity (positive attraction potential) in the micropores. Similarly, the Donnan potential, $\Delta\phi_D$, appears directly inside an exponential with a coefficient that depends on $\tilde{z}$. The definition of $\tilde{z}$ (in Eq. (2.23)) indicates that this exponential term enhances the effective ion exchange current density if the net valence of the reactants and products (weighted by stoichiometric coefficients) is of opposite sign to $\Delta\phi_D$, promoting electrosorption of reactive species into the micropores.

The hyperbolic sine term in Eq. (2.25) contains the total overpotential for Faradaic reactions, but we observe that there is a shift in the effective overpotential due to the attraction potentials. The effective overpotential (*i.e.,* the argument of the hyperbolic sine) is shifted in the positive direction (associated with net oxidation at the electrode) when reductants exhibit increased selectivity in the micropores and oxidants exhibit reduced selectivity. This finding aligns with our intuitive expectations.

Finally, we offer a brief note on how Eqs. (2.25) and (2.26) may be used to constrain the values of K_R and K_O by comparison to experimental polarization curves. We begin by considering the simplest possible case, wherein i) the attraction potentials, $\mu_{\mathrm{att},i}$, are set to constants and ii) the stoichiometric–coefficient–weighted sum of reactant and product valences, $\tilde{z}$, is zero (as is the case, for example, in reduction of a monovalent cation into a

monovalent anion via a two–electron reaction). For this case, comparison of experiments and simulations is straightforward: Dependence on $\Delta\phi_D$ is eliminated from Eqs. (2.25) and (2.26) because $\tilde{z} = 0$. All attraction potential terms are known constants, and we find furthermore that $(\tilde{\mu} - \tilde{\mu}^{\mathrm{eq}}) = 0$.

Therefore, for this simple case, i_0, is a constant, and the current density varies with total overpotential simply as $\sinh(n\eta'/2)$ (reminiscent of the classical Butler–Volmer model). The value of i_0 may be determined from a fit of experimental data for i and η' (*e.g.,* by use of the Tafel equation, in which the hyperbolic sine in Eq. (2.25) is approximated as an exponential for large overpotentials). For a measured (constant) value of i_0 and known (constant) attraction potentials, Eq. (2.26) serves as a simple algebraic constraint for the quantity $\sqrt{K_R K_O}$ for a given electrode.

For more complex cases, dependence on $\Delta\phi_D$ may remain in Eqs. (2.25) and (2.26), and the attraction potentials may have a specified functional dependence on the micropore activities. Since the attraction potentials and $\Delta\phi_D$ may be nonlinearly dependent on the rate coefficients themselves, an iterative fitting procedure is required. One option is an optimization approach using numerous simulated polarization curves with different values of $\sqrt{K_R K_O}$. The value of $\sqrt{K_R K_O}$ may be adjusted over successive iterations to minimize the error between simulated and experimentally–measured polarization curves. We do not attempt implementation of such a procedure in this work, but we envision that this approach may be of interest in future works.

Concluding remarks on kinetic parameters

Thus, we have offered a preliminary analysis of how reaction rate coefficients in our Faradaic reaction model are connected to experimentally measurable macroscopic properties of the electrodes and of the overall electrochemical cell. We anticipate that the thoughts presented here will be further developed and refined in future works, particularly those attempting quantitative validation of our model.

As an example of the need for further analysis, observe that there are four unknown kinetic rate coefficients to be determined (two per electrode), but the analysis in this section only provides three constraints (one based on the standard cell potential for the overall cell, and one for each electrode based on its individual exchange current density). Thus, an additional constraint is required to fully close the system. Furthermore, some applications may require generalization of our analysis for electrodes with multiple competing Faradaic

reactions. In that case, even more constraints are required to fully close the system and determine the rate coefficients for all reactions.

Up until this point, we have maintained generality while discussing the electrode kinetics and attraction potentials. In Section 2.4.3, we revisit this discussion and consider the specific reaction mechanisms pertinent to FTE CDI cells.

2.3 Numerical Methods and Solver Algorithm

In this section, we describe the numerical methods utilized in our solver. First, we write the governing equations in such a way that the unknown variables are clearly represented. We then write the discretized equations and outline the time advancement algorithm.

Consider an aqueous solution with N_M mobile ionic species and microporous electrodes with N_S chemical surface groups. Combining the equations in Section 2.2.1, we have the following:

$$\begin{aligned}\frac{\partial}{\partial t}\left(p_{\mathrm{mA}}c_{\mathrm{mA},i}+p_{\mathrm{mi}}c_{\mathrm{mi},i}\right) =& \frac{\partial}{\partial x}\left[\frac{D_i p_{\mathrm{mA}}}{\tau}\left(\frac{\partial c_{\mathrm{mA},i}}{\partial x}+z_i c_{\mathrm{mA},i}\frac{\partial \phi}{\partial x}\right)\right] \\ & -\frac{\partial}{\partial x}\left(u_{\mathrm{sup}}c_{\mathrm{mA},i}\right)+R_i\left(c_{\mathrm{mA}},c_{\mathrm{mi}},\phi_{\mathrm{mi}}\right),\end{aligned} \tag{2.27}$$

$$c_{\mathrm{mi},i} = c_{\mathrm{mA},i}\exp\left[z_i(\phi-\phi_{\mathrm{mi}})+\mu_{\mathrm{att},i}\right], \tag{2.28}$$

$$\sum_{i=\mathrm{mob.}} z_i c_{\mathrm{mA},i} = 0, \tag{2.29}$$

$$-\sigma_{\mathrm{elec}} = \sum_{i=\mathrm{mob.}} z_i c_{\mathrm{mi},i} + \sum_{j=\mathrm{surf.}} z_j c_{\mathrm{mi},j}, \tag{2.30}$$

and

$$\phi_{\mathrm{mi}} = \phi_e - \frac{F\sigma_{\mathrm{elec}}}{V_T C_S}. \tag{2.31}$$

Equation (2.27) is written once for each mobile species and once for each surface group ($N_M + N_S$ total). Recall that the macropore transport and reaction terms in Eq. (2.27) are removed for surface groups. Reaction terms in Eq. (2.27), R_i, are known functions of the local macropore concentrations, micropore concentrations, and micropore potential based on the kinetics discussed in Section 2.2. Equation (2.28) is written once for each mobile species (N_M total), and Eqs. (2.29) to (2.31) are individual equations. The result is a system of $2N_M + N_S + 3$ equations that may be solved for the variables $c_{\mathrm{mA},i=\mathrm{mob.}}$,

$c_{\mathrm{mi},i=\mathrm{mob.}}$, $c_{\mathrm{mi},j=\mathrm{surf.}}$, ϕ, ϕ_{mi}, and σ_{elec}.

We first discuss discretization of Eq. (2.27). For the remainder of this section, superscript indices refer to discrete spatial and temporal points. For example, the quantity $a^{(i,n)}$ refers to the variable a at the discrete location indexed by i and at the time step indexed by n. In our staggered mesh formulation, all unknown variables are stored at cell centers (indicated using integer–valued superscript index i) and the flux is computed at adjacent cell faces (indicated using half–integer–valued superscript index $i \pm \frac{1}{2}$). The flux is computed at time index n using second order finite differences and second order interpolation as

$$\begin{aligned} F^{\left(i\pm\frac{1}{2},n\right)} = &- \frac{D_i p_{\mathrm{mA}}}{\tau}\left(\frac{\pm c_{\mathrm{mA},i}^{(i\pm1,n)} \mp c_{\mathrm{mA},i}^{(i,n)}}{\Delta x} + z_i \frac{c_{\mathrm{mA},i}^{(i\pm1,n)} + c_{\mathrm{mA},i}^{(i,n)}}{2}\frac{\pm\phi^{(i\pm1,n)} \mp \phi^{(i,n)}}{\Delta x}\right) \\ &+ u_{\mathrm{sup}} \frac{c_{\mathrm{mA},i}^{(i\pm1,n)} + c_{\mathrm{mA},i}^{(i,n)}}{2}. \end{aligned} \tag{2.32}$$

The entire transport equation (Eq. (2.27)) is discretized, then, as

$$\begin{aligned} p_{\mathrm{mA}}\frac{c_{\mathrm{mA},i}^{(i,n)} - c_{\mathrm{mA},i}^{(i,n-1)}}{\Delta t} + p_{\mathrm{mi}}\frac{c_{\mathrm{mi},i}^{(i,n)} - c_{\mathrm{mi},i}^{(i,n-1)}}{\Delta t} = &- \frac{F^{\left(i+\frac{1}{2},n\right)} - F^{\left(i-\frac{1}{2},n\right)}}{\Delta x} \\ &+ R_i^{(i,n)}\left(c_{\mathrm{mA}}^{(i,n)}, c_{\mathrm{mi}}^{(i,n)}, \phi_{\mathrm{mi}}^{(i,n)}\right). \end{aligned} \tag{2.33}$$

Though we have described the scheme for a uniform mesh with N_c cells, the results presented in this work were computed using localized spatial refinement near interfaces. Second order implementation of a non–uniform mesh is achieved by inserting the appropriate local Δx values in Eqs. (2.32) and (2.33). Similarly, we have described the scheme using a first order implicit temporal discretization, but implementation of higher order schemes requires straightforward modification of the temporal terms in Eq. (2.33).

Discretization of the remaining equations (Eqs. (2.28) to (2.31), which are algebraic equations) is trivial — all quantities are evaluated at location and time indices i and n, respectively. Thus, we have:

$$c_{\mathrm{mi},i}^{(i,n)} = c_{\mathrm{mA},i}^{(i,n)} \exp\left[z_i(\phi^{(i,n)} - \phi_{\mathrm{mi}}^{(i,n)}) + \mu_{\mathrm{att},i}\right], \tag{2.34}$$

$$\sum_{i=\mathrm{mob.}} z_i c_{\mathrm{mA},i}^{(i,n)} = 0, \tag{2.35}$$

$$-\sigma_{\text{elec}}^{(i,n)} = \sum_{i=\text{mob.}} z_i c_{\text{mi},i}^{(i,n)} + \sum_{j=\text{surf.}} z_j c_{\text{mi},j}^{(i,n)}, \tag{2.36}$$

and

$$\phi_{\text{mi}}^{(i,n)} = \phi_e - \frac{F\sigma_{\text{elec}}^{(i,n)}}{V_T C_S}. \tag{2.37}$$

The discretized macropore and micropore quantities at time n are stored in separate vectors as

$$\overrightarrow{z_{\text{mA}}}^n = \begin{bmatrix} c_{\text{mA},1}^{(1,n)} \\ c_{\text{mA},2}^{(1,n)} \\ \vdots \\ c_{\text{mA},N_M}^{(1,n)} \\ \phi^{(1,n)} \\ c_{\text{mA},1}^{(2,n)} \\ c_{\text{mA},2}^{(2,n)} \\ \vdots \\ c_{\text{mA},N_M}^{(2,n)} \\ \phi^{(2,n)} \\ \vdots \\ \vdots \\ c_{\text{mA},1}^{(N_c,n)} \\ c_{\text{mA},2}^{(N_c,n)} \\ \vdots \\ c_{\text{mA},N_M}^{(N_c,n)} \\ \phi^{(N_c,n)} \end{bmatrix}, \qquad \overrightarrow{z_{\text{mi}}}^n = \begin{bmatrix} c_{\text{mi},1}^{(1,n)} \\ c_{\text{mi},2}^{(1,n)} \\ \vdots \\ c_{\text{mi},N_M+N_S}^{(1,n)} \\ \phi_{\text{mi}}^{(1,n)} \\ \sigma_{\text{elec}}^{(1,n)} \\ c_{\text{mi},1}^{(2,n)} \\ c_{\text{mi},2}^{(2,n)} \\ \vdots \\ c_{\text{mi},N_M+N_S}^{(2,n)} \\ \phi_{\text{mi}}^{(2,n)} \\ \sigma_{\text{elec}}^{(2,n)} \\ \vdots \\ \vdots \\ c_{\text{mi},1}^{(N_c,n)} \\ c_{\text{mi},2}^{(N_c,n)} \\ \vdots \\ c_{\text{mi},N_M+N_S}^{(N_c,n)} \\ \phi_{\text{mi}}^{(N_c,n)} \\ \sigma_{\text{elec}}^{(N_c,n)} \end{bmatrix}. \tag{2.38}$$

Alternating colored groupings in Eq. (2.38) indicate clusters of unknown variables that belong to the same computational cell. The dimensions of $\overrightarrow{z_{\text{mA}}}^n$ are $[N_c\,(N_M+1)\times 1]$, and the dimensions of $\overrightarrow{z_{\text{mi}}}^n$ are $[N_c\,(N_M+N_S+2)\times 1]$. In anticipation of solving the equations iteratively for each time step due to nonlinearity, we seek to linearize the equations around

the base states $\overrightarrow{z_{\mathrm{mA}}}^{\star}$ and $\overrightarrow{z_{\mathrm{mi}}}^{\star}$ by writing

$$\begin{aligned} \overrightarrow{z_{\mathrm{mA}}}^{n} &= \overrightarrow{z_{\mathrm{mA}}}^{\star} + \overrightarrow{\delta z_{\mathrm{mA}}} \\ \overrightarrow{z_{\mathrm{mi}}}^{n} &= \overrightarrow{z_{\mathrm{mi}}}^{\star} + \overrightarrow{\delta z_{\mathrm{mi}}}. \end{aligned} \tag{2.39}$$

We will proceed to linearize the system of equations and write the result as two separate (but coupled) sub–systems: one corresponding to the macropore variables in $\overrightarrow{z_{\mathrm{mA}}}^{n}$ and the other corresponding to the micropore variables in $\overrightarrow{z_{\mathrm{mi}}}^{n}$.

To derive the macropore sub–system, we substitute Eq. (2.39) into Eq. (2.33) (for only the specific equations corresponding to the N_M mobile ionic species) and into Eq. (2.35) and only retain terms up to first order in $\overrightarrow{\delta z_{\mathrm{mA}}}$ and $\overrightarrow{\delta z_{\mathrm{mi}}}$. As a result, the $N_c(N_M + 1)$ equations represented by Eqs. (2.33) and (2.35) for mobile ionic species and the macropore electric potential may be represented together as the linear system

$$\mathbf{M_1}\overrightarrow{\delta z_{\mathrm{mA}}} + \mathbf{M_2}\overrightarrow{\delta z_{\mathrm{mi}}} = \overrightarrow{g_1}\left(\overrightarrow{z_{\mathrm{mA}}}^{\star}, \overrightarrow{z_{\mathrm{mi}}}^{\star}\right), \tag{2.40}$$

where matrices $\mathbf{M_1}$ (size $[N_c\,(N_M + 1) \times N_c\,(N_M + 1)]$) and $\mathbf{M_2}$ (size $[N_c\,(N_M + 1) \times N_c\,(N_M + N_S + 2)]$) contain coefficients that depend only on the base–state variables. The right–hand side, $\overrightarrow{g_1}$ (size $[N_c\,(N_M + 1) \times 1]$), is a nonlinear function of the base–state variables.

To derive the micropore sub–system, Eq. (2.39) is substituted into Eq. (2.33) (for only the specific equations corresponding to the N_S surface group species) and into Eqs. (2.34), (2.36) and (2.37). Only terms up to first order in $\overrightarrow{\delta z_{\mathrm{mA}}}$ and $\overrightarrow{\delta z_{\mathrm{mi}}}$ are retained, allowing us to write the $N_c(N_M + N_S + 2)$ equations together as the linear system

$$\mathbf{M_3}\overrightarrow{\delta z_{\mathrm{mA}}} + \mathbf{M_4}\overrightarrow{\delta z_{\mathrm{mi}}} = \overrightarrow{g_2}\left(\overrightarrow{z_{\mathrm{mA}}}^{\star}, \overrightarrow{z_{\mathrm{mi}}}^{\star}\right), \tag{2.41}$$

where matrices $\mathbf{M_3}$ (size $[N_c\,(N_M + N_S + 2) \times N_c\,(N_M + 1)]$) and $\mathbf{M_4}$ (size $[N_c\,(N_M + N_S + 2) \times N_c\,(N_M + N_S + 2)]$) and the right–hand–side, $\overrightarrow{g_2}$ (size $[N_c\,(N_M + N_S + 2) \times 1]$), serve analogous purposes to their counterparts in Eq. (2.40).

Denoting the inverse of $\mathbf{M_4}$ as $\mathbf{M_4^{-1}}$, Eq. (2.41) is solved for $\overrightarrow{\delta z_{\mathrm{mi}}}$ and the result is substituted into Eq. (2.40) to reveal

$$\left[\mathbf{M_1} - \mathbf{M_2}\mathbf{M_4^{-1}}\mathbf{M_3}\right]\overrightarrow{\delta z_{\mathrm{mA}}} = \overrightarrow{g_1} - \mathbf{M_2}\mathbf{M_4^{-1}}\overrightarrow{g_2}. \tag{2.42}$$

Algorithm 2.1 Pseudocode for computation of $\overrightarrow{z_{\mathrm{mA}}}^{n}$ and $\overrightarrow{z_{\mathrm{mi}}}^{n}$, assuming $\overrightarrow{z_{\mathrm{mA}}}^{n-1}$ and $\overrightarrow{z_{\mathrm{mi}}}^{n-1}$ are known.

$\overrightarrow{z_{\mathrm{mA}}}^{\star} \leftarrow \overrightarrow{z_{\mathrm{mA}}}^{n-1}$
$\overrightarrow{z_{\mathrm{mi}}}^{\star} \leftarrow \overrightarrow{z_{\mathrm{mi}}}^{n-1}$
$\mathcal{R} \leftarrow \infty$
$\mathcal{R}_{\max} \leftarrow$ tolerance
while $\mathcal{R} \geq \mathcal{R}_{\max}$ **do**
    $\mathbf{M_1}$, $\mathbf{M_2}$, $\mathbf{M_3}$, $\mathbf{M_4}$, $\overrightarrow{g_1}$, $\overrightarrow{g_2}$ computed using $\overrightarrow{z_{\mathrm{mA}}}^{\star}$, $\overrightarrow{z_{\mathrm{mi}}}^{\star}$
    $\mathbf{M_4^{-1}}$ computed using $\mathbf{M_4}$
    $\overrightarrow{\delta z_{\mathrm{mA}}} \leftarrow \left[\mathbf{M_1} - \mathbf{M_2 M_4^{-1} M_3}\right]^{-1} \left(\overrightarrow{g_1} - \mathbf{M_2 M_4^{-1}} \overrightarrow{g_2}\right)$
    $\overrightarrow{\delta z_{\mathrm{mi}}} \leftarrow \mathbf{M_4^{-1}} \left(\overrightarrow{g_2} - \mathbf{M_3} \overrightarrow{\delta z_{\mathrm{mA}}}\right)$
    $\overrightarrow{z_{\mathrm{mA}}}^{\star} \leftarrow \overrightarrow{z_{\mathrm{mA}}}^{\star} + \overrightarrow{\delta z_{\mathrm{mA}}}$
    $\overrightarrow{z_{\mathrm{mi}}}^{\star} \leftarrow \overrightarrow{z_{\mathrm{mi}}}^{\star} + \overrightarrow{\delta z_{\mathrm{mi}}}$
    $\mathcal{R} \leftarrow ||\overrightarrow{\delta z_{\mathrm{mA}}}|| + ||\overrightarrow{\delta z_{\mathrm{mi}}}||$
end while
$\overrightarrow{z_{\mathrm{mA}}}^{n} \leftarrow \overrightarrow{z_{\mathrm{mA}}}^{\star}$
$\overrightarrow{z_{\mathrm{mi}}}^{n} \leftarrow \overrightarrow{z_{\mathrm{mi}}}^{\star}$

We may now use Eqs. (2.41) and (2.42) to solve Eqs. (2.33) to (2.37) iteratively for $\overrightarrow{z_{\mathrm{mA}}}^{n}$ and $\overrightarrow{z_{\mathrm{mi}}}^{n}$, taking $\overrightarrow{z_{\mathrm{mA}}}^{n-1}$ and $\overrightarrow{z_{\mathrm{mi}}}^{n-1}$ to be known from the previous time step or the initial condition. The final algorithm, which is equivalent to Newton–Raphson iteration within each time step, is written as pseudocode in Algorithm 2.1.

The algorithm discussed here may be coupled with any desired boundary conditions via appropriate modification of the discrete flux (Eq. (2.32)) at the boundaries. In order to provide a concrete example, we discuss the boundary conditions and initial condition for the full–cell FTE CDI simulations presented in Section 2.4.3.

At the inflow boundary, the macropore concentrations of all mobile species are known, and the electric potential is assigned a reference value of 0 V. We implement this in our solver by using the standard ghost–cell method for Dirichlet boundary conditions. At the outflow boundary, a convective boundary treatment is applied to all mobile species. We implement the convective boundary treatment by using one–sided finite differences to compute fluxes precisely at the outflow boundary. The homogeneous–Neumann condition is used for the electric potential. At initialization, the macropore and micropore concentrations for each of the mobile species are set to its inflow concentration, in a uniform manner across the entire cell. The electrodes are pristine (no chemical surface groups) and uncharged at initialization.

We assume uniform electric potential (equal to the reference value of 0 V) across the entire cell at initialization.

2.4 Results and Discussion

This section contains three major parts. In Section 2.4.1, we perform numerical verification by comparing simulated electrochemical impedance spectroscopy (EIS) against an analytical "transmission–line" (TL) circuit model. In Section 2.4.2, we explore the interplay between pH dynamics and surface chemistry by comparing our model's predictions against those of a model that employs a quasi–steady–state model for pH. In Section 2.4.3, we present full–cell FTE CDI simulation results for a set of nominal cases.

2.4.1 Numerical Verification Using EIS

As discussed in Section 2.1, porous electrode theory originally drew inspiration from the study of supercapacitors, starting when de Levie [64, 65] described the charging and discharging dynamics of porous electrodes in electrolyte solutions using linear circuit elements. Such TL models have since been constructed for hierarchically–porous electrodes, exhibiting good agreement with experimental EIS [66–68, 83]. In this section, we simulate EIS using the high–fidelity, nonlinear model introduced in Section 2.2.1 and the numerical implementation described in 2.3. We verify consistency of the solver by comparing results against the analytical TL model, which is valid in the limit of small voltage perturbations.

We use a binary electrolyte with species O^+ and R^- at initial concentrations $c_{0,O} = c_{0,R} = c_0$. We consider the Faradaic reaction $O^+ + 2\,e^- \longleftrightarrow R^-$ with kinetic parameters given by $K_O = K_R$ at both electrodes, ensuring an equilibrium cell potential of 0 V. For the validation exercise presented here, we set velocity equal to zero and employ a driving voltage with the form $\Delta V_{\mathrm{EIS}}(t) = V_{\mathrm{EIS}} \sin(2\pi f t)$, with $V_{\mathrm{EIS}} = 1\,\mathrm{mV}$ and f as the driving frequency. The driving voltage is a small perturbation around the equilibrium voltage of the cell, allowing us to perform comparison against a TL model of the equilibrium state.

The TL model was constructed by following the approach of Huang & Zhang [84] and Alfisi *et al.* [83] while neglecting resistance of the solid electrode phase. As shown in Fig. 2.2, the total impedance of the CDI cell, Z, is given by the sum of the electrode impedance, Z_e, and the separator impedance, Z_s. For a solution with conductivity σ given by $\sigma \equiv$

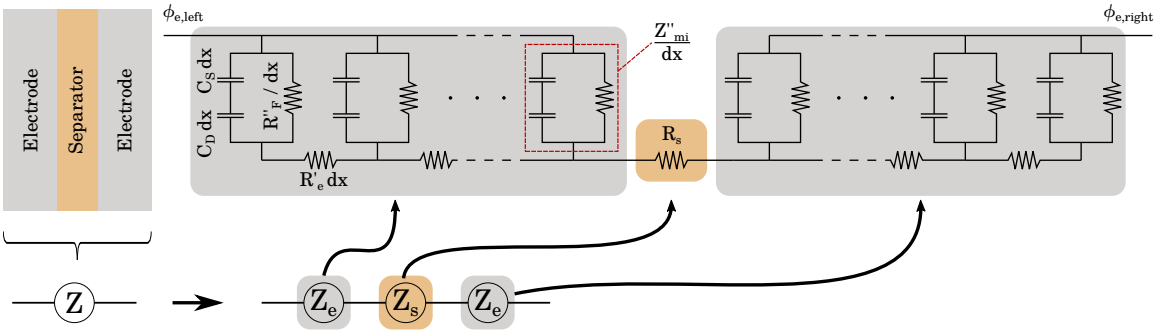

Figure 2.2: Transmission line (TL) model for the FTE CDI cell. Transport in the macropores is characterized by an Ohmic resistance. The micropore elements contain two capacitors in series, representing the capacitances associated with the Donnan and Stern potentials. Faradaic reactions in micropores are represented by a resistance placed in parallel to the two capacitors.

$\sum_i F z_i^2 c_i D_i / V_T$, impedance of the separator is

$$Z_s = R_{\mathrm{S}} = \frac{L_s \tau_s}{p_s A_e \sigma}, \tag{2.43}$$

where p_s and τ_s are the porosity and tortuosity for the separator membrane. The electrode impedance is given by

$$Z_e = \sqrt{\frac{R'_e Z''_{\mathrm{mi}}}{A_e}} \coth\left(L_e \sqrt{\frac{A_e R'_e}{Z''_{\mathrm{mi}}}}\right), \tag{2.44}$$

where $R'_e = \tau / p_{\mathrm{mA}} A_e \sigma$ is the macropore resistance per unit length. The linearized micropore interfacial impedance per unit volume is given by

$$Z''_{\mathrm{mi}} = \left(\frac{1}{R''_{\mathrm{F}}} + \left(\frac{1}{j\omega C_{\mathrm{D}}} + \frac{1}{j\omega C_{\mathrm{S}}}\right)^{-1}\right)^{-1}, \tag{2.45}$$

where j is the imaginary unit and $\omega = 2\pi f$. R''_{F} is the volumetric resistance from linearization of Eq. (2.11) for small overpotentials, resulting in

$$R''_{\mathrm{F}} = \frac{V_T}{p_{\mathrm{mi}} n^2 F \sqrt{K_R K_O} \sqrt{\prod_{k=\mathrm{ox.}} \hat{c}_{\mathrm{mi},k}^{s_k} \prod_{l=\mathrm{re.}} \hat{c}_{\mathrm{mi},l}^{s_l}}}. \tag{2.46}$$

In contrast to Alfisi *et al.* [83], we include both the Donnan and Stern layer capacitances in Eq. (2.45). C_S is a constant in this work, and the volumetric Donnan capacitance is given by $C_D = \sum_i p_{\mathrm{mi}} c_{\mathrm{mA},i} F / V_{\mathrm{T}}$.

Table 2.1: Summary of physical constants for EIS simulations.

Symbol	Description	Value
V_T	Thermal voltage	$25.85\,\mathrm{mV}$
T	Temperature	$298\,\mathrm{K}$
F	Faraday constant	$96\,485\,\mathrm{C\,mol^{-1}}$
D_{O^+}	O^+ diffusivity	$1.33 \times 10^{-9}\,\mathrm{m^2\,s^{-1}}$
D_{R^-}	R^- diffusivity	$2.03 \times 10^{-9}\,\mathrm{m^2\,s^{-1}}$

Table 2.2: Cell geometry and operating condition parameters for EIS simulations.

Symbol	Description	Value
L_e	Electrode thickness	$0.6\,\mathrm{mm}$
L_{S}	Separator thickness	$65\,\mu\mathrm{m}$
L_{res}	Inflow/outflow thickness	$3\,\mathrm{mm}$
A_e	Electrode area	$6.25\,\mathrm{cm^2}$
p_{mA}	Macropore porosity	0.8
p_{mi}	Micropore porosity	0.172
p_{S}	Separator porosity	0.8
τ	Macropore tortuosity	$p^{-0.5}$
τ_{S}	Separator tortuosity	$p_{\mathrm{S}}^{-0.5}$
V_{EIS}	EIS voltage amplitude	$1\,\mathrm{mV}$
f	EIS frequency	$\left[1 \times 10^{-3}\,\mathrm{s^{-1}}, 1 \times 10^{1}\,\mathrm{s^{-1}}\right]$
Q	Electrolyte flow rate	$0\,\mathrm{mL/min}$
C_{S}	Stern capacitance	$200\,\mathrm{F\,mL^{-1}}$
c_0	O^+, R^- bulk concentration	$5\,\mathrm{mM}$, $10\,\mathrm{mM}$, $20\,\mathrm{mM}$

The physical constants used for numerical EIS are printed in Table 2.1, and a summary of parameters describing the cell geometry and operating conditions is available in Table 2.2. We report the Faradaic reaction kinetic parameters in Table 2.3.

Nyquist plots of the total cell impedance are depicted in Fig. 2.3, where nonlinear simulation results are shown as discrete points and analytical results from the TL model are shown as continuous curves. In Fig. 2.3(a), the Faradaic reaction rate coefficients are fixed and the bulk electrolyte concentration is varied, while in Fig. 2.3(b), the bulk electrolyte concentration is fixed and the rate coefficients are varied (while preserving $K_R = K_O$).

The analytical curves in Fig. 2.3 align with intuitive expectations for the circuit in Fig. 2.2. In the high frequency limit ($\omega \to \infty$, at the lower left of each plot), Z''_{mi} tends

Table 2.3: Faradaic reaction kinetic parameters for EIS simulations.

Reaction	Parameter	Value
$\mathrm{O}^+ + 2\mathrm{e}^- \longleftrightarrow \mathrm{R}^-$	K_{R}	$5\,\mathrm{mol\,m^{-3}\,s^{-1}}$, $10\,\mathrm{mol\,m^{-3}\,s^{-1}}$, $20\,\mathrm{mol\,m^{-3}\,s^{-1}}$
	K_{O}	$5\,\mathrm{mol\,m^{-3}\,s^{-1}}$, $10\,\mathrm{mol\,m^{-3}\,s^{-1}}$, $20\,\mathrm{mol\,m^{-3}\,s^{-1}}$

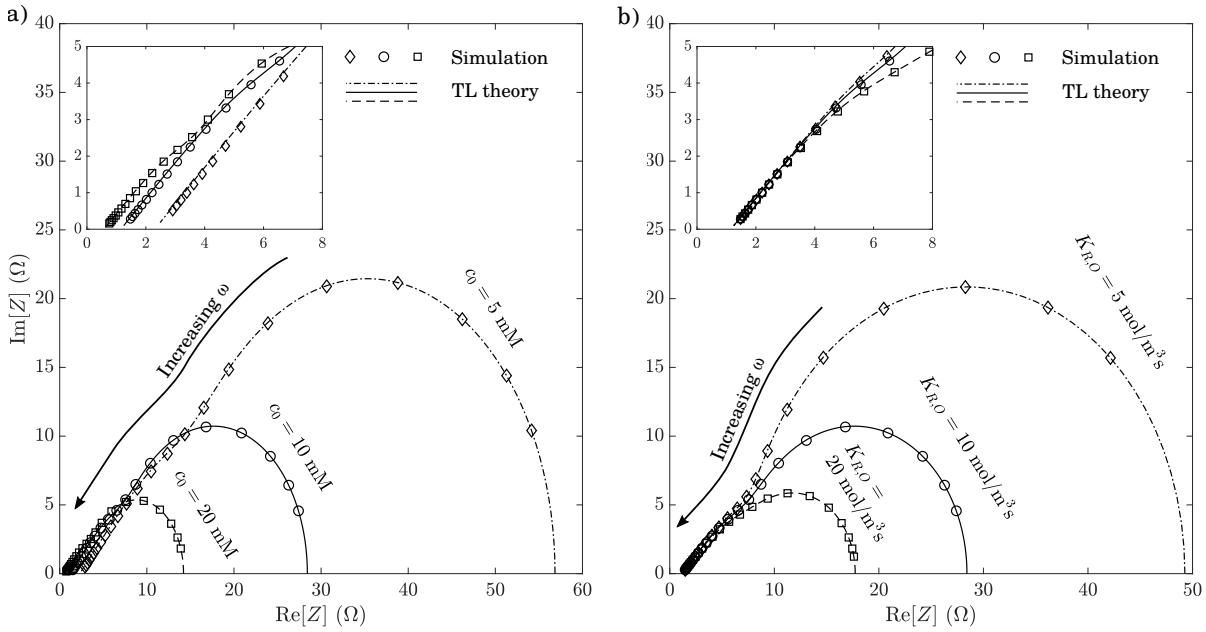

Figure 2.3: Nyquist plots comparing simulated EIS to the analytical TL model for small perturbations near equilibrium. (a) Electrolyte concentrations of 5 mM, 10 mM, and 20 mM, with fixed Faradaic reaction rate coefficient of $10\,\mathrm{mol\,m^{-3}\,s^{-1}}$ (b) Faradaic reaction rate coefficients of $5\,\mathrm{mol\,m^{-3}\,s^{-1}}$, $10\,\mathrm{mol\,m^{-3}\,s^{-1}}$, and $20\,\mathrm{mol\,m^{-3}\,s^{-1}}$, with fixed electrolyte concentration of 10 mM.

toward zero as the capacitors increasingly behave like effective short circuits. The total impedance for high frequencies is therefore dominated by the Ohmic resistance of the separator alone, which exhibits sensitivity to the bulk concentration in Fig. 2.3(a) but is invariant to the micropore Faradaic reaction kinetics in Fig. 2.3(b). In the high–frequency regime, higher bulk electrolyte concentrations are associated with lower resistance.

In the low frequency limit ($\omega \to 0$, at the right side of each plot), Z''_{mi} tends toward R''_F and the total impedance is determined by overall resistance through the cell, which is affected by both the bulk electrolyte concentration in Fig. 2.3(a) and the Faradaic reaction kinetics in Fig. 2.3(b). Higher bulk electrolyte concentration and faster electrode kinetics are associated with lower resistance.

For high–fidelity simulations, the impedance is directly calculated based on comparison of the driving voltage and the resulting current. Recall that $\Delta V_{\mathrm{EIS}}(t) = V_{\mathrm{EIS}} \sin(\omega t)$. The resulting current density has the form $I(t) = I_{\mathrm{EIS}} \sin(\omega t - \psi)$, where ψ is the phase lag between the signals. The complex impedance is computed as

$$Z = \frac{V_{\mathrm{EIS}}}{I_{\mathrm{EIS}}} \exp(\psi j), \tag{2.47}$$

where I_{EIS} and ψ are extracted from simulation results using a least–squares fitting approach. Quantitative agreement between the simulations and the TL theory is observed across all bulk concentrations and Faradaic reaction rate coefficients shown in Fig. 2.3.

Figure 2.4 depicts Bode plots from the EIS study, where analytical results are shown as curves while high–fidelity simulation results are shown as discrete symbols. Figure 2.4(a)–(b) shows cases with fixed Faradaic reaction rate coefficient of $K_R = K_O = 10\,\mathrm{mol\,m^{-3}\,s^{-1}}$ and different values of bulk electrolyte concentration. We observe excellent agreement across the entire frequency range. Examining Fig. 2.4(b), we see that phase lag tends toward zero in the low frequency and high frequency limits for all three cases, indicating that total impedance is dominated by resistance in both of those regimes. This behavior is expected based on limiting behavior of the analytical expressions, as discussed previously. Figure 2.4(a) indicates that the magnitude of the impedance is affected by the bulk electrolyte concentration, with higher concentration enabling lower resistance in both limiting regimes. Generally, this trend holds across the entire range of frequencies.

Figure 2.4(c)–(d) shows cases with fixed bulk electrolyte concentration of $c_{\mathrm{O^+}} = c_{\mathrm{R^-}} = c_0 = 10\,\mathrm{mM}$ and different values of Faradaic reaction rate coefficients (while preserving

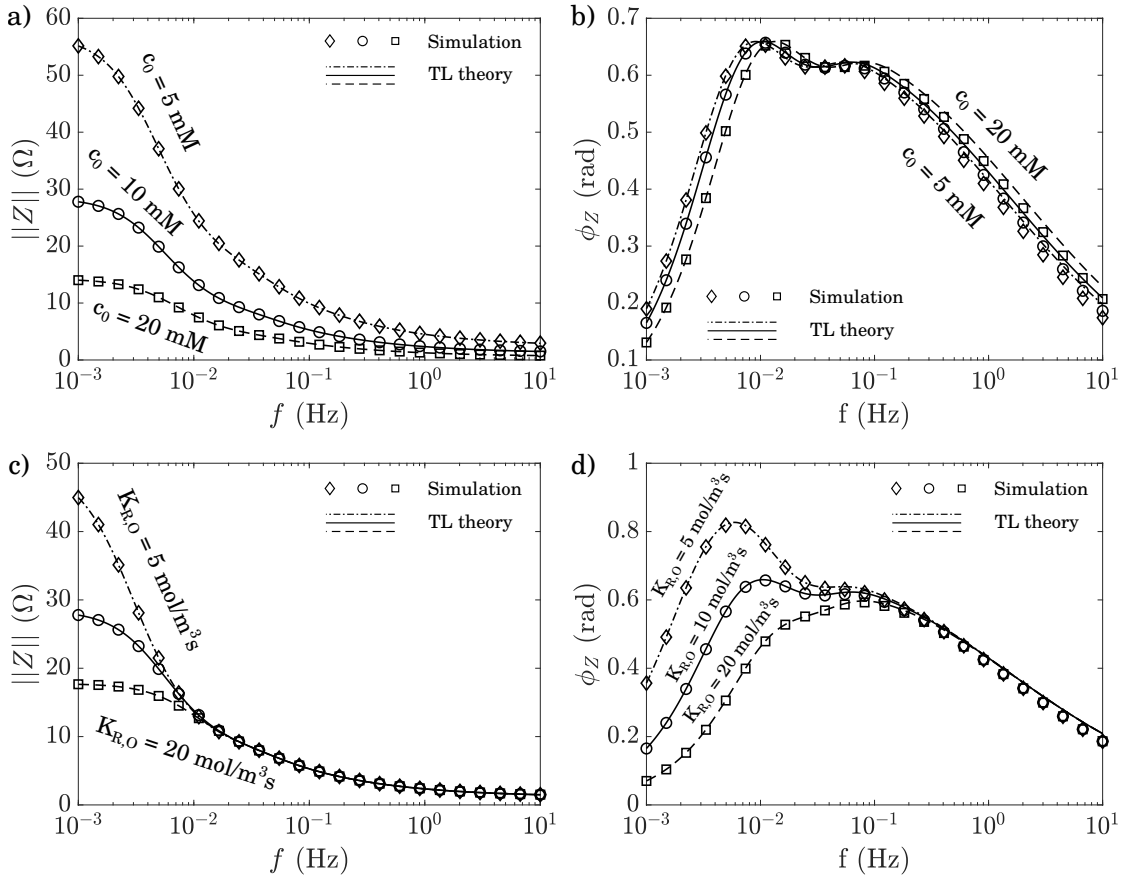

Figure 2.4: Bode plots showing impedance amplitude and phase lag as a function of applied frequency during EIS. Analytical results are shown as curves while simulation results are shown as discrete symbols. (a)–(b) Electrolyte concentrations of 5 mM, 10 mM, and 20 mM, with fixed Faradaic reaction rate coefficient of $10\,\mathrm{mol\,m^{-3}\,s^{-1}}$. (c)–(d) Faradaic reaction rate coefficients of $5\,\mathrm{mol\,m^{-3}\,s^{-1}}$, $10\,\mathrm{mol\,m^{-3}\,s^{-1}}$, and $20\,\mathrm{mol\,m^{-3}\,s^{-1}}$, with fixed electrolyte concentration of 10 mM.

$K_R = K_O$). As before, we observe excellent agreement between the analytical model and the high–fidelity simulation across the entire frequency range. Examining Fig. 2.4(d), we observe that phase lag tends toward zero in the low frequency and high frequency limits for all three cases, indicating once more that total impedance is dominated by resistance in both of those regimes. Note, however, that faster electrode kinetics is associated with substantially lower phase lag in the low–frequency regime. Finally, we examine impedance magnitude in Fig. 2.4(c) and find agreement with the limiting behaviors described previously. At low frequencies, the micropore capacitors act like effective open–circuits. The cell impedance is, therefore, determined by a combination of the resistive elements and exhibits dependence on electrode kinetics (with faster kinetics leading to lower resistance). The high–frequency regime is dominated instead by resistive impedance of the separator alone, because the micropore capacitors now act like effective short circuits. Thus, cell impedance in the high–frequency regime is invariant to changes in electrode kinetics.

To conclude this section, we note that agreement between the numerical results and the analytical solution in the linear limit serves as positive verification of consistency for the numerical solver.

2.4.2 Coupled pH Dynamics and Surface Chemistry

As mentioned in the introduction, Biesheuvel *et al.* [75] have performed simulations of a single redox–active porous electrode with a fixed concentration of reactive carboxylic/carboxylate sites. Conducting simulations of the same cell geometry and chemistry using the model presented in this work allows us to explore the physical implications of differences in modeling approaches. Though the two models are broadly similar, both employing porous electrode theory with the mD model for micropores, we demonstrate here that differences in the treatment of pH and surface chemistry may substantially impact the chemical composition of micropores — a key determinant of CDI degradation.

In terms of coupled pH dynamics and surface chemistry, there are two differences between the model proposed by Biesheuvel *et al.* [75] and our model: First, Biesheuvel *et al.* [75] enforce chemical equilibrium between the carboxylic/carboxylate groups and the pH precisely at the electrode surface (the so–called 0–plane). Second, Biesheuvel *et al.* [75] compute pH in the macropores using a quasi–steady model as $\mathrm{pH} = \mathrm{pH}_0 + \phi/\ln 10$ (see p. 586 of [75]), which may be derived by finding the steady solution of Eq. (2.1) for protons

(with recognition that proton flux is zero at steady state if Faradaic reactions do not involve protons or hydroxide ions). The term 'quasi–steady' here refers to substitution of the instantaneously–varying ϕ field into the steady–state expression for pH while resolving the temporal dynamics for all other species.

In contrast, our model includes surface chemical reactions at finite rates (at the Stern plane, as in the later works of Dykstra *et al.* [44] and He *et al.* [78]), and proton/hydroxide ion transport through the macropores is computed by solving Eq. (2.1) with all terms included. Regarding the first point of difference — the question of chemical equilibrium vs. finite–rate chemistry for surface groups — we find that the kinetic rate coefficients in our model are large enough to guarantee chemical equilibrium throughout our simulations. We show, however, that the second point of difference — quasi–steady macropore pH model vs. full H^+/OH^- transport model — strongly affects the micropore pH in certain regimes, substantially altering the equilibrium composition of the micropore surface.

We perform simulations of the same system studied by Biesheuvel *et al.* [75] using our model, in order to explore the impact of these differences. A single porous cathode is positioned next to a stagnant diffusion layer (SDL). The bulk electrolyte outside the SDL has fixed concentrations of $c_{0,O^{2+}} = 1\,\mathrm{mM}$, $c_{0,R^+} = 1\,\mathrm{mM}$, and $c_{0,A^-} = 3\,\mathrm{mM}$, with $\mathrm{pH}_0 = 7$. The Faradaic reaction occurring in micropores is $O^{2+} + e^- \longleftrightarrow R^+$. A 100 mM concentration of $-$COOH groups (pK = 7 for demonstration purposes) is initially present in the micropores, and the non–dimensional attraction potential is set to $\mu_{\mathrm{att}} = 1.5$ for all species. A galvanostatic operation mode is used, and an external parallel capacitor ensures a gradual increase in current flowing through the cell. We time–advance the governing equations until a physical time of $t = 2 \times 10^4\,\mathrm{s}$, which is several orders of magnitude longer than the diffusion time scale across the system (and, thus, initially appears to be a reasonable proxy for the steady state).

The physical constants used for the simulations in this section are printed in Table 2.4, and a summary of parameters describing the cell geometry and operating conditions is available in Table 2.5. We report the homogeneous reaction and non–Faradaic heterogeneous reaction kinetic parameters in Table 2.6, and the Faradaic reaction kinetic parameters in Table 2.7. Note the inclusion of diffusion coefficients for H^+ and OH^- in Table 2.4 and the presence of water dissociation/recombination in Table 2.6. These parameters were not required in the approach followed by Biesheuvel *et al.* [75], but they are necessary for our simulations.

Table 2.4: Summary of physical constants for single porous electrode simulations.

Symbol	Description	Value
V_T	Thermal voltage	$25.85\,\mathrm{mV}$
T	Temperature	$298\,\mathrm{K}$
F	Faraday constant	$96\,485\,\mathrm{C\,mol^{-1}}$
$D_{\mathrm{O^{2+}}}$	O^{2+} diffusivity	$0.792 \times 10^{-9}\,\mathrm{m^2\,s^{-1}}$
$D_{\mathrm{R^+}}$	R^+ diffusivity	$1.33 \times 10^{-9}\,\mathrm{m^2\,s^{-1}}$
$D_{\mathrm{A^-}}$	A^- diffusivity	$2.03 \times 10^{-9}\,\mathrm{m^2\,s^{-1}}$
$D_{\mathrm{H^+}}$	H^+ diffusivity	$9.31 \times 10^{-9}\,\mathrm{m^2\,s^{-1}}$
$D_{\mathrm{OH^-}}$	OH^- diffusivity	$5.27 \times 10^{-9}\,\mathrm{m^2\,s^{-1}}$

Table 2.5: Cell geometry and operating condition for single porous electrode simulations.

Symbol	Description	Value
L_e	Electrode thickness	$0.1\,\mathrm{mm}$
L_{SDL}	Staganant diffusion layer thickness	$0.1\,\mathrm{mm}$
p_{mA}	Macropore porosity	0.3
p_{mi}	Micropore porosity	0.3
τ	Macropore tortuosity	1
I_{ext}	Applied current density	$0.2,\ 0.4,\ 0.6,\ 0.8\,\mathrm{A\,m^{-2}}$
C_{S}	Stern capacitance	$100\,\mathrm{kF\,L^{-1}}$ [a]
C_{ext}	External parallel capacitance	$29.4\,\mathrm{F\,m^{-2}}$
$c_{0,\mathrm{O^{2+}}}$	O^{2+} bulk concentration	$1\,\mathrm{mM}$ [b,c]
$c_{0,\mathrm{R^+}}$	R^+ bulk concentration	$1\,\mathrm{mM}$ [b,c]
$c_{0,\mathrm{A^-}}$	A^- bulk concentration	$3\,\mathrm{mM}$ [b] $4 - 10^{-8}$ mM [c]
$c_{0,\mathrm{H^+}}$	H^+ bulk concentration	$1 \times 10^{-4}\,\mathrm{mM}$ [b] $1\,\mathrm{mM}$ [c]
$c_{0,\mathrm{OH^-}}$	OH^+ bulk concentration	$1 \times 10^{-4}\,\mathrm{mM}$ [b] $1 \times 10^{-8}\,\mathrm{mM}$ [c]

[a] Though the value reported by Biesheuvel *et al.* [75] is $C_{\mathrm{S}} = 100\,\mathrm{F\,L^{-1}}$, we have confirmed through private correspondence with P. M. Biesheuvel that the value used in computations is actually the value reported here.

[b] These values represent the $\mathrm{pH}_0 = 7$ bulk electrolyte used to compute the results presented in Figs. 2.5 and 2.7.

[c] These values represent the $\mathrm{pH}_0 = 3$ bulk electrolyte used to compute the results presented in Fig. 2.6.

Table 2.6: Homogeneous reaction and non–Faradaic heterogeneous reaction kinetic parameters for single porous electrode simulations.

Reaction	κ_f	$K_{\mathrm{eq}} \equiv \kappa_b/\kappa_f$
$\mathrm{OH^-(aq) + H^+(aq) \longleftrightarrow\ H_2O}$	$1 \times 10^8\,\mathrm{mol^{-1}\,m^3\,s^{-1}}$	$1 \times 10^{-14}\,\mathrm{mol^2\,m^{-6}}$
$\mathrm{COOH \longleftrightarrow\ COO^- + H^+(aq)}$	$1 \times 10^1\,\mathrm{s^{-1}}$	$1 \times 10^{-7}\ \mathrm{mol^{-1}\,m^3}$

Water auto–dissociation is modeled using zeroth–order kinetics, assuming fixed $c_{\mathrm{H_2O}} = 55.5\,\mathrm{M}$.

Table 2.7: Faradaic reaction kinetic parameters for single porous electrode simulations.

Reaction	Parameter	Value
$O^{2+} + e^- \leftrightarrow R^+$	K_R	$1.33 \times 10^{-2}\,\mathrm{mol\,m^{-3}\,s^{-1}}$
	K_O	$1.33 \times 10^{-2}\,\mathrm{mol\,m^{-3}\,s^{-1}}$

Macropore concentration profiles for the reductant and oxidant are shown in Fig. 2.5(a) for a variety of applied current densities (denoted I_{ext}). The SDL occupies the region $-1 \leq x < 0$ while the porous cathode occupies the region $0 < x \leq 1$. Results from Biesheuvel *et al.* [75] are shown as discrete points while the results of our simulations are shown as solid curves. As I_{ext} is increased, the increasing (decreasing) concentration of reductant (oxidant) reflects the Faradaic reaction occurring in the distributed micropores. Depletion of oxidant throughout a majority of the electrode at $I_{\mathrm{ext}} = 0.8\,\mathrm{A\,m^{-2}}$ signifies the transition from reaction–limited behavior to transport–limited behavior. We conclude that the two models offer nearly identical predictions of macropore reductant and oxidant concentration profiles for all current density values.

We next examine macropore pH distribution throughout the system in Fig. 2.5(b), which reveals large differences between the two modeling approaches. Results of the full H^+/OH^- transport model are shown as solid curves, while the quasi–steady pH given by $\mathrm{pH} = \mathrm{pH}_0 + \phi/\ln 10$ (which is computed using ϕ from our full transport simulations) is plotted as dashed curves. Since the quasi–steady profiles in Fig. 2.5(b) are computed using ϕ from the full H^+/OH^- transport model (and since the quasi–steady model is itself the steady limit of the full transport model), the profiles are expected to match perfectly at steady state for each current density.

Thus, the mismatch in Fig. 2.5(b) suggests the presence of a transient response governed by a time scale that is larger than 2×10^4 s. As protons are electrosorbed from the macropores into the micropores, pH in the macropores initially increases. However, the quasi–steady profiles indicate that macropore pH values are actually acidic at steady state — enough protons must accumulate in the electrode for the resulting diffusion flux to perfectly oppose the electromigration flux (yielding zero overall flux for protons). The time scale of proton accumulation in the electrode, however, is inversely proportional to the total proton flux, which is limited by the low concentration of protons in the bulk electrolyte ($\mathrm{pH}_0 = 7$). As a point of contrast, we show results for a case with $\mathrm{pH}_0 = 3$ in Fig. 2.6.

Examining Fig. 2.6, we see that results from the quasi–steady model are aligned indistinguishably with results from the full H^+/OH^- transport model for all current densities

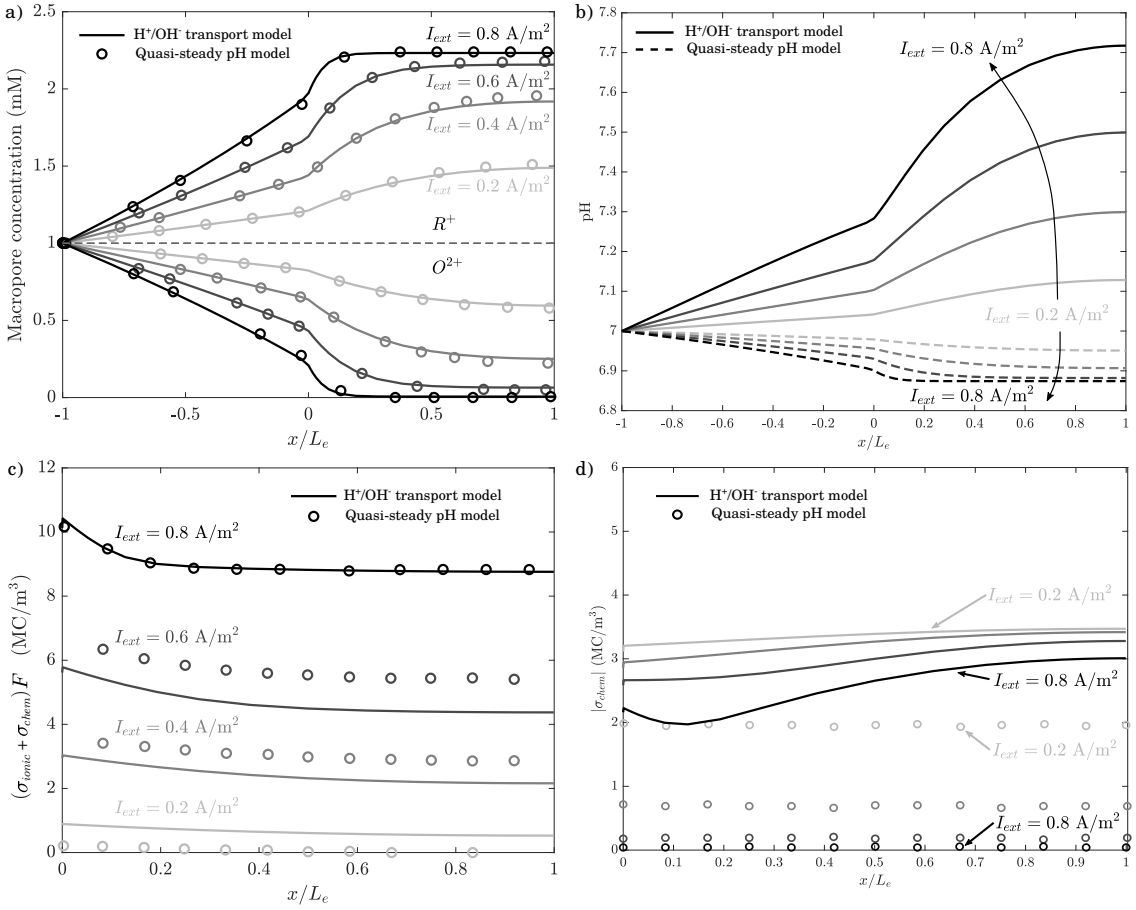

Figure 2.5: Comparison of results computed using a quasi–steady pH model and results computed with fully resolved H^+ and OH^- transport at $t = 2 \times 10^4$ s. (a) Macropore concentration profiles of oxidant and reductant for varying current densities. (b) Macropore pH profiles at varying current densities. (c) Micropore charge ($\sigma_{\text{ionic}} + \sigma_{\text{chem}}$) profiles for varying current densities. (d) Micropore chemical surface charge (σ_{chem}) profiles for varying current densities. Data shown as discrete symbols are from [75]. For the quasi–steady curves in (b), we show $\text{pH} = \text{pH}_0 + \phi/\ln 10$ using ϕ from our full transport simulations.

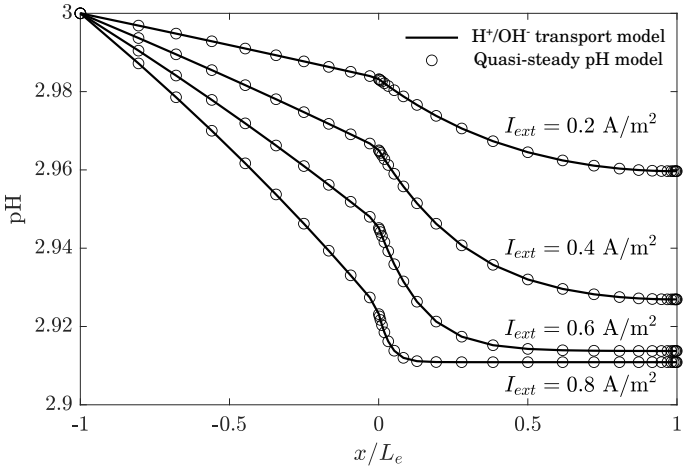

Figure 2.6: Comparison of macropore pH profiles computed using a quasi–steady pH model and results computed with fully resolved H^+ and OH^- transport at $t = 2 \times 10^4$ s, for a single porous cathode. $pH_0 = 3$. For the quasi–equilibrium pH curves, we compute $pH = pH_0 + \phi/\ln 10$ using the ϕ from transport–resolved simulations.

when $pH_0 = 3$. The substantially larger concentration of protons used in Fig. 2.6 permits a larger flux into the electrode, allowing the proton transport equation to reach steady state by $t = 2 \times 10^4$ s. As expected, the steady state concentration profiles indicate that diffusion and electromigration are in competition, yielding zero overall flux. The direction of electromigration can be intuited by recognizing that the electrode is polarized negatively with respect to the left boundary, such that the electric field points from left to right in the macropores.

Finally, we examine the micropore composition, which plays a critical role in CDI degradation. First, Fig. 2.5(c) depicts combined charge density from the ions in solution and the chemical surface groups for different current densities. Second, Fig. 2.5(d) depicts the charge density due to chemical surface groups alone ($-COO^-$ groups in this case). Though the combined charge density predicted by the two models appears to be reasonably close for all cases, the degree of carboxylic group dissociation is substantially different since the full H^+/OH^- transport results are still undergoing a transient response at $t = 2 \times 10^4$ s. The quasi–steady pH model reflects a state that is more acidic than the non–steady result, thereby inducing a relatively smaller degree of carboxylic group dissociation.

The degree of carboxylic group dissociation strongly affects the electrode's electrosorption capacity. Examining Fig. 2.7, we see that the quasi–steady pH model predicts a smaller

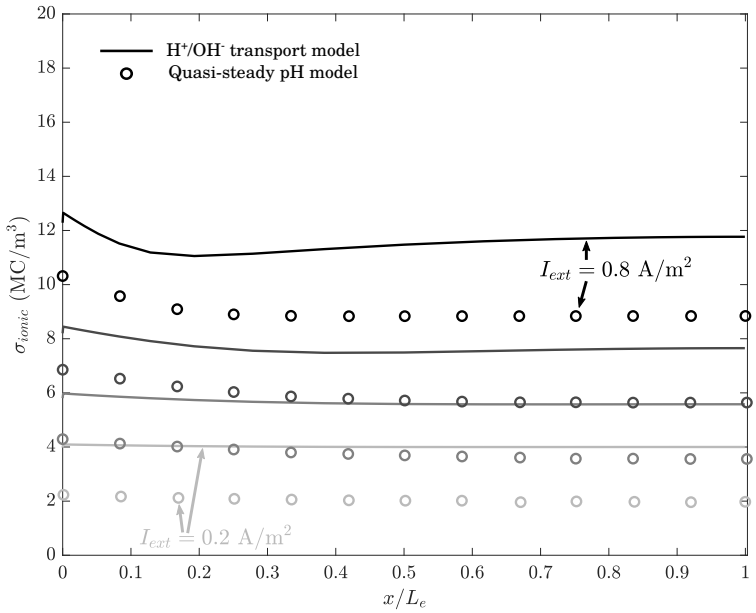

Figure 2.7: Comparison of micropore mobile ionic charge density computed using a quasi–steady pH model and computed with fully resolved H^+ and OH^- transport at $t = 2 \times 10^4$ s, for a single porous cathode. Data shown as discrete symbols are from [75].

amount of mobile ionic charge density across the entire range of current densities compared to the full transport model. This finding is particularly relevant to CDI performance, since the mobile ionic charge density during charging is intimately connected to the salt adsorption capacity of the electrode. For this specific choice of chemistry, additional negatively–charged cathodic surface groups would increase deionization performance, since their negative charge allows for additional electrosorption of mobile cations.

We conclude that though the quasi–steady pH model is accurate at steady state, the time scale required for proton/hydroxide concentration profiles to reach steady state for $pH_0 = 7$ electrolytes may be much longer than the typical charging/discharging time scales of CDI cells. Furthermore, we see that the amount of chemical surface charge, which is critical in determining CDI performance, is strongly sensitive to the pH dynamics. This example underscores the significance of accurately capturing the coupled behavior of pH dynamics and surface chemistry. In the next section, we employ our model to explore this coupled behavior within the context of FTE CDI.

Table 2.8: Summary of physical constants for full–cell FTE CDI simulations.

Symbol	Description	Value
V_T	Thermal voltage	$25.85\,\mathrm{mV}$
T	Temperature	$298\,\mathrm{K}$
F	Faraday constant	$96\,485\,\mathrm{C\,mol^{-1}}$
$D_{\mathrm{Na^+}}$	Na^+ diffusivity	$1.33 \times 10^{-9}\,\mathrm{m^2\,s^{-1}}$
$D_{\mathrm{Cl^-}}$	Cl^- diffusivity	$2.03 \times 10^{-9}\,\mathrm{m^2\,s^{-1}}$
$D_{\mathrm{H^+}}$	H^+ diffusivity	$9.13 \times 10^{-9}\,\mathrm{m^2\,s^{-1}}$
$D_{\mathrm{OH^-}}$	OH^- diffusivity	$5.16 \times 10^{-9}\,\mathrm{m^2\,s^{-1}}$
$D_{\mathrm{O_2}}$	O_2 diffusivity	$2.1 \times 10^{-9}\,\mathrm{m^2\,s^{-1}}$

2.4.3 Demonstration of FTE CDI Degradation

We now apply the model to a representative FTE CDI cell and demonstrate the collective performance impacts of the coupled phenomena that have been discussed. An electrolyte with pH = 7 and NaCl concentration of $c_0 = 10\,\mathrm{mM}$ flows into the cell with flow rate of $Q = 1\,\mathrm{mL\,min^{-1}}$. We choose a variety of V_{ch} values for the driving potential amplitude, but we fix the total cycle period to be $T_p = 200\,\mathrm{s}$, with symmetric charging and discharging durations. We select the upstream electrode to serve as the anode during the charging phase of the cycle, because this orientation is known to induce stronger degradation compared to the opposite orientation.

The simulations include four mobile ionic species (Na^+, Cl^-, H^+, and OH^-), dissolved O_2, and two immobile surface groups ($-COOH$ and $-COO^-$). The physical constants used in the simulations are printed in Table 2.8, and a summary of parameters describing the cell geometry and operating conditions is available in Table 2.9. We report the homogeneous reaction and non–Faradaic heterogeneous reaction kinetic parameters in Table 2.10, and the Faradaic reaction kinetic parameters in Table 2.11. We simulate the first 15 cycles of cell operation, which we find to be sufficient for demonstration purposes. The selection of reduction and oxidation rate coefficients in Table 2.11 merits further justification, which we discuss next.

Following the general discussion of Faradaic reaction kinetic parameters in Section 2.2.2, we are now interested in applying our findings to the FTE CDI system studied in this work. The pertinent reactions in both electrodes (which are identical) are shown in Table 2.11. Note, however, that the analysis in Section 2.2.2 was framed for electrodes that each permit a single Faradaic reaction. By considering the shape of the cell voltage waveform in conjunction with the distribution of reactants during CDI cell operation, we show here that one

Table 2.9: Cell geometry and operating condition parameters for full–cell FTE CDI simulations.

Symbol	Description	Value
L_e	Electrode thickness	0.6 mm
L_{S}	Separator thickness	65 µm
L_{res}	Inflow/outflow thickness	3 mm
A_e	Electrode area	6.25 cm^2
m_e	Combined electrode mass	0.218 g
p_{mA}	Macropore porosity	0.8
p_{mi}	Micropore porosity	0.172
p_{S}	Separator porosity	0.8
τ	Macropore tortuosity	$p^{-0.5}$
τ_{S}	Separator tortuosity	$p_{\mathrm{S}}^{-0.5}$
V_{ch}	Cell charging voltage	0.4 V, 0.6 V, 0.8 V
T_p	Cycle period	200 s
Q	Electrolyte flow rate	1 mL/min
C_{S}	Stern capacitance	200 kF L^{-1}
$c_{0,\mathrm{Na^+}}$	$\mathrm{Na^+}$ inflow concentration	10 mM
$c_{0,\mathrm{Cl^-}}$	$\mathrm{Cl^-}$ inflow concentration	10 mM
$c_{0,\mathrm{H^+}}$	$\mathrm{H^+}$ inflow concentration	1×10^{-4} mM
$c_{0,\mathrm{OH^-}}$	$\mathrm{OH^-}$ inflow concentration	1×10^{-4} mM
$c_{0,\mathrm{O_2}}$	$\mathrm{O_2}$ inflow concentration	0.25 mM
$\mu_{\mathrm{att},i}$	Attraction potential (all species)	0

Table 2.10: Homogeneous reaction and non–Faradaic heterogeneous reaction kinetic parameters for full–cell FTE CDI simulations. Note, water auto–dissociation is modeled using zeroth–order kinetics, assuming fixed $c_{\mathrm{H_2O}} = 55.5$ M

Reaction	k_f	$K_{\mathrm{eq}} \equiv k_b/k_f$
$\mathrm{OH^-(aq) + H^+(aq) \longleftrightarrow\ H_2O}$	$1 \times 10^8\ \mathrm{mol^{-1}\,m^3\,s^{-1}}$	$1 \times 10^{-14}\ \mathrm{mol^2\,m^{-6}}$
$\mathrm{COOH \longleftrightarrow\ COO^- + H^+(aq)}$	$1 \times 10^1\ \mathrm{s^{-1}}$	$1 \times 10^{-5.5}\ \mathrm{mol^{-1}\,m^3}$

Table 2.11: Faradaic reaction kinetic parameters for full–cell FTE CDI simulations.

Reaction	Parameter	Value
$\mathrm{C(H) + 2H_2O \longleftrightarrow\ COOH + 4H^+ + 4e^-}$	K_{R}	$1 \times 10^{-5}\ \mathrm{mol\,m^{-3}\,s^{-1}}$
	K_{O}	$1 \times 10^{-5}\ \mathrm{mol\,m^{-3}\,s^{-1}}$
$\mathrm{O_2 + 2H^+ + 2e^- \longleftrightarrow\ H_2O_2}$	K_{R}	$1 \times 10^{-5}\ \mathrm{mol\,m^{-3}\,s^{-1}}$
	K_{O}	$1 \times 10^{-5}\ \mathrm{mol\,m^{-3}\,s^{-1}}$

of the reactions in Table 2.11 is dominant in each electrode of the FTE CDI cell, allowing us to utilize the results from Section 2.2.2.

The charging/discharging cycle used in this work (shown in Fig. 2.1(e)) does not include polarity reversal. During charging, the upstream electrode acts as the anode, and the downstream electrode acts as the cathode. Substantial reversal of the current (such that reduction occurs in the upstream electrode and oxidation occurs in the downstream electrode) is not expected during operation of the cell.

For this orientation, we expect the first reaction in Table 2.11 (carbon oxidation) to be dominant in the anode (upstream electrode) during charging. The second reaction is prohibited in the anode because no peroxide is present in the inflow, and back–diffusion of peroxide generated in the cathode is neglected due to the large Péclet number (Pe = O(10)). Similarly, we expect the second reaction in Table 2.11 (oxygen reduction) to be dominant in the cathode (downstream electrode) during charging. The first reaction is prohibited in the cathode because $-$COOH groups are not present on a pristine electrode, and the cell voltage waveform used in this work is not expected to drive substantial oxidation in the downstream electrode at any point during cell operation.

Thus, in our implementation of the electrode kinetics, we only include the dominant reaction in each electrode. Before applying the analysis from Section 2.2.2, however, we make note of one crucial requirement. Since identical electrodes are used in the FTE CDI cell, the standard cell potential is expected to be $E^\circ_{\text{cell}} = 0$. However, the E°_a and E°_c for each dominant reaction (reported, for example, in the work by Holubowitch *et al.* [42]) implies a nonzero standard cell potential for the simulation cell (which is no longer symmetric, since there is a different reaction mechanism in each electrode). Despite selecting different reaction mechanisms for each electrode, we will preserve $E^\circ_{\text{cell}} = 0$ when selecting values for the reduction and oxidation rate coefficients. This choice ensures consistency with the thermodynamic requirement that the cell voltage at open–circuit and standard conditions should be 0 V for a cell with identical electrodes, even when our numerical solver artificially incorporates only the dominant mechanism in each electrode.

Thus, we take $E^\circ_{\text{cell}} = 0$. Additionally, in this work, we use $\mu_{\text{att.},i} = 0$ for all species. Under these conditions, Eq. (2.19) simplifies to

$$\left(\frac{K_R^c}{K_O^c}\right)^{1/2}\left(\frac{K_O^a}{K_R^a}\right)^{1/4} = 1. \tag{2.48}$$

For computation of the effective exchange current density in each electrode via Eq. (2.26), we recognize that $\tilde{\mu} = 0$ for both electrodes. Additionally, based on the dominant reaction mechanism in each electrode, $\tilde{z}^a = 4$ and $\tilde{z}^c = 2$ in the anode (upstream electrode) and cathode (downstream electrode) respectively. We incorporate these parameter values into Eq. (2.25) for the anode and for the cathode, finding

$$i^a = -8Fp^a_{\mathrm{mi}}\sqrt{K^a_R K^a_O}\exp\left(-2\Delta\phi_D\right)\sinh\left(2\eta'\right) \tag{2.49}$$

and

$$i^c = -4Fp^c_{\mathrm{mi}}\sqrt{K^c_R K^c_O}\exp\left(-\Delta\phi_D\right)\sinh\left(\eta'\right), \tag{2.50}$$

respectively.

We find that dependence on $\Delta\phi_D$ remains in both expressions, necessitating an iterative fitting procedure for the reaction rate coefficients (as discussed in Section 2.2.2). Such an endeavor is outside the scope of this work. Thus, the Faradaic reaction rate coefficients shown in Table 2.11 correspond to representative values at the anode and cathode for the purpose of demonstrating the model. Additionally, this choice of parameters satisfies Eq. (2.48), ensuring thermodynamic consistency.

Finally, we briefly point out that water electrolysis at the anode and cathode are not included in this work. The analysis by Holubowitch *et al.* [42] indicates that the Nernstian shift in the equilibrium overpotential due to pH variation in the electrodes is expected to prevent hydrogen/oxygen evolution in typical CDI operating conditions. Note that the activities of H_2O, e^-, and C(H) groups are set to unity throughout the simulations presented in this work.

Figure 2.8 depicts the total current density (blue, solid) over the first two and the last two cycles of the simulation for the case of $V_{\mathrm{ch}} = 0.8\,\mathrm{V}$. The current density is computed as

$$I = F\sum_{i=\mathrm{mob.}}\left[z_i\frac{D_i p_{\mathrm{S}}}{\tau_{\mathrm{S}}}\left(\frac{\partial c_{\mathrm{mA},i}}{\partial x} + z_i c_{\mathrm{mA},i}\frac{\partial\phi}{\partial x}\right)\right], \tag{2.51}$$

which may be evaluated at any location within the separator (which has macropore porosity p_{S} and tortuosity τ_{S}) and includes the contributions of both capacitive ion storage and redox reactions. Two well–defined peaks are visible for each period — a positive peak associated with the onset of the charging phase and a negative peak associated with the onset of discharging. A finite and positive charging current is observed after the charging peak, up

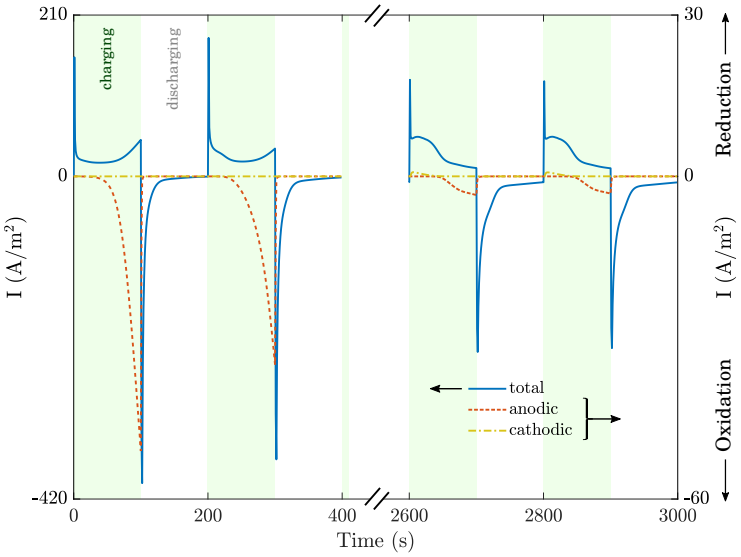

Figure 2.8: Current flowing through the FTE CDI cell over the first two and the last two cycles, for the case of $V_{\mathrm{ch}} = 0.8\,\mathrm{V}$. Total current is shown in solid blue (left axis). Current attributable to anodic and cathodic reactions is shown as dashed red and dash–dotted yellow respectively (right axis).

until the cell voltage is reversed. The discharging current, on the other hand, quickly decays toward zero from its negative peak for the first two cycles. For later cycles, a small and finite discharging current is observed until polarity reversal. Crucially, the magnitude of the positive and negative peaks decreases over successive cycles, implying that less salt is adsorbed/desorbed at later times, as discussed in detail below.

We now examine the current induced by redox reactions in particular, which are central to CDI degradation and a crucial part of our model. The current contributions due to anodic (dashed red) and cathodic (dash–dotted yellow) redox reactions are shown in Fig. 2.8. For these two curves, positive current is associated with reduction and negative current is associated with oxidation. Anodic oxidation occurs most strongly during the later portion of the charging phase for each cycle, by way of the first reaction in Table 2.11. The peak magnitude of the oxidation current decays over successive cycles, eventually reaching a slowly–varying state.

For this set of Faradaic reaction kinetic parameters, reduction at the cathode by way of the second reaction in Table 2.11 is much weaker than oxidation at the anode. The current is negligibly small for early cycles. At later times, a small increase in the reduction current

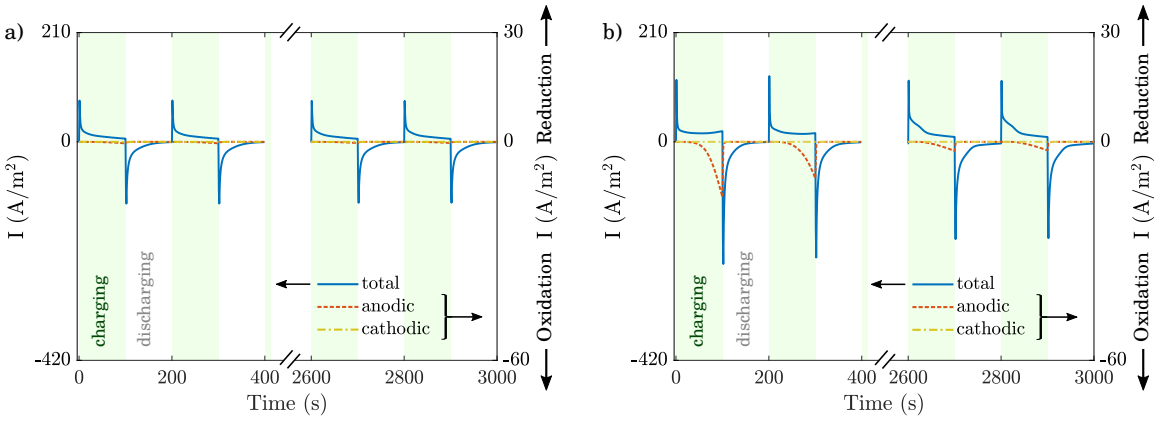

Figure 2.9: Current flowing through the FTE CDI cell over the first two and the last two cycles, for the case of (a) $V_{\rm ch} = 0.4\,\mathrm{V}$ and (b) $V_{\rm ch} = 0.6\,\mathrm{V}$. Total current is shown in solid blue (left axis). Current attributable to anodic and cathodic reactions is shown as dashed red and dash–dotted yellow respectively (right axis).

occurs at the beginning of each charging phase. Similar plots for the cases of $V_{\rm ch} = 0.4\,\mathrm{V}$ and $V_{\rm ch} = 0.6\,\mathrm{V}$ can be found in Fig. 2.9. Comparing the current vs. time curves for the cases of $V_{\rm ch} = 0.4\,\mathrm{V}$ and $V_{\rm ch} = 0.6\,\mathrm{V}$ in Fig. 2.9 to the analogous results for the case of $V_{\rm ch} = 0.8\,\mathrm{V}$ in Fig. 2.8, we observe similar features but with lower peak magnitude for total current and for redox reaction currents.

We now turn our attention toward the interplay between carboxylic/carboxylate groups and pH dynamics in the anode micropores. Fig. 2.10(a) shows the combined concentration of oxygen–containing groups ($-$COOH and $-$COO$^-$), created by the first reaction in Table 2.11. Electrode oxidation propagates upstream from the anode/separator interface in a stair–stepping fashion, showing that the oxidized region grows only during the charging phase of each cycle. At later times when temporal gradients are diminished (near the top of Fig. 2.10(a)), spatial gradients remain strong, with higher concentrations near the separator.

We examine the Faradaic reaction term in the anode in order to explain the spatial variation of electrode oxidation seen in Fig. 2.10(a). Recall from Section 2.2.1 that the anode Faradaic reaction term is given by

$$R_{\rm COOH} = 2p_{\rm mi}\sqrt{K_R^a K_O^a}\sqrt{\hat{c}^4_{{\rm mi},{\rm H}^+}\hat{c}_{\rm mi,COOH}}\,\sinh\left(\frac{n\eta}{2}\right), \tag{2.52}$$

where the overpotential $\eta \equiv \Delta\phi_S - \Delta\phi_{S,\rm eq}$. The quantity $\sinh n\eta/2$ is depicted in Fig. 2.11(a)

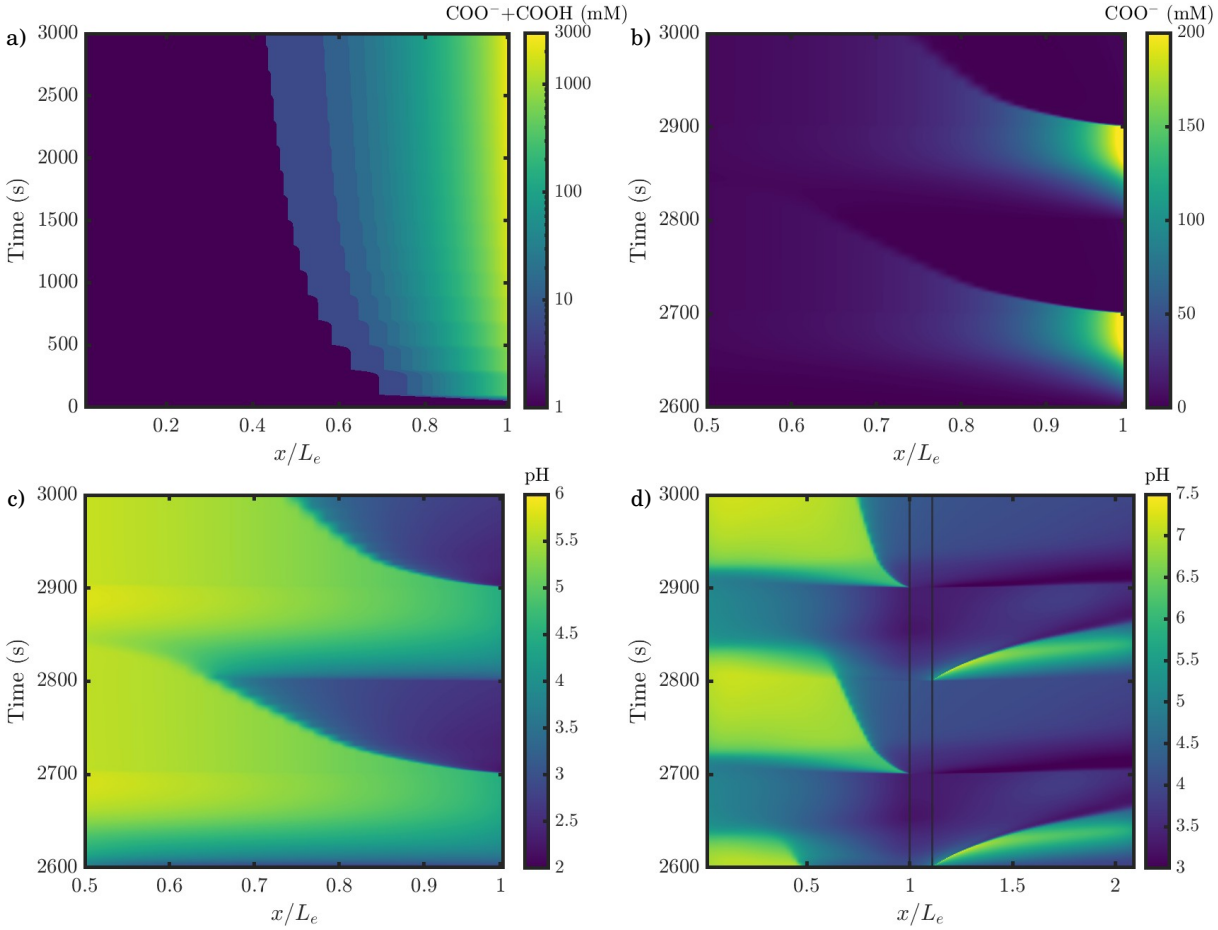

Figure 2.10: x–t diagram of species concentrations, for the case of $V_{\mathrm{ch}} = 0.8\,\mathrm{V}$ a) Combined $-\mathrm{COO}^-$ and $-\mathrm{COOH}$ concentration in the anode micropores for entire duration of the simulation. b) $-\mathrm{COO}^-$ concentration in the anode micropores for the last two cycles of the simulation. c) pH in the anode micropores for the last two cycles of the simulation. d) pH in the macropores (anode, separator, and cathode) for the last two cycles of the simulation. Interfaces between electrode and separator are indicated as solid black lines.

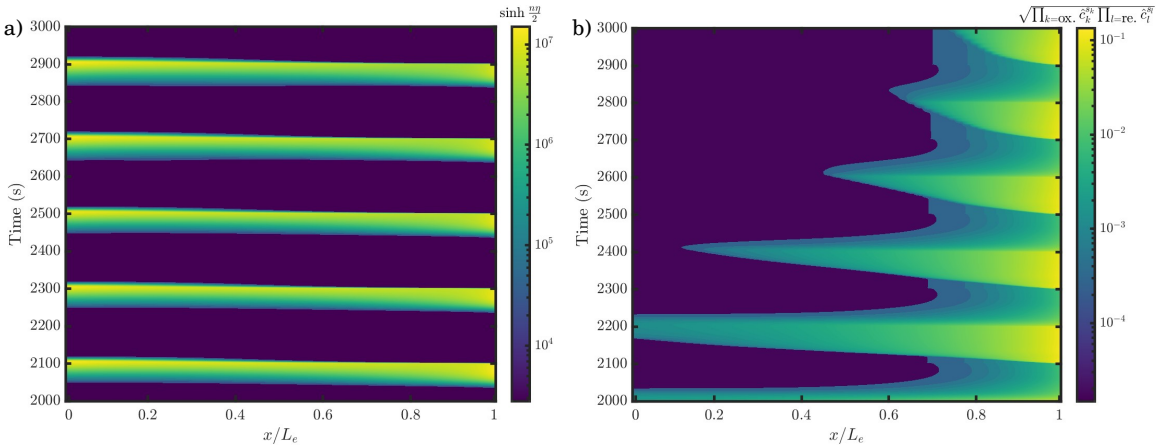

Figure 2.11: x–t diagram across the anode, showing (a) $\sinh n\eta/2$, where the overpotential $\eta \equiv \Delta\phi_S - \Delta\phi_{S,\text{eq}}$ and (b) $\sqrt{\prod_{k=\text{ox.}} \hat{c}_{\text{mi},k}^{s_k} \prod_{l=\text{re.}} \hat{c}_{\text{mi},l}^{s_l}}$ for the case of $V_{\text{ch}} = 0.8\,\text{V}$. Time domain spans the last five cycles of the simulation.

as a function of space and time for the last five cycles of the simulation. Midway through the charging phase, the jump to higher overpotential is relatively homogeneous in space — all parts of the cell experience a sharp response in time. The discharging part of the cycle shows a similarly homogeneous response.

In Fig. 2.11(b), we examine the quantity $\sqrt{\hat{c}_{\text{mi,H}^+}^4 \hat{c}_{\text{mi,COOH}}}$ appearing at the front of Eq. (2.52). We observe substantial variation in space and the presence of temporal fluctuations near the separator. The micropore activities for two species are present in this term: H^+ and COOH, both of which are responsible for the spatial variation seen in Fig. 2.10(a). Note the presence of large, streak–like structures seen in Fig. 2.11(b) — a feature that we proceed to show is connected to shock–like pH fronts that sweep across the anode. Additionally, the spatially–localized production of $-\text{COOH}$ groups near the separator acts to enhance the reaction rate selectively in those regions, encouraging further oxidation in locations where some oxidation has already occurred.

Next, Fig. 2.10(b) shows $-\text{COO}^-$ group concentration across the anode during the last two charging/discharging cycles. The concentration of carboxylate groups is largely determined by weak acid equilibrium with the local micropore pH, which is shown in Fig. 2.10(c). The charging phase is associated with H^+ expulsion from the micropores, increasing the pH therein. The first reaction in Table 2.10 promotes dissociation of $-\text{COOH}$ groups into $-\text{COO}^-$ groups as a result ($\text{pK}_\text{a} = 5.5$). Thus, the negatively charged carboxylate groups compete against mobile anion electrosorption in the micropores. During the discharging

phase, protons re–enter the micropores and induce re–protonation of the carboxylate groups.

As was the case for total oxygen–containing group concentration in Fig. 2.10(a), the protonation/deprotonation behavior in Fig. 2.10(b)–(c) also exhibits substantial spatial inhomogoneity. During the charging phase, pH in the micropores increases relatively uniformly across the electrode, but the carboxylate group concentration exhibits a maximum value near the separator due to the higher concentration of carboxylic groups in that region to start with. During discharging, a shock–like low–pH front propagates upstream from the separator as protons re–enter the micropores, inducing carboxylate group reprotonation. Similar features were reported by Shocron *et al.* [47], and to further explain this low–pH front that sweeps across the micropores, we examine behavior in the surrounding macropores.

The macropore pH across both electrodes (and the separator, in the center) is shown in Fig. 2.10(d), allowing correlation with the micropore pH shown in Fig. 2.10(c). The anodic macropores become more acidic during the charging phase as protons (which are continually produced in Faradaic reactions in the anode micropores during charging) are continually expelled from the micropores. At the onset of discharging, the anodic macropores become more alkaline as protons are re–adsorbed into the micropores. However, a low–pH front travels upstream from the separator as protons return from the separator and cathode regions. This discharging pH front in the anodic macropores explains the corresponding low–pH front seen across the micropores.

Note the presence of a shock–like pH front traveling downstream through the cathode during the charging phase of each cycle. Protons are electrosorbed into the cathode micropores at the onset of charging, leading to an initial increase in cathode macropore pH. However, advection continues to bring low–pH electrolyte (containing protons produced in and expelled from the anode micropores) into the cathode. Whereas the anodic discharging pH front travels opposite the direction of advection, the cathodic charging pH front is advected downstream. Examining pH vs. time near the cathode–reservoir interface ($x = 2L_e + L_s$), note qualitative agreement with the experiments of Algurainy & Call [85], who report transient oscillations of the effluent stream pH aligned with charging and discharging.

Similar plots to Fig. 2.10 are shown for the cases of $V_{\text{ch}} = 0.4\,\text{V}$ and $V_{\text{ch}} = 0.6\,\text{V}$ in Fig. 2.12 and Fig. 2.13, respectively. Compared to the case of $V_{\text{ch}} = 0.8\,\text{V}$, similar results are seen for the case of $V_{\text{ch}} = 0.6\,\text{V}$, albeit with weaker and more slowly–propagating

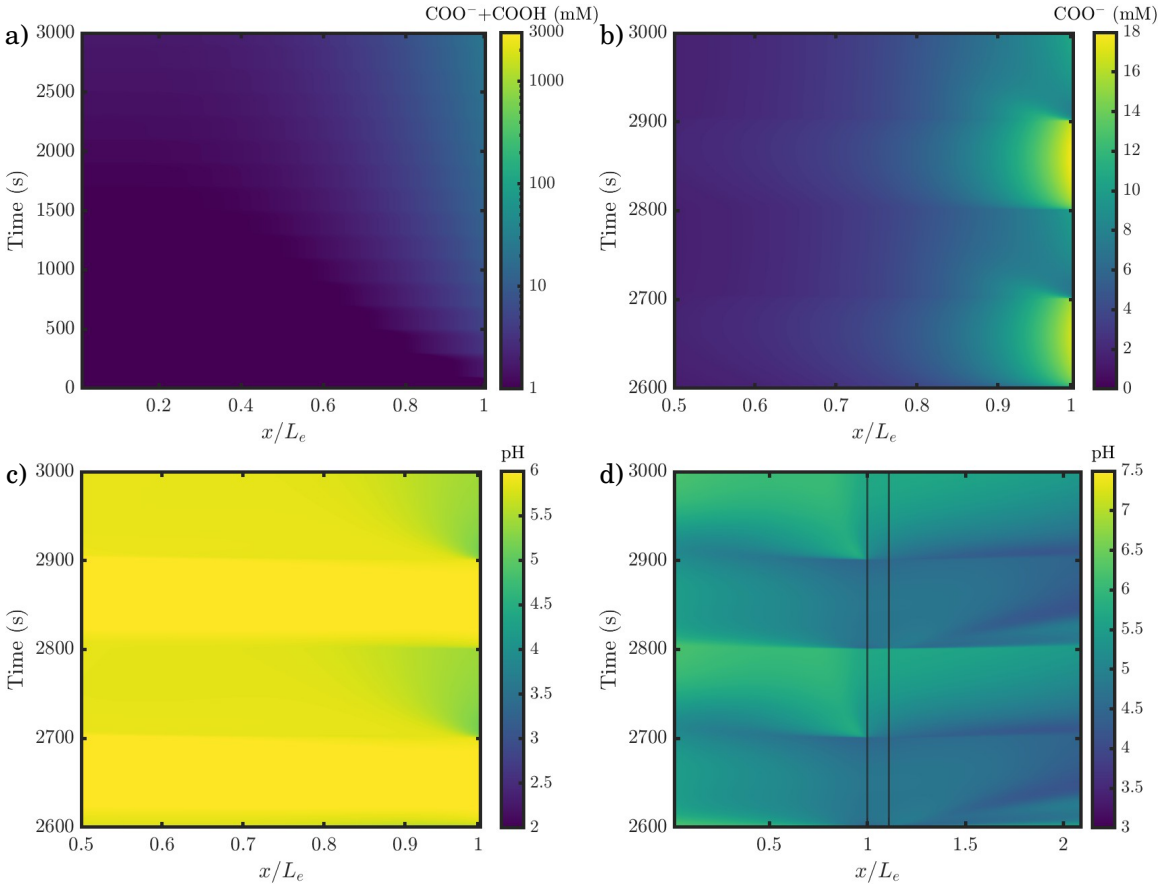

Figure 2.12: x–t diagram of species concentrations, for the case of $V_{\mathrm{ch}} = 0.4\,\mathrm{V}$ a) Combined $-\mathrm{COO}^-$ and $-\mathrm{COOH}$ concentration in the anode micropores for entire duration of the simulation. b) $-\mathrm{COO}^-$ concentration in the anode micropores for the last two cycles of the simulation. c) pH in the anode micropores for the last two cycles of the simulation. d) pH in the macropores (anode, separator, and cathode) for the last two cycles of the simulation. Interfaces between electrode and separator are indicated as solid black lines.

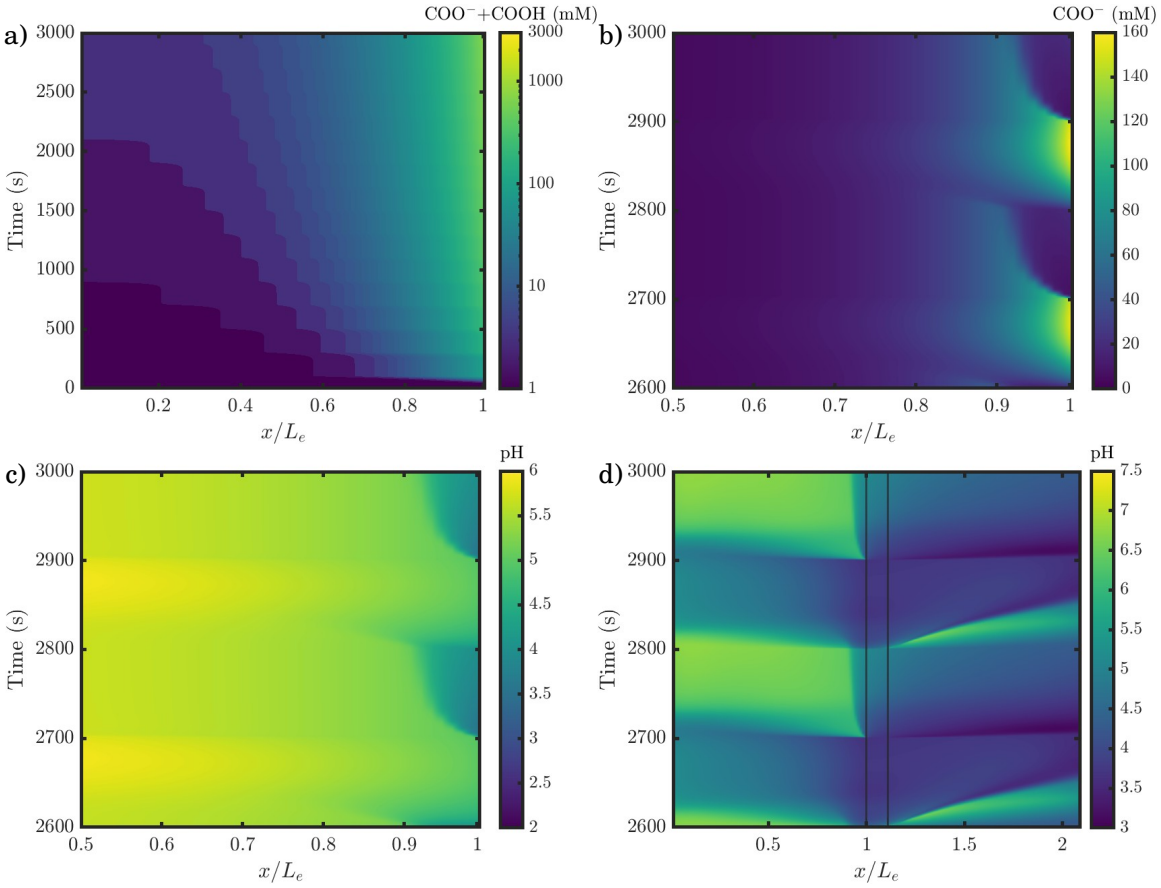

Figure 2.13: x–t diagram of species concentrations, for the case of $V_{\mathrm{ch}} = 0.6\,\mathrm{V}$ a) Combined $-\mathrm{COO}^-$ and $-\mathrm{COOH}$ concentration in the anode micropores for entire duration of the simulation. b) $-\mathrm{COO}^-$ concentration in the anode micropores for the last two cycles of the simulation. c) pH in the anode micropores for the last two cycles of the simulation. d) pH in the macropores (anode, separator, and cathode) for the last two cycles of the simulation. Interfaces between electrode and separator are indicated as solid black lines.

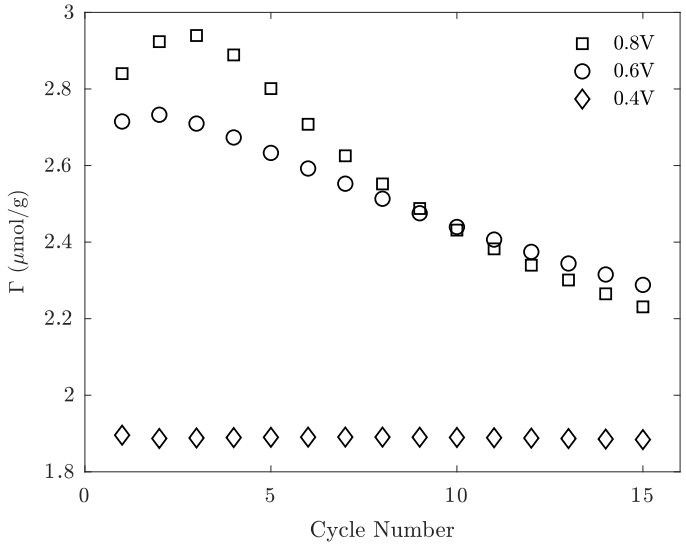

Figure 2.14: Salt adsorption capacity (reported in moles of salt per dry mass of electrodes) over successive cycles, for three different cases of charging voltage.

discharging pH fronts. For the case of $V_{\text{ch}} = 0.4\,\text{V}$, pH fronts are even weaker in magnitude.

As expected, the total oxygen–containing group concentration is substantially lower when V_{ch} is lower — particularly for the case of $V_{\text{ch}} = 0.4\,\text{V}$. This finding clearly illustrates that electrode oxidation occurs more strongly at higher cell voltage magnitudes. As further evidence of this, note that the anode micropores during charging are more acidic for higher cell voltages. The increased acidity is due to the increased rate of proton production via anode oxidation, a finding that is supported by comparing the oxidation currents in Fig. 2.8 and in Fig. 2.9.

Finally, we explore the consequences of oxidation on overall cell performance. Figure 2.14 depicts the salt adsorption capacity, which is defined for cycle number N_c as

$$\Gamma = \frac{Q}{m_e} \int_{N_c T_p}^{N_c T_p + \frac{T_p}{2}} \left[c_{0,\text{salt}} - c_{\text{eff,salt}}\left(t\right) \right] \text{dt}, \tag{2.53}$$

where $c_{0,\text{salt}}$ and $c_{\text{eff,salt}}$ refer to the inflow and effluent salt concentrations (which are determined from the individual ionic concentrations based on the chemical identity of the salt). m_{e} is the dry mass of both electrodes combined. The two higher voltage case in Fig. 2.14 exhibit a transient increase in Γ followed by a pronounced decline that persists until the end of the simulation. The reduced salt adsorption capacity results from the accumulation

of oxygen–containing groups over time. During the charging phase, deprotonation of carboxylic groups into negatively–charged carboxylate groups reduces the capacity for mobile salt anion storage in the cathode.

Since the electrolyte must retain electroneutrality in macropores, the reduced anion storage capacity in the anode also limits cation removal at the cathode. We also observed in Fig. 2.10, however, that the reduced anion storage capacity is balanced in part by a substantial reduction in the average effluent pH. This behavior qualitatively corroborates experimental observations reporting gradual acidification of the effluent stream [56, 86]. The additional anions remaining in the effluent are compensated partially by additional protons, which are produced in the anodic oxidation reaction and are only partially consumed by oxygen reduction at the cathode.

The salt adsorption capacity for $V_{\rm ch} = 0.4\,{\rm V}$ is much flatter than for the higher voltage cases, indicating that degradation does not occur as strongly for this case. This result is supported by the detailed space–time diagrams depicted in Figs. 2.12 and 2.13. However, such low voltages are not practical for CDI due to the low salt adsorption capacity. Thus, we conclude that the model is able to capture the fundamental trade–off between cell performance and longevity, opening a pathway toward computational optimization for CDI.

2.5 Concluding Remarks

In this study, we introduced and numerically solved a comprehensive model for corrosive electrode degradation in FTE CDI. We included five nonlinearly coupled phenomena that are pertinent in CDI degradation: i) electrodiffusive transport, ii) advective transport, iii) electrosorption, iv) electrochemical charge transfer, and v) weak acid/base surface chemistry. Though a number of previous authors have addressed subsets of these effects, we have shown here that a wide range of rich physio-chemical phenomena are seen in full-cell simulations that consider all five phenomena together within the context of modeling long–term FTE CDI cell performance.

The primary contributions contained in this work are i) an introduction of the model, ii) a description of the algorithm and numerical methods required to efficiently solve the equations, iii) verification of our solver's consistency, and iv) preliminary investigation of the emergent physio–chemical processes. We verified consistency of the solver by ensuring that

the high–fidelity model's predictions match analytical results in the limit of small voltage perturbations. Furthermore, we applied our model to a simple, single–electrode geometry, shedding light on the complex interactions between pH dynamics and surface chemistry. Finally, we demonstrated use of the model for a representative FTE CDI cell, revealing the presence of shock–like pH fronts and substantial spatiotemporal inhomogeneity in electrode corrosion.

We anticipate this work moving forward in two directions. The first step, naturally, is formal validation of the model via quantitative comparison against experimental data. We have not attempted such a comparison here, since such an analysis is outside of the scope of this work. However, we remark that such an endeavor is the focus of our ongoing efforts. Second, we envision that the model and numerical algorithm shared in this work enable low–cost, computational optimization studies for CDI, since computations may easily be performed with varying parameters for the cell geometry and operating conditions.

In conclusion, the results presented here qualitatively explain the decline of salt adsorption capacity observed in FTE CDI cells over multiple cycles. Furthermore, the model offers access to detailed pH and chemical surface group concentration fields in macropores and micropores, revealing that the interplay between them leads to spatially and temporally inhomogeneous behavior across the electrodes. We posit that with continued validation efforts underway, full–cell numerical simulations represent a viable computational approach to the optimization of FTE CDI cell performance and longevity.

THIS PAGE DELIBERATELY LEFT BLANK

Chapter 3

Intermixed Hydrophobic/Hydrophilic Catalysts

3.1 Background

Electrochemical synthesis is a linchpin process in multiple contemporary research endeavors, such as electrification/decarbonization of commodity chemical production [87] and storage/dispatch of renewable energy as chemical fuels [88]. This class of electrocatalytic methods presents an alternative to emission–intensive thermochemical processes that require petrochemically–derived feedstocks, offering a pathway toward the production of simple hydrocarbons (*e.g.* ethylene, methanol, formic acid, and other such oxygenates and carboxylic acids), hydrogen gas, or ammonia at low temperature and pressure using renewable electricity and $CO_2/H_2O/N_2$ as feedstocks [89]. Microporous electrodes are naturally suited to such applications due to their large catalytically–active surface areas and ability to mitigate aqueous solubility and mass transport limitations associated with reactants like CO_2 and N_2 [90].

Recent studies have demonstrated that selectivity toward desired products, a critical determinant of commercial viability, is strongly sensitive to the local microenvironment within porous electrodes [90–92]. In addition to microstructure of the porous medium itself, the 'microenvironment' includes local pH, concentration of reactants, and chemical

identity of spectator species — features governed by the nonlinearly–coupled dynamics of electrodiffusive transport through the porous medium and electron–transferring reactions at electrode–electrolyte interfaces.

For CO_2 electroreduction (either directly or in two steps with CO as an intermediate), gas diffusion electrode (GDE) cells are capable of achieving high synthesis rates [93–95]. However, direct CO_2 electroreduction lacks both the carbon efficiency (fraction of CO_2 converted to C2+ products) and energy efficiency necessary to achieve widespread commercial use [96–104]. For direct reduction of CO_2, the primary source of this low efficiency is the so–called "CO_3^{2-} problem": a mechanism that is characterized by the thermodynamically favorable and kinetically facile reaction between dissolved CO_2 and OH^- ions to form HCO_3^-, with subsequent reactions to form CO_3^{2-} [105]. At steady state, this process results in substantial cell voltage increases and parasitically consumes CO_2. This problem can be avoided by operating at low pH, but this leads to unacceptable voltage increases due to the requirement of a bipolar membrane or the Nernstian pH shift of the anode potential away from the cathode potential [105–108].

In addition to carbon efficiency and energy efficiency, high synthesis rates of a single product are particularly valuable because product separation is energy intensive [109]. Multi–carbon products like C_2H_4 have more direct routes to the commodity chemical market, including, for example, polymerization to form polyethylene [99].

Our primary motivation in this work is viewing catalyst design as an avenue to improve carbon efficiency, energy efficiency, and product selectivity for CO_2 and CO electroreduction cells. Specifically, we focus on understanding the transport of ions, gases, and electrons in low-temperature CO_2 electrocatalysts in order to guide their continued development. Porous (and hydrophilic) Cu catalysts are known to produce multi–carbon species and exhibit large active surface areas, but recent investigations have shown that the inclusion of sporadically–distributed porous (and hydrophobic) PTFE regions creates additional pathways for the delivery of gaseous reactants, mitigating transport limitations seen in pure Cu catalysts [110–113]. We focus specifically on modeling the multi–scale and multi–phase physicochemical processes occurring in such intermixed hydrophobic/hydrophilic catalysts.

A schematic of the cell and catalyst–GDE assembly is shown (with CO electroreduction chemistry as an example) in Fig. 3.1. The catalyst layer (CL) comprises two distinct regions, as indicated by the colors in Fig. 3.1(c). It is a matrix of porous PTFE regions (shown in green) and porous Cu regions (shown in orange). The PTFE regions resist wetting due to

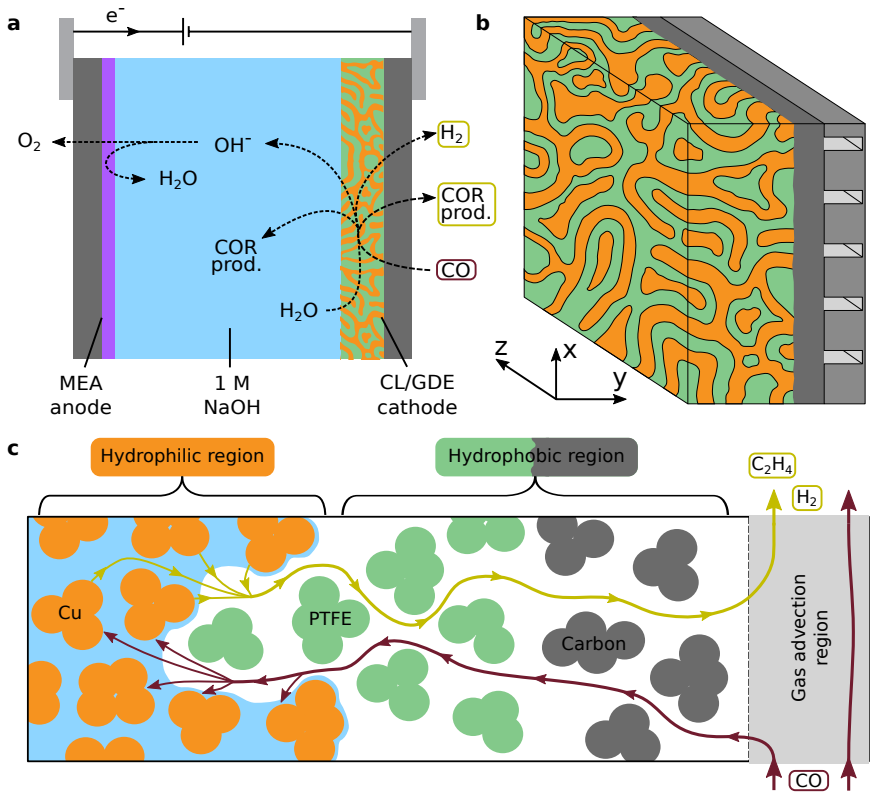

Figure 3.1: a) Full electrochemical cell for CO/CO_2 electroreduction. Catalyst/GDE cathode is located at the right side of the cell. b) 3D representation of catalyst/GDE cathode, showing intermixed hydrophobic and hydrophilic regions. c) Schematic of transport and reactions throughout the catalyst/GDE cathode. Schematic is shown with chemistry for CO reduction, although the same setup may also be used for direct CO_2 reduction.

hydrophobicity, allowing the transport of gaseous products and reactants. The Cu region, on the other hand, is amenable to wetting. The bulk electrolyte, which flows in the space between the cathode and anode, is represented as blue in Fig. 3.1(a) and readily enters the interstitial space in the Cu structure. The large surface area of contact between Cu and PTFE regions is expected to enable high transport rates between the gaseous and aqueous phases, while dissolved CO/CO_2 reduction occurs at the embedded Cu–electrolyte interfaces. Note the catalyst's morphological complexity: The two phases are intermixed randomly as a result of the deposition process whereby the matrix is constructed from Cu and PTFE nanoparticles [113, 114].

The length scales present in the problem span a wide range. The largest is the scale of the cell itself, which extends $L_x^C = L_z^C = 1\,\text{cm}$ in the x and z directions, respectively. The partial pressures of gaseous reactants and products are expected to vary substantially in the z direction as gaseous species are transported through the interdigitated gas channels at the right side of the catalyst in Fig. 3.1(b). The inlet stream consists of pure CO (or CO_2), while the outlet stream is a mixture of CO (or CO_2), C_2H_4, and H_2, depending on the cell's carbon efficiency. The partial pressure of each gaseous reactant determines the local aqueous concentration at the gas–electrolyte interface through Henry's law. Thus, we also expect the formation of aqueous reactant concentration gradients in the z direction, mirroring gradients in the gas phase and producing a strong variation in microenvironment conditions over the entire z dimension.

The cross–sectional length scale of Cu regions in the catalyst (the characteristic width of Cu regions, that is) is only $O(5\,\mu\text{m})$. Since dissolution of gaseous reactants only occurs at the interfaces between the PTFE and Cu regions, aqueous diffusion through the electrolyte phase is responsible for transporting gaseous reactants deeper into the Cu regions. This suggests the formation of reaction–diffusion layers at the boundaries of the Cu regions, since CO (or CO_2) is being consumed by a variety of heterogeneous reactions as it diffuses inward. The dynamics of this process offer an avenue for optimization and improvement of system–level performance metrics. If CO (or CO_2) is wholly consumed before diffusing fully into the Cu regions, the development of zones that are starved of gaseous reactants will lead to H_2 evolution becoming the dominant Faradaic reaction, reducing selectivity toward desired products.

Note that the pores in the Cu and PTFE regions have their own length scale, with size $O(1\,\text{nm})$. Furthermore, the thickness of electric double layers, which form at the numerous

Cu–electrolyte interfaces within the Cu region, is expected to be the smallest continuum scale in the problem. For solutions with concentration of O(1 M), the double layers are expected to have sub–nm thickness [115]. Correct representation of the Cu–electrolyte interfaces is crucial because Faradaic reactions at these interfaces produce the desired products and are entirely responsible for steady–state current flowing through the cell. In all, we conclude that the variation of length scales in the problem is over seven orders of magnitude, and that significant physical phenomena occur over the entirety of these length scales.

The large variation in length scales, coupled with the morphological complexity shown in Fig. 3.1(b), poses a significant computational challenge. First, the complex morphology of the catalyst is difficult to accurately measure and represent in all three dimensions. Second, even if 3D representation of the morphology were approximated, the presence of numerous sub–nm double layers produces meshing and time–step requirements so severe that simulations capturing more than a few individual 3D pores would not be tractable. Furthermore, capturing only a few individual pores would not allow for detailed examination of transport across the entire electrolysis cell. As argued above, not only are device–scale concentration gradients expected to occur, they are expected to significantly affect the model's ability to predict system–level behavior. This computational challenge inspires a modeling challenge, the goal of which is to find a computationally efficient and physically accurate representation of the system.

The remainder of this chapter is divided into four parts. We begin in Section 3.2 with the mathematical description of our model, which is designed to retain essential physicochemical features and processes while reducing computational complexity. Next, in Section 3.3, we describe the specialized numerical methods that enable low–cost, parallelized solution of the governing equations. In Section 3.4, we discuss simulation results for two different chemistries: CO reduction is used as a validation case, while CO_2 reduction is investigated with the goal of addressing the $CO_3{}^{2-}$ problem. Finally, we offer concluding remarks in Section 3.5.

3.2 Theory

The schematic of an intermixed hydrophobic/hydrophilic catalyst layer and GDE in Fig. 3.1(b) depicts several of the features that contribute to difficulty of high–fidelity modeling for this

problem. In this section, we construct a model that preserves essential features while neglecting those that may be considered higher–order effects. The result is a mixed–fidelity model that is simple enough to permit straightforward implementation of a numerical solver, but still retains sensitivity to design parameters that most strongly affect cell performance.

3.2.1 Geometric simplification

The first point we address is geometric complexity of the intermixed phases. A high–fidelity modeling/simulation approach would require construction of intricate computational meshes with selective refinement near the hydrophobic–hydrophilic interfaces (where reactants are introduced via dissolution). A low–fidelity approach, on the other hand, would involve the application of volume–averaging over the entire catalyst layer, thereby assuming uniform composition and electric potential throughout the catalyst.

In our medium–fidelity approach, we regularize the catalyst geometry into a rectilinear form that captures the dominant reaction–diffusion balance while permitting the development of device–scale gradients in composition and electric potential. Though SEM images [113] reveal that the the hydrophobic and hydrophilic regions are randomly distributed, we assume that the locally–volume–averaged statistics of the distribution (*e.g.,* the volume fraction and characteristic length scale of each of the phases) are constant throughout the catalyst layer. Based on this assumption, we propose the simplified catalyst geometry in Fig. 3.2(a).

The randomly– and isotropically–distributed structure in Fig. 3.1(b) has been modeled as the periodically–repeating and directionally–aligned array in Fig. 3.2(a). In doing so, we choose to neglect macroscopic tortuosity — that is, the tortuosity associated with the distribution of phases. Additionally, this modeling choice quantitatively alters the amount of interfacial surface area between the hydrophobic and hydrophilic phases, and it does not account for the presence of isolated hydrophobic or hydrophilic clusters. Crucially, however, the structured model captures the volume fraction and the characteristic thickness of hydrophilic regions.

Large gradients across the catalyst layer are expected in the y and z directions but not in the x direction. Therefore, aligning the hydrophobic/hydrophilic structures as shown in Fig. 3.2(a) permits us to take advantage of periodicity in the x direction by examining a single unit cell of the repeating pattern, as shown in Fig. 3.2(b). We neglect edge effects that may occur near the outermost edges of the device. The characteristic thickness of

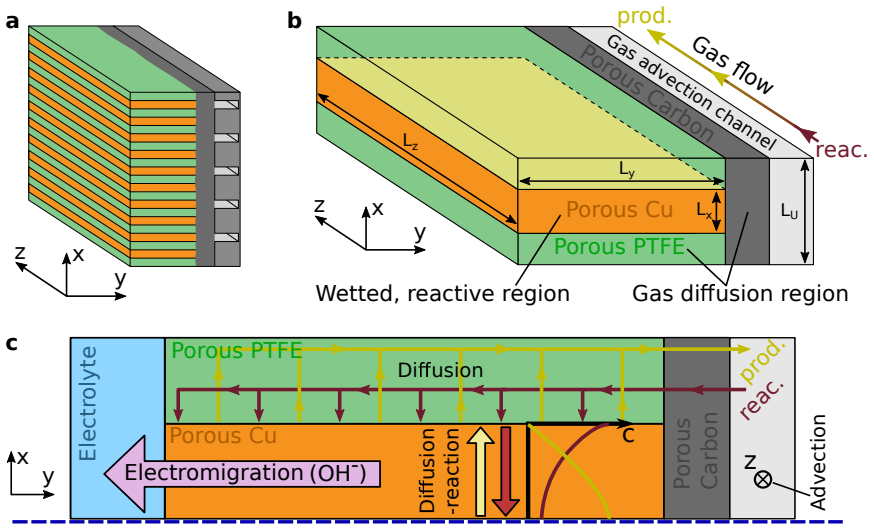

Figure 3.2: a) Structured model for catalyst/GDE cathode. b) Representation of a single unit cell of the structure shown in (a). c) Cross-sectional diagram of the unit cell in (b), showing dominant transport mechanisms.

Cu regions is represented by a single parameter L_x, and the associated volume fraction of the Cu region is given by L_x/L_U, where L_U is the width of the unit cell itself. This simplification substantially reduces the effective simulation cost while retaining essential features, as discussed next.

The dominant reaction–transport processes in various parts of the catalyst layer are shown in Fig. 3.2(c), which is a cross sectional slice of the unit cell shown in Fig. 3.2(b). Diffusion is the dominant transport mechanism for gaseous reactants and products. The most important feature for predicting cell performance is the presence of a diffusion–reaction zone inside the hydrophilic phase, near the interface at which reactants are dissolved and products are outgassed. For the case shown in the schematic, hydroxide ions are also produced in Faradaic reactions; they are transported to the anode by migration. We argue that the processes described here are essential for accurate prediction of cell performance. Previously neglected phenomena (*e.g.,* macroscopic tortuosity and alteration of effective interfacial surface area) may be incorporated as corrections to the fundamental model presented in this work, though we do not do so in this work.

Finally, we consider gas transport in the hydrophobic phase and coupling between the two regions. Figure 3.3(a) depicts the interdigitated channels through which reactants are introduced and products are removed. Since gas flowing into the GDE encounters a dead–

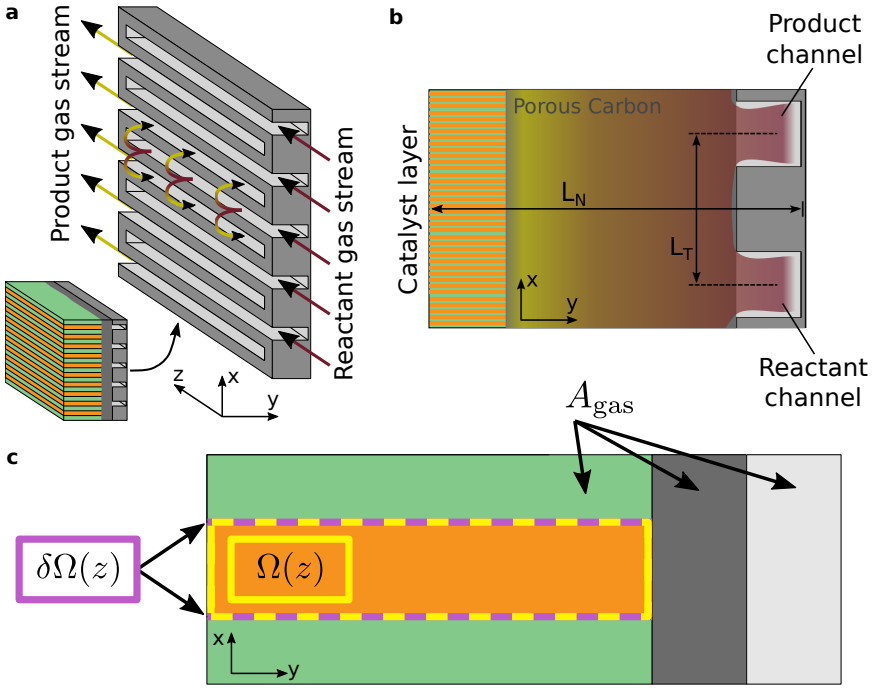

Figure 3.3: a) Interdigitated channels for flow of gaseous reactants/products. b) Cross–sectional slice of catalyst/GDE assembly, drawn with accurate visual scale. c) Effective control volume for gaseous phase, over which averaging is performed.

end, it is forced through the carbon/PTFE region before reaching the exit channel. A scaled cross–sectional drawing of the catalyst/GDE structure is shown in Fig. 3.3(b). We depict a single periodic unit of the structure, including one reactant channel and one product channel separated by distance L_T. The full thickness of the catalyst/GDE structure is L_N. The subscripts T and N refer to tangential and normal directions with respect to the cell. Note that the unit cell depicted in Fig. 3.2(b) (which is the domain for which we develop and solve the governing equations) has a much narrower width, L_U, than the gas channel separation length, L_T.

Diffusion is the dominant gas transport mechanism in the transverse and normal directions. The transverse–direction diffusion time scale is given by $\tau_{\mathrm{D},T} = L_T^2/D$, where length scale $L_T \approx 160\,\mu\mathrm{m}$ and diffusion through the gaseous phase is characterized by $D \approx 1 \times 10^{-5}\,\mathrm{m^2\,s^{-1}}$, resulting in $\tau_{\mathrm{D},T} = O(1 \times 10^{-3}\,\mathrm{s})$. Similarly, the normal–direction diffusion time scale is computed using $L_N \approx 430\,\mu\mathrm{m}$ as $\tau_{\mathrm{D},N} = O(1 \times 10^{-2}\,\mathrm{s})$.

In the axial direction, z, the Peclet number (ratio of advection velocity and diffusion velocity) is given by $\mathrm{Pe} = Q\mathrm{d}z/2L_g^2D = O(100)$, where gas flow rate $Q = 1\,\mathrm{sccm}$ and dz is the length scale associated with discretization in the axial direction. We confirm in our simulations that $\mathrm{d}z = L_z/10 = 1\,\mathrm{mm}$ is sufficient to resolve variation across the length of the cell. The large Peclet number suggests that advection is the dominant transport mechanism in the axial direction.

The characteristic residence time associated with gas transport through a cross–sectional control volume with thickness $\mathrm{d}z$ is given by $\tau_{\mathrm{A}} = \mathrm{d}zL_gL_x^C/2Q = O(1\times10^{-2}\,\mathrm{s})$. We find that $\tau_{\mathrm{D},T} \ll \tau_{\mathrm{A}}$, suggesting that the gas phase is expected to be well–mixed in the transverse direction, as shown in Fig. 3.3(b). Note that we find $\tau_{\mathrm{D},N} \approx \tau_{\mathrm{A}}$, which suggests that gradients in the gaseous species concentrations may develop in the y direction.

In keeping with our motivation to retain only essential phenomena, we neglect gas–phase gradients in the y direction. In essence, we assume $\tau_{\mathrm{D},T} \ll \tau_{\mathrm{A}}$ *and* $\tau_{\mathrm{D},N} \ll \tau_{\mathrm{A}}$, thereby taking the gaseous phase to be perfectly mixed by diffusion in the x and y directions. As a result, the gas phase may be modeled very simply in 1D using a "plug–flow" approach, accounting for sources/sinks as species dissolve into and are outgassed from the Cu phase.

Returning to the unit cell shown in Fig. 3.2(b), transport in the gas phase is accounted for using the effective control volume shown in Fig. 3.3(c). Gas partial pressures are averaged over an extruded cross–section with thickness $\mathrm{d}z$ that includes (porous) PTFE, (porous) carbon and open advection channels, under the assumption of rapid mixing within each

Table 3.1: Geometric parameters describing the full electrochemical cell and catalyst. This set of parameters corresponds to a nominal reference case; we later vary some parameters to demonstrate their effects on cell performance.

Symbol	Parameter	Value
L_x^{C}	Total cell x dimension length	1 cm
L_z^{C}	Total cell z dimension length	1 cm
L_y^{GC}	Interdigitated gas channel height	80 µm
L_y^{GDL}	Gas diffusion layer (GDL) height (porous carbon layer)	275 µm
L_y^{CL}	Catalyst layer (CL) height	75 µm
L_x	x dimension size of porous copper domain in unit problem	5 µm
L_y	y dimension size of porous copper domain in unit problem	75 µm
L_z	z dimension size of porous copper domain in unit problem	1 cm
R_{GC}	Open fraction of gas channel	0.5
R_{Cu}	Volume fraction of porous copper domain in total CL	0.5

control volume. As before, we neglect edge effects and assume that the unit cell is a valid representation at every x station across the entire width of the cell.

A list of typical geometric parameters for the simplified geometry is shown in Table 3.1. In conclusion, we have developed a compact and geometrically simplified unit–cell representation that captures the essential physics of transport through various parts of the catalyst/GDE structure. In the following sections, we detail the governing equations for transport and reactions in the aqueous and gaseous regions, and we briefly describe the specialized numerical methods that enable development of a highly–efficient, parallelized solver for the equations.

3.2.2 Governing equations

Aqueous region

In this section, we make use of porous electrode theory to write governing equations for the aqueous region — or, more specifically, the electrolyte–filled porous Cu region of the simplified unit problem, depicted as orange in Fig. 3.2(b). Invoking standard porous electrode theory, the transport of species i with concentration c_i is given by

$$\epsilon_a \frac{\partial c_i}{\partial t} + \overrightarrow{\nabla} \cdot \left[-\frac{\epsilon_a D_i}{\tau_a} \left(\overrightarrow{\nabla} c_i + \frac{z_i e}{k_B T} c_i \overrightarrow{\nabla} \phi \right) \right] = R_{\mathrm{hom.},i} + R_{\mathrm{Far.},i}. \tag{3.1}$$

D_i is the mass diffusivity of the species at infinite dilution and z_i is its valence. Porosity ϵ_a and tortuosity τ_a describe the pore structure, which reduces the effective diffusion coefficient

for each species. The constants e, k_B, and T are the fundamental charge, Boltzmann's constant, and the ambient temperature respectively.

Two source terms appear on the right side of Eq. (3.1): the first representing homogeneous reactions occurring within the electrolyte, and the second representing Faradaic reactions occurring at the distributed interfaces between electrolyte and Cu. First, consider a general first order or second order reversible homogeneous reaction with the form

$$\sum_{k=\text{reac.}} s_k S_k \underset{k_b}{\overset{k_f}{\rightleftharpoons}} \sum_{l=\text{prod.}} s_l S_l, \tag{3.2}$$

where k is used to index reactants, l is used to index products, capital S represents the participating species, and lower case s represents the stoichiometric coefficients. k_f and k_b are the forward and backward reaction rate coefficients, respectively. The homogeneous reaction term in Eq. (3.1) for species ξ, which, for demonstration purposes, is a product in the forward direction for Eq. (3.2), is written as

$$R_{\text{hom.},\xi} = \epsilon_a s_\xi \left(k_f \prod_{k=\text{reac.}} c_k^{s_k} - k_b \prod_{l=\text{prod.}} c_l^{s_l} \right). \tag{3.3}$$

If multiple reactions produce or consume species ξ, the total $R_{\text{hom.},\xi}$ is the sum of the individual reaction terms. The relationship between forward and backward reaction rates is provided by equilibrium constant $K_{\text{eq}} = k_f/k_b$ for each reaction.

Next, consider a general Faradaic reaction with the form

$$\sum_{k=\text{ox.}} s_k \text{Ox}_k + ne^- \rightleftharpoons \sum_{l=\text{re.}} s_l \text{Re}_l, \tag{3.4}$$

where Ox_k are oxidants indexed by k, and Re_l are reductants indexed by l. n is the number of electrons transferred in the reaction. Since our work is tailored to the catalyst microenvironment for C_{2+} production at the cathode, we neglect the reverse direction for Eq. (3.4). Thus, for species ξ, which is taken to be a reductant in Eq. (3.4) for demonstration purposes, the Faradaic reaction term in Eq. (3.1) is written using Butler–Volmer kinetics

as

$$R_{\text{Far.},\xi} = \frac{i_0 s_\xi}{ne}\left(\prod_{k=\text{ox.}} \frac{c_k}{c_k^0}\right) \exp\left[-\frac{\alpha e}{k_B T}\left(\phi_E - \phi - U_0\right)\right] \exp\left(-\frac{E_a}{N_A k_B T}\right). \tag{3.5}$$

The parameter i_0 is the volumetric exchange current density, which has units of $\mathrm{A\,m^{-3}\,s}$. α is the transfer coefficient for the reaction, ϕ_E is the electric potential of the Cu material in the GDE, ϕ is the local electric potential in the liquid, and U_0 is the standard reduction potential for the reaction. Finally, the activation energy is given by E_a, and N_A is Avogadro's number. If multiple reactions produce or consume species ξ, the total $R_{\text{Far.},\xi}$ is the sum of the individual reaction terms.

Finally, the equation for conservation of charge is written as

$$\sum_i z_i e \overrightarrow{\nabla} \cdot \left[-\frac{\epsilon_l D_i}{\tau_l}\left(\overrightarrow{\nabla} c_i + \frac{z_i e}{k_B T}\overrightarrow{\nabla}\phi\right)\right] = \sum_i z_i e R_{\text{Far.},i}, \tag{3.6}$$

where the source term on the right hand side is necessary due to Faradaic reactions. Note the absence of a time derivative term in Eq. (3.6): we have assumed instantaneous quasi–electroneutrality throughout the liquid phase. In essence, we assume that the charge of the solid electrode phase is locally shielded by equilibrium double layers that form at the pore walls and have negligible thickness, leading to bulk electroneutrality through the centers of the pores. The potential drop across these electric double layers (both the compact and diffuse portions) is the driving overpotential for Butler–Volmer kinetics.

Gaseous region

As discussed previously, we assume that the gaseous regions are perfectly mixed in the x and y directions, such that species variation in the gas phase can be represented using 1D profiles varying only in the z direction. The concentration of gaseous species i is parameterized by the partial pressure $\overline{p}_i = \overline{X}_i p_0$ for total pressure p_0 (which is taken to be constant throughout the gas phase) and mole fraction $\overline{X}_i$. The over–lines for gas–phase variables indicate averages in the transverse directions, taken over the effective cross section shown in Fig. 3.3(c).

Recognizing that transport in the axial direction (z direction) is dominated by advection

due to the large Peclet number, the equation for transport of species i is written as

$$\frac{\partial \overline{p}_i}{\partial t} + \frac{\partial}{\partial z}\left(\overline{u}_z \overline{p}_i\right) = S_{\text{Diss.},i} + S_{\text{Far.},i}, \tag{3.7}$$

where $\overline{u}_z$ is the transverse–averaged gas velocity. The source and sink terms on the right hand side of Eq. (3.7) represent coupling to the aqueous region. We explain these two terms in the next section.

An equation for the transverse–averaged gas velocity may be determined by summing the individual transport equations in Eq. (3.7) and enforcing that the the partial pressures guarantee $\sum_i \overline{p}_i = p_0$. The resulting equation reads

$$\frac{\partial \overline{u}_z}{\partial z} = \frac{1}{p_0}\sum_i \left(S_{\text{Far.},i} + S_{\text{Diss.},i}\right). \tag{3.8}$$

Equation (3.8) maintains a constant total pressure and determines the mean gas velocity as a function of z by accounting for differences in the net production of moles of gas along the z direction.

Coupling aqueous and gaseous regions

Coupling between the aqueous and gaseous regions is represented mathematically as a boundary condition for Eq. (3.1) and as source/sink terms Eq. (3.7). Though the same physical principle captures both dissolution and outgassing of gaseous species at a gas–liquid interface (Henry's Law), we treat the two processes differently in order to improve efficiency of the numerical solver.

For gaseous reactants, Henry's law is implemented in a straightforward way - the aqueous concentration at the interface between aqueous and gaseous phases is given by the product of the local partial pressure of that species in the gas phase and the Henry's Law constant for that species. For the aqueous region, this may be implemented as a Dirichlet–type boundary condition. For the gaseous region, this mechanism appears on the right side of Eq. (3.7) as $S_i^{\text{Diss.}}$. The term is defined as

$$S_{\text{Diss.},i} = \frac{N_A k_B T}{A_{\text{gas}}} \int\limits_{\mathrm{d}\Omega(z)} \frac{\epsilon_a D_i}{\tau_a} \overrightarrow{\nabla} c_i \cdot \hat{n}\, \mathrm{d}s. \tag{3.9}$$

in which the diffusive flux of gaseous species dissolving into solution at some axial location

z is integrated along the interface between gaseous and aqueous regions (represented as $\mathrm{d}\Omega(z)$, as depicted in Fig. 3.3(c)). Since the gaseous region is treated as perfectly mixed in the transverse directions, the effect of dissolution across the interface denoted $\mathrm{d}\Omega$ has been represented as a volumetric source/sink term.

Since the oxidation direction for Eq. (3.4) is neglected at the cathode, the aqueous concentrations of dissolved gaseous products (*i.e.* hydrogen and ethylene) are not expected to have a substantial impact on the physioichemical dynamics of the system. Therefore, in order to reduce computational cost, we neglect dissolved gaseous products. Instead, the instantaneous rate of gas production via Faradaic reactions appears as the volumetric source term $S_i^{\mathrm{Far.}}$ in Eq. (3.7), which is defined as

$$S_{\mathrm{Far.},i} = \frac{N_A k_B T}{A_{\mathrm{gas}}} \iint\limits_{\Omega(z)} R_{\mathrm{Far.},i} \mathrm{d}A. \tag{3.10}$$

Integration in Eq. (3.10) is performed over the aqueous region cross section at some location z, which is represented as $\Omega(z)$, as depicted in Fig. 3.3(c). The local Faradaic production rate for gaseous species, $R_{\mathrm{Far.},i}$ may be computed using Eq. (3.5).

Finally, we conclude with a summary of the boundary conditions for the gaseous and aqueous regions. The unit cell is depicted schematically in Fig. 3.4. Beginning with the gaseous region in Fig. 3.4(a), we note that each of Eqs. (3.7) and (3.8) requires one boundary condition in z. We enforce the boundary condition at the inlet, where the partial pressures are well known (*e.g.,* pure CO or pure CO_2) and the transverse–averaged gas velocity is set based on the feed flow rate.

For the aqueous region, each of Eq. (3.1) and Eq. (3.6) requires two boundary conditions in each of the spatial dimensions. In the x direction, the aqueous region is bounded at both ends by the interface with the gaseous region. A no–flux boundary condition is applied for ionic species, and the concentration of dissolved gaseous species is set as $c_i = k_H \overline{p}_i$, where $k_{H,i}$ is the Henry's law coefficient. In accordance with quasi–electroneutrality, a homogeneous Neumann boundary condition is applied for electric potential. This is summarized in Fig. 3.4(b).

As shown in Fig. 3.4(a), in the y direction, the bulk electrolyte region is represented using Dirichlet boundary conditions for species concentrations and for the electric potential. The y–boundary between the aqueous and gaseous regions is represented with a no–flux boundary condition for all species. Though gas dissolution via Henry's law is expected at this

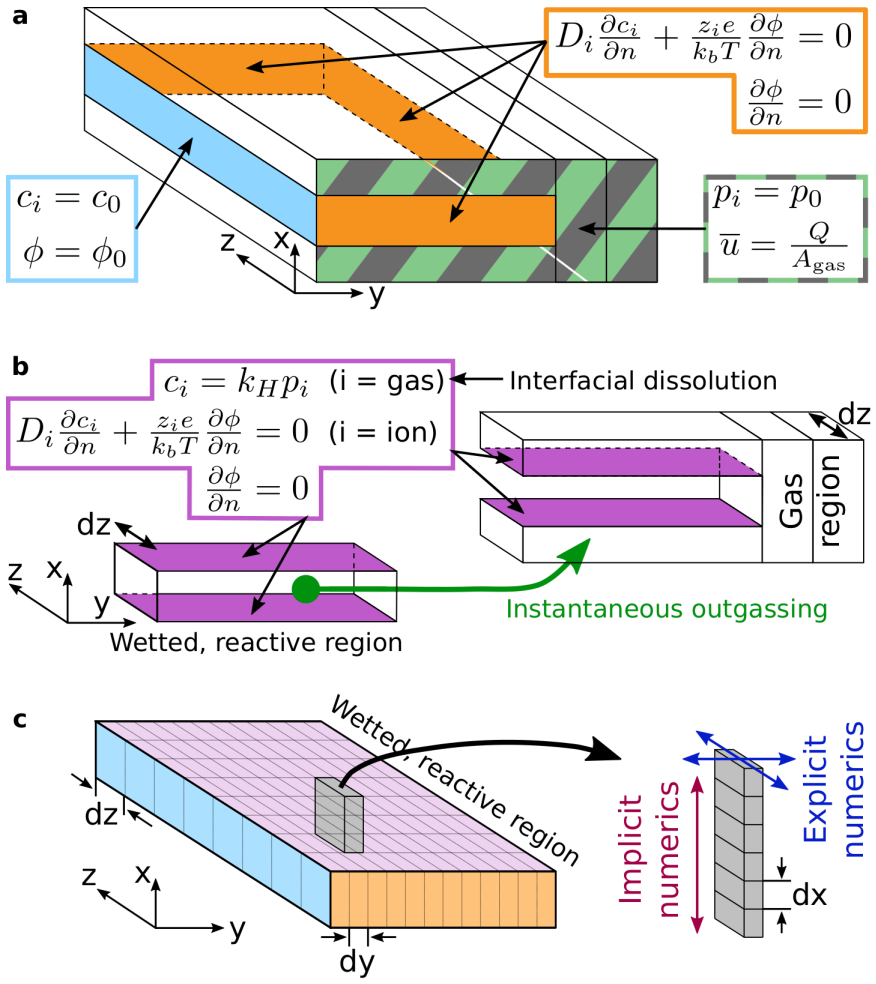

Figure 3.4: a) Inlet boundary condition for the gas flow; Bulk electrolyte boundary condition and no–flux boundary condition for the aqueous domain. b) Coupling between the aqueous and gaseous domains appears as an x–direction boundary condition for the aqueous domain, and as volumetric source/sink terms for the gaseous domain. c) Decomposition of the aqueous domain with "pencil decomposition" and semi–implicit spatial numerics.

portion of the interface as well, we neglect this effect since its surface area is approximately 3% of the total interfacial area between aqueous and gaseous regions. By doing so, we improve computational efficiency by removing the need to resolve a thin reaction–diffusion zone layer in the y direction.

In the z direction, a no–flux boundary condition is used for all species, with a homogeneous Neumann boundary condition for the electric potential. This is depicted in Fig. 3.4(a).

In summary, Eqs. (3.1) and (3.6) to (3.8) are a system of partial differential equations describing transport of aqueous and gaseous species throughout the catalyst/GDL structure. The equations may be solved in a domain representing a single unit cell of the geometrically simplified structure, with the boundary conditions shown in Fig. 3.4(a)–(b).

3.3 Numerical Methods and Solver algorithm

In this section, we describe the specialized numerical methods that allow us to solve the governing equations efficiently. We use scaling arguments to assess the spatiotemporal scales associated with transport in each of the dimensions, selecting implicit numerical methods for only the numerically–stiffest physicochemical phenomena. This analysis enables development of an efficient parallel solver for the governing equations.

We begin our discussion with treatment of the aqueous region. Observe in Fig. 3.2(b) that the geometrically simplified aqueous region has large aspect ratio: $L_x \ll L_y, L_z$. Consequently, the discrete mesh size associated with each dimension is expected to satisfy $\Delta x \ll \Delta y, \Delta z$. Noting that the diffusion time scale is $\tau_{\mathrm{D},x} \approx \Delta x^2/D$ (with similar definitions for transport in the y and z directions), we conclude that $\tau_{\mathrm{D},x} \ll \tau_{\mathrm{D},y}, \tau_{\mathrm{D},z}$. The time scale associated with diffusive transport across the width of the aqueous region poses a much stricter time step requirement than the other dimensions.

Based on this analysis, we choose to utilize a time–implicit scheme for terms associated with x direction transport (and for reaction terms, which are local terms), while using an explicit method for transport in the other directions. As we proceed to show, this choice enables a parallel decomposition of the aqueous domain. Strips of the domain oriented along the x direction may be solved independently of the others for each time step, as shown in Fig. 3.4(c).

We index discrete variables using superscripts i, j, k, and n. For example, $c_i^{(i,j,k,n)}$ is the

concentration of species i at the computational cell center located at $\left(x^i, y^j, z^k\right)$, and at at time t^n. We use a staggered mesh methodology, whereby fluxes are computed at cell faces, which are denoted using half–integer superscripts. For example, the flux of species i in the x direction is computed at the adjacent $x^{i\pm1/2}$ faces using second order central differencing as

$$\begin{aligned}\overrightarrow{F}_{i,x}^{(i\pm1/2,j,k,n)} = -\frac{\epsilon_a D_i}{\tau_a}\Bigg(&\frac{\pm c_i^{(i\pm1,j,j,n)} \mp c_i^{(i,j,k,n)}}{\Delta x^{i\pm\frac{1}{2}}} \\ &+\frac{z_i e}{k_B T}\frac{c_i^{(i\pm1,j,j,n)} + c_i^{(i,j,k,n)}}{2}\frac{\pm\phi^{(i\pm1,j,k,n)} \mp \phi^{(i,j,k,n)}}{\Delta x^{i\pm\frac{1}{2}}}\Bigg).\end{aligned} \tag{3.11}$$

Similar terms may be written for fluxes in the y and z directions. Note that indexing of the mesh–size variable, Δx, is employed to account for nonuniform meshes with additional refinement near the boundaries.

Using this notation, Eq. (3.1) is written discretely as

$$\frac{c_i^{(i,j,k,n)} - c_i^{(i,j,k,n-1)}}{\Delta t} = f_i^{i,j,k,n-1} + g_i^{i,j,k,n}, \tag{3.12}$$

where f and g are defined as

$$\begin{aligned}f_i^{i,j,k,n-1} = &-\frac{F_{i,y}^{\left(i,j+\frac{1}{2},k,n-1\right)} - F_{i,y}^{\left(i,j-\frac{1}{2},k,n-1\right)}}{\Delta y^i} \\ &-\frac{F_{i,z}^{\left(i,j,k+\frac{1}{2},n-1\right)} - F_{i,z}^{\left(i,j,k-\frac{1}{2},n-1\right)}}{\Delta z^i}\end{aligned} \tag{3.13}$$

and

$$\begin{aligned}g_i^{i,j,k,n} = &-\frac{F_{i,x}^{\left(i+\frac{1}{2},j,k,n\right)} - F_{i,x}^{\left(i-\frac{1}{2},j,k,n\right)}}{\Delta x^i} \\ &+ R_{\text{hom.},i}^{i,j,k,n} + R_{\text{Far.},i}^{i,j,k,n},\end{aligned} \tag{3.14}$$

respectively. The state of the system is known at time $n-1$ from the previous time step or initial condition; the system is time–advanced by solving for the variables at time n. We observe that terms represented in f are treated explicitly in time (as indicated by temporal index $n-1$, resulting in a forward Euler scheme) while those in g are implicit (as indicated by temporal index n, resulting in a backward Euler scheme).

Note that we have made use of a simple, low–order temporal discretization in writing Eq. (3.12), since the main purpose of this section is explaining how selection of efficient numerical methods is inspired by the innate physicochemical dynamics of the system. Our production solver is implemented using higher order explicit and implicit schemes for f and g, respectively.

The discrete version of Eq. (3.6) is given by

$$\sum_i z_i e \left(f_i^{i,j,k,n} + g_i^{i,j,k,n} \right) = 0, \tag{3.15}$$

wherein readers should note that both f and g are evaluated at time n, ensuring that the computed fields satisfy charge conservation at time n.

We now show how the directional separation of implicit and explicit terms allows construction of a parallel solver. We introduce the vector quantities $\overrightarrow{c}^n$ and $\overrightarrow{\phi}^n$, which represent the data stored at time n for all discrete points in space. Note that $\overrightarrow{c}^n$ contains data for all species interlaced together.

Since iteration is required due to nonlinearity of the governing equations, we linearize the equations around the base states $\overrightarrow{c}^\star$ and $\overrightarrow{\phi}^\star$ by writing

$$\begin{aligned} \overrightarrow{c}^n &= \overrightarrow{c}^\star + \overrightarrow{\delta c} \\ \overrightarrow{\phi}^n &= \overrightarrow{\phi}^\star + \overrightarrow{\delta \phi}. \end{aligned} \tag{3.16}$$

First, we substitute Eq. (3.16) into Eq. (3.12) and only retain terms up to first order in $\overrightarrow{\delta c}$ or $\overrightarrow{\delta \phi}$. The resulting equation can be represented as a linear system for the delta variables as

$$\mathbf{M_1^{j,k}} \overrightarrow{\delta c}^{j,k} + \mathbf{M_2^{j,k}} \overrightarrow{\delta \phi}^{j,k} = \overrightarrow{b_1}^{j,k}. \tag{3.17}$$

Crucially, the superscript indices in Eq. (3.17) indicate that an independent linear system can be written for each pencil–like strip of the domain comprising contiguous cells in the x direction (as shown in Fig. 3.4(c), with location in the y–z plane indexed by j and k). For a system with N_s aqueous species and N_x computational cells in the x direction, matrices $\mathbf{M_1^{j,k}}$ and $\mathbf{M_2^{j,k}}$ have sizes $[N_x N_s \times N_x N_s]$ and $[N_x N_s \times N_x]$, respectively. The vector quantity $\overrightarrow{b_1}$ is purely a function of the base state and previous time steps.

Similarly, we substitute Eq. (3.16) into Eq. (3.15) and only retain terms up to first order

in $\overrightarrow{\delta c}$ or $\overrightarrow{\delta \phi}$, yielding

$$\mathbf{M_3}\overrightarrow{\delta c} + \mathbf{M_4}\overrightarrow{\delta \phi} = \overrightarrow{b_2}. \tag{3.18}$$

Here, the domain is not decomposed into separate regions since all terms are discretized at time n. Matrices $\mathbf{M_3}$ and $\mathbf{M_2}$ have sizes $[N_x N_y N_z \times N_x N_y N_z N_s]$ and $[N_x N_y N_z \times N_x N_y N_z]$, respectively (where N_y and N_z are number of computational cells in each direction).

Finally, we perform a similar treatment for the gaseous region. For the sake of brevity, we will proceed straight to discretized equations presented in forms similar to Eqs. (3.17) and (3.18). Equation (3.7) is written discretely as

$$\frac{\overline{p}_i^{k,n} - \overline{p}_i^{k,n-1}}{\Delta t} = q_i^{k,n-1} + s_i^{k,n-1}, \tag{3.19}$$

where q represents standard RK–4 treatment of the advection term in Eq. (3.7), with second order central differences in space. s, which contains a forward Euler treatment of the aqueous coupling terms, is defined as

$$s_i^{k,n-1} = S_{\text{Far.},i}^{k,n-1} + S_{\text{Diss.},i}^{k,n-1}. \tag{3.20}$$

An RK–4 scheme permits stability for discretization of the advection term, whose modes possess imaginary eigenvalues. In order to avoid the need for multiple iterative solves of the aqueous and gaseous regions, however, we take $\overline{u}_z$ to be fixed at time value $n-1$ in q (as opposed to updating its value along with $\overline{p}_i$ in each sub–step of the RK–4 scheme). This assumption is justified if the velocity field evolves slowly compared to the time step, which we confirm in our results.

Introducing vector quantity $\overrightarrow{\overline{p}}^{\,n}$ as the partial pressure data for all species and computational cells at time n, Eq. (3.7) is written in discretized vector form as

$$\overrightarrow{\overline{p}}^{\,n} = \overrightarrow{\overline{p}}^{\,n-1} + \Delta t \overrightarrow{b_3} + \Delta t \overrightarrow{b_4}, \tag{3.21}$$

where $\overrightarrow{b_3}$ represents standard RK–4 treatment of the advection term with second order central differences in space, and $\overrightarrow{b_4}$ contains a forward Euler treatment of the aqueous coupling terms. All vector quantities in Eq. (3.19) have size $[N_g N_z \times 1]$, where N_g is the

Algorithm 3.1 Pseudocode for computation of $\overrightarrow{c}^n$, $\overrightarrow{\phi}^n$, $\overrightarrow{p}$, and $\overrightarrow{u_z}^n$, taking all variables to be known at time $n-1$.

$\overrightarrow{b_3}$, $\overrightarrow{b_4}$ computed using $\overrightarrow{u_z}^{n-1}$, $\overrightarrow{p}^{n-1}$, $\overrightarrow{c}^{n-1}$, $\overrightarrow{\phi}^{n-1}$
$\overrightarrow{p}^n \leftarrow \overrightarrow{p}^{n-1} + \Delta t \overrightarrow{b_3} + \Delta t \overrightarrow{b_4}$
$\overrightarrow{c}^\star \leftarrow \overrightarrow{c}^{n-1}$
$\overrightarrow{\phi}^\star \leftarrow \overrightarrow{\phi}^{n-1}$
$\mathcal{R}_1 \leftarrow \infty$
$\mathcal{R}_{\max} \leftarrow$ tolerance
while $\mathcal{R}_1 \geq \mathcal{R}_{\max}$ **do**
    for $j = [1, N_y], k = [1, N_Z]$ **do**
        $\mathbf{M_1^{j,k}}$, $\overrightarrow{b_1}^{j,k}$ computed using $\overrightarrow{c}^\star$, $\overrightarrow{\phi}^\star$
        $\overrightarrow{\delta c}^{j,k} \leftarrow \mathbf{M_1^{j,k^{-1}}} \overrightarrow{b_1}^{j,k}$
    end for
    $\overrightarrow{c}^\star \leftarrow \overrightarrow{c}^\star + \overrightarrow{\delta c}$
    $\mathcal{R}_2 \leftarrow \infty$
    while $\mathcal{R}_2 \geq \mathcal{R}_{\max}$ **do**
        $\mathbf{M_4}$, $\overrightarrow{b_2}$ computed using $\overrightarrow{c}^\star$, $\overrightarrow{\phi}^\star$
        $\overrightarrow{\delta\phi} \leftarrow \mathbf{M_4^{-1}} \overrightarrow{b_2}$
        $\overrightarrow{\phi}^\star \leftarrow \overrightarrow{\phi}^\star + \overrightarrow{\delta\phi}$
        $\mathcal{R}_2 \leftarrow ||\overrightarrow{\delta\phi}||$
    end while
    $\mathcal{R}_1 \leftarrow ||\overrightarrow{\delta c}||$
end while
$\overrightarrow{c}^n \leftarrow \overrightarrow{c}^\star$
$\overrightarrow{\phi}^n \leftarrow \overrightarrow{\phi}^\star$
$\mathbf{M_5}$, $\overrightarrow{b_5}$ computed using $\overrightarrow{c}^n$
$\overrightarrow{u_z} \leftarrow \frac{1}{p_0} \mathbf{M_5^{-1}} \overrightarrow{b_5}$

number of gaseous species. Similarly, the discrete version of Eq. (3.8) is written as

$$\mathbf{M_5} \overrightarrow{u_z}^n = \frac{1}{p_0} \overrightarrow{b_5}, \tag{3.22}$$

where $\mathbf{M_5}$ (size $[N_z \times N_z]$) is the second order central differencing operator and $\overrightarrow{b_5}$ (size $[N_z \times 1]$) is the net mole production rate computed from summation of the aqueous coupling terms.

We may now use Eqs. (3.17), (3.18), (3.21) and (3.22) to solve iteratively for $\overrightarrow{c}^n$, $\overrightarrow{\phi}^n$, $\overrightarrow{p}$, and $\overrightarrow{u_z}^n$, taking all variables to be known at time $n-1$ and making use of parallel

decomposition for the aqueous region. The final algorithm is presented in Algorithm 3.1.

We briefly point out a few features of Algorithm 3.1. First, the outer while loop (beginning on line 7) is used to iteratively couple Eqs. (3.1) and (3.6), which are solved separately for improved efficiency. Equation (3.1) is solved starting with the for–loop on line 8, which may be performed in parallel over all pairs of j and k indices. Note that $\mathbf{M_2^{j,k}}$ in Eq. (3.17) has been dropped in order to improve efficiency — Eq. (3.1) is linear with respect to concentration when considering fixed electric potential, allowing solution of Eq. (3.1) in a single step.

Similarly, Equation (3.6) is solved starting with the inner while loop on line 14. Analogous to the treatment of species transport equations, we drop $\mathbf{M_3^{j,k}}$ from Eq. (3.18), taking concentrations to be fixed while solving for electric potential. In this case, however, iteration is still required — even with fixed concentration profiles, the equation is nonlinear with respect to $\overrightarrow{\phi}$ due to the Faradaic reaction terms.

3.4 Results and Discussion

We present results for two different cases. First, we consider the case of CO electroreduction for validation, comparing our simulation results to published experimental data. Second, we return to the case of CO_2 reduction, performing a parameter study in order to determine the impact that geometric and chemical parameters have on the formation of ${CO_3}^{2-}$ and overall cell performance.

3.4.1 CO Electroreduction Full Results

In this section, we examine the full simulation results for the case of CO electroreduction for fixed catalyst loading of $2500\,\mu g\,cm^{-2}$ (which corresponds to catalyst thickness of $L_y = 92.5\,\mu m$) and Cu volume fraction of $R_{Cu} = 0.433$. The simulations are run in galvanostatic mode until steady–state, for current densities varying between $50\,mA\,cm^{-2}$ and $300\,mA\,cm^{-2}$. The bulk electrolyte is 1 M NaOH. A complete list of geometric parameters, operating conditions, and physical constants for the full range of CO validation cases is provided in Table 3.2, a list of homogeneous reaction kinetic parameters is provided in Table 3.3, and a list of Faradaic reaction kinetic parameters is provided in Table 3.4. As in recent work [113], we group liquid–phase products of CO reduction into a single category (LIQ) for the sake of modeling the kinetics. Additionally, we note that the parameters in

Table 3.2: Geometric parameters, operating conditions, and physical constants for CO electroreduction validation cases.

Symbol	Parameter	Value
L_x^{C}	Total cell x dimension length	1 cm
L_z^{C}	Total cell z dimension length	1 cm
L_y^{GC}	Interdigitated gas channel height	80 µm
L_y^{GDL}	Gas diffusion layer (GDL) height (porous carbon layer)	275 µm
L_y^{CL}	Catalyst layer (CL) height	20 µm to 100 µm
L_x	x dimension size of porous copper domain in unit problem	1 µm to 10 µm
L_y	y dimension size of porous copper domain in unit problem	20 µm to 100 µm
L_z	z dimension size of porous copper domain in unit problem	1 cm
R_{GC}	Open fraction of gas channel	0.5
R_{WCR}	Volume fraction of porous copper domain in total CL	0.1 to 0.9
T	Temperature	298 K
$\dot{Q}$	Gas flow rate	1 sccm
p_0	Total pressure	1 bar
k_B	Boltzmann's constant	$1.38 \times 10^{-23}\,\mathrm{J\,K^{-1}}$
e	Charge of electron	$1.602 \times 10^{-19}\,\mathrm{C}$
N_A	Avogadro's number	6.022×10^{23}

Table 3.3: Homogeneous reaction kinetic parameters for CO electroreduction validation cases. Note, water auto–dissociation is modeled using zeroth–order kinetics, assuming fixed $c_{\mathrm{H_2O}} = 55.5\,\mathrm{M}$.

Reaction	k_f	$K_{\mathrm{eq}} \equiv k_b/k_f$
$\mathrm{OH^-(aq) + H^+(aq) \leftrightarrow H_2O}$	$1 \times 10^8\,\mathrm{mol^{-1}\,m^3\,s^{-1}}$	$1 \times 10^{-14}\,\mathrm{mol^2\,m^{-6}}$

Table 3.4: Faradaic reaction kinetic parameters for CO electroreduction validation cases. As in recent work [2, 113], we group liquid–phase products of CO reduction into a single category (LIQ) for the sake of modeling the kinetics. Water transport is not included in the model; we take fixed $c_{\mathrm{H_2O}} = 55.5\,\mathrm{M}$. Transport of liquid phase products is not included in the model, we assume their presence affects the system negligibly.

Reaction	Parameter	Value
$\mathrm{2CO(aq) + 6H_2O + 8e^-}$ $\leftrightarrow \mathrm{C_2H_4(g) + 8OH^-(aq)}$	i_0	$1.45 \times 10^{-1}\,\mathrm{A\,m^{-3}}$
	E_a	0 J
	U^0	0.17 V
	c_r^0	$6 \times 10^{-4}\,\mathrm{M}$
	α	0.7565
$\mathrm{CO + 3.5e^- + xH_2O}$ $\leftrightarrow \mathrm{yLIQ + 3.5OH^-(aq)}$	i_0	$3.53 \times 10^{1}\,\mathrm{A\,m^{-3}}$
	E_a	0 J
	U^0	0.22 V
	c_r^0	$6 \times 10^{-4}\,\mathrm{M}$
	α	0.4931
$\mathrm{2H_2O + 2e^-}$ $\leftrightarrow \mathrm{H_2(g) + 2OH^-(aq)}$	i_0	$9.81 \times 10^{2}\,\mathrm{A\,m^{-3}}$
	E_a	0 J
	U^0	0 V
	c_r^0	1 M
	α	0.4714

Table 3.4 are selected based on Tafel analysis of experiments [2, 113].

Steady–state ion concentration profiles along the domain center–lines in all three dimensions are shown in Fig. 3.5 for a variety of current densities, demonstrating substantial variation as current density is modulated. Note, in particular, the formation of reaction–diffusion layers in the x direction, as is seen in the concentration profile for CO. CO concentration is higher near the Cu–PTFE interfaces (the boundaries in the x direction) than in the center of the aqueous domain, and depletion of CO from the aqueous domain progresses as current density is increased.

Similarly, note the presence of a reactant (CO) concentration gradient in z, reflecting the progressive consumption of CO along the axial direction. Increasing consumption of CO in the axial direction reduces its partial pressure in the gas phase. As per Henry's law, reduced partial pressure of CO leads to reduced concentration in the aqueous phase as well. For this case, the highest current density is associated with near total depletion of CO from later parts of the aqueous region, suggesting that the $z/L_z > 0.8$ portion of the cell is (relatively) starved of reactants. As a result, it is possible that this region contributes more strongly to H_2 evolution than to C_2H_4 formation. We directly confirm this hypothesis later, when considering the case of CO_2 reduction.

Finally, note in Fig. 3.5 the subtle pH gradient in the y and z directions, indicating the importance of resolving microenvironment variation within the catalyst layer in all three spatial dimensions. This variation is expected to become more significant for the case of CO_2 electroreduction due to pH sensitivity of the homogeneous reaction mechanism, as investigated later in this chapter.

In Fig. 3.6 we examine steady–state electric potential profiles in all three dimensions. As before, profiles are plotted along the aqueous domain centerlines in all three dimensions. Notable features here are potential gradients in the y and z directions. The former is responsible for transport of ions between the anode and cathode of the cell, while the latter develops at high current densities as a consequence of variation in solution composition in the axial direction.

In Fig. 3.7, we examine the gas–phase partial pressures as a function of the axial coordinate, z. Note the presence of strong gradients in the z direction, particularly for higher current densities. CO is consumed, while the products H_2 and C_2H_4 are generated progressively at downstream axial locations. Additionally, the gas phase velocity is plotted in Fig. 3.7, demonstrating that the spanwise–averaged flow rate at each axial station must be

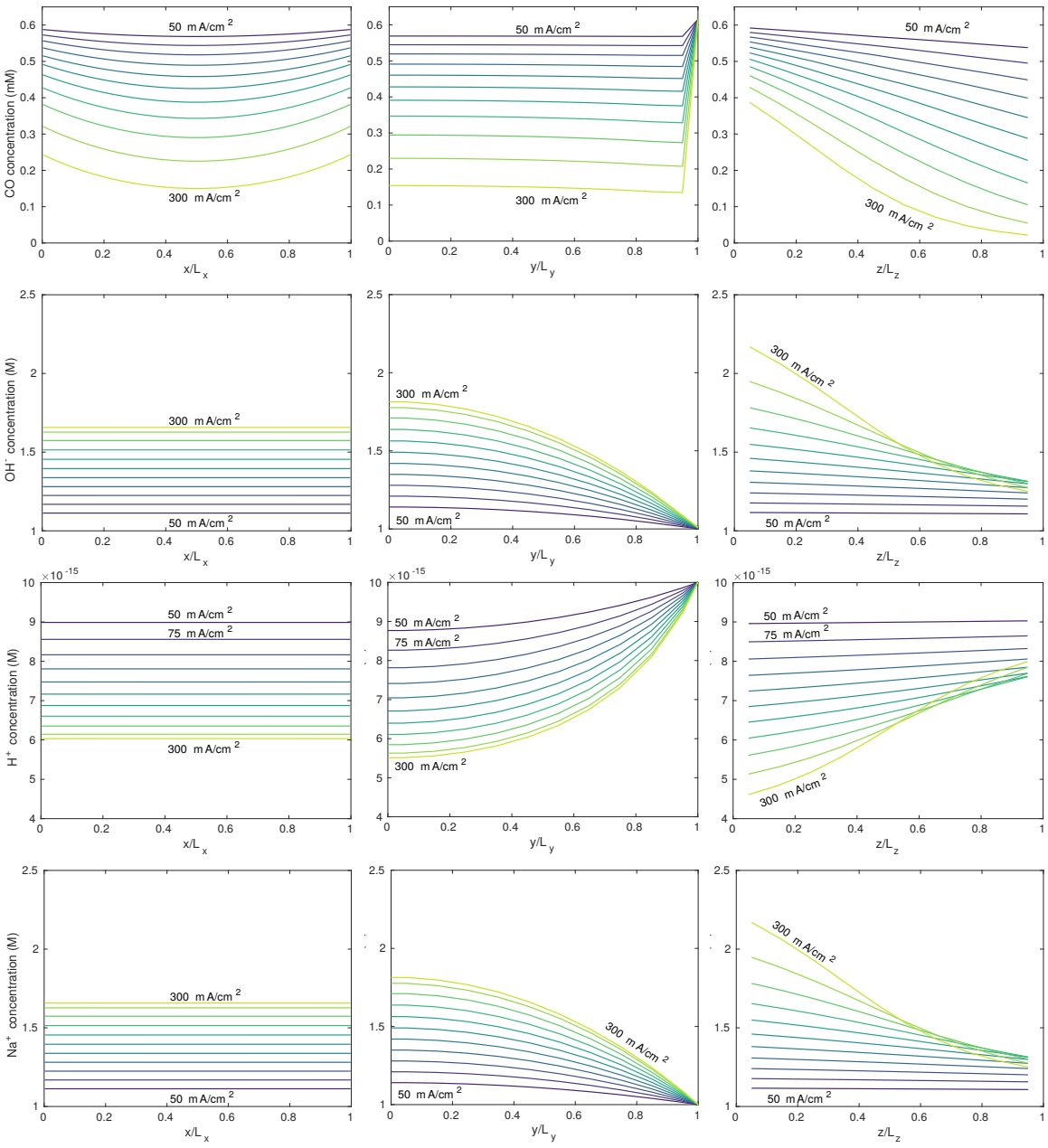

Figure 3.5: Steady–state concentration profiles for CO reduction, measured along the center–lines in each of the three dimensions. Catalyst loading is fixed to $2500\,\mu g\,cm^{-2}$, and current density is varied from $50\,mA\,m^{-2}$ to $300\,mA\,m^{-2}$.

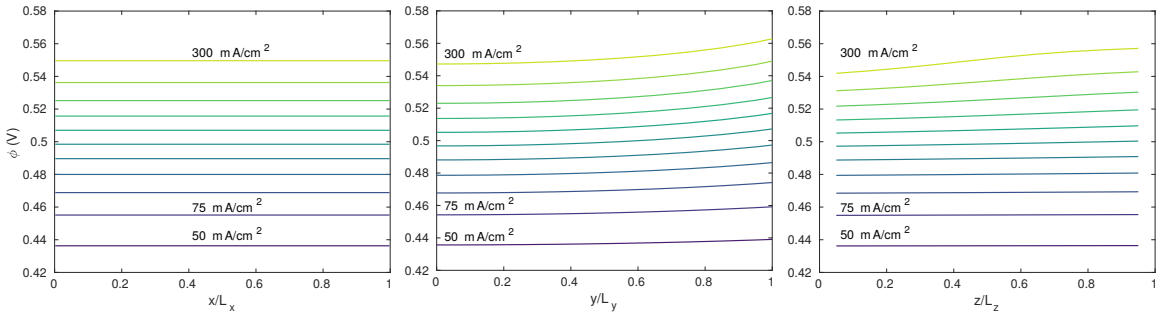

Figure 3.6: Steady–state electric potential profiles for CO reduction, measured along the center–lines in each of the three dimensions. Catalyst loading is fixed to $2500\,\mu g\,cm^{-2}$, and current density is varied from $50\,mA\,m^{-2}$ to $300\,mA\,m^{-2}$.

adjusted to account for the net molar balance of species dissolving into the aqueous phase vs. species produced in Faradaic reactions and outgassed from the aqueous phase.

In Fig. 3.8, we examine the current density and cell voltage as a function of time, demonstrating convergence toward the steady state results for all current densities and for all catalyst loading values. These results validate the choice of 10 s for a simulation cutoff time that serves as a reasonable approximation for true steady state.

To complete this section, we present complete concentration profiles for a set of cases in which current density is fixed to $250\,mA\,cm^{-2}$ and the catalyst loading (which, recall, corresponds to thickness of the catalyst) is varied from $500\,\mu g\,cm^{-2}$ to $5000\,\mu g\,cm^{-2}$. We begin in Fig. 3.9, which shows the ion concentration profiles along the domain centerlines in all three dimensions. The key takeaway can be observed by examining the CO concentration profiles in all three dimensions, which shows that lower catalyst loading is associated with lower CO concentrations in the aqueous domain. Recall that current density is fixed for all cases. A decrease in the catalyst loading corresponds to an increase in the cell voltage required to drive current through the cell, since the amount of electrochemically active area has been reduced. Consequently, the local rate of CO consumption is elevated, resulting in the trend seen in Fig. 3.9. As was the case in previous results for which catalyst loading was held fixed and current density was varied, we observe pH variation in the y and z directions, particularly for high catalyst loading values.

Finally, we conclude with the electric potential profiles and gas phase variables in Fig. 3.10 and Fig. 3.11, respectively. As mentioned previously, we observe that higher potential is required to drive the same current through catalysts with lower loading, due

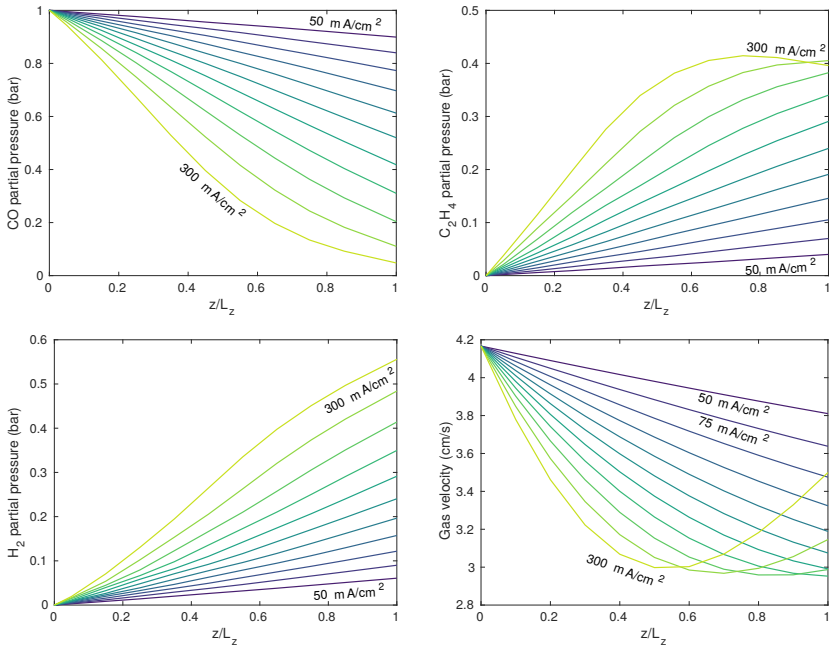

Figure 3.7: Steady–state gas–phase partial pressure and velocity profiles for CO reduction. Catalyst loading is fixed to 2500 µg cm^{-2}, and current density is varied from 50 mA m^{-2} to 300 mA m^{-2}.

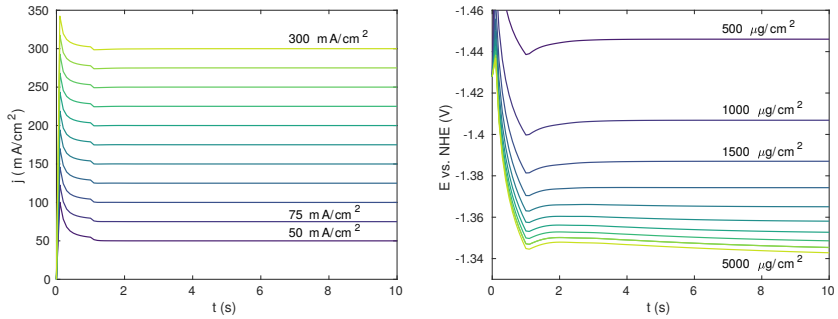

Figure 3.8: Time series of current density and electric potential, showing convergence to steady state for the case of CO reduction. On the left, catalyst loading is fixed to 2500 µg cm^{-2}, and current density is varied from 50 mA m^{-2} to 300 mA m^{-2}. On the right, current density is fixed to 250 mA m^{-2} and catalyst loading is varied from 500 µg cm^{-2} to 5000 µg cm^{-2}.

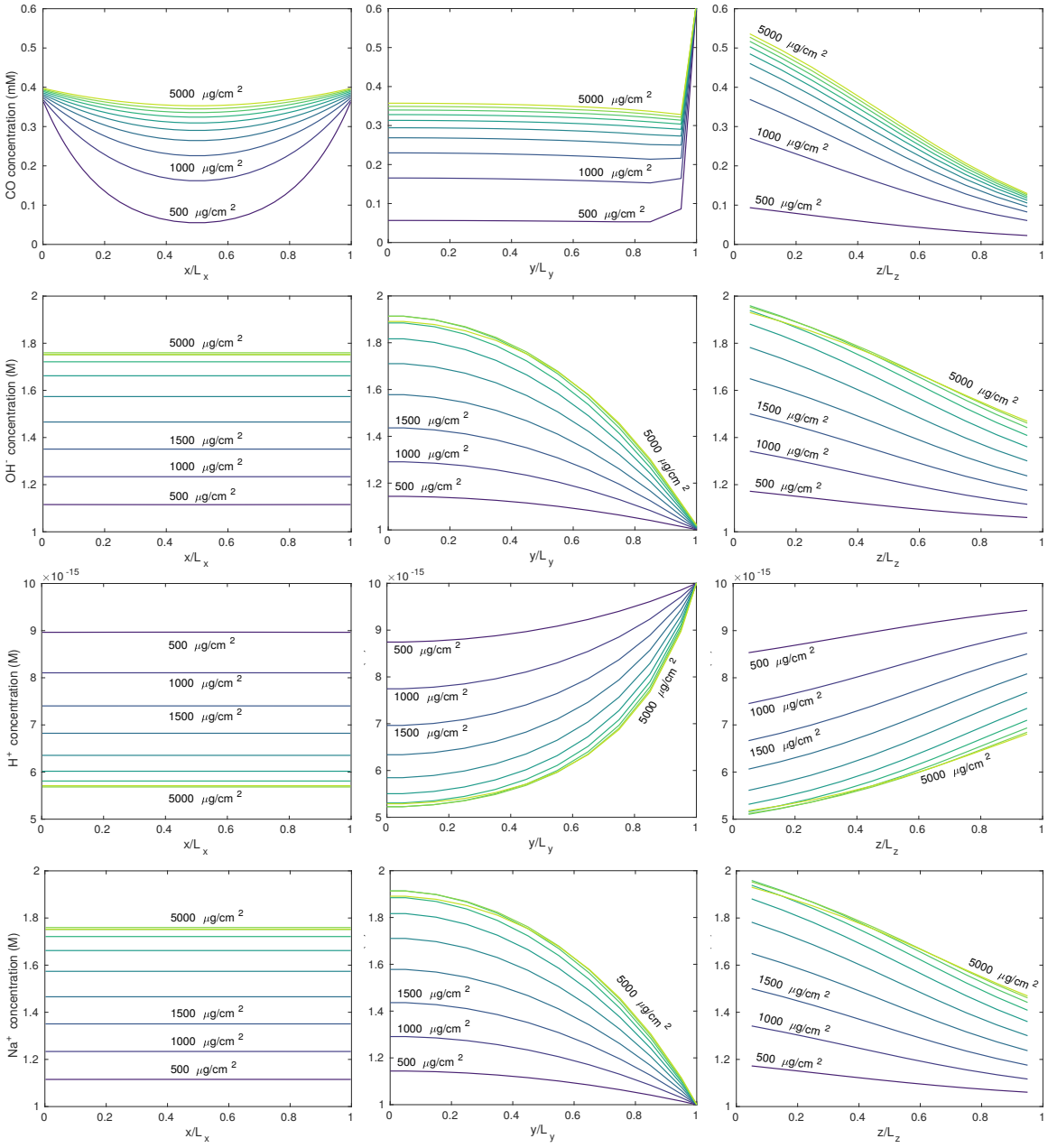

Figure 3.9: Steady–state concentration profiles for CO reduction, measured along the center–lines in each of the three dimensions. Current density is fixed to $250\,\mathrm{mA\,cm^{-2}}$ and the catalyst loading is varied from $500\,\mu\mathrm{g\,cm^{-2}}$ to $5000\,\mu\mathrm{g\,cm^{-2}}$.

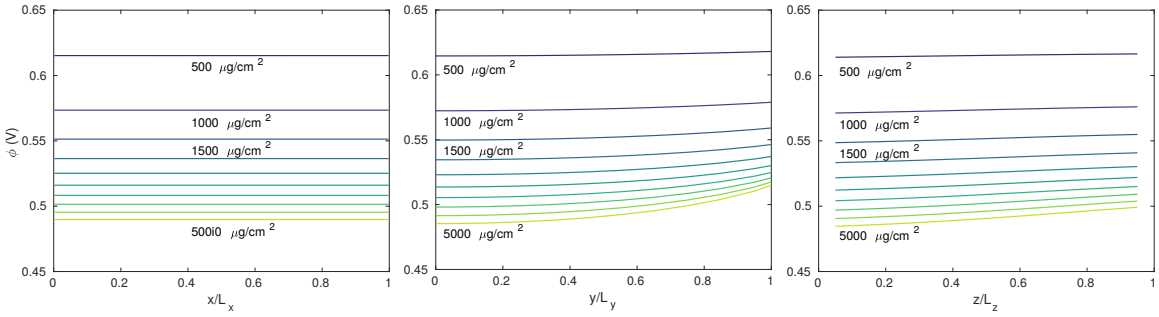

Figure 3.10: Steady–state electric potential profiles for CO reduction, measured along the center–lines in each of the three dimensions. Current density is fixed to $250\,\mathrm{mA\,cm^{-2}}$ and the catalyst loading is varied from $500\,\mu\mathrm{g\,cm^{-2}}$ to $5000\,\mu\mathrm{g\,cm^{-2}}$.

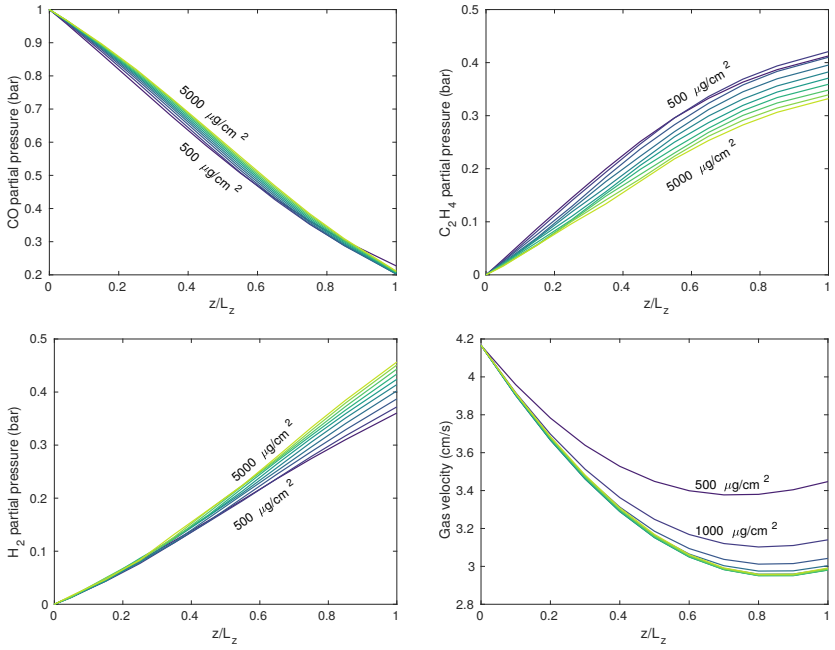

Figure 3.11: Steady–state gas–phase partial pressure and velocity profiles for CO reduction. Current density is fixed to $250\,\mathrm{mA\,cm^{-2}}$ and the catalyst loading is varied from $500\,\mu\mathrm{g\,cm^{-2}}$ to $5000\,\mu\mathrm{g\,cm^{-2}}$.

to the reduction in electrochemically active area. The gas–phase partial pressure profiles are, however, relatively insensitive to the catalyst loading, though subtle differences are noticeable.

3.4.2 CO Electroreduction Validation

We now present a comparison of the results generated by our simulation and the findings of Rabinowitz *et al.* [113] for electroreduction of CO using hydrophobic/hydrophilic catalysts. We begin with variation of catalyst loading, which is reported in mass of copper per unit geometric area of the catalyst (that is, per total x–z area of the cell). Variation of the catalyst loading is parameterized as variation of the catalyst height (L_y), assuming invariance in the distribution of Cu and PTFE as more material is added. This is shown schematically in Fig. 3.12(a).

Comparing simulation results to experimental results, we begin by examining the current–voltage curve for a variety of different values of catalyst loading, shown in Fig. 3.12(b). Here (and for all plots in this section), simulation results are shown as curves and experimental results from Rabinowitz *et al.* [113] are shown as discrete points. Note the presence of three simulation curves that are drawn thickly relative to the others, indicating that these simulations correspond to the exact cases examined in the experimental benchmark work. We observe qualitative agreement, demonstrating that the model is able to capture the correct trends with regard to power consumption vs. cell current density. Furthermore, the model accurately captures the trend with respect to variation of catalyst loading, demonstrating higher power requirement for thinner catalysts.

A comparison of single pass conversion efficiency, the fraction of gaseous CO entering the cell that is converted either to ethylene or to various liquid products, is shown in Fig. 3.12(c). Once more, we capture the qualitative trend with variation in catalyst loading. Thicker catalysts exhibit more complete conversion of CO into various products, due primarily to the larger interfacial area between the hydrophobic and hydrophilic regions. Recall that this interface between Cu and PTFE regions is where dissolution of CO into solution occurs.

Figure 3.12(d)–(f) are different ways of examining the distribution of products of the Faradaic reactions, which is expected to exhibit substantial sensitivity to the catalyst microenvironment. Generally, reaction of CO at Cu surfaces produces C_2H_4 in addition to various liquid products such as propanol and ethanol, which have been grouped together for convenience in this work. Additionally, H_2 evolution is a prominent competing reaction,

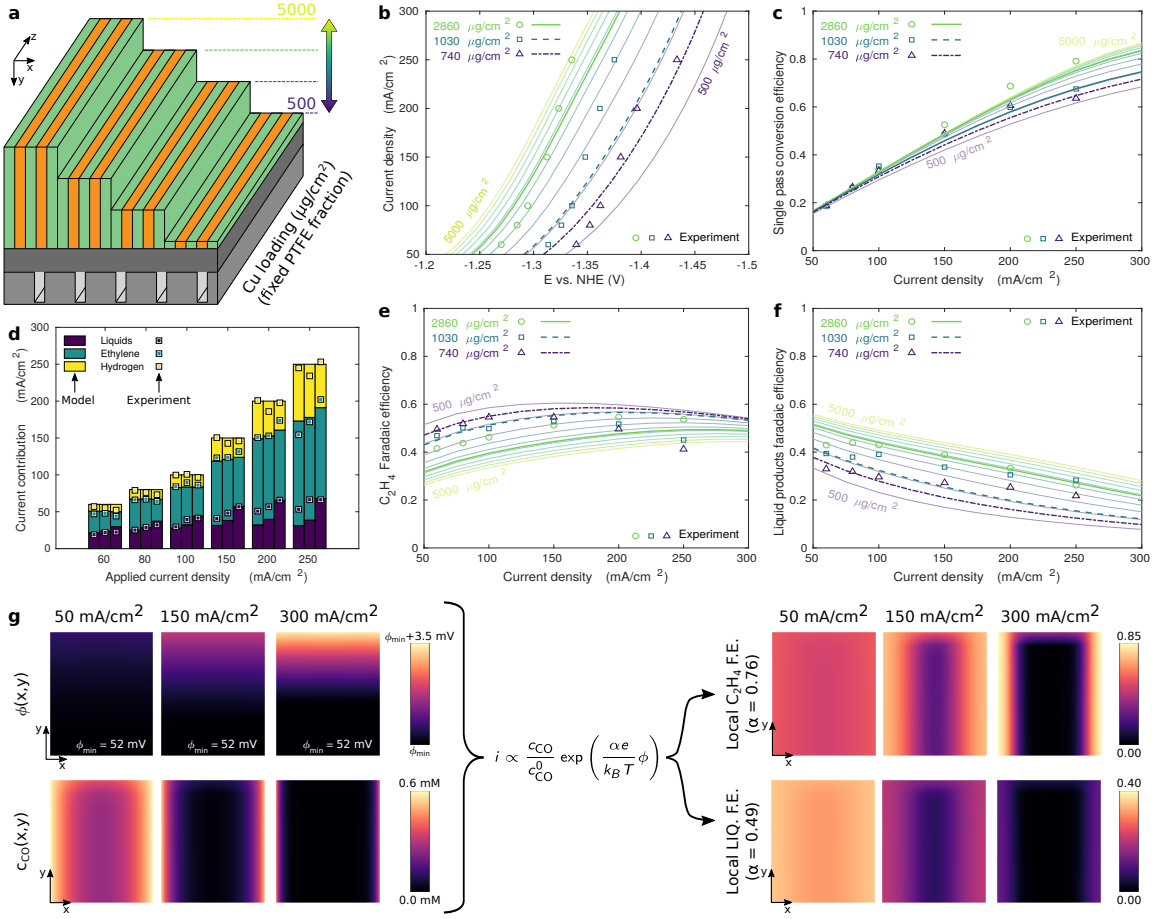

Figure 3.12: Comparison of experimental and simulation results for variation of catalyst loading. a) Variation of catalyst loading is equivalent to variation of catalyst layer thickness. b) Current–voltage curves for different catalyst loadings. c) Single pass conversion efficiency for different catalyst loadings. d) Distribution of current toward dominant products. e) Faradaic efficiency for C_2H_4 production. f) Faradaic efficiency for production of liquid products. g) Concentration and electric potential fields (left), local Faradaic efficiency for ethylene and liquid products (right).

particularly at higher current densities. As mentioned previously, a key performance metric is selectivity toward desired products (here, C_2H_4), since additional cost would be incurred if product separation is required.

In Fig. 3.12(d), we examine the product distribution directly for the three different cases of catalyst loading considered in experiments, observing qualitative agreement with the trends exhibited by experimental data. In Fig. 3.12(e)–(f), we observe the Faradaic efficiency (fraction of current attributable toward production of a certain product) for production of ethylene and the liquid products, both of which are substantially dependent on the catalyst loading for fixed current density.

We first discuss Faradaic efficiency of ethylene, shown in Fig. 3.12(e). Generally, thinner catalyst layers are responsible for enhanced Faradaic efficiency of ethylene. Interestingly, ethylene Faradaic efficiency exhibits a local maximum at moderate current density for all values of catalyst loading — a trend that is seen in experiments and captured by the model. Additionally, note that at current densities lower than the optimal value, the experimental results indicate that lower catalyst loadings are preferred, while the opposite is true at higher current densities. The simulation result appear to capture this phenomenon qualitatively, but the crossover current appears to be much higher compared to experiments.

For liquid products, on the other hand, Faradaic efficiency decreases monotonically with increasing current density for all cases, as shown in Fig. 3.12(f). The simulation results capture this trend, in addition to the reduction in Faradaic efficiency with decreasing catalyst loading.

Finally, in Fig. 3.12(g), we analyze concentration and electric potential slices (slices of the x–y plane, at the midpoint in z) in order to uncover the underlying reasons for aforementioned variation in the Faradaic efficiency of different products. The gradient in electric potential in the y direction, which is more prominent for higher current densities, is responsible for the flow of ions between the anode and cathode as expected. Additionally, note the presence of reaction diffusion layers at the interfaces between Cu and PTFE domains. Gradients near the boundaries become steeper at higher currents, due to more complete depletion of CO from the center of the Cu domain at higher current densities.

The reactant (CO) concentration and electric potential (at steady state) is sufficient to use the Butler–Volmer equation to determine the local Faradaic efficiency for each product, as shown on the right side of Fig. 3.12(g) for two different reactions. The transfer coefficient, α, plays a large role in determining relative Faradaic efficiency of the different products.

For larger α, which is the case for C_2H_4 production, the influence of electric potential is magnified, leading to enhancement of the reaction rate at higher electric potentials. As evidence of this, note that the local Faradaic efficiency for C_2H_4 develops two–dimensional structure at higher current densities, mirroring the y–gradient seen for electric potential at higher current densities. For liquid products, on the other hand, the influence of electric potential is reduced due to the lower α value. For reactions that produce liquid products, the Faradaic efficiency remains strongly a function of x alone and is largely determined by availability of CO, even at higher current densities.

We now examine simulation results for variation of PTFE mass fraction. Changes in the structure of the catalyst are shown in Fig. 3.13(a). Since catalyst loading (mass of copper per area of electrode) is fixed while the PTFE mass fraction is varied, variation of the total catalyst layer thickness is expected coincidentally with variation in the relative amount of Cu and PTFE regions. Additionally, note the variation in characteristic thickness of the Cu regions as PTFE mass fraction is varied. The deposition process used to create the catalyst layers is not able to maintain the characteristic thickness associated with Cu regions while the ratio of the two regions is varied. Rather, increase in the relative amount of PTFE is associated with substantial reduction of the length scale associated with Cu regions.

In Fig. 3.13(b), we show current vs. voltage curves for several different PTFE mass fractions. Simulations reveal a monotonic trend, wherein higher PTFE mass fraction is associated with lower cell voltage for fixed current density (indicating that lower power is required). The trend for experiments, however, is non–monotonic: We see that at sufficiently high values of catalyst loading, the power requirement increases and higher voltages are required to drive the same current. We hypothesize that this discrepancy is due to electrical isolation of some Cu regions for the experimental catalyst at high PTFE mass fractions. As "islands" of the copper region become disconnected from the electrode and are unable to conduct electron–transferring reactions, a higher cell voltage must be applied in order to drive the same current through a smaller electrochemically active area. This effect is not adequately captured by our simplified model. However, we conclude that the regime of extremely large PTFE mass fraction is not practically relevant for CO and CO_2 electroreduction unless the structural problem of isolated Cu islands can be overcome via improvement of the manufacturing process.

In Fig. 3.13(c), we examine the single pass conversion efficiency for different PTFE mass fractions, demonstrating that higher PTFE mass fraction is associated with more complete

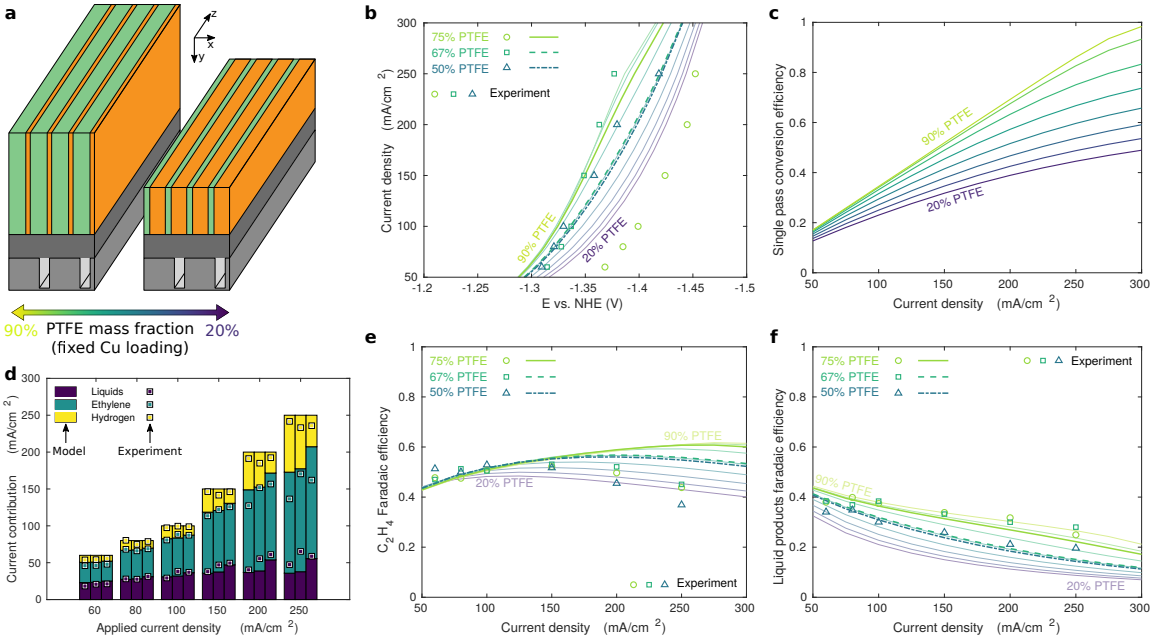

Figure 3.13: Results for CO reduction, for variation of PTFE mass fraction. a) Depiction of change in catalyst structure for varying PTFE mass fraction. b) Current–voltage curves for different PTFE mass fractions. c) Single pass conversion efficiency for different PTFE mass fractions. d) Distribution of current toward dominant products. e) Faradaic efficiency for C_2H_4 production. f) Faradaic efficiency for production of liquid products.

conversion. This finding is intuitive, since more PTFE corresponds to improved transport of gaseous reactants. Finally, in Fig. 3.13(d)–(f) we examine the distribution of products at different current densities for different PTFE mass fractions. Starting with Fig. 3.13(d), we observe qualitative agreement for the distribution of current toward different products at various PTFE mass fractions and current densities. However, examining the Faradaic efficiency for C_2H_4 and liquid products (in Fig. 3.13(e) and Fig. 3.13(f), respectively) reveals discrepancies that are aggravated at higher current densities, particularly for C_2H_4.

3.4.3 CO_2 Electroreduction Reference Case

Having completed validation of the model for the case of CO electroreduction, we now return our attention to electroreduction of CO_2 directly. In this section, we introduce figures of merit and briefly discuss the results of a reference case. This reference case serves as a common comparison point for the cases shown in the next section, where we modulate geometric and operating condition parameters in order to determine the impacts on cell performance.

First, we discuss the figures of merit that will be used to evaluate performance of the CO_2 reduction cell. Ultimately, a cell needs to perform at high carbon efficiency, energy efficiency, and synthesis rate. These figures of merit are considered under steady state operating conditions, where transport, consumption, and production of chemical species are constant in time.

The Faradaic efficiency for a reaction that produces species ξ is introduced as

$$\mathrm{FE}_{\xi} = \frac{n_{\xi} e R_{\mathrm{Far.},\xi}}{\sum_{s} n_s e R_{\mathrm{Far.},s}}, \tag{3.23}$$

where the summation in the denominator of the right hand side is equivalent to the total current flowing through the cell at steady state. The Faradaic efficiency for a certain species is equal to 1 if all the current at steady state is attributable to the reaction that produces the species in question, and it is equal to 0 if all the current at steady state is attributable to the other reactions. The single pass conversion efficiency (SPCE) is defined as

$$SPCE = 1 - \frac{\overline{u}_z \overline{p}_{\mathrm{CO_2}}|_{z=L_z}}{\overline{u}_z \overline{p}_{\mathrm{CO_2}}|_{z=0}}. \tag{3.24}$$

The SPCE is equal to 0 if the flux of gaseous CO_2 leaving the GDE is the same as the flux

Table 3.5: Homogeneous reaction kinetic parameters for CO_2 electroreduction cases. Note, water auto–dissociation is modeled using zeroth–order kinetics, assuming fixed $c_{H_2O} = 55.5\,\mathrm{M}$. Values are from work by Zhang *et al.* [116].

Reaction	k_f	$K_{eq} \equiv k_b/k_f$
$CO_2(aq) + H_2O \longleftrightarrow H_2CO_3(aq)$	$3.0 \times 10^{-2}\,\mathrm{mol\,m^{-3}\,s^{-1}}$	1.7×10^{-3}
$CO_2(aq) + OH^-(aq) \longleftrightarrow HCO_3^-(aq)$	$2.2 \times 10^{3}\,\mathrm{mol\,m^{-3}\,s^{-1}}$	4.27×10^{7}
$H_2CO_3(aq) + H_2O \longleftrightarrow HCO_3^-(aq) + H_3O^+(aq)$	$2.51 \times 10^{6}\,\mathrm{mol\,m^{-3}\,s^{-1}}$	2.51×10^{-4}
$HCO_3^-(aq) + H_2O \longleftrightarrow CO_3^{2-}(aq) + H_3O^+(aq)$	$4.8 \times 10^{-1}\,\mathrm{mol\,m^{-3}\,s^{-1}}$	4.8×10^{-11}
$2\,HCO_3^-(aq) \longleftrightarrow CO_3^{2-}(aq) + H_2CO_3(aq)$	$1.9 \times 10^{3}\,\mathrm{mol\,m^{-3}\,s^{-1}}$	1.9×10^{-7}
$H_2CO_3(aq) + OH^-(aq) \longleftrightarrow HCO_3^-(aq) + H_2O$	$1 \times 10^{10}\,\mathrm{mol\,m^{-3}\,s^{-1}}$	2.5×10^{10}
$HCO_3^-(aq) + OH^-(aq) \longleftrightarrow CO_3^{2-}(aq) + H_2O$	$1 \times 10^{8}\,\mathrm{mol\,m^{-3}\,s^{-1}}$	4.8×10^{3}
$2\,H_2O \longleftrightarrow OH^-(aq) + H_3O^+(aq)$	$1 \times 10^{-4}\,\mathrm{mol\,m^{-3}\,s^{-1}}$	1×10^{-14}

Table 3.6: Faradaic reaction kinetic parameters for CO_2 electroreduction cases. Parameters are the same as reported by Disselkoen [2].

Reaction	Parameter	Value
$2\,CO_2 + 8\,H_2O + 12\,e^- \longrightarrow C_2H_4(g) + 12\,OH^-$	$i_0 \exp\left(-\frac{E_{a,j}}{N_A k_B T}\right)$	$1.37 \times 10^{2}\,\mathrm{A\,m^{-3}}$
	U^0	$8 \times 10^{-2}\,\mathrm{V}$
	c_r^0	$7 \times 10^{-3}\,\mathrm{M}$
	α	0.364
$2\,H_2O + 2\,e^- \longrightarrow H_2(g) + 2\,OH^-$	$i_0 \exp\left(-\frac{E_{a,j}}{N_A k_B T}\right)$	$6.11 \times 10^{5}\,\mathrm{A\,m^{-3}}$
	U^0	$0\,\mathrm{V}$
	c_r^0	N/A
	α	0.089

entering at the gas inlet, indicating that no CO_2 was dissolved into the the aqueous phase. SPCE of 1 occurs when all available CO_2 is dissolved into the aqueous phase as it travels in the z direction. Generally, operation at high gas flow rate for a fixed current density is expected to decrease SPCE because some fraction of the CO_2 will exit the domain without sufficient residence time to permit dissolution and consumption.

Once CO_2 is dissolved into the aqueous phase, it may react Faradaically or homogeneously. As described previously, the former is desirable since it is directly responsible for ethylene production. The latter, meanwhile, ultimately results in carbonate formation. The full carbonic acid homogeneous chemistry associated with dissolved CO_2 is provided in Table 3.5, and the Faradaic reaction mechanism associated with CO_2 is provided in Table 3.6. We define the C_2 production efficiency (C2PE) as

$$C2PE = \frac{R_{\mathrm{Far.},CO_2}}{R_{\mathrm{Far.},CO_2} + R_{\mathrm{hom.},CO_2}}, \tag{3.25}$$

Table 3.7: Operating conditions for the CO_2 reduction reference case.

Symbol	Parameter	Value
L_x^{C}	Total cell x dimension length	1 cm
L_z^{C}	Total cell z dimension length	1 cm
L_y^{GC}	Interdigitated gas channel height	80 µm
L_y^{GDL}	Gas diffusion layer (GDL) height (porous carbon layer)	275 µm
L_y^{CL}	Catalyst layer (CL) height	75 µm
L_x	x dimension size of porous copper domain in unit problem	5 µm
L_y	y dimension size of porous copper domain in unit problem	75 µm
L_z	z dimension size of porous copper domain in unit problem	1 cm
R_{GC}	Open fraction of gas channel	0.5
R_{WCR}	Volume fraction of porous copper domain in total CL	0.4
T	Temperature	298 K
$\dot{Q}$	Gas flow rate	3 sccm
p_0	Total pressure	1 bar
k_B	Boltzmann's constant	$1.38 \times 10^{-23}\,\mathrm{J\,K^{-1}}$
e	Charge of electron	$1.602 \times 10^{-19}\,\mathrm{C}$
N_A	Avogadro's number	6.022×10^{23}

which represents the fraction of local CO_2 consumption due to Faradaic reactions, out of total CO_2 consumption in both Faradaic and homogeneous reactions.

Finally, using the single pass conversion efficiency and C_2 production efficiency, we may then define the overall carbon efficiency (CE) as

$$CE = SPCE * C2PE. \tag{3.26}$$

The CE represents the overall ability for the cell to convert CO_2 to valuable C_2 products, accounting for losses at the dissolution and reaction stages of the process. A summary of the operating conditions and physical constants is shown in Table 3.7, showing values for a nominal reference case that is designed to match practical conditions.

We begin by displaying steady–state slices of aqueous species concentration for the reference case in Fig. 3.14, demonstrating substantial ${CO_3}^{2-}$ formation. The mechanism for carbonate production involves two steps, the first of which is OH^- production due to both Faradaic reactions in Table 3.6. Subsequently, the second and fifth homogeneous reactions in Table 3.5 lead to ${CO_3}^{2-}$ formation. Figure 3.14(b) indicates that OH^- concentration is higher near the gas outlet, at $z = 1\,\mathrm{cm}$. This result is caused by limited availability of CO_2: The CO_2 profile in Fig. 3.14(d) exhibits high concentrations near the x boundaries, with

worsening depletion along the axial (z) direction. As will be the case for several of the data sets presented in this section, starvation of CO_2 at later portions of the cell leads to higher H_2 evolution rates and the presence of lingering OH^- ions in those regions.

Steady–state electric potential slices for the reference case are shown in Fig. 3.15. Note that potential is higher near the top of the catalyst layer and lower near the base, generating an electromigration flux that transports anions out of the catalyst and into the overlying bulk electrolyte. Additionally, note the presence of an electric potential gradient along the z direction, which contributes to ion transport within the catalyst.

The gas–phase partial pressure and velocity profiles for the reference case are shown in Fig. 3.16. Pure CO_2 at pressure of 1 bar flows into the GDE. As CO_2 dissolves into the catalyst and H_2 and C_2H_4 outgas from the catalyst into the gas stream, the partial pressures evolve accordingly. For this set of parameters, more H_2 is present in the outflow than C_2H_4. The reduced CO_2 concentration near the gas outlet is responsible for the increased presence of OH^- in this region, as discussed previously. Note that CO_2 transport in the aqueous phase is too slow to adequately mix the aqueous reactants in the z direction. The gas velocity is shown in Fig. 3.16(a). The decrease in velocity is caused by the net mole balance of the overall dissolution and reaction mechanisms. The molar rate of CO_2 dissolution into the aqueous phase outpaces the molar rate of C_2H_4 and H_2 production, leading to a decrease in velocity along the z direction.

We may post–process the reference case results to compute the local C_2 production efficiency and Faradaic efficiency, as shown in Fig. 3.17(a) and Fig. 3.17(b), respectively. First, note that C_2 production efficiency does not vary in the x direction, even though the CO_2 profile varies significantly in x (see Fig. 3.14(d)). Both homogeneous and Faradaic reaction rates vary linearly with CO_2 concentrations, and therefore, the ratio of the two does not vary with CO_2 concentration. However, variation in the z direction is evident: the increased OH^- concentration near the outlet enhances the homogeneous reaction rate without providing a similar benefit to Faradaic reactions. Thus, we see that C_2 production efficiency is lower in the outlet region. Finally, note that the C_2 production efficiency is higher near the top of the catalyst layer. This is due to higher electric potential near $y = 75\,\mu m$, as shown in Fig. 3.12(g). The higher electric potential benefits Faradaic reactions, which exhibit exponential dependence on the potential drop between the electrolyte and the Cu pore walls.

The Faradaic efficiency, shown in Fig. 3.17(b), is near 100% at the interfaces between

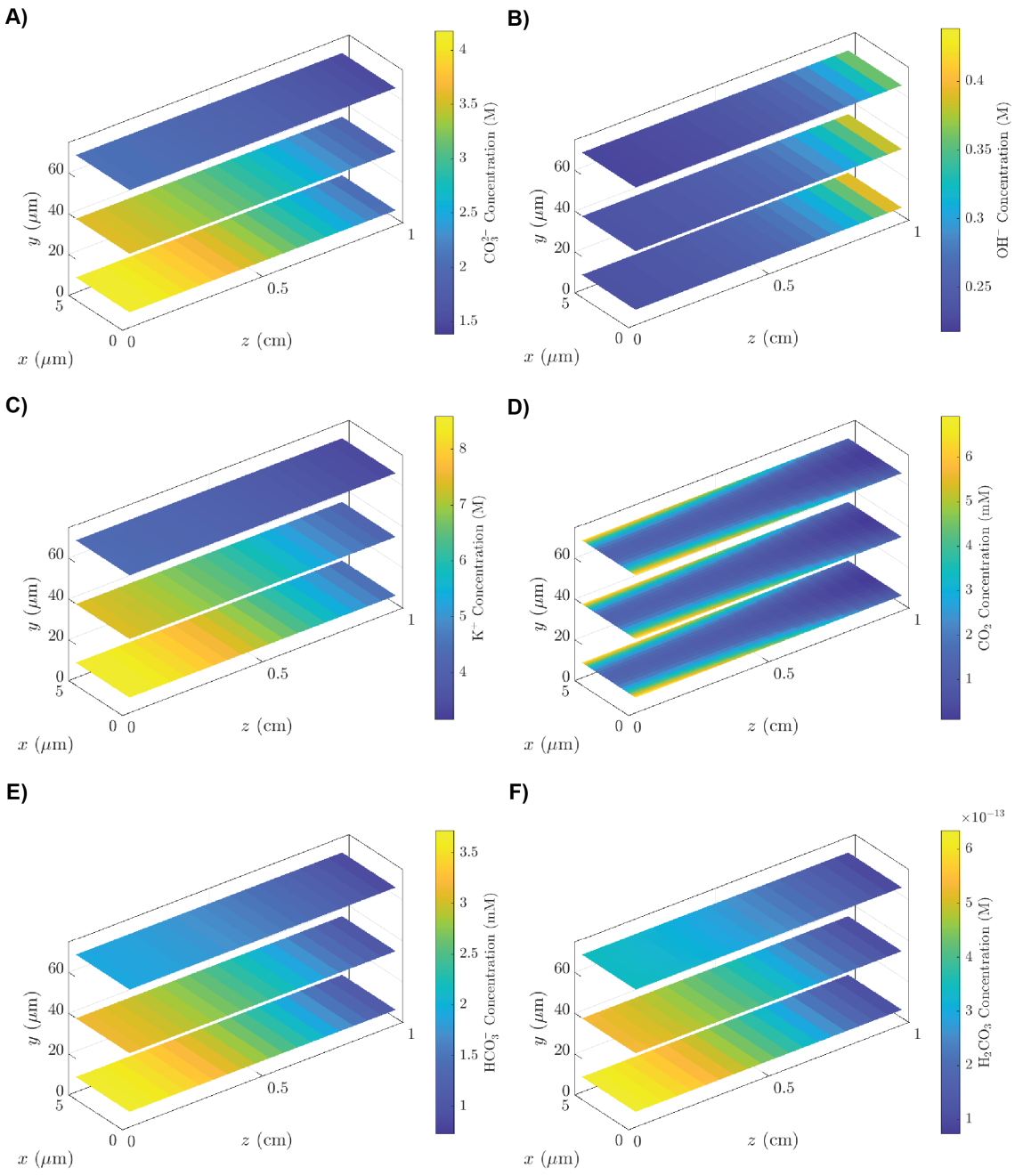

Figure 3.14: Steady–state slices of concentration for CO_2 reduction reference case. (A) ${CO_3}^{2-}$ (B) OH^- (C) K^+ (D) CO_2 (E) ${HCO_3}^-$ (F) H_2CO_3.

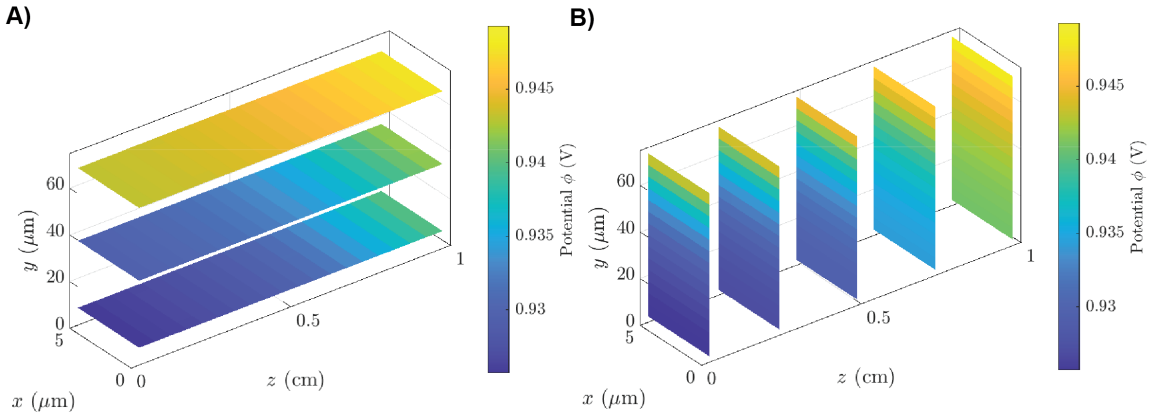

Figure 3.15: Steady–state slices of electric potential for CO_2 reduction reference case, oriented in two different directions.

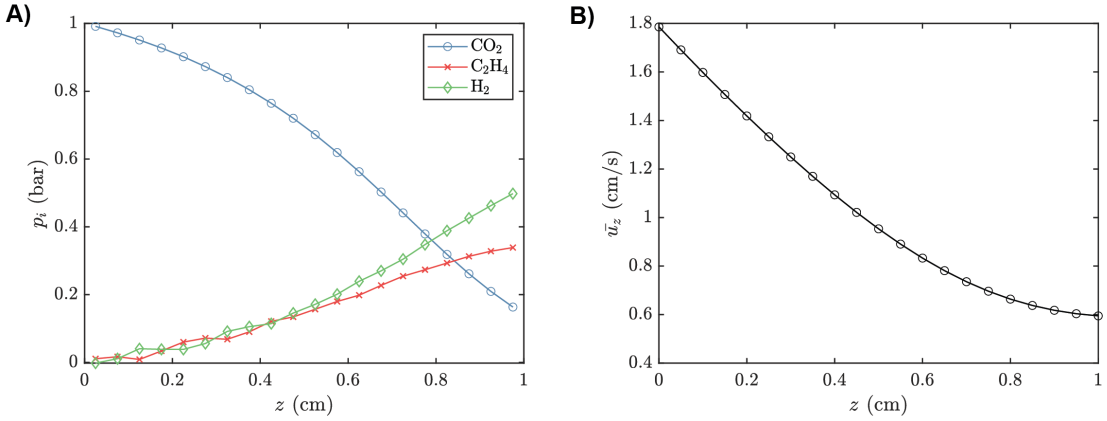

Figure 3.16: Profiles of species partial pressures and total gas velocity for CO_2 reduction reference case. (A) Partial pressures of gaseous reactants and products. (B) Velocity of gas mixture.

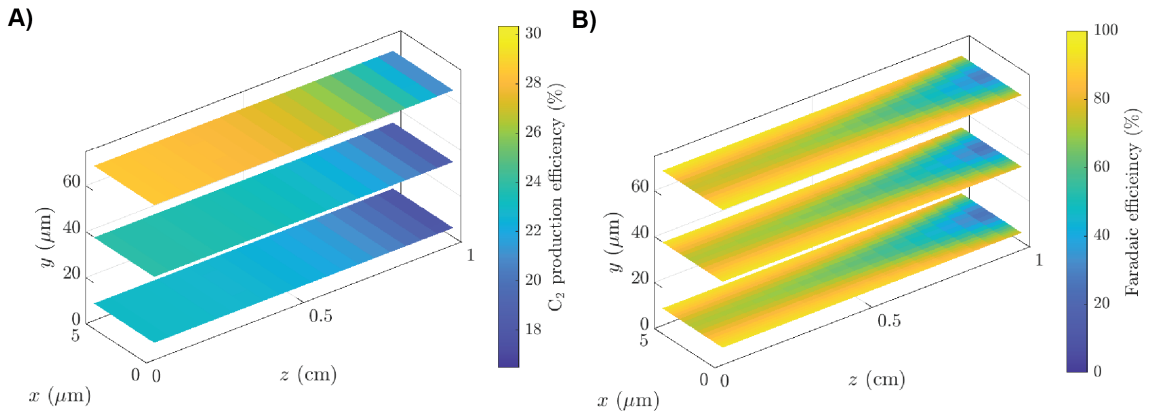

Figure 3.17: 3D profiles of key efficiency metrics for CO_2 reduction reference case. (A) C_2 production efficiency. (B) Faradaic efficiency.

Cu and PTFE phases, where CO_2 dissolution produces large CO_2 concentrations. Note that the largest gradients in the Faradaic efficiency profile are in the x and z directions, correlating with the CO_2 concentration gradients. The relative invariance in the y direction indicates that variation in electric potential, which is strongest in the y direction, does not significantly affect the local Faradaic efficiency. Instead, the Faradaic efficiency is strongly affected by the availability of CO_2.

3.4.4 CO_2 Electroreduction Parameter Study

We now consider the dependence of cell performance on the variety of geometric parameters and operating conditions represented in the model. In order to understand the underlying physicochemical processes, we consider the impact of changing one parameter at a time; all of the other parameters are set to their reference values, which are listed in Table 3.7. To establish expectations for the reference case and demonstrate the impact of CO_2 availability, we examine pertinent performance metrics for two example cases in Fig. 3.18.

For Fig. 3.18(a)–(b), the flow rate has been halved to 1.5 sccm while in Fig. 3.18(c)–(d), all parameters are assigned their reference values. Note, in particular, the anion flux proportion, which depicts the fraction of current carried across the cell by OH^- ions (with the remainder carried by $CO_3{}^{2-}$ ions). We observe from the SPCE in Fig. 3.18(b) that all the CO_2 entering the GDE is fully consumed for the lower flow rate, even at moderate applied voltage. This results in H_2 evolution becoming the dominant Faradaic reaction

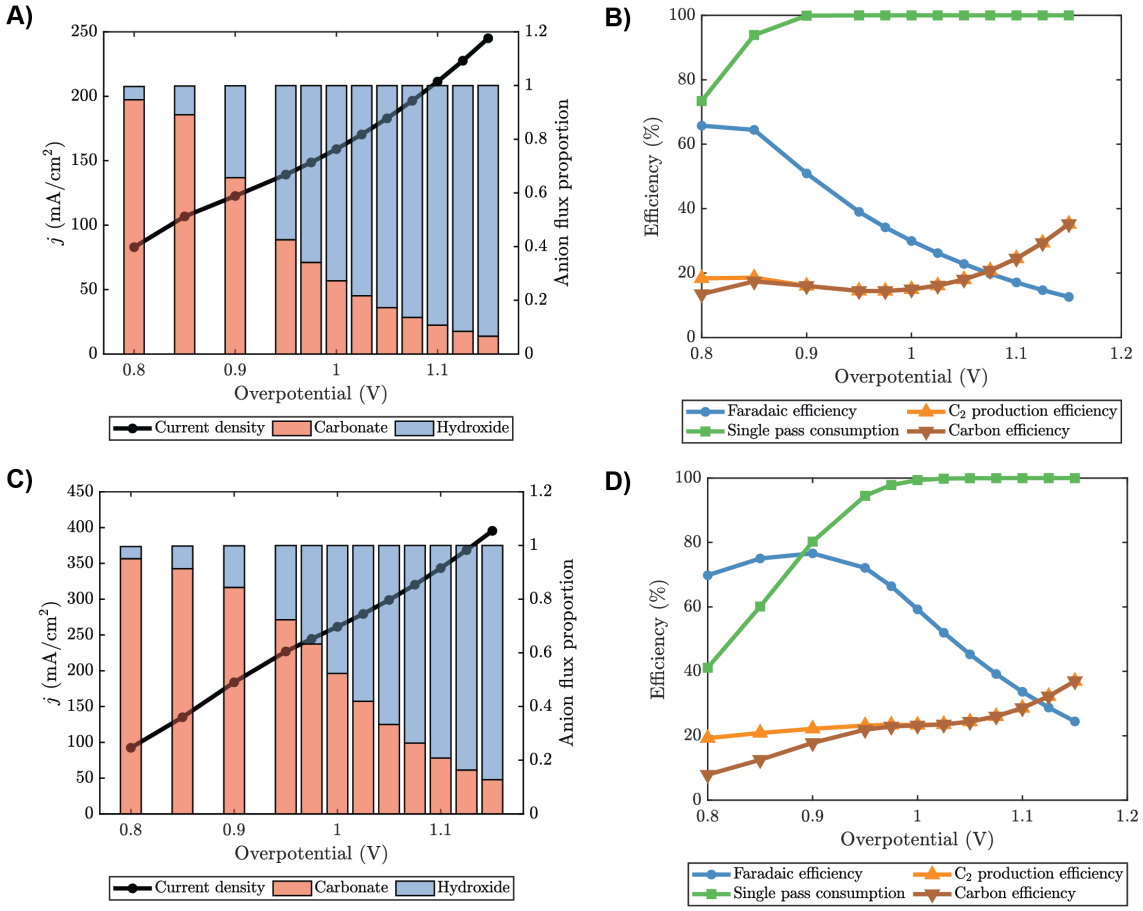

Figure 3.18: Current–voltage curve (left plot, left axis), anion flux proportion (left plot, right axis), and efficiency metrics (right plot) for two reference cases with parameters from Table 3.7. A–B) Gas flow rate is halved compared to reference value, to 1.5 sccm. C–D) All parameters are equal to reference values.

at high applied voltage, which drives down the Faradaic efficiency for C_2H_4 accordingly. The increased H_2 evolution and relative absence of dissolved CO_2 subsequently generates a significant flux of OH^- ions across the cell, as shown on the right axis of Fig. 3.18(a). However, larger applied voltages do benefit the C2PE (and thus the CE), since the rate of Faradaic reaction increases exponentially with higher overpotential while the homogeneous reaction rate remains the same.

Doubling the gas flow rate and re–examining the efficiency metrics in Fig. 3.18(d) reveals similar dynamics, but we observe that a higher potential is required for saturation of the single pass conversion efficiency. As seen in Fig. 3.18(c), however, a crucial advantage of increasing the gas flow rate is substantial enhancement of the current density at a given overpotential. Better gas delivery also leads to slightly improved Faradaic efficiency as well. Having established efficiency trends for the reference case (with standard flow rate and halved flow rate), we now begin a systematic study of system response to variation of each input parameter. For all results presented in the remainder of this section, simulations are run in a potentiostatic mode, such that the overpotential is fixed while a single parameter is varied in each data set.

To probe the impact of changing flow rates more explicitly, Fig. 3.19(a)–(b) show the aforementioned figures of merit plotted directly against gas flow rate. First, observe that as gas flow rate is increased, the current density increases as well before reaching a plateau. However, despite improved energy efficiency, the dominant current carrier transitions from OH^- ions to ${CO_3}^{2-}$ ions, leading to the motivating dilemma described in Section 3.1. Since CO_2 is delivered more uniformly and plentifully along the z–dimension at higher flow rates, the C_2H_4 Faradaic efficiency is improved. However, higher flow rates are associated with lower SPCE (and re–formation of CO_2 at the anode due to ${CO_3}^{2-}$ ion crossover). For the most extreme flow rate examined here, more than half of the CO_2 leaves the channel without even dissolving into the aqueous phase. We do see, however, a local optimum in the total carbon efficiency and a trade–off between SPCE and Faradaic efficiency.

As shown in Fig. 3.19(c)–(d), higher gas total pressure is also associated with higher current density for fixed overpotential and a gradual increase in the fraction of current carried by ${CO_3}^{2-}$ ions. While single pass conversion efficiency is already maximized for the full range of total pressures studied, observe that Faradaic efficiency increases monotonically as total pressure is increased. C2PE also exhibits modest improvement with increase in total pressure. This suggests that operation at elevated gas pressures may pose a new avenue

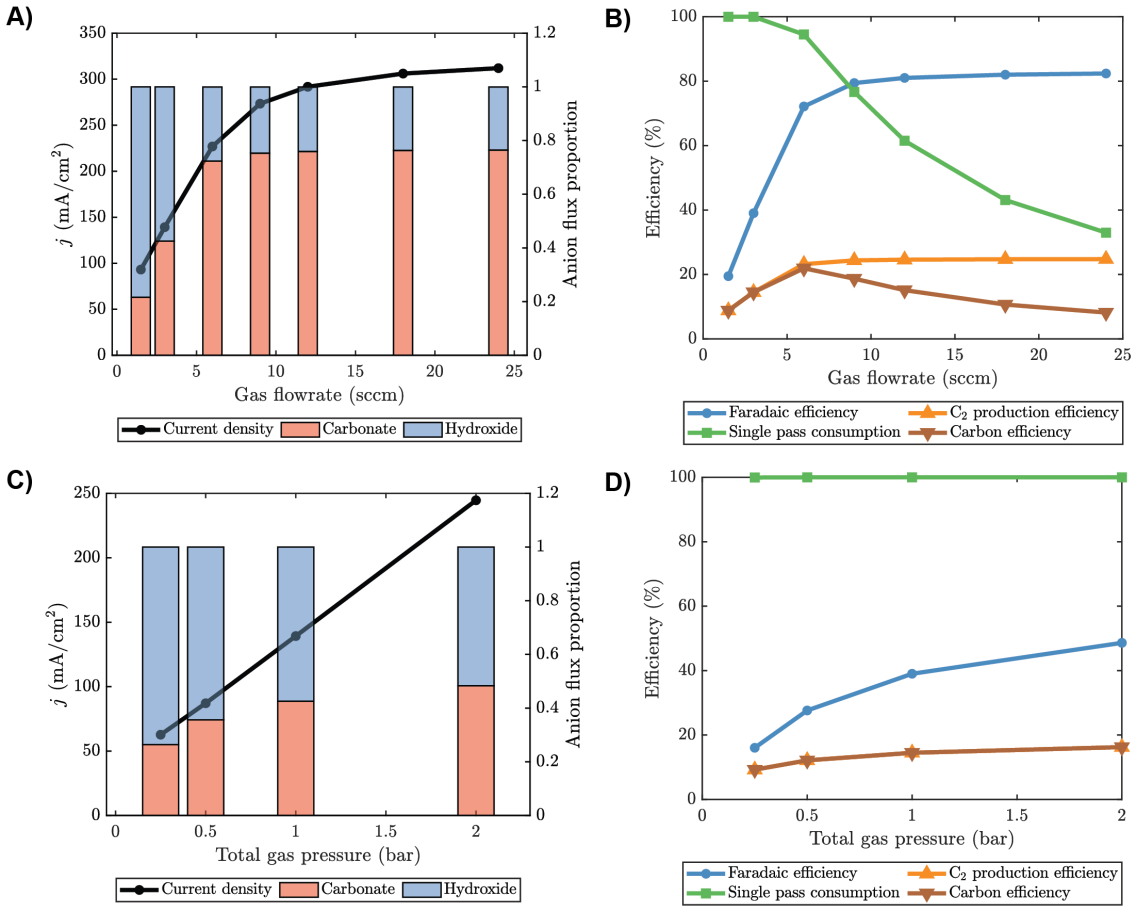

Figure 3.19: Current–voltage curve (left plot, left axis), anion flux proportion (left plot, right axis), and efficiency metrics (right plot) demonstrating sensitivity to (A)–(B) variation of gas flow rate and (C)–(D) variation of gas total pressure.

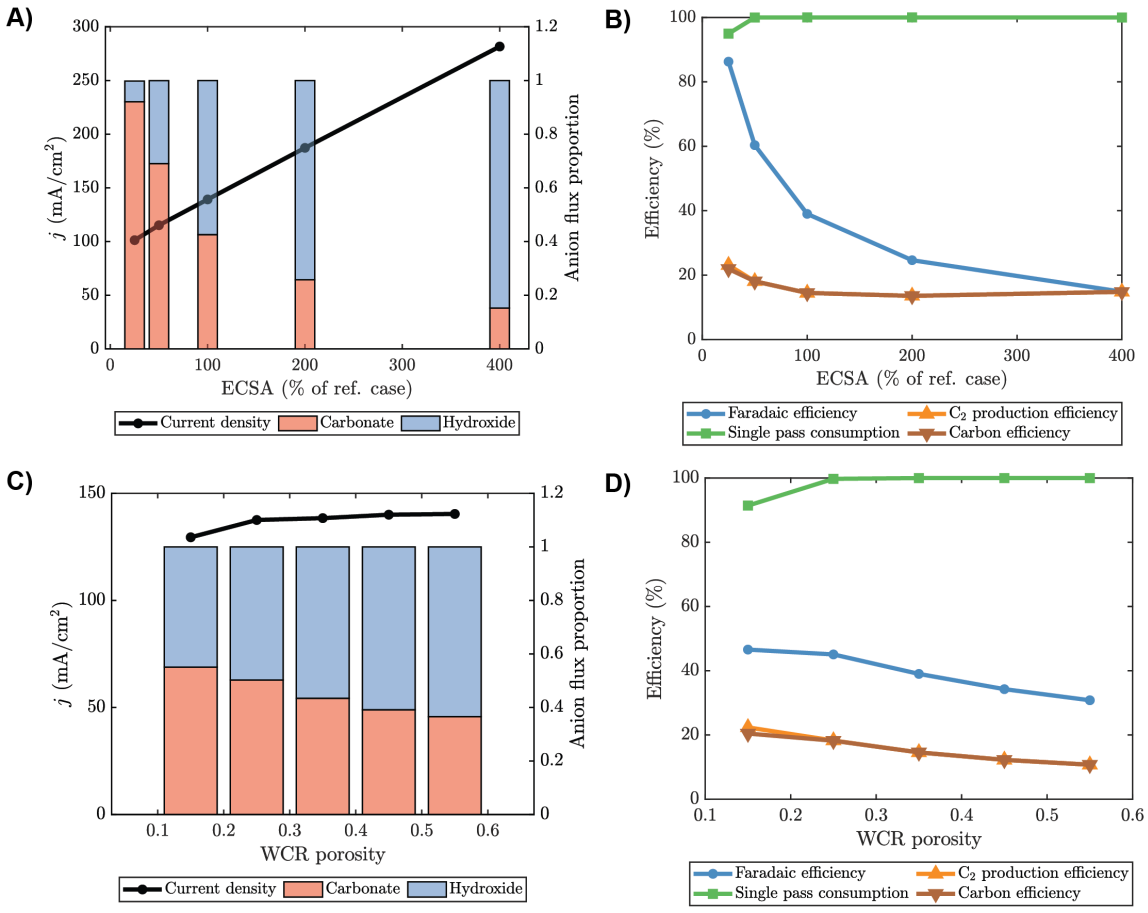

Figure 3.20: Current–voltage curve (left plot, left axis), anion flux proportion (left plot, right axis), and efficiency metrics (right plot) demonstrating sensitivity to (A)–(B) variation of ECSA and (C)–(D) variation of Cu region (wetted catalyst region, WCR) porosity.

toward improvement of cell performance.

Next, we examine the impact of increasing electrochemically active surface area (ECSA), which is parameterized here by modulating the volumetric exchange current density i_0. Since exchange current density is an interfacial characterization that is represented as current density per unit surface area, the volumetric exchange current density contains an embedded assumption of the amount of Cu–electrolyte interfacial area per unit of control volume for the porous electrode theory description of the Cu region. This set of simulations is intended to probe scenarios in which the amount of interfacial area per unit volume is varied. Results are displayed in 3.20(a)–(b).

As expected, increase in the ECSA leads to increase in the current density for fixed

overpotential. Additionally, higher ECSA is associated with transition toward hydroxide ions as the main current carrier. Examining the efficiency metrics, however, we see that high ECSA is associated with low Faradaic efficiency and saturation of the single pass conversion efficiency. This is indicative of CO_2 starvation, which leads to H_2 evolution becoming the dominant Faradaic reaction. Thus, it is clear that increase in ECSA must be paired with a corresponding increase in the CO_2 gas flow rate or pressure in order to prevent this situation.

Next, we examine variation of the porosity of the Cu region in 3.20(c)–(d). Note that by choosing to vary ECSA and porosity separately, we neglect any dependence between the two parameters. Such dependence is expected to exist, since both parameters are descriptions of the porous microstructure of the Cu region. For this work, we ignore any such dependence. Changing the porosity impacts the diffusion coefficients of all dissolved species, but the primary effect is on the effective homogeneous reaction rate. Since homogeneous reactions occur only in the fluid phase of a given control volume, decrease in the volume of fluid phase (*i.e.,* lower porosity) reduces the effective rate of homogeneous reactions. This effect leads to higher C2PE and CE for lower porosity values. However, the current–voltage plot shows that reduction in porosity is associated with modest reduction of current density for fixed overpotential, in addition to modest reduction of the SPCE.

Now, we examine scenarios in which the macroscopic geometry of the catalyst is modified. In Fig. 3.21(a)–(b), we display cases in which the volume fraction of Cu in the catalyst is varied between 0.1 and 0.8. Generally, a larger fraction of wetted catalyst region (WCR) is associated with higher current density and larger fraction of current carried by OH^- ions. We note, however, a reduction in Faradaic efficiency and C2PE as single pass conversion efficiency reaches saturation (*i.e.* as CO_2 starvation begins to limit C_2H_4 production). In Fig. 3.21(c)–(d), we examine variation of total cell length in the axial direction. Longer cell lengths are associated with lower current densities and higher fractions of current carried by OH^- ions, as single pass conversion efficiency saturates at 100% and CO_2 starvation leads to reduction in Faradaic efficiency of C_2H_4 production and C2PE. Here, we have demonstrated the balance between inlet gas flow rate and cell length — either parameter may be tuned in response to the other, in order to prevent complete CO_2 starvation (and consequent reduction in Faradaic efficiency) while minimizing incomplete conversion of CO_2.

In Fig. 3.22, we present two ways in which we study variation of the catalyst layer thickness. We begin in Fig. 3.22(a)–(b) with fixing the other structural properties while simply varying the overall catalyst height. in Fig. 3.22(c)–(d), we vary the Cu–PTFE ratio

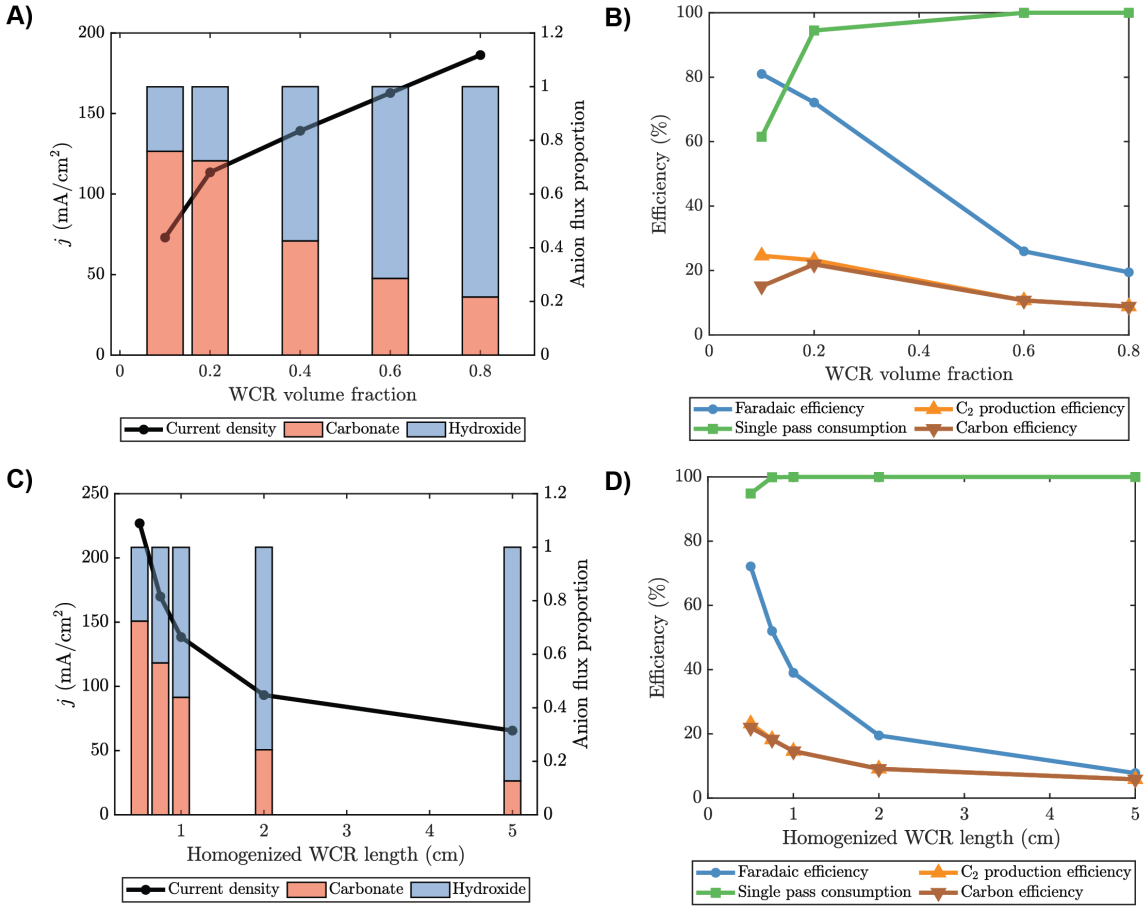

Figure 3.21: Current–voltage curve (left plot, left axis), anion flux proportion (left plot, right axis), and efficiency metrics (right plot) demonstrating sensitivity to (A)–(B) variation of wetted catalyst region (WCR) volume fraction (*i.e.* fraction of Cu in catalyst) (C)–(D) variation of total cell length in the axial direction.

in tandem with the catalyst layer height, such that the total volume of Cu is preserved as catalyst height is varied. Comparison of the two datasets immediately reveals that the total volume of Cu plays a substantial role — in the absence of variation in the total Cu volume, performance metrics are relatively constant despite variation in catalyst layer height. When catalyst layer height is varied and the total volume of Cu is allowed to vary as well (as would be the case for deposition processes in which the structural properties remain the same as additional material is deposited), the additional electrochemically active volume permits higher current density. However, CO_2 starvation is apparent, leading to increased H_2 evolution.

The next parameter we study, shown in Fig. 3.23, is bulk concentration of the working electrolyte. The current–voltage curve and efficiency metrics indicate that lower bulk electrolyte concentration is advantageous. As shown in Fig. 3.24, we find that ionic concentrations of all species in the catalyst are lower: most relevantly, low local OH^- concentrations decrease the homogeneous reaction rate. The result is improved C2PE. Additionally, because less CO_2 is consumed homogeneously, the Faradaic efficiency rises as well, making this parameter a particularly valuable means of optimization. We point out, however, that lower bulk concentrations would reduce the ionic conductivity of the cell, thereby increasing the energetic cost due to Ohmic losses. Such an effect is not included in our model, which only considers the cathode GDE of the cell.

We further explore the concentration slices of ionic species to understand the reaction and transport dynamics under high (Fig. 3.24(b)–(d)) and low (Fig. 3.24(a)–(c)) bulk electrolyte concentrations. In particular,Fig. 3.24(c)–(d) demonstrate an order of magnitude difference in OH^- concentration, which consequently changes the rate of ${CO_3}^{2-}$–producing homogeneous reactions by an order of magnitude. We also examine steady–state slices of critical efficiency metrics in Fig. 3.25, demonstrating substantial spatial variation in local catalyst performance. Plots on the left are shown for bulk electrolyte concentration of 0.1 M, while plots on the right are for the case of 3 M. First, a region of high Faradaic efficiency extends farther in the z–direction in Fig. 3.25(a) than in Fig. 3.25(b), because CO_2 is not consumed as quickly by homogeneous reactions due to the lower concentration of OH^- ions in the former. The C2PE also exhibits much more uniform performance in the z–direction for the 0.1 M OH^- case, and higher performance overall.

The final parameter we study is characteristic length scale of the Cu regions in the geometrically simplified model (that is, thickness L_x of the wetted catalyst regions (WCR)

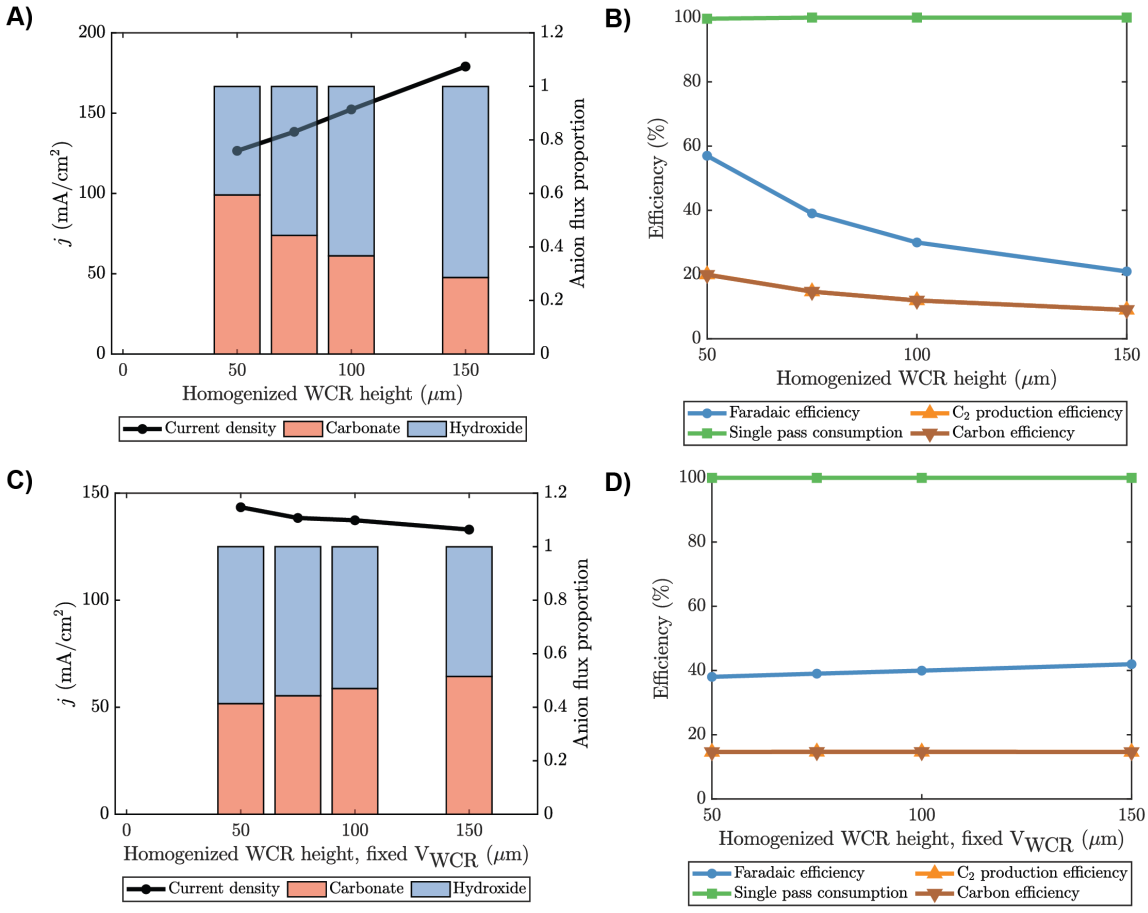

Figure 3.22: Current–voltage curve (left plot, left axis), anion flux proportion (left plot, right axis), and efficiency metrics (right plot) demonstrating sensitivity to (A)–(B) variation of the catalyst layer height without preserving total volume of Cu (C)–(D) variation of the catalyst layer height with preservation of total volume of Cu (achieved via simultaneous variation of the ratio between Cu and PTFE regions).

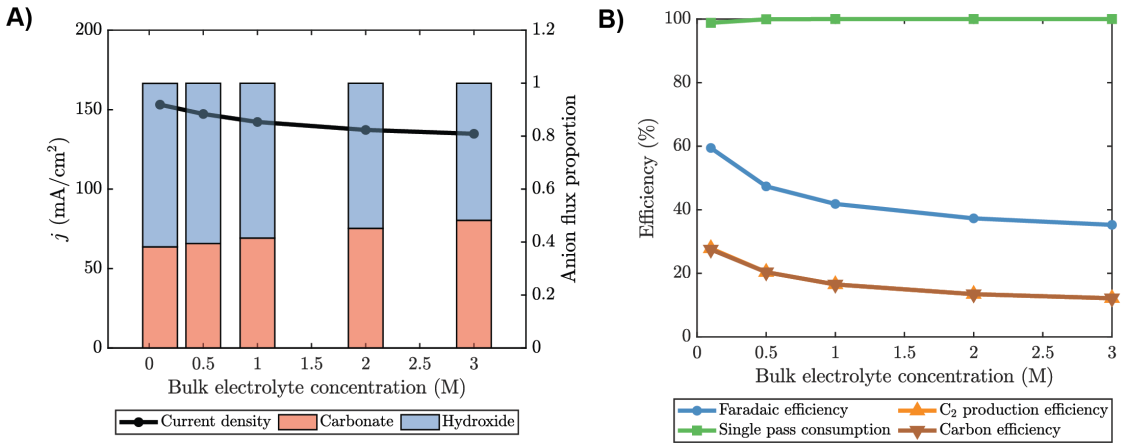

Figure 3.23: Current–voltage curve (left plot, left axis), anion flux proportion (left plot, right axis), and efficiency metrics (right plot) demonstrating sensitivity to variation of bulk electrolyte concentration.

depicted as orange in Fig. 3.2(b)). In Fig. 3.26, we preserve the ratio of Cu to PTFE while varying the characteristic thickness of Cu regions. Thinner Cu regions are associated with more rapid CO_2 transport to the middle of the Cu domain from the x boundaries (as seen in the corresponding concentration profile displayed in Fig. 3.27(a)), but nearly all of the CO_2 is consumed in first 0.25 cm of the cell's z axis, leading to CO_2 starvation for later parts of the cell. This portion of the cell is responsible for the decrease in Faradaic efficiency, C2PE, and overall carbon efficiency, as shown in the 3D plots of local efficiency parameters in Fig. 3.28(a),(d) and in the trend for extremely thin Cu regions in Fig. 3.26(b).

Considering substantially thicker Cu regions, however, we observe that this geometry does not provide sufficient interfacial area between the Cu and PTFE regions, limiting the rate at which CO_2 may enter the aqueous phase at all. This is reflected in the decrease in single pass conversion efficiency in Fig. 3.26(b), along with concomitant reduction in Faradaic efficiency. Observing the CO_2 concentration profile in Fig. 3.27(c) and Faradaic efficiency profile in Fig. 3.28(c), we see that the reaction–diffusion layer is much narrower than the total width of the Cu region, and the region of high efficiency is restricted to this narrow zone. Most of the center of the Cu domain is starved of CO_2.

The results considered thus far suggest that an intermediate Cu region thickness will present the optimal balance between providing sufficient area of contact between Cu and PTFE regions to facilitate rapid dissolution of CO_2 and remaining narrow enough to avoid

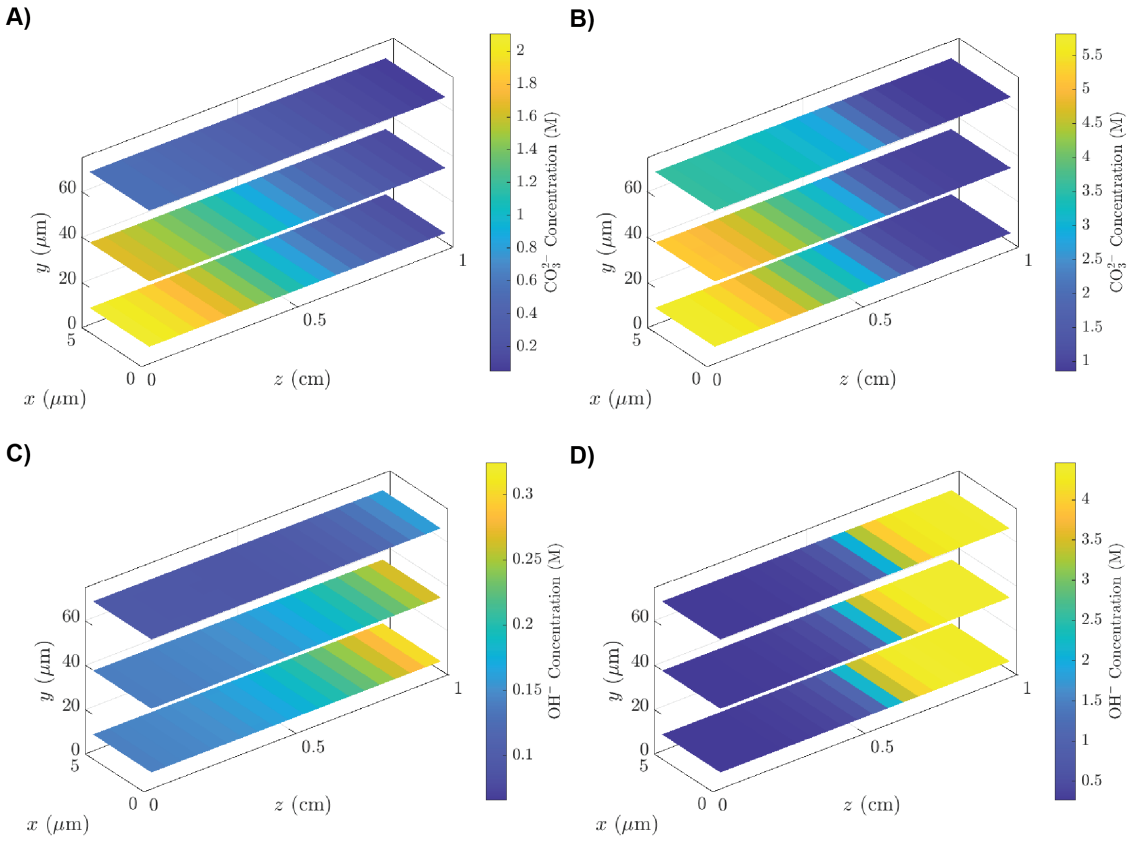

Figure 3.24: Steady–state slices of concentrations of two anions in the porous Cu region for different bulk electrolyte concentrations. (A)–(C) 0.1 M bulk electrolyte concentration. (C)–(D) 3 M bulk electrolyte concentration.

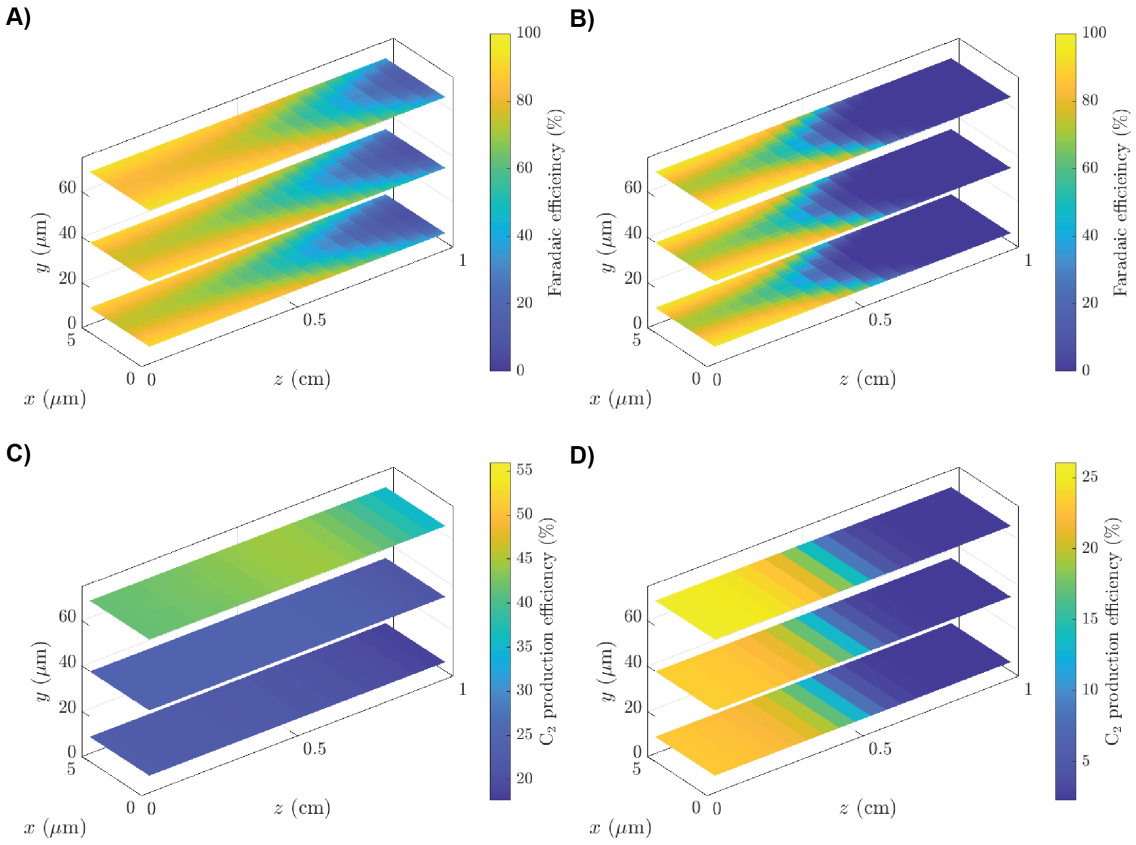

Figure 3.25: Steady–state slices of Faradaic efficiency ((A)–(B)) and C2PE ((C)–(D)) for different bulk electrolyte concentrations. (A)–(C) 0.1 M bulk electrolyte concentration. (B)–(D) 3 M bulk electrolyte concentration.

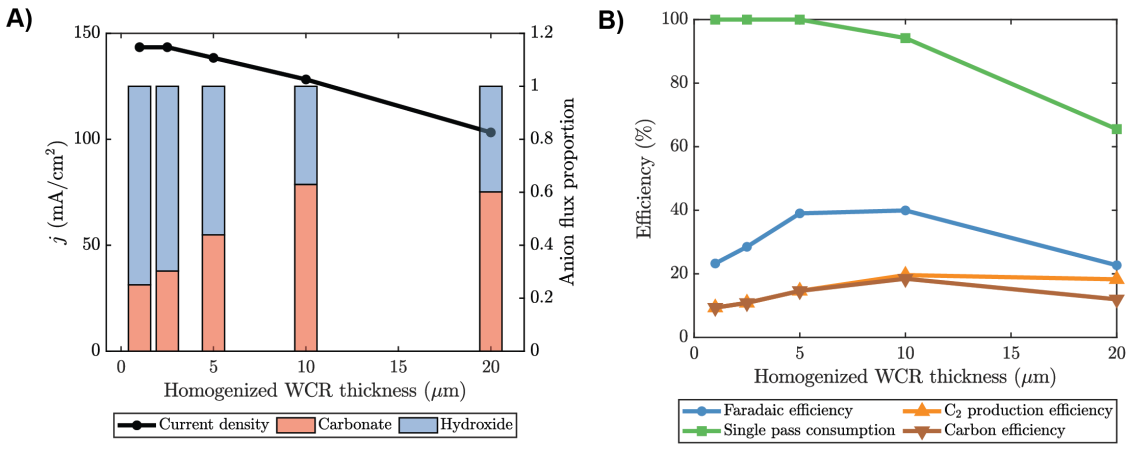

Figure 3.26: Current–voltage curve (left plot, left axis), anion flux proportion (left plot, right axis), and efficiency metrics (right plot) demonstrating sensitivity to variation of bulk electrolyte concentration.

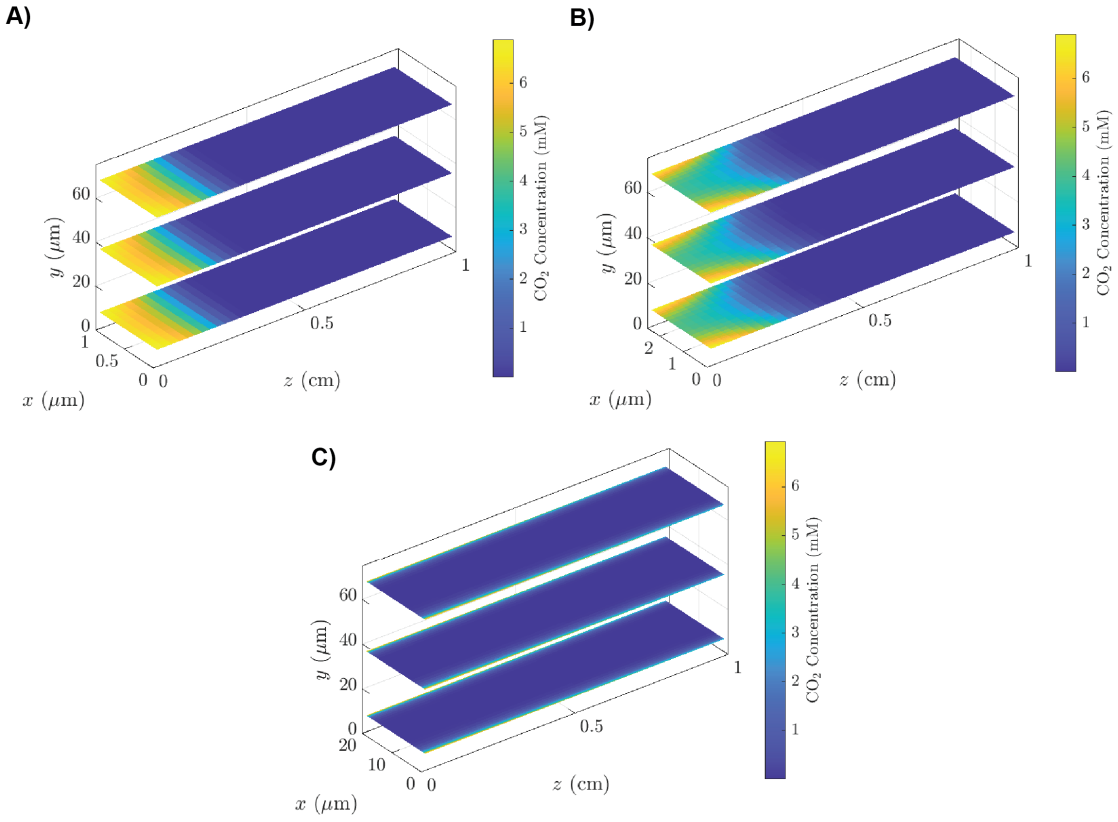

Figure 3.27: Steady–state slices of CO_2 concentration for varying Cu region thickness. (A) 1 µm thickness. (B) 2.5 µm thickness. (C) 20 µm thickness.

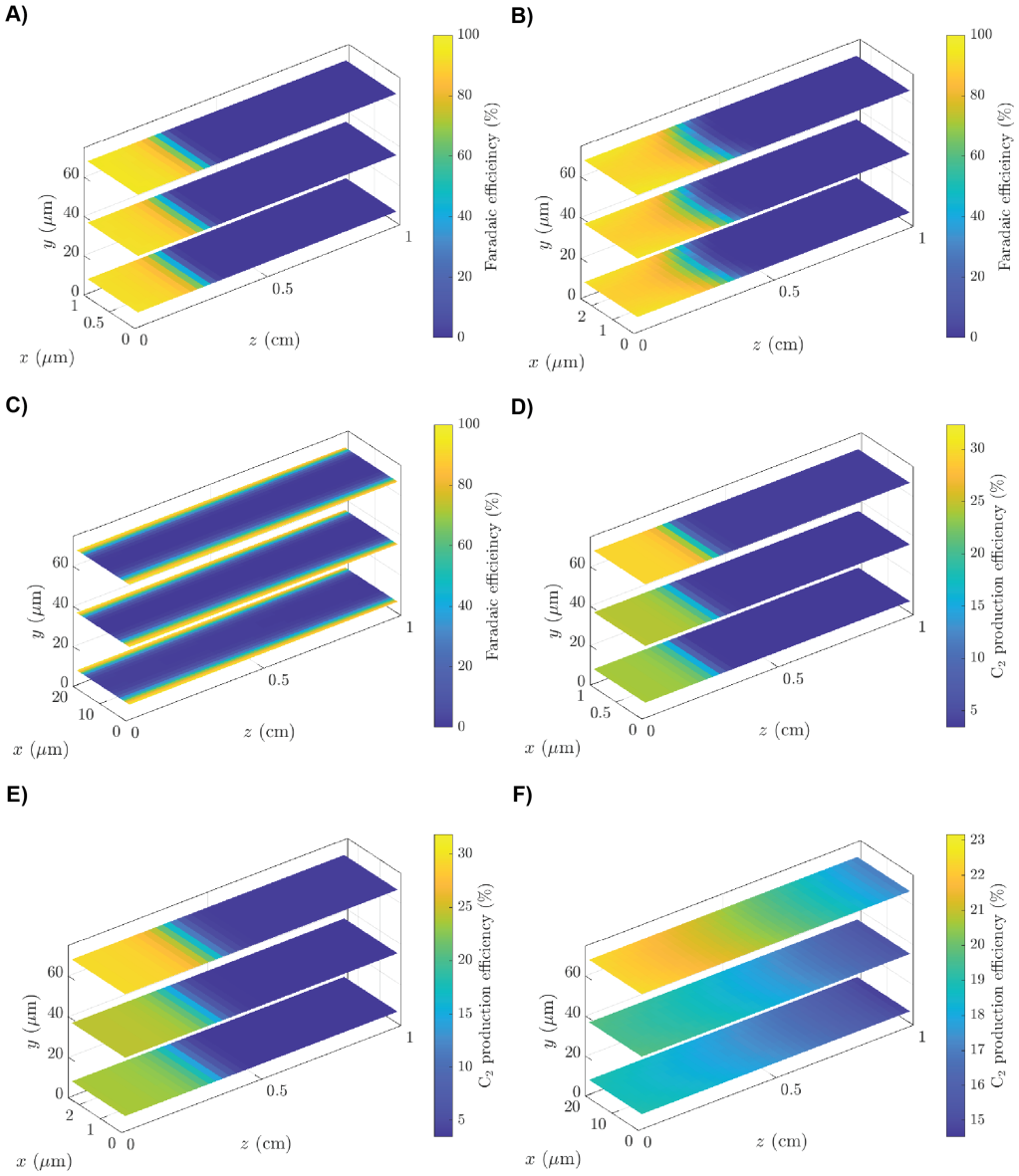

Figure 3.28: Steady–state slices of Faradaic efficiency ((A)–(C)) and C2PE ((D)–(F)) for different Cu region thicknesses. (A),(D) 1 µm thickness. (B),(E) 2.5 µm thickness. (C),(F) 20 µm thickness.

CO_2 depletion and starvation near the centers of the Cu regions. Additionally, the length of the cell (or the flow rate and total pressure of gas) may be adjusted to prevent CO_2 starvation at later axial stations in the cell.

3.5 Concluding Remarks

Our primary focus in this work was construction of a reduced order model for multi–phase and multi–scale reaction and transport processes in CO and CO_2 electroreduction catalysts with randomly intermixed hydrophobic and hydrophilic regions. In doing so, we aimed to retain essential physicochemical features while neglecting higher order effects. We constructed the model by making use of geometric simplification based on scaling analyses and intuitive physicochemical arguments about dominant transport and reaction mechanisms in various parts of the GDE. Additionally, we described the numerical methods that allow solution of the governing equations efficiently, in a manner that is amenable to parallelization.

The solver and numerics were validated via comparison to published results for CO electroreduction experiments. We found that the model is able to capture qualitative trends seen in the experimental data, and that input parameters to the model are related to measurable geometric and electrochemical characteristics of the GDE. Additionally, we identified key areas in which additional model development is required — specifically, the formation of electrically isolated Cu regions cannot be captured by the present model as currently formulated.

After validating the model, we transitioned our focus toward direct CO_2 reduction. Controlling the competition between the homogeneous and Faradaic reaction rates for CO_2 consumption is key to achieving high carbon efficiency and energy efficiency. A key advantage of our model and numerics is the computational efficiency, which allowed us to perform an extensive parameter study. We examined the trade–offs between Faradaic efficiency and carbon efficiency with respect to numerous parameters, allowing us to offer practical design advice for the next generation of CO_2 electroreduction cells.

The local OH^- concentration plays a substantial role in the carbonate formation mechanism. A well–designed GDE must promote a high steady–state OH^- ion flux (as opposed to a ${CO_3}^{2-}$ ion flux), consisting of OH^- ions that are produced in the same Faradaic reaction as C_2H_4. However, a low local steady–state OH^- concentration in the Cu region is key to minimizing the homogeneous reactions that produce ${CO_3}^{2-}$ ions. The precise nature of the

balance between advantages and disadvantages of bulk electrolytes with low conductivity is still open for investigation. This endeavour would require connection of the model presented here with a representation (at similar or reduced fidelity) of the rest of the electrochemical cell as opposed to the cathode in isolation.

The single pass conversion efficiency is also a critical metric for avoiding product separation costs. The reactant gas must be delivered at the appropriate rate, based on the target current density and the other relevant geometric cell parameters and operating conditions. Insufficient gas flow leads to low Faradaic efficiency, while excess gas flow leads to un–reacted gas exiting the cell. Our model provides a framework for understanding transport and reactions in complex electrosynthesis cells, highlighting the significance of distributing CO_2 evenly throughout the length, width, and height of electrochemically active regions. Additionally, our work lays a theoretical foundation for future optimization of catalyst design, demonstrating one possible path toward energy– and carbon–efficient CO_2 electroreduction devices.

THIS PAGE DELIBERATELY LEFT BLANK

Chapter 4

Eddy Diffusivity for Chaotic Electroconvection

4.1 Background

The problem of coupled ion transport and fluid flow appears in practical systems across a wide variety of applications. Electrodialysis [117], a process in which applied electric fields are used in conjunction with ion–selective membranes in order to remove ions from an electrolyte, is relevant in water desalination [118], industrial and municipal wastewater treatment [119], industrial chemical separations [120], and food processing [121]. Similarly rich physics are found in electrodeposition, where the coupling between electrolyte flow and surface morphology has long been known [122, 123]. A contemporary application of crucial significance is batteries, where dendrite formation is substantially influenced by electroconvective flows [124–127].

The focus of this work is electroconvection. In contrast to the branch of electrohydrodynamics (EHD) concerning coupled ion and electrolyte transport in weakly–conducting fluids [128, 129], this work is squarely centered in the realm of electrokinetics, where electrolytes are taken to contain a large number of charged ions of both signs [130, 131]. In EHD, charge is distributed along fluid interfaces, but current is allowed to pass through the fluid by means of a small and constant Ohmic conductivity. In electrokinetics, however, relatively large ion concentrations are present throughout the fluid, allowing for a finite net charge density and enabling bulk electric forcing of the electrolyte in the presence of electric fields and salinity gradients.

Consider a simple electrodialysis cell in which current is driven through a cation–exchange–membrane by an applied electric field. The current–voltage curve (or j–V curve) of such a system typically exhibits three regions: (i) an Ohmic region, in which the current–voltage relation is linear, (ii) a limiting region, in which concentration polarization leads to saturation of the current at a value known as the limiting current, and (iii) an over-limiting region, in which the current again increases with voltage and begins to exhibit unsteady, chaotic fluctuations [132]. The overlimiting phenomenon was shown to result from chaotic, electrically–driven convection, which mixes the electrolyte and helps mitigate the ion depletion caused by concentration polarization [133–135].

Various methods have since been employed to investigate electroconvection [136–139], including early theoretical works focused on the instability at the root of the phenomenon. Notably, Rubinstein and Zaltzman published a series of studies in which they applied the method of matched asymptotic expansions and stability analyses to develop a mathematical description of the electroconvective instability [140–142]. In the underlimiting regime, the system may be described by 'outer' and 'inner' zones. Most of the bulk falls into the former category, which is largely electroneutral. The inner zone, located adjacent to the ion–selective membrane, is a highly–charged region governed by Boltzmann equilibrium. This inner zone, the electric double layer (EDL), has a thickness given by the Debye length,

$$\lambda_D = \sqrt{\frac{\epsilon_0 \epsilon_R k_B T}{2 z^2 e^2 c_0}}, \tag{4.1}$$

which, for aqueous systems with electrolyte concentrations on the order $c_0 \approx 1\,\mathrm{mmol\,L^{-1}}$, produces a length scale of $\lambda_D \approx O(10\,\mathrm{nm})$. Here, ϵ_0 is the vacuum permittivity, ϵ_R is the relative permittivity of the electrolyte, k_B is Boltzmann's constant, T is the solution temperature, z is the valence of a binary electrolyte, and e is the fundamental charge. Beginning in the limiting regime, a new zone appears in between the two mentioned previously. Referred to as the extended space charge (ESC) layer [143], this zone is neither electroneutral nor in Boltzmann equilibrium. In the presence of tangential electric fields (e.g. near curved surfaces), the electrolyte may exhibit an asymptotically–zero–thickness slip velocity with respect to the membrane surface. Dukhin categorized the slipping phenomenon as either 'of the first kind' or 'of the second kind' depending on whether it resulted from slip of the EDL or the ESC respectively [144, 145]. Rubinstein and Zaltzman's work, however, addressed

the problem of inherent stability of the quiescent electrolyte in the absence of applied tangential electric fields or curvature. Whereas instability was unlikely for realistic electrolytes (ionic species with realistic values of mass diffusivity) when considering only slip of the first kind [146], inclusion of the ESC layer (slip of the second kind) leads to instability behavior that compares well with experiments [147].

Experimental and computational works have since explored the full nonlinear evolution of electroconvection. A number of authors performed current/voltage measurements and 2D visualization of electrodialysis cells using tracer particles and fluorescent dyes, with or without the presence of crossflow [147–150]. There has also been recent interest in the 3D structure of electroconvective vortices, particularly concerning their interaction with crossflow [151, 152] and spacers [153, 154]. We particularly emphasize recent papers in which particle tracking velocimetry (PTV) has been used to measure the 3D velocity fields in electroconvection, allowing for detailed analysis of the instability in its incipient stage, the statistics of stationary electroconvection, and the associated energy spectra [155–157] — a depth of analysis that was previously limited to computational work based on direct numerical simulation (DNS) of the Poisson–Nernst–Planck–Stokes equations [158–163]. Several very recent works have focused on the effects of membrane heterogeneity, including variation in selectivity and geometric undulations [164–169]. Such factors strongly affect the nature of electroconvection, potentially increasing the current density compared to that of fully homogeneous membranes. Furthermore, various authors have investigated the coupling between electroconvection and other phenomena, including Rayleigh–Benard convection [170, 171], viscoelasticity [125], imperfect membrane selectivity [172], and electrodeposition [124–127, 173, 174].

DNS of the Poisson–Nernst–Planck–Stokes system in the overlimiting regime is considerably expensive. Consider the non–dimensional Debye length $\epsilon_D = \lambda_D/L$, where L corresponds to the width of the electrolyte reservoir (which is commonly taken to be the size of the computational domain). The cost of simulations scales inversely with this ratio of length scales, since it determines the number of mesh points required to span the largest length scale while also resolving the smallest feature. Realistic values may be as small as $\epsilon_D = O(10^{-7})$ for $1\,\mathrm{mol\,L^{-1}}$ electrolytes in a 1 mm cell. Prior EDL–resolving computational works have utilized choices of ϵ_D ranging from $\epsilon_D = 1 \times 10^{-2}$ to $\epsilon_D = 1 \times 10^{-5}$ [151, 158, 159, 161–163, 170, 175–183]. Of the works that performed 3D simulations, the smallest value considered was $\epsilon_D = 5 \times 10^{-4}$. Furthermore, it has been shown that the number

of dimensions [163] and the nondimensional Debye length [181] can affect the dynamics of electroconvection quantitatively.

The motivation for this work comes from two observations. First, despite the chaotic fluctuation of the current density (or voltage, in the case of galvanostatic measurements) in strongly overlimiting cases, the mean current density and mean voltage are sufficient to predict the power usage and ion exchange rate for the design of practical systems. The natural symmetry of planar electrochemical cells implies that averaging in the electrode/membrane–parallel directions is appropriate, yielding a smooth, 1D representation of the concentration and electric potential fields [161, 163]. Averaging in time may also be performed for practical systems operating in a stationary state. This smooth and lower–dimensional representation alone — not the detailed fluctuations contained in the unsteady, chaotic 3D solution — is sufficient to compute the desired mean quantities. Second, a demonstrably accurate model for chaotic electroconvection exists in the form of the Poisson–Nernst–Planck–Stokes equations, but determination of mean quantities through this route requires expensive DNS.

Prior work has not yet yielded a method for direct computation of the mean fields without the need for DNS. Cai and co–authors utilized deep learning to demonstrate a data–assimilation framework for non–chaotic electroconvection, but their primary goal was prediction of the full electroconvection fields based on partial measurements of one of the fields [184]. In a recent work, Guan and co–authors developed a sparse nonlinear model for chaotic electroconvection during unipolar charge injection in EHD, wherein a regression–based method is used to predict the nonlinear evolution of the coherent structures associated with the first few proper–orthogonal–decomposition (POD) modes of the charge density fields [185]. By enforcing phase–space symmetries of the POD coefficients as part of the regression, the authors find agreement between the sparse nonlinear model and POD analysis of the DNS results. Though it is conceivable to apply the same method to electrokinetic flows, it is unclear how many modes are required to accurately represent quantities like the current density. Additionally, whereas Guan and co–authors seek to reproduce the chaotic dynamics accurately, we are chiefly motivated to determine the time– and space–averaged averaged effects of the underlying chaotic dynamics. Thus, we now introduce the methodology used in this work to enable direct computation of the mean fields.

Since the techniques used in this work are drawn from a different field of study, we briefly introduce an analogous problem in which a similar dilemma appears — scalar mixing in turbulent flows [186]. At high Reynolds numbers, the Navier–Stokes equations admit

chaotic solutions in which velocity fields exhibit spatiotemporal fluctuations with broadband spectra. Fine–scale eddies are responsible for mixing solute dissolved in the fluid, but the mean velocity and concentration fields are of considerable interest in practical applications. This gave rise to the Reynolds–averaging procedure, whereby one may derive equations that directly govern the evolution of mean fields. Some form of modeling is required in order to close the nonlinear terms in these equations, whether algebraic in form or comprising additional transport equations. Two prior works have recognized this analogy in the context of EHD [187] and electrokinetics [161]. In the latter, Druzgalski and co–authors derive Reynolds–averaged analogs of the Poisson–Nernst–Planck–Stokes equations in the course of analyzing their DNS of the system, demonstrating the presence of two unclosed terms: one resulting from advection and the other from electromigration. In that work and in a follow–up [163], the authors demonstrated that the advection–related term is dominant in the bulk — as may be intuited since the bulk is largely electroneutral. Thus, closure of this advection term in particular appears to be a priority.

Mani and Park introduced the Macroscopic Forcing Method (MFM) within the context of Reynolds Averaged Navier Stokes (RANS) modeling of turbulent transport, as a tool for the evaluation of differential operators to close the averaged equations [188]. Mirroring their terminology, we refer to the chaotically–fluctuating fields as 'microscopic' fields and the averaged fields as 'macroscopic' fields. A similar distinction is drawn between the microscopic and macroscopic equations. Using MFM, it is possible to determine a macroscopic representation of transport due to microscopic fluctuations by examining how solutions to the microscopic equations respond to various imposed forcing terms. In the original work, Mani and Park are able to compute general (i.e., spatiotemporally nonlocal and anisotropic) operators to close the macroscopic equations in a number of example scalar– and momentum–transport problems. Given space–time–resolved velocity fields, the MFM procedure may be used to determine a corresponding closure operator in the form of an eddy diffusivity (which, in its most general form, is a tensorial kernel that captures spatiotemporal non–locality and anisotropy).

However, the conventional MFM procedure entails significant computational cost, since 3D DNS results are required as inputs to the procedure. Considering that each simulation would need to be performed with a realistic Debye length, the prospect of performing MFM on an electroconvection system quickly becomes intractable. Therefore, as opposed to using DNS fields as inputs to the procedure, we incorporate 3D, time–resolved velocity field

measurements from particle tracking velocimetry (PTV) experiments. The experimentally measured velocity fields are fed into a variant of the MFM procedure referred to as the Inverse Macroscopic Forcing Method (IMFM), which is designed to efficiently compute spatial moments of the eddy diffusivity kernel using a single forced simulation per moment.

Thus, by combining novel computational and experimental techniques, we circumvent the tractability problem associated with MFM and measure a closure operator for the dominant unclosed term in the Reynolds–averaged Poisson–Nernst-Planck–Stokes equations. As we will show, transport due to microscopic electroconvection may be represented to leading order as a gradient–diffusion term in the macroscopic space. Furthermore, we use our combined numerical and experimental technique to directly measure the corresponding eddy diffusivity. Finally, we show that *a posteriori* analysis of our closure operator exhibits excellent agreement with experiments.

The rest of this chapter is organized as follows: In section 4.2, we introduce the general framework for our reduced order model. The application of Reynolds averaging to the Poisson–Nernst–Planck–Stokes equations leads to a closure problem, but we demonstrate how one may measure the leading order macroscopic representation of the unclosed terms: namely, as a gradient diffusion term with a spatially–varying eddy diffusivity. In section 4.3, we describe the experimental measurement of 3D, time–resolved velocity fields using PTV. In Section 4.4, we describe the numerical methods and algorithms used to generate the computational results presented in this work. In section 4.5, we display the measured eddy diffusivity profiles and we demonstrate their *a posteriori* accuracy by performing simulations of the closed macroscopic equations. Two approaches are shown: First, we use the exact measurements of diffusivity profiles for the cases corresponding to experiments. Second, we propose a voltage–dependent form that allows interpolation between the applied voltage values for which experimental measurements are available. Finally, in section 4.6, we discuss the impacts of this work and offer concluding remarks.

4.2 Theory

The objective of this section is developing the framework for a model to represent mean transport due to chaotic electroconvection. Although Reynolds's averaging is a promising approach, the associated closure problem must be addressed. We show rigorously that the unclosed flux can be represented to leading order as a gradient–diffusion term with a

spatially–varying diffusivity coefficient, and we outline a method by which this eddy diffusivity can be measured from experimental data. This section is subdivided into two parts: The first part rigorously defines the microscopic and macroscopic equations for electroconvection, revealing the unclosed terms in the macroscopic equations. The second part introduces the MFM procedure and explains how velocity fields from experiments are incorporated therein, bypassing computationally intractable steps and yielding a measurement of the eddy diffusivity.

4.2.1 Microscopic and Macroscopic Equations

We begin with the microscopic equations, which capture the full, space–time–resolved physics of electroconvection at continuum scales. It is well known that the combined Poisson–Nernst–Planck–Stokes equations can accurately model electrolyte flow and ion transport in systems with electroconvection [136, 141, 142, 161, 163]:

$$\frac{\partial c_i}{\partial t} + \overrightarrow{\nabla} \cdot \overrightarrow{F_i} = 0, \tag{4.2}$$

$$\overrightarrow{F_i} = \overrightarrow{u}\, c_i - D_i \overrightarrow{\nabla} c_i - D_i \frac{z_i e}{k_B T} c_i \overrightarrow{\nabla} \phi, \tag{4.3}$$

$$-\varepsilon_0 \varepsilon_r \nabla^2 \phi = \sum_i e z_i c_i, \tag{4.4}$$

$$\frac{\partial \overrightarrow{u}_i}{\partial t} = -\frac{1}{\rho} \overrightarrow{\nabla} p + \nu \nabla^2 \overrightarrow{u} - \frac{1}{\rho} \sum_i e z_i c_i \overrightarrow{\nabla} \phi, \tag{4.5}$$

and

$$\overrightarrow{\nabla} \cdot \overrightarrow{u} = 0. \tag{4.6}$$

Together, Eqs. (4.2) and (4.3) describe ion transport due to advection, diffusion, and electromigration of some species i whose concentration is given by c_i. Equation (4.3) is the Nernst–Planck flux supplemented with an advection term. Note that Einstein's relation has been used to write the electric mobility μ_i in terms of mass diffusivity D_i: $\mu_i = D_i z_i e / k_B T$. Equation (4.4) is Poisson's equation for the electric potential, ϕ. Given the low Reynolds numbers at which electroconvection typically occurs, Eqs. (4.5) and (4.6) are the Stokes equations for the electrolyte velocity, $\overrightarrow{u}$, and the hydrodynamic pressure, p. Note the presence of an electric body force, the last term in Eq. (4.5). The constants D_i, z_i, e, k_B, T, ϵ_0, ϵ_R, ρ, and ν, are ion mass diffusivity, ion valence, elementary charge, Boltzmann's constant,

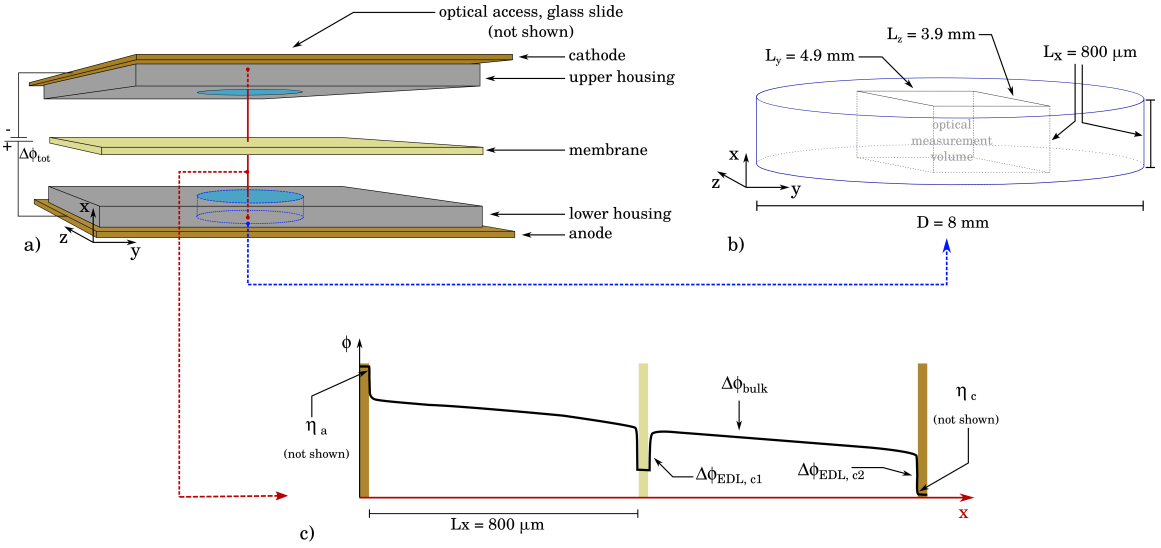

Figure 4.1: Note: Figure not drawn to scale. (a) An exploded schematic of the experimental apparatus, showing two electrolyte reservoirs and the cation–selective membrane sandwiched between copper electrodes. (b) An inset of the anolyte chamber, showing the volume over which PTV is performed and velocity fields are measured in experiments. This optical measurement volume is also the domain for the computational component of this study. (c) A representative sketch of electric potential along the red reference line shown in (a), indicating potential drops that occur at various locations in the electrochemical cell. Additional details regarding the apparatus may be found in [157].

system temperature, vacuum permittivity, electrolyte relative permittivity, electrolyte mass density, and electrolyte kinematic viscosity, respectively.

The conventional DNS approach would entail discretizing and solving the microscopic equations (Eqs. (4.2) to (4.6)) with the appropriate boundary conditions, yielding the microscopic fields c_i, ϕ, $\overrightarrow{u}$, and p. Instead, we seek to directly predict the macroscopic fields, which are smoother and occupy a lower–dimensional space.

Averaging is proposed as the means of analytically bridging the microscopic and macroscopic spaces, but the specific type of averaging to be employed — spatial, temporal, or ensemble — depends on the specific problem geometry. Therefore, we now introduce in Fig. 4.1 the geometry that will be used in both the computational and experimental components of this study. The full electrochemical cell is shown in Fig. 4.1(a); both the anolyte and catholyte chambers are initially filled with a $1\,\mathrm{mmol\,L^{-1}}$ solution of copper sulfate. Since electroconvection is only expected in the anolyte chamber, we restrict our analysis to this region alone. Note in Fig. 4.1(b) the rectilinear 3D domain with dimensions L_x, L_y,

and L_z, located within the anolyte chamber and bounded below and above by a copper electrode and cation–exchange–membrane respectively.

The aspect ratio of the anolyte chamber shown in Fig. 4.1(b) ensures that assuming statistical homogeneity in the y and z dimensions is appropriate everywhere except for a thin zone near the edges of the chamber. This suggests that a 1D representation varying only in x is appropriate after averaging in the other spatial dimensions. Additionally, for a fixed applied electric potential or current, the system is expected to reach a statistically stationary state once electroconvection is established. Consequently, for some microscopic field f, we introduce the macroscopic field $\overline{f}$ as

$$\overline{f}\,(x) = \frac{1}{T}\int_0^T \frac{1}{L_z}\int_0^{L_z} \frac{1}{L_y}\int_0^{L_y} f\,(x,y,z,t)\,dydzdt. \tag{4.7}$$

The averaging operation performed in Eq. (4.7) can be viewed as a projection from the microscopic space inhabited by $f(x,y,z,t)$ to the macroscopic space inhabited by $\overline{f}(x)$. The duration of measurement T must be much longer than the time scale of fluctuations in electroconvection. Similarly, L_y and L_z must be larger than the size of vortices in the flow.

We now seek to derive a set of macroscopic analogs of Eqs. (4.2) to (4.6) that will govern the evolution of macroscopic fields. We begin with the velocity field, immediately realizing a key feature of working in the macroscopic space: $\overline{\overline{u}} = 0$, which follows from continuity (Eq. (4.6)) in addition to the no–penetration boundary conditions at the electrode/membrane and statistical homogeneity/symmetry in the y and z directions. Therefore, we do not need to develop macroscopic analogs for Eqs. (4.5) and (4.6). Treatment of the remaining equations requires the introduction of Reynolds' decomposition of fields into mean and fluctuating components: $f' \equiv f - \overline{f}$, such that $f = \overline{f} + f'$ [186]. Applying Reynolds' decomposition and averaging to Eqs. (4.2) to (4.4), we arrive at

$$\frac{\partial \overline{c}_i}{\partial t} + \frac{\partial}{\partial x}\left(-D_i\frac{\partial \overline{c}_i}{\partial x} - D_i\frac{z_i e}{k_B T}{}_i\,\overline{c}_i\frac{\partial \overline{\phi}}{\partial x}\right) = -\frac{\partial}{\partial x}\left(\overline{u_x' c_i'} - D_i\frac{z_i e}{k_B T}\overline{c_i'\frac{\partial \phi'}{\partial x}}\right) \tag{4.8}$$

and

$$-\varepsilon_0\varepsilon_r\frac{\partial^2\overline{\phi}}{\partial x^2} = \sum_i e z_i \overline{c}_i. \tag{4.9}$$

We have used the facts that differentiation in x commutes with the averaging operation defined in Equation (4.7) and that gradients in homogeneous dimensions are analytically

zero for macroscopic quantities. The unsteady term has been retained despite temporal averaging because artificial time stepping will be used to compute the steady–state $\overline{c}_i$ in section 4.5.2.

Note that Eq. (4.9) is expressed entirely in terms of the macroscopic variables $\overline{\phi}$ and $\overline{c}_i$. Meanwhile, two unclosed terms — the first involving $(\overline{u'_x c'_i})$ and the second involving $(\overline{c'_i \partial \phi' / \partial x})$ — are present on the right side of Eq. (4.8). Prior *a priori* analysis of the unclosed terms in Eq. (4.8) for a similar system found that the first term $(\overline{u'_x c'_i})$ is dominant except in a thin region near the membrane [161, 163]. In order to capture the leading–order physics, we focus our modeling efforts on the first term alone.

Physically, the first unclosed term in Eq. (4.8) represents the mean effect of mixing due to velocity field fluctuations. We will continue with our analysis in the limit of vanishing Debye length, assuming electroneutrality in regions with appreciable advective mixing. This simplification allows analysis of species transport via a single equation governing the behavior of an electroneutral salt, in which the only remaining terms are due to ambipolar diffusion and advection. In the next part, we determine the advective closure operator based on this transport equation for an electroneutral salt, and we assume that the same operator governs advective mixing for individual species in Eq. (4.8).

4.2.2 MFM Procedure with Experimental Velocity Fields

We now outline the MFM procedure. Whereas the conventional MFM technique would require velocity fields from 3D DNS simulations as inputs, we instead use the 3D, time–resolved velocity fields from experiments. Such a workaround is crucial, since full microscopic simulations using an accurate Debye length are prohibitively expensive [182].

As a first step, we reconsider Eqs. (4.2) to (4.4) in the limit of electroneutrality for a binary electrolyte, where we may take $\Sigma_i z_i c_i = z_+ c_+ + z_- c_- = 0$. The positive and negative subscript refer to the cation and anion respectively. We aim to write a transport equation for $c \equiv (z_+ c_+ - z_- c_-)/(z_+ - z_-)$, which is the electroneutral salt concentration. For a binary and symmetric electrolyte, the electroneutral salt concentration is simply the arithmetic mean of the individual cation and anion concentrations. Furthermore, considering the electroneutrality constraint, we may write that $c = c_+ = c_-$ for a binary and symmetric electrolyte.

Utilizing the definition of c introduced above and the electroneutrality constraint, the individual ionic transport equations may be combined to eliminate the electric potential,

yielding

$$\frac{\partial c}{\partial t} + \overrightarrow{\nabla} \cdot \left(\overrightarrow{u} c - D_{\mathrm{A}} \overrightarrow{\nabla} c \right) = 0, \tag{4.10}$$

where the ambipolar diffusivity is given generally (i.e., for binary symmetric or binary asymmetric electrolytes) by $D_{\mathrm{A}} \equiv (z_+ - z_-) D_+ D_- / (z_+ D_+ - z_- D_-)$. Finally, Reynolds averaging is performed to determine the macroscopic equation

$$\frac{\partial \overline{c}}{\partial t} - \frac{\partial}{\partial x} \left(D_{\mathrm{A}} \frac{\partial \overline{c}}{\partial x} \right) = - \frac{\partial}{\partial x} \left(\overline{u_x' c'} \right). \tag{4.11}$$

Under the assumption of electroneutrality, the unclosed term in Eq. (4.11) is identical to the unclosed advection term appearing in Eq. (4.8). Therefore, we may use Eqs. (4.10) and (4.11) as the microscopic and macroscopic equations for the MFM procedure, and the resulting closure operator is expected to be valid for use in Eq. (4.8) as well.

Following [188, 189], we introduce a general representation of the unclosed term in Equation (4.11) by writing

$$-\overline{u_x' c'}(x) = \int_0^{L_x} \mathcal{D}(x, \tilde{x}) \left. \frac{\partial \overline{c}}{\partial x} \right|_{\tilde{x}} d\tilde{x}. \tag{4.12}$$

The diffusivity kernel $\mathcal{D}(x, \tilde{x})$ quantifies the influence of $\partial \overline{c} / \partial x|_{\tilde{x}}$, the macroscopic scalar gradient at location $\tilde{x}$, on the closure flux at location x. We emphasize that this representation does not impose physical constraints on the closure flux, since we have not yet specified the diffusivity kernel $\mathcal{D}$. In fact, the primary goal of the MFM method is measurement of the kernel based on the inherent details of the microscopic fields.

Following [188], Eq. (4.12) can be represented using the Kramers–Moyal expansions by writing $\partial \overline{c} / \partial x|_{\tilde{x}}$ in terms of its Taylor series expansion around x. This results in

$$-\overline{u_x' c'}(x) = D^0(x) \frac{\partial \overline{c}}{\partial x} + D^1(x) \frac{\partial^2 \overline{c}}{\partial x^2} + D^2(x) \frac{\partial^3 \overline{c}}{\partial x^3} + \ldots, \tag{4.13}$$

where $D^j(x)$ is the j–th spatial moment of $\mathcal{D}(x, \tilde{x})$ in the $\tilde{x}$ space, weighted by the inverse factorial of j:

$$D^j(x) = \int_0^{L_x} \frac{(\tilde{x} - x)^j}{j!} \mathcal{D}(x, \tilde{x}) \, d\tilde{x}. \tag{4.14}$$

Within this context, characterization of the advective closure operator is reduced to quantification of each D^j. Mani and Park demonstrated that each D^j may be determined through

a procedure they refer to as the Inverse Macroscopic Forcing Method (IMFM). As explained in the original work, IMFM differs from the general MFM method insofar as its objective is to utilize a specific forcing function to determine an individual moment of the diffusivity kernel per forced simulation, as opposed to using a large sample of forcing functions to determine the entire kernel element by element.

While IMFM may be used to determine an arbitrary number of the D^j fields, we utilize this technique to only compute $D^0(x)$, approximating the closure operator by only retaining the leading order term in Eq. (4.13). The type of truncation yields the Boussinesq–limit eddy diffusivity, in which $\mathcal{D}(x, \tilde{x})$ is implied to be a Dirac delta function centered around $\tilde{x} = x$, limiting the sensitivity of the closure flux to local mean gradients [188]. This approximation is formally valid when there is separation in magnitude between the macroscopic and microscopic length scales. However, our analyses of closures in other problems suggests that even without a clear separation of scales, the leading order term in Eq. (4.13) represents the dominant portion of the total closure flux [188, 190–192]. As shown in Section 4.5, the same approximation for the problem considered here leads to reasonable predictions of system–level behavior compared to experiments.

Following the IMFM procedure [188], D^0 may be determined by performing a forced simulation of Eq. (4.10) using

$$\frac{\partial c}{\partial t} + \overrightarrow{\nabla} \cdot \left(\overrightarrow{u} c - D_{\mathrm{A}} \overrightarrow{\nabla} c \right) = s, \tag{4.15}$$

where s is a forcing term that belongs to the macroscopic space: $\overline{s} = s$. Here, s is purely a function of x and steady in time. We take the microscopic velocity field $\overrightarrow{u}$ to be known in advance from experiments, as opposed to determining them through an expensive two–way coupled simulation with the momentum equations.

The goal of IMFM is to select a forcing function $s(x)$ such that the resulting concentration field c will yield an average $\overline{c}$ that matches a pre–specified target profile $\overline{c}_T(x)$, thereby allowing for determination of individual moments of the diffusivity kernel. For example, say one chooses $\overline{c}_T = x$ and simulates Eq. (4.15) using an $s(x)$ that guarantees $\overline{c} = \overline{c}_T(x) = x$. Applying Eq. (4.13), $D^0(x)$ is determined by computing $-\overline{u'_x c'}(x)$ from the resulting fields. In other words, $D^0 = -\overline{u'_x c'}(x)$ for this specific forced simulation. Similarly, higher order D^j may be successively computed by setting $\overline{c}_T(x)$ equal to higher order polynomials and running additional simulations.

The s required to yield a target $\overline{c}_T(x)$ is given by

$$s = \frac{\overline{c}_T - \overline{c}}{\Delta t} + \overrightarrow{\nabla} \cdot \left(\overrightarrow{u}\overline{c} - D_{\mathrm{A}} \overrightarrow{\nabla}\overline{c} \right), \tag{4.16}$$

which is presented in the context of a temporal discretization with time step Δt. As previously described [188], this choice of s constrains the macroscopic concentration profile while permitting microscopic fluctuations.

Once $D^0(x)$ is determined through forced simulation of Eqs. (4.15) and (4.16) using $\overline{c}_T = x$, we are left with a simple gradient–diffusion model for the mixing due to electroconvection, given by the leading order term in Eq. (4.13). The eddy diffusivity, given by $D^0(x)$, captures the leading–order mean effects of mixing due to chaotic velocity fields, and is a function of space that we directly measure from a combined numerical and experimental technique. Thus, we have provided a closure for the unclosed term in Eq. (4.11), and, as discussed, the same closure flux is expected to capture the leading order effect of the unclosed advection term in Eq. (4.8). Recall that of the two unclosed terms in Eq. (4.8), the advection term is dominant for a vast majority of the domain. Neglecting the other unclosed term, Eq. (4.8) may now be written in closed form as

$$\frac{\partial \overline{c}_i}{\partial t} + \frac{\partial}{\partial x}\left(-D_i \frac{\partial \overline{c}_i}{\partial x} - D_i \frac{z_i e}{k_B T}_i \overline{c}_i \frac{\partial \overline{\phi}}{\partial x} \right) = -\frac{\partial}{\partial x}\left(-D^0(x) \frac{\partial \overline{c}_i}{\partial x} \right) \tag{4.17}$$

and solved in conjunction with Eq. (4.9).

4.3 Experimental Measurement of Velocity Fields

The primary objective of this section is describing the experiments in which 3D, time–resolved velocity fields are directly measured using PTV. As noted previously, these measured velocity fields allow us to eschew a DNS of the Poisson–Nernst–Planck–Stokes equations as a precursor to the MFM procedure, saving significantly on cost and circumventing the need to introduce artificially thickened electric double layers or other numerical tricks. Since the experimental procedure used here is the same as that described by Stockmeier and co–authors [156, 157], we only offer a brief sketch of the relevant details here and refer readers to the original publications for a more exhaustive description.

Note that the experiments described in this section were performed by a collaborator, not by the author of this dissertation. Nonetheless, a description of the experiments is included

here for completeness, particularly since space–time–resolved experimental velocity fields play a central role in the procedure for this work.

An exploded view of the full electrochemical cell is shown in Fig. 4.1. The center cation–exchange membrane (Nafion N117, Chemours, Wilmington, Delaware, USA), electrodes (copper, 25 mm × 75 mm × 0.5 mm), and 3D–printed housing parts form a pair of electrochemical half–cells. Both chambers are filled with a $1\,\mathrm{mmol\,L^{-1}}$ solution of copper sulfate, $CuSO_4$, but the anolyte is seeded with inert, fluorescent polystyrene tracer particles (0.001 wt%, 3.2 µm diameter, Thermo Scientific, Waltham, MA, USA). The Zeta potential of the tracer particles was measured to be −14.9 mV using a Malvern Zetasizer Nano ZS (Malvern Panalytical Ltd). Due to their charge, the particles are influenced by the electric field. However, similar to prior experimental works [150, 155], the velocity induced by electric fields is at least an order of magnitude smaller than that due to advection.

Details about the optical measurement setup are shown in Fig. 4.2. A stereo microscope (SteREO Discovery.V20, Carl Zeiss Microscopy Deutschland GmbH, Germany) with a 1× objective (Plan-Aprochromat 1×, Carl Zeiss Microscopy Deutschland GmbH, Germany) is focused within the optical measurement volume. A high–frequency Nd:YAG laser (532 nm, DM150, Photonics Industries International Inc.) illuminates the tracer particles, and their emitted fluorescent light is recorded by two high-speed cameras (Phantom VEO 710L, Vision Research Inc.). At a magnification of 5.12× with a halfway–closed aperture, it is possible to record the complete membrane-to-electrode distance. The particle tracks are processed in DaVis (version: 10.0.5.47779, LaVision GmbH, Göttingen, Germany), resulting in a velocity field with a size of 0.8 mm×4.9 mm×3.1 mm and 21 px×128 px×80 px resolution in space, and 20 Hz in time. Examples of the tracer particle paths and reconstructed Eulerian velocity fields are shown in Fig. 4.3.

During each experiment, a DC current is applied to the cell and the difference in electric potential between the electrodes is measured. Though the experiment is performed galvanostatically, measurements are taken when the applied electric potential reaches a statistically stationary state (details may be found in the original experimental work [156, 157] and in other recent works that investigate the stationary portion of chronopotentiometric measurements [193, 194]). We take the potential difference between electrodes, $\Delta\phi_{\mathrm{tot}}$, to be a time–averaged value in the stationary state, allowing us to use a potentiostatic simulation approach in Section 4.5.2. $\Delta\phi_{\mathrm{tot}}$ comprises all the contributions shown in Fig. 4.1(c). Meanwhile, the computational procedure will only include the anolyte region,

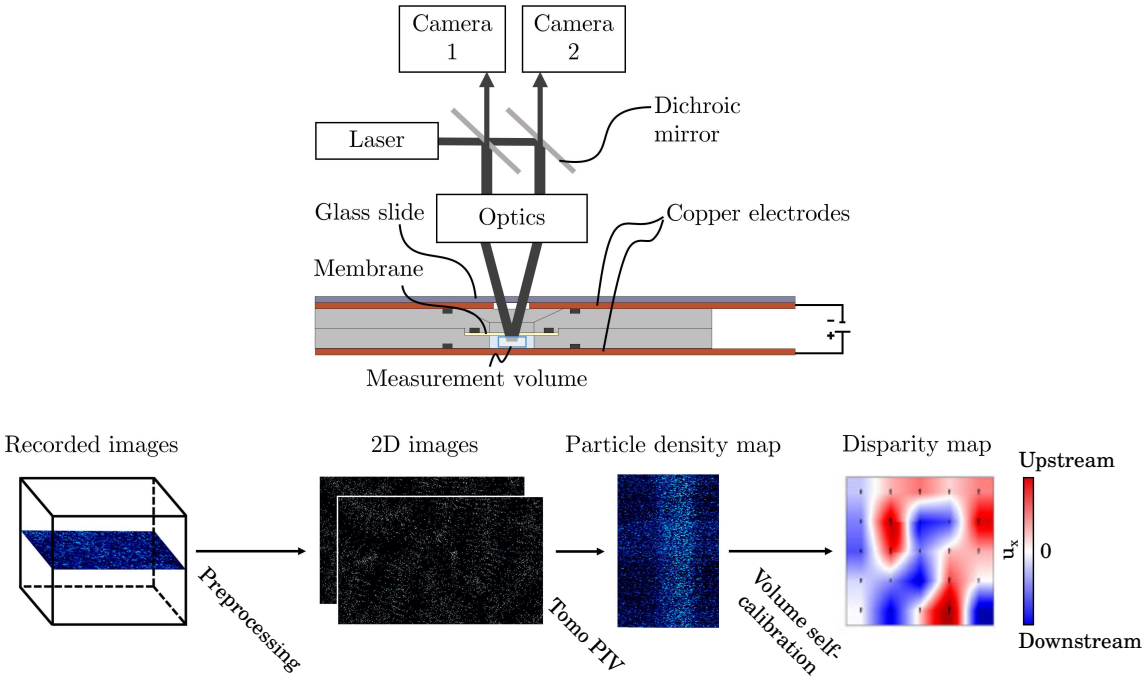

Figure 4.2: Schematic of the experimental setup for stereo PTV. A laser illuminates the fluorescent tracer particles in the measurement volume, which are recorded by a stereo camera pair. The stereo images of the volume acquired over time are pre–processed to reduce noise and improve the visibility of particles. The spatial boundaries of the volume are then determined in the membrane–normal direction using tomographic PIV. In the last step, volume self–calibration is used to increase the accuracy of the calibration and to correct image distortion due to light refraction at the surface. Additional details may be found in the work by Stockmeier and co–authors [156, 157]. Partially reprinted from Journal of Membrane Science, 640, Stockmeier *et al.*, "Direct 3D observation and unraveling of electroconvection phenomena during concentration polarization at ion-exchange membranes", 119846, Copyright (2021), with permission from Elsevier.

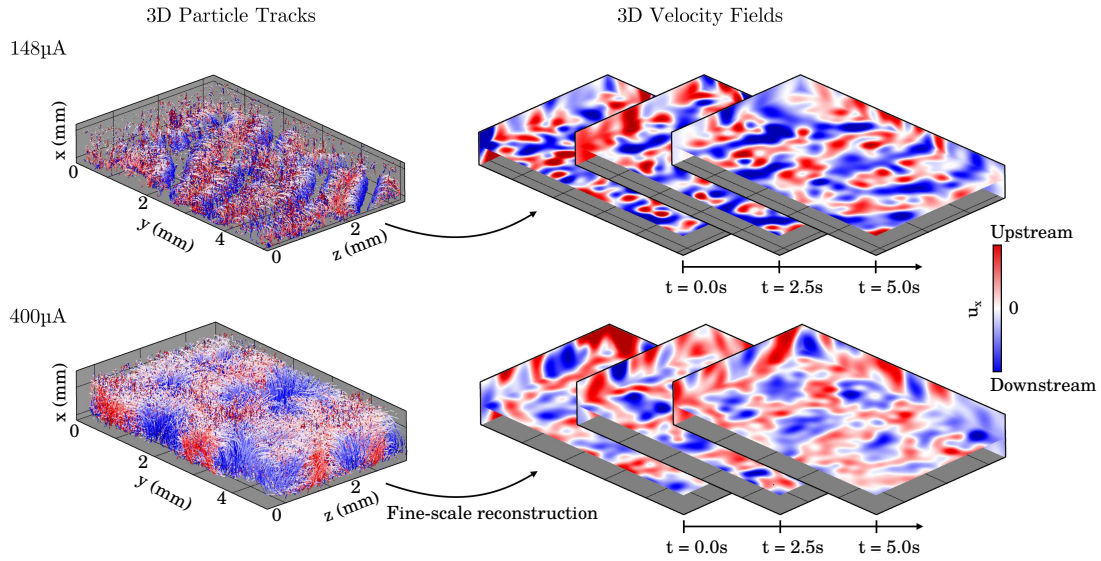

Figure 4.3: Construction of 3D velocity fields from 3D particle tracks using the fine–scale reconstruction method. The colors indicate the velocity component in membrane–normal direction. Example cases are shown at applied DC current values of 148 µA and 400 µA, as indicated. Additional details may be found in the work by Stockmeier and co–authors [156, 157].

since electroconvection only occurs in this half of the electrochemical cell. The potential difference across the anolyte — which we refer to simply as $\Delta\phi$ — may be written as $\Delta\phi = \Delta\phi_{\text{tot}} - \eta_a - \eta_c - \Delta\phi_{\text{EDL,c1}} - \Delta\phi_{\text{EDL,c2}} - \Delta\phi_{\text{bulk}}$, where each of these components is shown in Fig. 4.1.

The overpotential η due to copper dissolution and deposition at the electrodes may be modeled using the Butler–Volmer equation as

$$i = i_0 \left[\exp\left(\frac{\beta e}{k_B T}\eta\right) - \exp\left(\frac{(2-\beta)\, e}{k_B T}\eta\right)\right], \tag{4.18}$$

where i is the current density, i_0 is the exchange current density, and $\beta = 0.5$ is the symmetry factor [195, 196]. The mechanism shown in Eq. (4.18) may be adapted to both the anode and cathode, allowing for computation of η_a and η_c based on the measured mean current density. We adopt a value of $i_0 = 3.7 \times 10^{-3}\,\text{mA}\,\text{cm}^{-2}$, based on the value measured for a copper electrode adjacent to $0.5\,\text{mol}\,\text{L}^{-1}$ copper sulfate solution [197], along with an analytical correction for the discrepancy in electrolyte concentration [195, 196].

An Ohmic model is employed for the catholyte bulk using resistivity ρ_{bulk} and length L_{bulk} as

$$\Delta\phi_{\text{bulk}} = i\rho_{\text{bulk}} L_{\text{bulk}}. \tag{4.19}$$

Additionally, the total potential difference across both EDLs in the catholyte region is taken to be a constant. The values of $\rho_{\text{bulk}} L_{\text{bulk}} = 8.11 \times 10^{-2}\,\Omega\,\text{m}^2$ and $(\Delta\phi_{\text{EDL,c1}} + \Delta\phi_{\text{EDL,c2}}) = 8.93\,\text{mV}$ are determined based on comparison to 1D simulations of the Poisson–Nernst–Planck equations in the ohmic regime, where electroconvection is not expected and a 1D approach is justified. Thus, these two fitting parameters allow for matching of the conductivity and open–circuit–potential in the Ohmic regime (see the black and red curves in Fig. 4.11).

4.4 Numerical Methods and Solver Algorithm

In this section, we describe the numerical methods used to compute the results displayed in this chapter. First, interpolation of the experimentally measured velocity fields in space and in time is required prior to inserting the fields into the MFM simulation. We describe how this interpolation may be performed in a manner that ensures discrete mass conservation for the interpolated fields. Second, we describe the numerical methods for the MFM simulation.

Third, we describe the numerical methods for the macroscopic, 1D simulations using the eddy diffusivity.

4.4.1 Velocity Field Interpolation

Through the course of our investigation, we found that spatial under–resolution during the MFM procedure leads to large oscillations in the measured eddy diffusivity profile for the under–resolved regions. The region most prone to under–resolution is the zone near the membrane, toward which vortices are more closely confined at higher applied voltages. Generally, these unphysical oscillations lead to substantial misprediction of the j–V curves.

Note, however, that the available experimental data is limited to fixed resolution of $21\,\text{px}\times128\,\text{px}\times80\,\text{px}$. Therefore, spatial interpolation of the velocity fields (in the x direction in particular) is required to achieve acceptably smooth eddy diffusivity profiles. Additionally, the time step stability limit for MFM simulations (simulation of the forced microscopic equation, Eq. (4.15)) scales with the square of the mesh size due to the diffusion term. Since the frequency of experimental measurements is fixed at 20 Hz, temporal interpolation of the measured velocity fields is required for time steps that are $\Delta t < 5\times10^{-2}\,\text{s}$.

For incompressible flows, the microscopic velocity fields must satisfy the continuity equation given by Eq. (4.6). We denote the cell–center locations for the experimental measurement mesh using the triplet (x_i, y_j, z_k), where the indices i, j, and k take integer values between 1 and $N_{x,y,z}$ (inclusive, taking $N_{x,y,z}$ to be the number of cells in each direction). We use a staggered mesh for all parts of this work. Thus, each component of the velocity field is stored at the orthogonal cell faces (as opposed to the cell centers), allowing for straightforward computation of advection flux at the cell faces. For the cell with center indexed by (i,j,k), the velocity components at the cell faces at time n are given by $u^{(i\pm1/2,j,k,n)}$, $v^{(i,j\pm1/2,k,n)}$, and $w^{(i,j,k\pm1/2,n)}$, in the x, y, and z directions, respectively. We consider cell centers (indexed by integer indices) to be located at the midpoint of adjacent cell faces (indexed by half integers) in all directions.

For this staggered mesh formulation, the left side of Eq. (4.6) may be written discretely using second order central differences as

$$\overrightarrow{\nabla}^D \cdot \overrightarrow{u}^{(i,j,k,n)} = \frac{u^{(i+1/2,j,k,n)} - u^{(i-1/2,j,k,n)}}{\Delta x^{(i,j,k)}} + \frac{v^{(i,j+1/2,k,n)} - v^{(i,j-1/2,k,n)}}{\Delta y^{(i,j,k)}} + \frac{w^{(i,j,k+1/2,n)} - w^{(i,j,k-1/2,n)}}{\Delta z^{(i,j,k)}}. \tag{4.20}$$

The index n refers to a discrete point in time, and the symbol $\overrightarrow{\nabla}^D$ is used to signify a discrete gradient operator. Indexing of the mesh size variables Δx, Δy, and Δz is used to denote the local distance between cell faces in each direction, which exhibits spatial variation for nonuniform meshes.

We start with the question of temporal interpolation. Say we are interested in computing the velocity field at some time index n', representing time $t^{n'}$. The time of interest lies in the interval $t^n < t^{n'} < t^{n+1}$, and experimentally measured velocity fields are available at times t^n and t^{n+1}. Each velocity field coming directly from experiments satisfies discrete mass conservation, $\overrightarrow{\nabla}^D \cdot \overrightarrow{u}^{(i,j,k,n)} = \overrightarrow{\nabla}^D \cdot \overrightarrow{u}^{(i,j,k,n-1)} = 0$, by virtue of the processing steps in its construction. Therefore, we employ linear interpolation in time and observe that

$$\begin{aligned} \overrightarrow{\nabla}^D \cdot \overrightarrow{u}^{(i,j,k,n')} &= \overrightarrow{\nabla}^D \cdot \left[\left(1 - \frac{t^{n'} - t^n}{t^{n+1} - t^n} \right) \overrightarrow{u}^{i,j,k,n} + \left(\frac{t^{n'} - t^n}{t^{n+1} - t^n} \right) \overrightarrow{u}^{i,j,k,n+1} \right] \\ &= 0. \end{aligned} \tag{4.21}$$

Thus, temporally interpolated velocity fields are also guaranteed to satisfy discrete mass conservation.

The same cannot be said, however, for spatially interpolated velocity fields. For the arbitrary time given by index n', consider linear (or higher order, if desired) interpolation of the 3D velocity field from points represented by the triplet (i, j, k) onto points represented by the triplet (i', j', k'). Near the membrane and electrode boundaries, utilization of the no–slip and no–penetration boundary condition as part of the interpolation ensures that velocity fields smoothly approach zero. The 3D velocity field resulting from such an interpolation is represented as $\overrightarrow{v}^{(i',j',k',n')}$, and, generally speaking, $\overrightarrow{\nabla}^D \cdot \overrightarrow{v}^{(i',j',k',n')} \neq 0$.

In order to project $\overrightarrow{v}^{(i',j',k',n')}$ onto the space of discretely–divergence–free velocity fields, we consider a scalar field given by $\psi^{i',j',k',n'}$ and write the desired divergence–free velocity field discretely as

$$\overrightarrow{u}^{i',j',k',n'} = \overrightarrow{v}^{i',j',k',n'} + \overrightarrow{\nabla}^D \psi^{i',j',k',n'}. \tag{4.22}$$

Applying the discrete divergence operator from Eq. (4.20) to Eq. (4.22) and enforcing the divergence–free condition for $\overrightarrow{u}^{i',j',k',n'}$ allows us to write the discrete Poisson's equation for ψ as

$$\nabla^{2D} \psi^{(i',j',k',n')} = -\overrightarrow{\nabla}^D \cdot \overrightarrow{v}^{(i',j',k',n')}. \tag{4.23}$$

To determine boundary conditions for Eq. (4.23), we recognize that applying $\overrightarrow{\nabla} \psi \cdot \hat{n} = 0$ for

Algorithm 4.1 Pseudocode for velocity field interpolation, demonstrated for an instantaneous point in time. Taking $\overrightarrow{u}^{(i,j,k,n)}$ and $\overrightarrow{u}^{(i,j,k,n-1)}$ to be known from experiments, we seek to compute $\overrightarrow{u}^{(i',j',k',n')}$.

1: $\overrightarrow{u}^{i,j,k,n'} \leftarrow \left(1 - \frac{t^{n'}-t^n}{t^{n+1}-t^n}\right) \overrightarrow{u}^{i,j,k,n} + \left(\frac{t^{n'}-t^n}{t^{n+1}-t^n}\right) \overrightarrow{u}^{i,j,k,n+1}$
2: $\overrightarrow{v}^{i',j',k',n'}$ computed via spatial interpolation of $\overrightarrow{u}^{i,j,k,n'}$
3: $\overrightarrow{b} \leftarrow -\overrightarrow{\nabla}^D \cdot \overrightarrow{v}^{(i',j',k',n')}$
4: $\overrightarrow{\psi} \leftarrow \mathbf{M_1^{-1}} \overrightarrow{b}$
5: $\overrightarrow{u}^{(i',j',k',n')} \leftarrow \overrightarrow{v}^{(i',j',k',n')} + \overrightarrow{\nabla}^D \psi^{(i',j',k',n')}$

normal vector $\hat{n}$ at each of the boundaries prevents alteration of the boundary velocities in $\overrightarrow{v}$. Therefore, as long as the interpolation scheme used to compute $\overrightarrow{v}$ from the raw experimental velocity fields preserves the measured velocity values at the boundaries, utilization of a homogeneous Neumann boundary condition for Eq. (4.23) ensures that $\overrightarrow{u}^{(i',j',k',n')}$ will have the correct boundary velocities.

The right side of Eq. (4.23) is computed the same way as in Eq. (4.20). The left side of Eq. (4.23), a discrete Laplacian, is computed using standard second order central differencing as

$$
\begin{aligned}
\nabla^{2D}\psi^{(i',j',k',n')} = \\
&\frac{1}{\Delta x^{(i',j',k')}}\left(\frac{\psi^{(i'+1,j',k',n')} - \psi^{(i',j',k',n')}}{\Delta x^{(i'+1/2,j',k')}} - \frac{\psi^{(i',j',k',n')} - \psi^{(i'-1,j',k',n')}}{\Delta x^{(i'-1/2,j',k')}}\right) \\
&+ \frac{1}{\Delta y^{(i',j',k')}}\left(\frac{\psi^{(i',j'+1,k',n')} - \psi^{(i',j',k',n')}}{\Delta y^{(i',j'+1/2,k')}} - \frac{\psi^{(i',j',k',n')} - \psi^{(i',j'-1,k',n')}}{\Delta y^{(i',j'-1/2,k')}}\right) \\
&+ \frac{1}{\Delta z^{(i',j',k')}}\left(\frac{\psi^{(i',j',k'+1,n')} - \psi^{(i',j',k',n')}}{\Delta z^{(i',j',k'+1/2)}} - \frac{\psi^{(i',j',k',n')} - \psi^{(i',j',k'-1,n')}}{\Delta z^{(i',j',k'-1/2)}}\right),
\end{aligned}
\tag{4.24}
$$

allowing Eq. (4.23) to be expressed as a linear system for ψ:

$$
\mathbf{M_1}\,\overrightarrow{\psi}^{n'} = \overrightarrow{b}^{n'}, \tag{4.25}
$$

where matrix $\mathbf{M_1}$ is the 3D discrete Laplacian operator, $\overrightarrow{\psi}^{n'}$ is a vector containing all values of ψ at time $t^{n'}$, and $\overrightarrow{b}^{n'}$ is a vector quantity containing the discrete divergence of $\overrightarrow{v}^{n'}$ at all points.

The final algorithm for computing an interpolated and mass–conserving 3D velocity

field is given in Algorithm 4.1. The algorithm, which is presented here for a single point in time, must be performed once in each time step of the MFM simulation. It is also possible to perform the interpolation a–priori and save the interpolated velocity fields for use in the MFM simulation, if desired. The discrete gradient operator employed in line 5 of Algorithm 4.1 and in Eq. (4.22) may be computed using second order differentiation and interpolation as

$$\begin{aligned}
&\overrightarrow{\nabla}\psi^{(i',j',k',n')} = \\
&\frac{1}{2}\left(\frac{\psi^{(i'+1,j',k',n')}-\psi^{(i',j',k',n')}}{\Delta x^{(i'+1/2,j',k')}}+\frac{\psi^{(i',j',k',n')}-\psi^{(i'-1,j',k',n')}}{\Delta x^{(i'-1/2,j',k')}}\right)\hat{x} \\
&\quad+\frac{1}{2}\left(\frac{\psi^{(i',j'+1,k',n')}-\psi^{(i',j',k',n')}}{\Delta y^{(i',j'+1/2,k')}}+\frac{\psi^{(i',j',k',n')}-\psi^{(i',j'-1,k',n')}}{\Delta y^{(i',j'-1/2,k')}}\right)\hat{y} \\
&\quad+\frac{1}{2}\left(\frac{\psi^{(i',j',k'+1,n')}-\psi^{(i',j',k',n')}}{\Delta z^{(i',j',k'+1/2)}}+\frac{\psi^{(i',j',k',n')}-\psi^{(i',j',k'-1,n')}}{\Delta z^{(i',j',k'-1/2)}}\right)\hat{z},
\end{aligned} \tag{4.26}$$

where $\hat{x}$, $\hat{y}$, and $\hat{z}$ are unit vectors in each of the spatial dimensions.

4.4.2 MFM Simulation for Measurement of Eddy Diffusivity

The MFM simulation requires discretization of the 3D, unsteady advection–diffusion equation with a forcing term, as described by Eqs. (4.15) and (4.16). We combine the equations and print them here for convenience as

$$\frac{\partial c}{\partial t}+\overrightarrow{\nabla}\cdot\left(\overrightarrow{u}c-D_{\mathrm{A}}\overrightarrow{\nabla}c\right)=\frac{\overline{c}_T-\overline{c}}{\Delta t}+\overrightarrow{\nabla}\cdot\left(\overrightarrow{u}\overline{c}-D_{\mathrm{A}}\overrightarrow{\nabla}\overline{c}\right). \tag{4.27}$$

Recall that $\overline{c}_T$ is a prescribed target profile in the macroscopic space. Additionally, velocity fields are treated using the staggered mesh formulation, as described in the previous section. For simplicity, the entirety of Eq. (4.27) is discretized using an explicit Euler scheme in time and second order central differences in space. Boundary conditions were described in Section 4.2.

After discretization, Eq. (4.27) may be written as

$$\frac{c^{i,j,k,n} - c^{i,j,k,n-1}}{\Delta t} + \overrightarrow{\nabla}^D \cdot \left(\overrightarrow{u}^{i,j,k,n-1} c^{i,j,k,n-1} - D_\mathrm{A} \overrightarrow{\nabla} c^{i,j,k,n-1} \right) = \frac{\overline{c}_T - \overline{c^{i,j,k,n-1}}}{\Delta t} + \overrightarrow{\nabla}^D \cdot \left(\overrightarrow{u}^{n-1} \overline{c^{i,j,k,n-1}} - D_\mathrm{A} \overrightarrow{\nabla} \overline{c^{i,j,k,n-1}} \right), \quad (4.28)$$

where the discrete gradient operator is defined the same way as in Eq. (4.20) and the averaging operator for the forcing terms is defined in Eq. (4.7). We assume that space–time–interpolated velocity fields are available from Algorithm 4.1, such that spatial and temporal indices used here correspond to the appropriate mesh and time step for MFM simulations, *not* the mesh and time step for experimentally–measured velocity fields.

Rearranging in order to permit straightforward representation of the time advancement scheme, we write Eq. (4.28) as

$$\begin{aligned} c^{i,j,k,n} = c^{i,j,k,n-1} &- \Delta t \overrightarrow{\nabla}^D \cdot \left(\overrightarrow{u}^{i,j,k,n-1} c^{i,j,k,n-1} - D_\mathrm{A} \overrightarrow{\nabla} c^{i,j,k,n-1} \right) \\ &+ \frac{\overline{c}_T - \overline{c^{i,j,k,n-1}}}{\Delta t} \\ &+ \overrightarrow{\nabla}^D \cdot \left(\overrightarrow{u}^{i,j,k,n-1} \overline{c^{i,j,k,n-1}} - D_\mathrm{A} \overrightarrow{\nabla} \overline{c^{i,j,k,n-1}} \right), \end{aligned} \quad (4.29)$$

where the averaging operator from Eq. (4.7) is represented discretely as

$$\overline{c^{i,j,k,n-1}} = \frac{1}{N_y N_z} \sum_{l=1}^{N_y} \sum_{m=1}^{N_z} c^{i,l,m,n-1}. \quad (4.30)$$

For convenience, Eq. (4.29) is written concisely as

$$\overrightarrow{c}^n = \overrightarrow{c}^{n-1} + \Delta t \overrightarrow{f} \left(\overrightarrow{c}^{n-1} \right), \quad (4.31)$$

where $\overrightarrow{f}$ may be determined by identifying the appropriate terms in Eq. (4.29). Vector quantities are used to indicate storage of all spatial data at a defined point in time.

Equation (4.31) may be time advanced, assuming that $\overrightarrow{c}^{n-1}$ is known from the previous time step or the initial condition. As described in Section 4.2, $D^0(x)$ is computed by determining $-\overline{u'c'}$ for this simulation. The average is computed in space (homogeneous directions) and in time, excluding the first 5 s of simulation time in order to mitigate the impact of any transients induced by the initial condition. The final algorithm is printed in

Algorithm 4.2 Pseudocode for MFM simulation and corresponding computation of $D^0(x)$.

$\overrightarrow{c}^{n-1} \leftarrow$ initial condition
$D^0(x) \leftarrow 0$
for $n = 1$ to N_t **do**
    $\overrightarrow{c}^{n} \leftarrow \overrightarrow{c}^{n-1} + \Delta t \overrightarrow{f}\left(\overrightarrow{c}^{n-1}\right)$
    if $t^n > 5\,\mathrm{s}$ **then**
        $D^0(x) \leftarrow \left[(n-1)\,D^0(x) - \overline{u^n\left(c^n - \overline{c}_T\right)}\right]/n$ ▷ Running average
    end if
end for

Algorithm 4.2.

4.4.3 Macroscopic Simulation with Eddy Diffusivity

Macroscopic simulations require solution of Eq. (4.17) in tandem with Eq. (4.9). We first discuss discretization of Eq. (4.17). In our staggered mesh formulation, all unknown variables are stored at cell centers (indicated in this section using integer–valued superscript index i) and the flux is computed at adjacent cell faces (indicated using half–integer–valued superscript index $i \pm \frac{1}{2}$). The flux is computed at time index n using second order finite differences and second order interpolation as

$$\begin{aligned} F_i^{\left(i\pm\frac{1}{2},n\right)} = &- \left[D_i + D^0\left(x^{(i\pm1/2)}\right)\right] \frac{\pm\overline{c}_i^{(i\pm1,n)} \mp \overline{c}_i^{(i,n)}}{\Delta x^{(i\pm1/2)}} \\ &- D_i \frac{z_i e}{k_B T} \frac{\overline{c}_i^{(i\pm1,n)} + \overline{c}_i^{(i,n)}}{2} \frac{\pm\overline{\phi}^{(i\pm1,n)} \mp \overline{\phi}^{(i,n)}}{\Delta x^{(i\pm1/2)}} \end{aligned} \tag{4.32}$$

The entire transport equation (Eq. (4.17)) is discretized, then, as

$$\frac{\overline{c}_i^{(i,n)} - \overline{c}_i^{(i,n-1)}}{\Delta t} = -\frac{F^{\left(i+\frac{1}{2},n\right)} - F^{\left(i-\frac{1}{2},n\right)}}{\Delta x^{(i)}}, \tag{4.33}$$

using an implicit–Euler temporal scheme for simplicity of explanation and implementation. Utilization of higher order schemes requires straightforward modification of the unsteady term and right–hand–side indexing in Eq. (4.33), but we found first order numerics to be sufficient in our work.

Finally, Eq. (4.9) is discretized using second order central differences as

$$-\varepsilon_0\varepsilon_r\frac{1}{\Delta x^{(i)}}\left(\frac{\overline{\phi}^{(i+1,n)}-\overline{\phi}^{(i,n)}}{\Delta x^{(i+1/2)}}-\frac{\overline{\phi}^{(i,n)}-\overline{\phi}^{(i-1,n)}}{\Delta x^{(i-1/2)}}\right)=\sum_i ez_i\overline{c}_i^{(i,n)}. \tag{4.34}$$

Considering a mesh with N_x computational cells and a system with N_s ionic species, the discretized macroscopic concentration and electric potential values are represented in vector form at time index n as

$$\overrightarrow{\overline{z}}^n=\begin{bmatrix}\overline{c}_1^{(1,n)}\\ \overline{c}_2^{(1,n)}\\ \vdots\\ \overline{c}_{N_s}^{(1,n)}\\ \overline{\phi}^{(1,n)}\\ \overline{c}_1^{(2,n)}\\ \overline{c}_2^{(2,n)}\\ \vdots\\ \overline{c}_{N_s}^{(2,n)}\\ \overline{\phi}^{(2,n)}\\ \vdots\\ \vdots\\ \overline{c}_1^{(N_x,n)}\\ \overline{c}_2^{(N_x,n)}\\ \vdots\\ \overline{c}_{N_s}^{(N_x,n)}\\ \overline{\phi}^{(N_x,n)}\end{bmatrix} \tag{4.35}$$

Alternating colored groupings in Eq. (4.35) indicate clusters of unknown variables that belong to the same computational cell. The dimensions of $\overrightarrow{\overline{z}}^n$ are $[N_x\,(N_s+1)\times 1]$.

In anticipation of solving the equations iteratively for each time step due to nonlinearity, we seek to linearize the equations around the base state $\overrightarrow{\overline{z}}^\star$ by writing

$$\overrightarrow{\overline{z}}^n=\overrightarrow{\overline{z}}^\star+\overrightarrow{\delta z}. \tag{4.36}$$

We substitute Eq. (4.36) into Eqs. (4.33) and (4.34) and only retain terms up to first order

Algorithm 4.3 Pseudocode for single time step of macroscopic simulation, taking $\overrightarrow{z}^{n-1}$ to be known from the previous time step or the initial condition.

$\overrightarrow{z}^{\star} \leftarrow \overrightarrow{z}^{n-1}$
$\mathcal{R} \leftarrow \infty$
$\mathcal{R}_{\max} \leftarrow$ tolerance
while $\mathcal{R} \geq \mathcal{R}_{\max}$ **do**
    $\mathbf{M_2}$ and $\overrightarrow{g_1}$ computed using $\overrightarrow{z}^{\star}$
    $\overrightarrow{\delta z} \leftarrow \mathbf{M_2^{-1}}\overrightarrow{g_1}$
    $\overrightarrow{z}^{\star} \leftarrow \overrightarrow{z}^{\star} + \overrightarrow{\delta z}$
    $\mathcal{R} \leftarrow ||\overrightarrow{\delta z}||$
end while
$\overrightarrow{z}^{n} \leftarrow \overrightarrow{z}^{\star}$

in $\overrightarrow{\delta z}$. As a result, the $N_x(N_s+1)$ equations represented by Eqs. (4.33) and (4.34) may be represented together as the linear system

$$\mathbf{M_2}\overrightarrow{\delta z} = \overrightarrow{g_1}\left(\overrightarrow{z}^{\star}\right), \tag{4.37}$$

where matrix $\mathbf{M_2}$ (size $[N_x\left(N_s+1\right) \times N_x\left(N_s+1\right)]$) contains coefficients that depend only on the base–state variables. The right–hand side, $\overrightarrow{g_1}$ (size $[N_x\left(N_s+1\right) \times 1]$), is a nonlinear function of the base–state variables.

We may now use Eq. (4.37) to solve Eqs. (4.33) and (4.34) iteratively for $\overrightarrow{z}^{n}$, taking $\overrightarrow{z}^{n-1}$ to be known from the previous time step or the initial condition. The final algorithm, which is equivalent to Newton–Raphson iteration within each time step, is written as pseudocode in Algorithm 4.3.

4.5 Results and Discussion

We remind readers that we concluded section 4.2 with Eq. (4.17), which, in tandem with Eq. (4.9), constitutes a closed system of partial differential equations for the macroscopic $\overline{c}_i$ and $\overline{\phi}$ fields. We also described the procedure whereby the eddy diffusivity $D^0(x)$ may be computed using the experimentally–measured velocity fields. Consequently, this section is divided into two parts. In the first part, we describe our implementation of the MFM procedure and display the resulting eddy diffusivity profiles. Two approaches are shown: (i) We measure a separate eddy diffusivity profile for each value of $\Delta\phi$ used in experiments.

(ii) We propose a voltage–dependent profile that allows interpolation between the cases for which experimental measurements are available. In the second part, we evaluate *a posteriori* performance of the eddy diffusivity by directly solving the macroscopic equations for the mean fields and current density and comparing the results against experiments.

4.5.1 Measurement of Eddy Diffusivity

As described previously, measurement of D^0 requires numerical solution of Eqs. (4.15) and (4.16) with the target mean concentration profile given by $\bar{c}_T = x$. The computational domain corresponds to the optical measurement volume shown in Fig. 4.1, which is a 3D, rectangular sub–region of the anolyte chamber.

Generally, boundary conditions for c in the forced microscopic simulation should be consistent with the target profile $\bar{c}_\mathrm{T}$. Therefore, Dirichlet conditions are used in x, corresponding to the linear profile given by $\bar{c}_T = x$. We exploit homogeneity in y and in z by choosing periodic boundary conditions in those dimensions. Strictly speaking, the experimentally–measured velocity fields are not instantaneously periodic in the y and z dimensions, thereby inducing errors when periodic boundary conditions are used for the microscopic salt concentration field. However, we expect these errors to be confined to the near–boundary regions. Thus, the y and z averaging performed to compute $D^0(x) = -(\overline{u'_x c'})$ will mitigate the influence thereof.

Note that the cell thickness L_x varies slightly from case to case due to changes in the experimental setup. Though we target $L_x = 800\,\mu\mathrm{m}$ for each experiment, the cell assembly procedure does not guarantee enough precision to use the nominal value of L_x in the MFM procedure. Since the optical measurement and reconstruction procedure allows for measurement of the actual L_x for each experiment, we use the measured L_x value for each applied electric potential, as detailed in Table 4.1.

Additionally, since the cation–selective membrane is not rigid, local pressure fluctuations may induce deformations in its shape. As a result, some points in space may be intermittently occupied by the membrane itself, leading to intermittency in the velocity measurements at those points. We neglect data at points for which velocity measurements are intermittent. Instead, we use linear interpolation between the adjacent boundary (where velocity is zero due to the no–slip condition) and the closest point in the domain that has velocity data available for every point in time.

The MFM procedure must be performed with sufficient spatial resolution to capture thin

Table 4.1: Value of domain length, L_x, for each experimental case. Variation occurs due to imprecision in the cell construction process.

$\Delta\phi$	L_x
0.5347 V	729 µm
0.5572 V	614 µm
0.6343 V	614 µm
1.3341 V	614 µm
2.1051 V	729 µm
2.6134 V	729 µm
3.6780 V	803 µm

Table 4.2: Physical constants used in MFM procedure and in the subsequent simulation of the closed macroscopic equations.

Constant	Species	Value	Source
D_i	Cu^{2+}	$0.714 \times 10^{-9}\,m^2\,s^{-1}$	[198]
	$SO_4{}^{2-}$	$1.065 \times 10^{-9}\,m^2\,s^{-1}$	[198]
z_i	Cu^{2+}	$+2$	-
	$SO_4{}^{2-}$	-2	-
D_A	-	$0.855 \times 10^{-9}\,m^2\,s^{-1}$	-
e	-	$1.602 \times 10^{-19}\,C$	[198]
k_B	-	$1.380 \times 10^{-23}\,J\,K^{-1}$	[198]
T	-	300 K	-
ε_0	-	$8.85 \times 10^{-12}\,F\,m^{-1}$	[198]
ε_r	-	80	[198]

features that develop in the salt concentration field. Thus, each measured velocity field is linearly interpolated onto a staggered mesh with size $84 \times 128 \times 128$. Furthermore, the mesh is nonuniform with exponential refinement near the electrode and membrane interfaces. A standard projection method is used to ensure that the spatially–interpolated velocity fields are divergence–free, such that they obey hydrodynamic mass conservation. Finally, since the time step $\Delta t = 2 \times 10^{-3}\,s$ is smaller than the interval between velocity field measurements, inter–measurement velocity fields are computed using linear interpolation.

Second–order central differences are used in space and a forward–Euler scheme is used to advance in time. The resulting concentration field is used to compute $D^0(x) = -(\overline{u_x' c'})$. Since the initial condition for c is a uniform concentration, early–time results are subject to transient phenomena that may contaminate the eddy diffusivity. We found that 5 s is sufficient for transients to dissipate; only data from after this time are used to compute $D^0(x)$. The values of physical constants used in all simulations are shown in Table 4.2.

The measured eddy diffusivity profiles are shown in Fig. 4.4, where each curve corre-

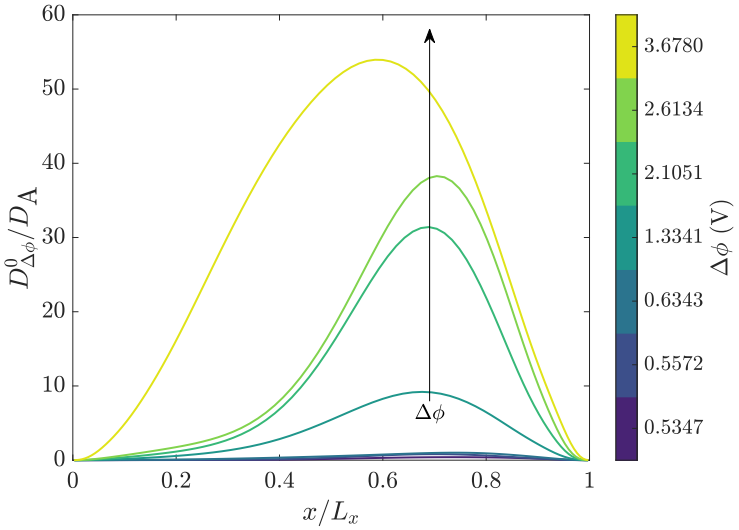

Figure 4.4: Eddy diffusivity profiles for different applied potentials, normalized by the ambipolar diffusivity for copper sulfate. The subscript $\Delta\phi$ in $D^0_{\Delta\phi}(x)$ signifies that each profile is only valid for the specific $\Delta\phi$ value corresponding to the experiment in which velocity fields were measured for that case.

sponds to a single experiment conducted at a fixed mean applied electric potential. The profiles have been normalized by the ambipolar diffusivity, demonstrating that electroconvection may effectively enhance transport by over an order of magnitude in comparison to the diffusion of an electroneutral salt. Larger $\Delta\phi$ values are associated with further enhancements in effective transport. Additionally, the profiles are asymmetric, exhibiting a global maximum that is closer to the cation–selective membrane than the anode. The eddy diffusivity's dependence on $\Delta\phi$ and its spatial asymmetry corroborate the findings of several prior studies demonstrating that stronger advection is present at larger applied electric potentials, and that vortical structures in the flow tend to be concentrated near the ion–selective membrane.

The intuitive connection between scalar mixing and the eddy diffusivity is seen through examination of the instantaneous salt concentration fields in Fig. 4.5. These are not the c fields computed via Eq. (4.15) as part of the MFM procedure. Rather, the unforced fields from simulation of a passive scalar (Eq. (4.10)) are shown in order to exemplify the correspondence between the eddy diffusivity and the unaltered system for which the eddy diffusivity is measured.

Without electroconvection, the instantaneous salt concentration profiles are expected to

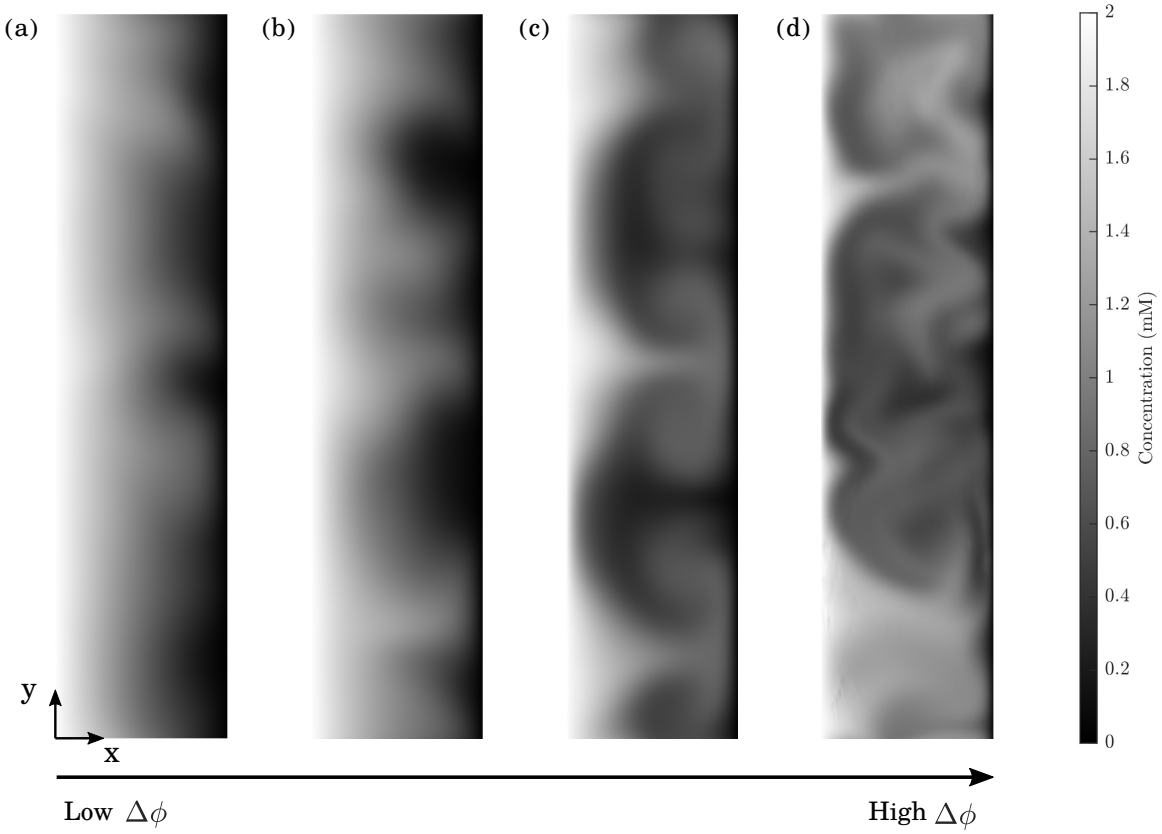

Figure 4.5: Instantaneous salt concentration fields computed via Eq. (4.10) for (a) $\Delta\phi = 0.5347$, (b) $\Delta\phi = 0.6343$, (c) $\Delta\phi = 2.1051$, and (d) $\Delta\phi = 3.6780$. These are not the c fields computed via Eq. (4.15) as part of the MFM procedure. Rather, the unforced fields are shown in order to develop an intuitive connection between the eddy diffusivity and the unaltered system for which the eddy diffusivity is measured.

be purely 1D, varying only in x. All cases shown in Fig. 4.5 contain variations in y (and in z, though not displayed here), which develop when the electrolyte is mixed by advection. Electroconvection first develops at the electrolyte–membrane interface, which occurs at the right side of each panel in Fig. 4.5. As $\Delta\phi$ is increased, the perturbations in the concentration fields become stronger, extending further from the membrane. Figure 4.5(c) in particular exhibits mushroom–like structures, which are indicative of vortical flow penetrating deep into the electrolyte. Additionally, the higher $\Delta\phi$ cases are associated with thinner features in the concentration fields, which are more prone to mixing via molecular diffusion. Thus, the enhancement in mixing captured by the eddy diffusivity may be attributed to both i) the direct stirring of the electrolyte by velocity fields and ii) the subsequent molecular diffusion of thin features that form when the electrolyte is stirred.

As structures in the velocity and concentration fields grow in size, they may be increasingly influenced by confinement due to the anode and its no–slip condition at the left side of the domain. This effect is seen in Fig. 4.5(d), the highest $\Delta\phi$ case. The fine–scale structures in Fig. 4.5(d) signify a flow field that contains multiple vortices with varying sizes. However, the x–extent of the domain is no longer large enough to contain the largest vortices that would be present were the equations solved in a semi–infinite domain. This offers an explanation for the qualitative difference between the eddy diffusivity for the largest $\Delta\phi$ case and for the other profiles in Fig. 4.4.

We refer to the set of profiles shown in Fig. 4.4 as $D^0_{\Delta\phi}(x)$, where the subscript signifies that each profile is only valid at a specific $\Delta\phi$ value corresponding to the experiment in which velocity fields were measured for that case. We now consider one approach to construct an eddy diffusivity profile that will be valid for intermediate values of applied electric potential. We refer to this second notion of eddy diffusivity as $D^0(x, \Delta\phi)$, signifying that it should be a continuous function of the applied electric potential. First, note that all the profiles shown in Fig. 4.4 contain a global maximum. We define $x_{\max}$ as the location of this maximum value for each case. As shown in Fig. 4.6, $x_{\max}$ does not vary significantly from case to case, with the exception of the largest $\Delta\phi$. We display the mean value of $x_{\max}$ with and without the largest $\Delta\phi$ case, since the largest case exhibits a significant qualitative difference from the other cases due to the effects of confinement. The maximum value of $D^0_{\Delta\phi}(x)$ is shown in Fig. 4.6(b). In this work, we compute a linear fit using the least squares method, resulting in $\max(D^0_{\Delta\phi}/D_A) = \alpha\Delta\phi + \gamma$ with $\alpha = 17.82\,\mathrm{V}^{-1}$ and $\gamma = -9.87$.

Note that the critical $\Delta\phi_{\mathrm{cr}}$ for onset of electroconvection occurs when $\alpha\Delta\phi_{\mathrm{cr}} + \gamma = 0$,

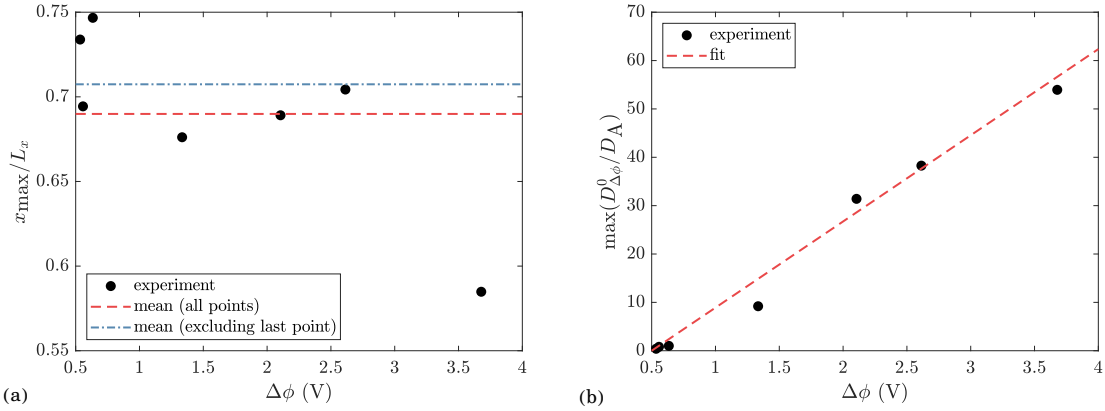

Figure 4.6: Analysis of the shape and the magnitude of the eddy diffusivity profiles measured at different applied electric potentials. (a) $x_{\max}$, the location of the maximum value of $D^0_{\Delta\phi}(x)$. The mean is shown with and without the last point, since the diffusivity profile corresponding to that case is qualitatively different from the other cases due to the effects of confinement. (b) The maximum value of $D^0_{\Delta\phi}(x)$ for different $\Delta\phi$. Also shown is a linear fit based on least–squares regression.

yielding $\Delta\phi_{\text{cr}} = 0.55\,\text{V}$. This prediction agrees well with prior experimental, theoretical, and computational predictions of the critical applied potential for the onset of electroconvection [142, 156, 161]. Furthermore, the linear form chosen here naturally guarantees that $\max(D^0_{\Delta\phi}/D_A)$ is precisely zero for $\Delta\phi = \Delta\phi_{\text{cr}}$ and positive for $\Delta\phi > \Delta\phi_{\text{cr}}$.

Based on the observations in Fig. 4.6, we construct a simple voltage–dependent form for the eddy diffusivity. We begin by attempting to collapse the diffusivity profiles for different applied electric potentials. In Fig. 4.7, we display the results of scaling each diffusivity profile by $\alpha\Delta\phi + \gamma$. The qualitative similarity of the different profiles and tight variation in $x_{\max}$ (for all cases except the largest applied potential) suggest that we may model the scaled diffusivity profiles using a common reference profile. In this work, we simply select $D^0_{\Delta\phi}/(\alpha\Delta\phi + \gamma)$ for the case of $\Delta\phi = 2.6134\,\text{V}$ as the reference profile (shown as a dashed black line in Fig. 4.7, denoted D^0_{ref}). Note that in Fig. 4.6(a), the shape of the profile for this case is such that the location of the maximum ($x_{\max}$) falls closest to the average for all cases excluding the largest $\Delta\phi$.

Thus, we can write an eddy diffusivity with analytically–prescribed dependence on $\Delta\phi$ that is valid for all overlimiting applied potential values. We write

$$D^0\left(x, \Delta\phi\right) = \left(\alpha\Delta\phi + \gamma\right) D^0_{\text{ref}}\left(x\right), \tag{4.38}$$

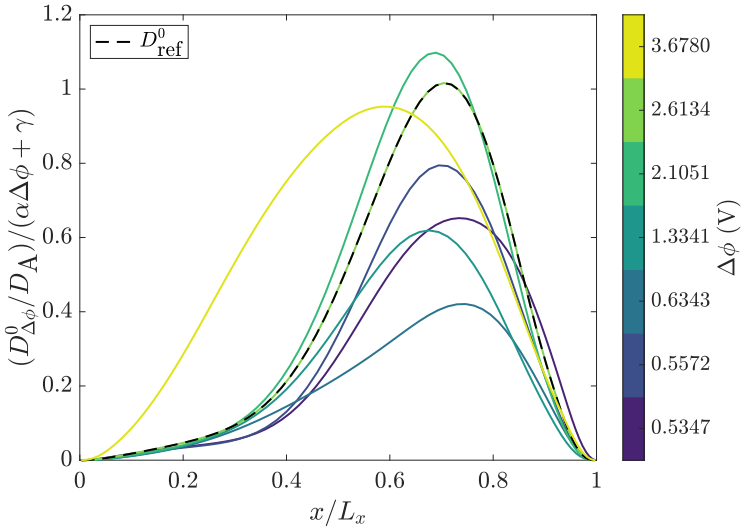

Figure 4.7: Each of the $D^0_{\Delta\phi}$ profiles has been scaled by $\alpha\Delta\phi+\gamma$, where α and γ are found from a linear fit of the maximum of $D^0_{\Delta\phi}$ as a function of $\Delta\phi$. We may construct a voltage–dependent form of the eddy diffusivity by selecting one of these profiles as the reference profile D^0_{ref}, indicated here as black dashed curve.

which is valid for $\Delta\phi \geq \Delta\phi_{\mathrm{cr}}$. No supplementary eddy diffusivity is required for underlimiting and limiting applied electric potentials (i.e., $\Delta\phi < \Delta\phi_{\mathrm{cr}}$).

4.5.2 One Dimensional Simulations with Eddy Diffusivity

Finally, we present a realistic, *'a posteriori'* evaluation of how well the measured 1D eddy diffusivity profiles capture the macroscopic transport effects of chaotic, 3D electroconvection and thereby enable accurate prediction of system performance without expensive 3D DNS. We begin by recapitulating the macroscopic ion transport equations, which we present here in their fully closed form:

$$\frac{\partial \overline{c}_i}{\partial t} = \frac{\partial}{\partial x}\left\{\left[D_i + D^0(x)\right]\frac{\partial \overline{c}_i}{\partial x} + D_i\frac{z_i e}{k_B T}\overline{c}_i\frac{\partial \overline{\phi}}{\partial x}\right\} \tag{4.39}$$

and

$$-\varepsilon_0\varepsilon_r\frac{\partial^2\overline{\phi}}{\partial x^2} = \sum_i e z_i \overline{c}_i. \tag{4.40}$$

Eqs. (4.39) and (4.40) are simply the Reynolds–averaged Poisson-Nernst-Planck equations, in which the advective closure flux is modeled using D^0. We concluded the previous section

with two version of the eddy diffusivity: $D^0_{\Delta\phi}(x)$ is measured exactly at each corresponding $\Delta\phi$ value that was applied in the experiment, while $D^0(x, \Delta\phi)$ is a fitted profile. We asses the performance of each option in turn. Regardless of which form of the eddy diffusivity is used in place of $D^0(x)$ in Eq. (4.39), the additional cost of including $D^0(x)$ in Eqs. (4.39) and (4.40) is negligible, allowing time–to–solution of seconds or minutes on desktop computers.

We now describe the boundary conditions and initial condition for Eqs. (4.39) and (4.40). An electrode is present at $x = 0$, where the no-flux condition is applied for ${SO_4}^{2-}$ and a Dirichlet condition is applied for Cu^{2+}. Meanwhile, the electric potential at the electrode is assigned a reference value of zero:

$$\left[-\left(D_i + D^0\left(x\right)\right)\frac{\partial \overline{c}_i}{\partial x} - D_i \frac{z_i e}{k_B T}\overline{c}_i \frac{\partial \overline{\phi}}{\partial x}\right]_{x=0} = 0 \qquad \text{for } i = {SO_4}^{2-}, \tag{4.41a}$$

$$\overline{c}_i\left(x = 0\right) = c_E \qquad \text{for } i = Cu^{2+}, \tag{4.41b}$$

$$\overline{\phi}\left(x = 0\right) = 0. \tag{4.41c}$$

We use a value of $c_E = 1\,\mathrm{mmol\,L^{-1}}$ in Eq. (4.41). An electric double layer is expected to form at the electrode, in which ${SO_4}^{2-}$ ions accumulate and Cu^{2+} ions are depleted. Though the choice of c_E affects the concentration profiles inside this EDL, we have confirmed that concentration and electric potential profiles outside of the EDL are not affected by the specific choice of c_E, as long as c_E is smaller than the Cu^{2+} concentration just outside the EDL. Examination of Fig. 4.8(a) permits after–the–fact confirmation that our choice of $c_E = 1\,\mathrm{mmol\,L^{-1}}$ satisfies this condition. Additionally, we have confirmed that the influence of variation in c_E on the current–voltage curve is negligible: changing c_E by an order of magnitude leads to 0.2% variation in the simulated current density).

The cation–selective membrane is present at $x = L_x$. A no-flux condition is applied to ${SO_4}^{2-}$ ions, representing perfect co–ion exclusion. Meanwhile, a Dirichlet condition is applied for Cu^{2+} ions and for the electric potential:

$$\left[-\left(D_i + D^0\left(x\right)\right)\frac{\partial \overline{c}_i}{\partial x} - D_i \frac{z_i e}{k_B T}\overline{c}_i \frac{\partial \overline{\phi}}{\partial x}\right]_{x=L_x} = 0 \qquad \text{for } i = {SO_4}^{2-}, \tag{4.42a}$$

$$\overline{c}_i\left(x = L_x\right) = c_M \qquad \text{for } i = Cu^{2+}, \tag{4.42b}$$

$$\overline{\phi}\left(x = L_x\right) = -\Delta\phi. \tag{4.42c}$$

The boundary conditions in Eq. (4.42) are asymptotically valid for a cation–selective membrane, provided c_M is larger than the bulk electrolyte concentration [142]. Dependence on c_M has been shown to be practically non–existent in prior high–fidelity simulations [160]. In this work, we select a value of $c_M = 2\,\mathrm{mmol\,L^{-1}}$.

At $t = 0$ in all simulations, the ion concentration throughout the domain is fixed at

$$\overline{c}_i(t = 0) = 1\,\mathrm{mmol\,L^{-3}}, \tag{4.43}$$

and the electric potential is taken to have a linear profile between the boundary condition values. The simulation is time-advanced until steady-state, and the values of all physical constants used in these simulations can be found in Table 4.2. We use second order central differences in space and a second order implicit scheme in time [161].

We begin by examining results obtained using the measured $D^0_{\Delta\phi}$ profiles. The resulting mean concentration and electric potential profiles are shown in Fig. 4.8. Mean Cu^{2+} concentration is shown as a solid line, while mean ${SO_4}^{2-}$ concentration is shown as a dashed line. In Fig. 4.8(a), a linear profile is seen for lower applied potentials, and an inflection point develops as applied potential is increased and electroconvection becomes stronger. On average, electroconvection helps transport ions from the electrode toward the membrane, as evidenced by the enhanced ion concentration on the right side of the domain and reduced concentrations on the left for larger values of $\Delta\phi$. The cation and anion curves are visibly indistinguishable in Fig. 4.8(a), since the electrolyte is largely electroneutral outside of the thin double layers. We do, indeed, resolve the EDLs, as shown in Fig. 4.8(b). Furthermore, an ESC region is clearly visible here for all cases. The mean electric potential profiles are shown in Fig. 4.8(c) and Fig. 4.8(d), demonstrating that a significant portion of the potential drop occurs in the near–membrane region — in the ESC and EDL layers specifically, which suffer from lower conductivity due to relative ion depletion.

We now wish to determine the extent to which the features described above are a direct consequence of the measured eddy diffusivity profiles. In Fig. 4.9(a), we solve the macroscopic equations (Eqs. (4.39) and (4.40)) without including any kind of eddy diffusivity (i.e., by setting $D^0 = 0$), in order to demonstrate the consequences of neglecting the unclosed fluxes entirely. In the absence of any representation of mixing due to electroconvection, the concentration profiles remain linear in the electroneutral bulk. This behavior is expected based on analysis of Eqs. (4.39) and (4.40) in the limit of quasi–electroneutrality, where the

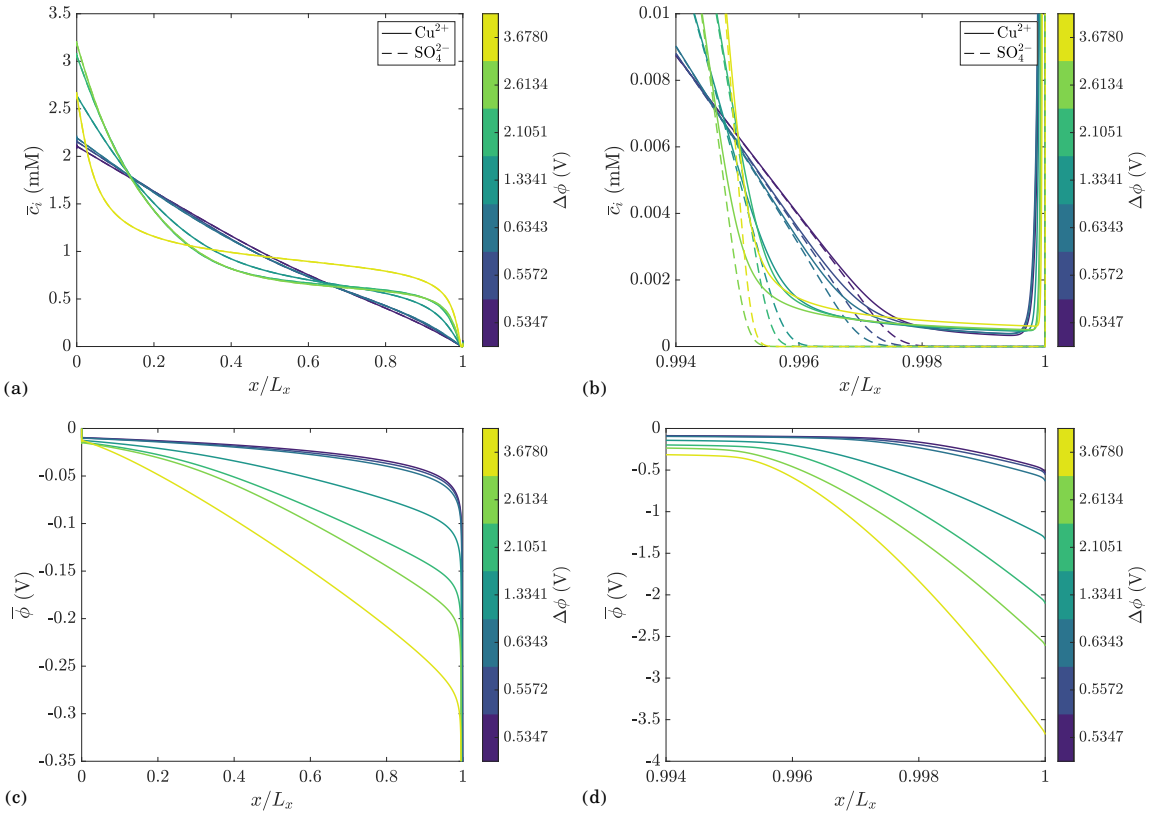

Figure 4.8: Mean concentration and electric potential profiles computed directly from the closed macroscopic equations using $D^0_{\Delta\phi}$. Mean Cu^{2+} concentration is shown as a solid line, while mean ${SO_4}^{2-}$ concentration is shown as a dashed line. Electric potential is shown as a solid line. (a) A view of the entire domain. Due to electroneutrality throughout most of the domain, the two species' concentration curves are indistinguishable. (b) A zoomed–in view of the near–membrane region, highlighting the double layer and extended space charge regions. (c) Electric potential, over the entire domain. (d) Electric potential in the near–membrane region.

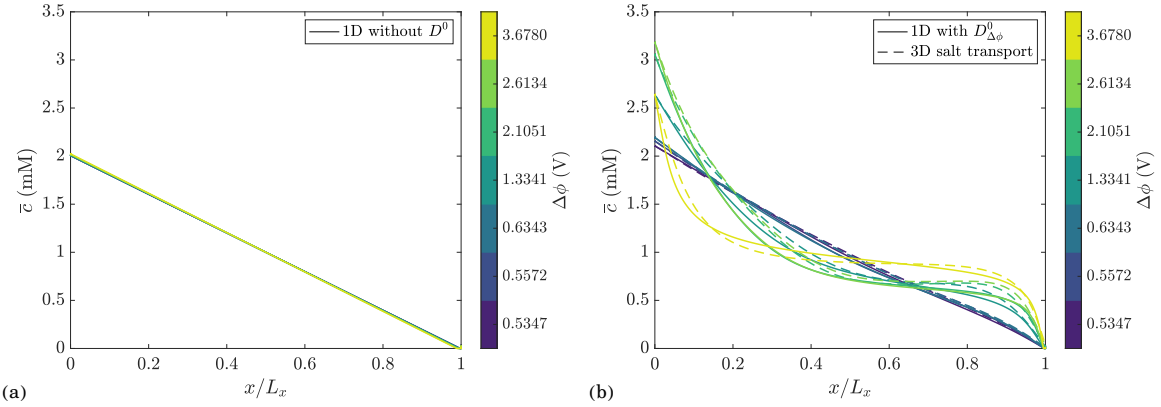

Figure 4.9: (a) Mean electroneutral salt concentration computed using the standard 1D Poisson–Nernst–Planck equations in the absence of D^0. Without the representation of mixing due to microscopic vortices, the profiles remain linear. (b) Mean electroneutral salt concentration computed via two different methods. The direct 1D simulations of Eqs. (4.39) and (4.40) using $D^0_{\Delta\phi}$ are shown as solid curves. The dashed curves are computed via y, z, and t averaging applied to the fields resulting from 3D simulation of Eq. (4.10), in which the measured velocity fields mix the electroneutral salt. Quantitative agreement demonstrates that the leading order eddy diffusivity is capable of capturing the macroscopic transport effects of electroconvection.

method of matched asymptotic expansions may be used to determine an "outer solution" that is valid outside of the EDL and ESC zones [140]. The contrast between Fig. 4.9(a) and Fig. 4.8(a) demonstrates that inclusion of the eddy diffusivity plays a dominant role in the system's dynamics.

In order to assess how accurately the eddy diffusivity serves as a macroscopic representation of microscopic mixing, we may directly compare the mean profiles generated via the macroscopic and microscopic routes. In Fig. 4.9(b), the mean profiles computed directly by solving the macroscopic equations using $D^0_{\Delta\phi}$ are shown as solid curves. Alternatively, we may compute the mean profiles by first solving an equation for instantaneous 3D (microscopic) transport of an electroneutral salt via Eq. (4.10) (as was performed to show the concentration profiles in Fig. 4.5) and then performing averages in y, z, and t. The results of the latter approach are shown as dashed curves in Fig. 4.9(b), exhibiting good agreement with the directly–computed 1D results. Discrepancies between the two approaches can be attributed to the fact that we have only retained the leading order term in Eq. (4.13) for our eddy diffusivity model. As seen, however, the leading order term alone is sufficient to provide accurate mean concentration profiles across a wide range of applied electric potential in the overlimiting regime.

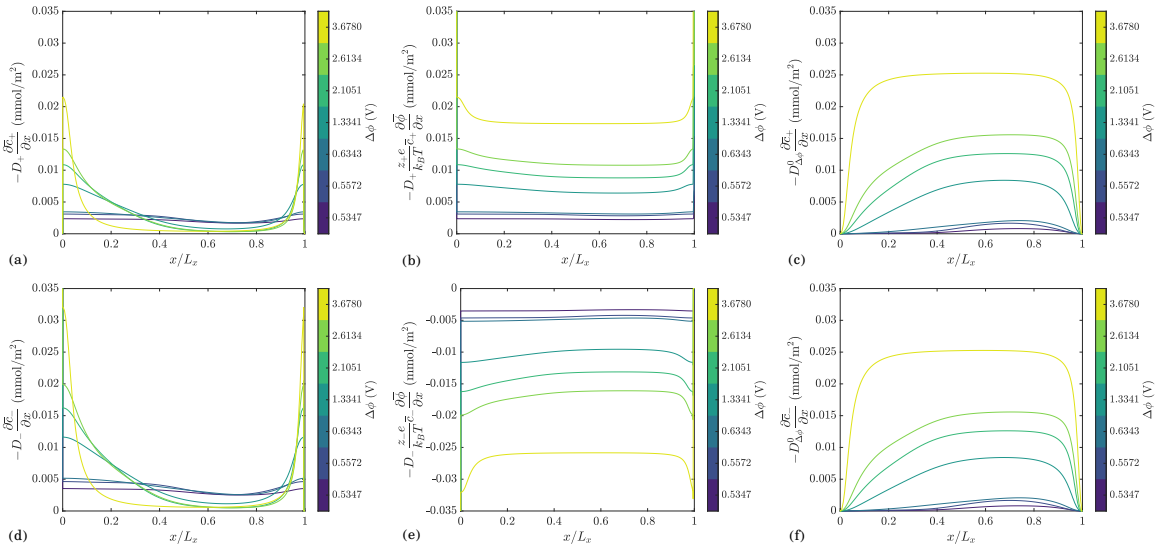

Figure 4.10: Contributions of individual terms to the overall ionic flux in the electroneutral bulk region. (a)–(c) are the diffusion flux, electromigration flux, and advective closure flux respectively for Cu^{2+}. (d)–(f) are the diffusion flux, electromigration flux, and advective closure flux respectively for ${SO_4}^{2-}$. Electromigration and diffusion are the dominant terms throughout most of the electroneutral bulk region at lower applied electric potentials, while electromigration and the advective closure flux are the dominant terms at higher applied electric potentials.

Starting from the macroscopic ionic concentration and electric potential profiles shown in Fig. 4.8, we may build a more detailed understanding of transport by examining the influence of the flux terms in Eq. (4.39), the macroscopic species transport equation. Each term is plotted in Fig. 4.10, where a positive flux corresponds to transport in the positive x direction (i.e., aligned with the electric field). We have verified that a summation of the individual flux terms yields a constant total flux across the entire domain for the cation and zero total flux across the entire domain for the anion, as expected at equilibrium for every case given the boundary conditions in Eqs. (4.41) and (4.42).

At low applied electric potentials, the advective closure flux is negligible while the diffusion and electromigration fluxes are dominant and of similar order to each other. The two dominant fluxes sum together to produce a finite flux for cations, while they cancel out to produce zero–flux for the anions (due to a sign difference in the electromigration term between the cation and the anion). At high applied electric potentials, the diffusion flux is negligible compared to the advective closure and electromigration fluxes, providing additional evidence that the advective closure plays a dominant role in the macroscopic

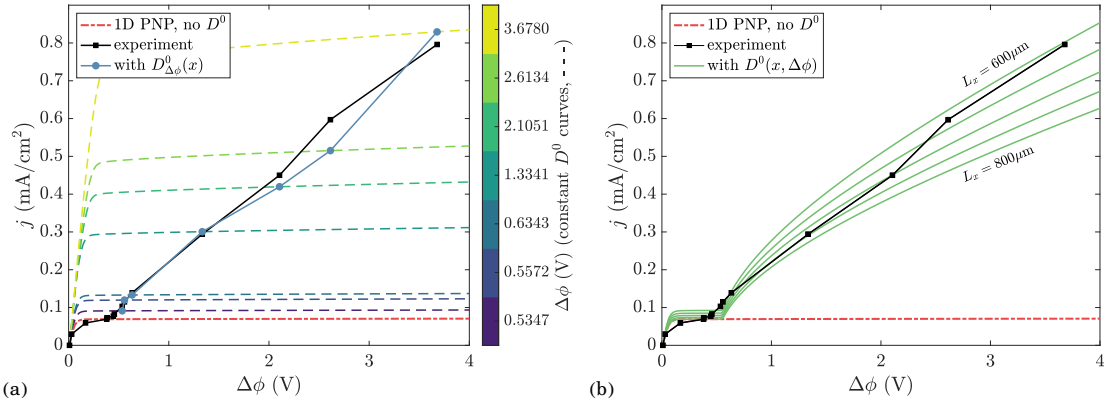

Figure 4.11: Mean current–voltage curves produced using the eddy diffusivity. In both panels, results of the standard 1D Poisson–Nernst–Planck equations are shown as dash–dot red curves, and the experiment points are shown using black squares. (a) The current density computed using each of the directly measured diffusivity profiles $D^0_{\Delta\phi}$ is shown as a blue circle. The dashed curves correspond to j–V sweeps in which the same eddy diffusivity profile was used for the entire range of applied electric potentials. (b) The j–V curves computed using the $\Delta\phi$–dependent diffusivity profiles, $D^0(x, \Delta\phi)$, for a range of L_x values.

physics. The interaction of the dominant fluxes is similar to the previously described case: the dominant fluxes sum to a finite flux for cations and zero–flux for anions.

Next, we compute the mean current density for each $D^0_{\Delta\phi}$ and compare the resulting j–V curve against that measured in experiments. Since Fig. 4.10 indicates that all current is carried by cations, we may write the current density as

$$j = z_+ eF \left[-\left(D_+ + D^0\left(x\right)\right) \frac{\partial \overline{c}_+}{\partial x} - D_i \frac{z_+ e}{k_B T} \overline{c}_+ \frac{\partial \overline{\phi}}{\partial x} \right], \tag{4.44}$$

which may be evaluated at any point in space since the total flux is constant. F is Faraday's constant. The result is shown in Fig. 4.11(a). The standard 1D Poisson–Nernst–Planck equations (dash–dot red curve) compare well to experiments (solid black curve) in the under–limiting and limiting regimes. As soon as electroconvection begins, however, utilization of the eddy diffusivity is necessary and produces remarkable quantitative agreement with the experiments (solid blue curve vs. solid black curve).

The dashed curves in Fig. 4.11(a) are j–V sweeps that were performed with a fixed $D^0_{\Delta\phi}$ profile throughout each sweep, corresponding to the $\Delta\phi$ shown in the colorbar. The dashed curves reveal a broad limiting region for each eddy diffusivity profile, over which variation in applied voltage leads to small changes in the measured current. Therefore, errors in the

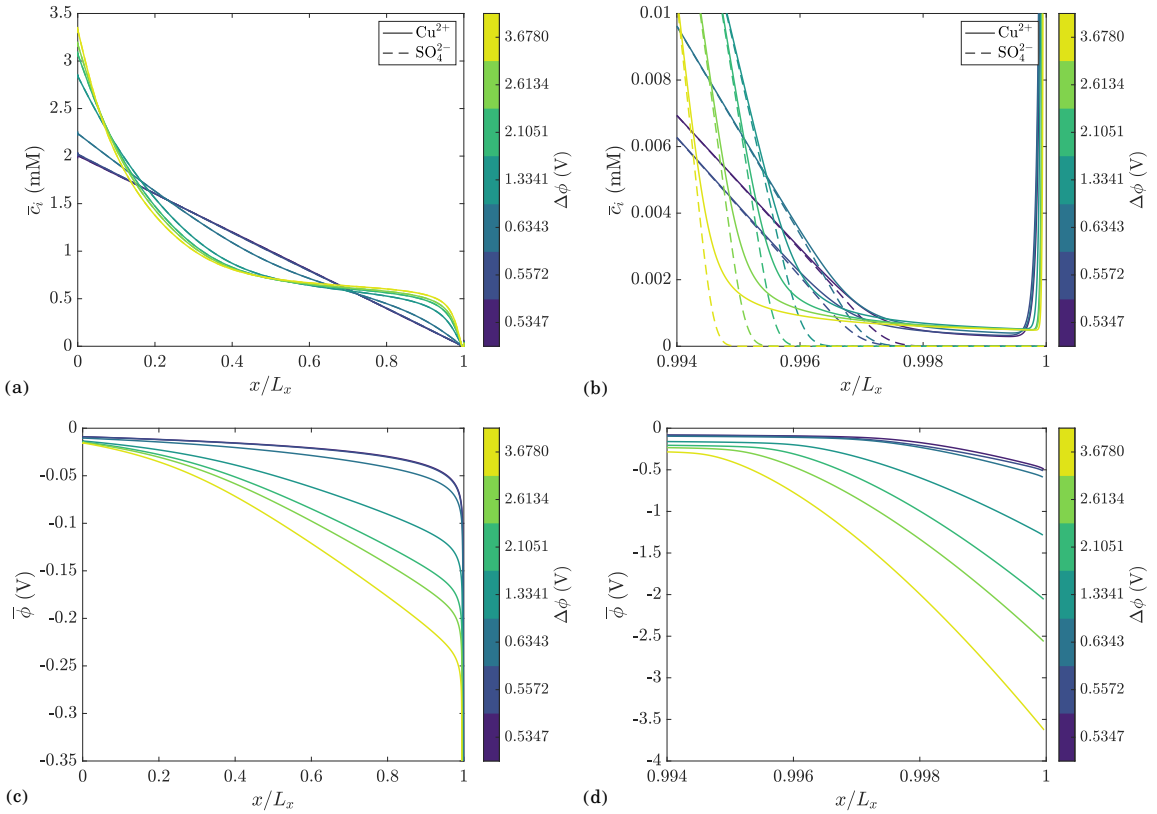

Figure 4.12: Mean concentration and electric potential profiles computed directly from the closed macroscopic equations using $D^0(x, \Delta\phi)$. Mean Cu^{2+} concentration is shown as a solid line, while mean ${SO_4}^{2-}$ concentration is shown as a dashed line. Electric potential is shown as a solid line. (a) A view of the entire domain. Due to electroneutrality throughout most of the domain, the two species' concentration curves are indistinguishable. (b) A zoomed–in view of the near–membrane region, highlighting the double layer and extended space charge regions. (c) Electric potential, over the entire domain. (d) Electric potential in the near–membrane region.

potential–correction procedure described in Section 4.3 are not expected to significantly alter the results. Modification of parameters like β, i_0, or $\rho_{\text{bulk}} L_{\text{bulk}}$ will in turn modify the $\Delta\phi$ that must be used in *a posteriori* simulations, but changes in $\Delta\phi$ ultimately lead to minimal changes in the measured current density.

Next, we demonstrate usage of the semi–analytically–fitted $\Delta\phi$–dependent diffusivity profile given by $D^0(x, \Delta\phi)$ in Eq. (4.38). The macroscopic concentration and electric potential profiles are shown in Fig. 4.12. Recall that the parameter L_x varies from case to case due to imprecision in the experimental setup. Thus, the value of L_x used for each simulation matches the value measured in experiments, as shown in Table 4.1. Generally,

we observe qualitative similarity to the results shown in Fig. 4.8, which were computed using $D^0_{\Delta\phi}$. Closer examination reveals quantitative differences, particularly for the largest value of applied electric potential.

Recall that the diffusivity profile measured for the case of $\Delta\phi = 3.6780\,\mathrm{V}$ bears significant qualitative differences compared to the other cases, as is evident from Figs. 4.4, 4.6 and 4.7. Though the maximum value generally follows the linear trend with respect to $\Delta\phi$, the location of the maximum value is much closer to the center of the domain than in all the other cases. Examination of Fig. 4.5 revealed that this case is affected by confinement, since vortical structures in the flow have grown large enough to interact with the no–slip electrode at $x = 0$.

Because of the way $D^0(x, \Delta\phi)$ is computed (linear extrapolation in $\Delta\phi$ starting at an intermediate value, as shown in Eq. (4.38)), the profile given by $D^0(x, \Delta\phi = 3.6780\,\mathrm{V})$ is not affected by confinement — its shape remains similar to that of the other profiles, with a maximum value that is located closer to the membrane than to the electrode. Furthermore, as a result of the $\Delta\phi$–dependent eddy diffusivity's smooth and monotonic variation in $\Delta\phi$, the macroscopic concentration profiles computed using $D^0(x, \Delta\phi)$ also exhibit smooth, monotonic variation with respect to $\Delta\phi$. This can be seen by comparing Fig. 4.8(a)–(b) to Fig. 4.12(a)–(b), specifically examining the concentration profile for the largest applied electric potential.

We note, however, that results generated using $D^0(x, \Delta\phi)$ may not be accurate for the largest value of $\Delta\phi$, precisely because they do not account for confinement. Confinement is expected to occur and must be accounted for once coherent structures associated with the velocity field are large enough to interact with the no–slip boundary condition at the electrode. The large qualitative difference in the measured diffusivity profile for the largest applied electric potential is the measured effect of confinement at the electrode, which leads to a differently–shaped diffusivity profile and invalidates usage of $D^0(x, \Delta\phi)$. For intermediate $\Delta\phi$ values, on the other hand, $D^0(x, \Delta\phi)$ is still expected to produce accurate results.

Finally, we will proceed to discussion of j–V curves that are produced using this form of the eddy diffusivity. The main benefit of using $D^0(x, \Delta\phi)$ in place of $D^0_{\Delta\phi}$ is the ability to produce j–V curves that are smooth functions of the applied electric potential. Recall that comparison with the experiments is complicated by the presence of experimental errors, since the parameter L_x varies from case to case due to imprecision in the experimental setup.

In order to allow a reasonable comparison, we consider a range of L_x values between 600 µm and 800 µm. One j–V curve is produced for each choice of L_x, as shown in Fig. 4.11(b), exhibiting good agreement between the model and experiments. The j–V curves produced using $D^0(x, \Delta\phi)$ exhibit a noticeable downward–concavity for all choices of L_x, particularly for low–overlimiting applied potentials. The curves gradually approach linear behavior at larger $\Delta\phi$ values. This result is qualitatively similar to Druzgalski and co–authors' DNS of chaotic electroconvection [161], though quantitative agreement is prohibited by differences in the values of non–dimensional parameters between the two works (particularly since the ions in this work are divalent).

4.6 Concluding Remarks

The motivation for this work lay in the observation that mean concentration and electric potential fields are sufficient to determine the power usage and ion exchange rate for the practical design of systems that exhibit electroconvection, despite the presence of chaotic spatiotemporal fluctuations at much smaller scales. We utilized this observation as the guiding principle for our model reduction approach, but the application of Reynolds–averaging to the microscopic equations leads to a closure problem that must be addressed before the macroscopic system can be solved. The MFM procedure allowed us to develop a leading order representation of the dominant unclosed flux, revealing a simple gradient–diffusion operator. Furthermore, we measured the corresponding eddy diffusivity from experiments by inserting experimental velocity fields into the MFM procedure, circumventing the need for prohibitively expensive DNS–derived velocity fields. We found that 1D simulations using the measured eddy diffusivity produce current–voltage curves that agree quantitatively with experiments.

There are three limitations of this work that are worth briefly discussing. First, the utilization of averaging as an avenue for model–reduction leads to strong dependence on the geometry of the cell in which electroconvection occurs. For example, in a simple planar geometry operating in a stationary state, a 1D and steady representation is wholly appropriate. However, membrane heterogeneity in the y and z directions (an area of recent interest [165–168, 183]) would complicate the reduction of those dimensions. Consider the worst–case scenario, in which some electrochemical system lacks homogeneity in all three spatial dimensions and is operating in an unsteady (i.e. pulsed, for example) fashion. In

this case, only ensemble averaging may be performed. Though the number of dimensions has not been reduced, the solution may be represented more coarsely in time and space since ensemble averaging will still eliminate fine–scale structures. Ultimately, however, the eddy diffusivity computed using our method is still geometrically contingent on the original problem setup. Future researchers who seek to develop a standalone reduced order model for electroconvection may use our diffusivity profiles as a benchmark for their work.

Second, though there were two unclosed terms in Eq. (4.8), we only developed a closure model for the dominant term while neglecting the other. Our results indicate that this approach is sufficient to achieve quantitative agreement with the experiments. Nonetheless, the determination of a closure model for the lesser of the unclosed terms in Eq. (4.8) may be worthy of additional consideration in some circumstances. As was the case for the error induced by working with the electroneutral salt transport equation instead of individual ionic transport equations, we expect the error due to neglecting the second unclosed term to be dependent on the Debye length. As such, these effects may become important in situations where the double layers are relatively thick and regions featuring strong advection also exhibit appreciable non–electroneutrality.

Third, recall that the utilization of experimental velocity fields is central to this work. Though the incorporation of experimental data into a largely computational technique allowed us to bypass expensive DNS of the full Poisson–Nernst–Planck–Stokes equations, the purely computational approach would be free of the sources of error in experiments — *e.g.*, variation of the domain size from case to case and deformation of the membrane during each experiment. Thus, a purely computational approach may allow for a more precise determination of the correct reference diffusivity profile D^0_{ref} for use in $D^0(x, \Delta\phi)$. Additionally, while we have used a simple linear fit to describe how the magnitude of the eddy diffusivity varies with the applied electric potential, performing the purely computational MFM procedure for a large number of $\Delta\phi$ values may reveal a more complicated relationship.

The physical insight demonstrated in this work — namely, a quantitative demonstration that the macroscopic effects of microscopic mixing may be represented as an effective diffusion process — brings new insight to the study of electroconvection, since such an approach has not been used before to develop a reduced order model in this field. We've also demonstrated a methodological innovation, wherein components of a chiefly computational procedure were replaced with data from experiments, allowing us to directly measure the closure operator associated with experimental velocity fields. Such a technique may be

applied to other geometries in which electroconvection occurs, and to problems other than electroconvection, in which a macroscopic representation of mixing due to chaotic, fine–scale velocity fields is desired.

THIS PAGE DELIBERATELY LEFT BLANK

Chapter 5

Conclusion

This dissertation commenced with a brief analysis of its title. Returning to this line of thought, we conclude by summarizing aspects of the analysis that are pertinent to each of the technical chapters while identifying key areas for impactful follow–up studies.

In Chapter 2, we investigated the coupled effects of transport, electrosorption, redox reactions, and acid/base surface chemistry in practical FTE CDI cells. Our model can be thought of as *macroscopic* in its treatment of the hierarchically–porous electrodes. Though it is possible to write a continuum–scale model at the pore scale, resolving transport within the pores and reactions at the pore walls, we make use of porous electrode theory and assume quasi–steady Donnan equilibrium between macropores and micropores, allowing us to write continuum equations at scales much larger than the pore size. As a result, we are able to perform simulations of the entire FTE CDI cell over multiple cycles, revealing the presence of substantial spatial and temporal inhomogeneity in the physicochemical dynamics governing electrode degradation.

The natural next step for this project is formal validation of the model against experimental data. Qualitative agreement with experimental results is apparent in the data presented here, but the model we propose holds the potential to quantitatively predict the performance of real–world FTE CDI cells. After validation, our model and solver serve as powerful tools for the optimization of CDI technology, permitting low–cost exploration of the large parameter space associated with FTE CDI cells. For example, one may explore the impact of differences in the driving voltage or current signal, ionic species with different valence or ionic radius, and variation of critical geometric parameters for each electrode.

Additionally, the same modeling philosophy may be extended to two–dimensional simulations of the flow–by CDI geometry, permitting direct comparison of the degradation process for the two cases. It is our hope that systematic investigation of the broad parameter space enables performance and longevity improvement for future CDI technology.

In Chapter 3, we focused on understanding the transport of ions, gases, and electrons in low-temperature CO_2 electrocatalysts with intermixed hydrophobic and hydrophilic regions. We developed a medium–fidelity model for the multi–scale and multi–phase physicochemical processes occurring in such catalysts, retaining the most essential physicochemical features while neglecting higher order effects that would have substantially increased the complexity of the model and numerical solver. We made use of scaling arguments to select different numerical methods for different spatial dimensions, permitting construction of a solver that makes use of parallelization and iterative coupling of the governing equations to reduce cost. We investigated both direct CO_2 reduction and CO reduction, finding qualitative agreement with experimental results and exploring the influence of several parameters associated with the catalyst.

We hypothesize that additional experimental characterization of the catalysts may enable more precise selection of parameter values, enabling closer agreement between simulations and experiments. Additionally, the validation exercise that was performed for the case of CO reduction may be improved and repeated for the case of CO_2 reduction. We demonstrated that the efficiency of our model and solver enables low–cost exploration of a large parameter space. Thus, the solver may be efficient enough for utilization as part of an optimization algorithm, which will explore the parameter space more systematically and determine optimal operating conditions. Additionally, our cathode model and simulation may be coupled to a larger simulation of the entire cell, allowing for analysis of the impacts that catalyst design may have on bulk pH and anode kinetics. Continued effort in this direction may be broadly applicable to a variety of electrosynthesis systems.

Finally, in Chapter 4, we formulated a closure model for chaotic electroconvection governed by the Reynolds–averaged Poisson–Nernst–Planck–Stokes equations, and used the MFM to measure the eddy diffusivity associated with mixing by vortices in the flow. Here, we circumvented the need for expensive forced DNS simulations by making use of experimentally measured velocity fields. After measuring the eddy diffusivity from these fields, we found that direct computation of the Reynolds–averaged fields using the eddy diffusivity is sufficient to predict the current–voltage curve with remarkable accuracy while saving

substantial computational cost compared to high–fidelity simulations.

The reduced–order model proposed in this chapter is strongly dependent on the problem geometry, since spatial averaging in homogeneous directions is used as the bridge between *microscopic* and *macroscopic* descriptions. However, the results presented in this work may serve as a baseline for the development of stand–alone models for use in different geometries. Additionally, repeating this work using forced DNS as part of the classical MFM procedure would offer a useful point of comparison between the hybrid experimental–computational approach and the purely computational one.

The results presented in each of the three technical chapters of this dissertation represent substantial, original contributions to the body of research. Interestingly, each contribution also opens new avenues toward continued improvement in our understanding of reaction and transport processes in emerging electrochemical technologies.

THIS PAGE DELIBERATELY LEFT BLANK

References

1. Balaji–Wright, A. *et al.* "Understanding degradation of capacitive deionization cells: Full–cell simulations with anode corrosion". *Desalination* **587,** 117924 (2024).
2. Disselkoen, K. R. *Continuum modeling to understand and optimize CO2 and CO reduction gas diffusion electrodes.* PhD thesis (Stanford University, 2023).
3. Balaji–Wright, A., Stockmeier, F., Dunkel, R., Wessling, M. & Mani, A. "Measurement of an eddy diffusivity for chaotic electroconvection using combined computational and experimental techniques". *Physical Review Fluids* **9,** 023701 (2024).
4. Schewe, J. *et al.* "Multimodel assessment of water scarcity under climate change". *Proceedings of the National Academy of Sciences of the United States of America* **111,** 3245–3250 (2014).
5. Famiglietti, J. S. "The global groundwater crisis". *Nature Climate Change* **4,** 945–948 (2014).
6. Urban, J. J. "Emerging Scientific and Engineering Opportunities within the Water-Energy Nexus". *Joule* **1,** 665–688 (2017).
7. Zimmerman, J. B., Mihelcic, J. R. & Smith, J. "Global Stressors on Water Quality and Quantity". *Environmental Science & Technology* **42,** 4247–4254 (2008).
8. Montgomery, M. A. & Elimelech, M. "Water And Sanitation in Developing Countries: Including Health in the Equation". *Environmental Science & Technology* **41,** 17–24 (2007).
9. Shannon, M. A. *et al.* "Science and technology for water purification in the coming decades". *Nature* **452,** 301–310 (2008).

10. Anderson, M. A., Cudero, A. L. & Palma, J. "Capacitive deionization as an electrochemical means of saving energy and delivering clean water. Comparison to present desalination practices: Will it compete?" *Electrochimica Acta* **55,** 3845–3856 (2010).

11. Oren, Y. "Capacitive deionization (CDI) for desalination and water treatment - past, present and future (a review)". *Desalination* **228,** 10–29 (2008).

12. Porada, S., Zhao, R., Van Der Wal, A., Presser, V. & Biesheuvel, P. M. "Review on the science and technology of water desalination by capacitive deionization". *Progress in Materials Science* **58,** 1388–1442 (2013).

13. Suss, M. E. *et al.* "Water desalination via capacitive deionization: What is it and what can we expect from it?" *Energy and Environmental Science* **8,** 2296–2319 (2015).

14. Folaranmi, G., Bechelany, M., Sistat, P., Cretin, M. & Zaviska, F. "Towards Electrochemical Water Desalination Techniques: A Review on Capacitive Deionization, Membrane Capacitive Deionization and Flow Capacitive Deionization". *Membranes* **10,** 96 (2020).

15. Tang, W. *et al.* "Various cell architectures of capacitive deionization: Recent advances and future trends". *Water Research* **150,** 225–251 (2019).

16. Zhao, X., Wei, H., Zhao, H., Wang, Y. & Tang, N. "Electrode materials for capacitive deionization: A review". *Journal of Electroanalytical Chemistry* **873,** 114416 (2020).

17. Tauk, M. *et al.* "Recent advances in capacitive deionization: A comprehensive review on electrode materials". *Journal of Environmental Chemical Engineering* **11,** 111368 (2023).

18. Blair, J. W. & Murphy, G. W. in *Saline Water Conversion* 206–223 (American Chemical Society Applied Publications, 1960).

19. Johnson, A. M. & Newman, J. "Desalting by Means of Porous Carbon Electrodes". *Journal of The Electrochemical Society* **118,** 510–517 (1971).

20. Lee, J.-B., Park, K.-K., Eum, H.-M. & Lee, C.-W. "Desalination of a thermal power plant wastewater by membrane capacitive deionization". *Desalination* **196,** 125–134 (2006).

21. Lee, J., Kim, S., Kim, C. & Yoon, J. "Hybrid capacitive deionization to enhance the desalination performance of capacitive techniques". *Energy and Environmental Science* **7,** 3683–3689 (2014).

22. Smith, K. C. & Dmello, R. "Na-Ion Desalination (NID) Enabled by Na-Blocking Membranes and Symmetric Na-Intercalation: Porous-Electrode Modeling". *Journal of The Electrochemical Society* **163,** A530–A539 (2016).

23. Jeon, S.-i. *et al.* "Desalination via a new membrane capacitive deionization process utilizing flow-electrodes". *Energy and Environmental Science.* **6,** 1471–1475 (2013).

24. Guyes, E. N., Simanovski, A. & Suss, M. E. "Several orders of magnitude increase in the hydraulic permeability of flow-through capacitive deionization electrodes via laser perforations". *RSC Advances* **7,** 21308–21313 (2017).

25. Hawks, S. A. *et al.* "Quantifying the flow efficiency in constant-current capacitive deionization". *Water Research* **129,** 327–336 (2018).

26. Hawks, S. A. *et al.* "Performance metrics for the objective assessment of capacitive deionization systems". *Water Research* **152,** 126–137 (2019).

27. Choi, J., Dorji, P., Shon, H. K. & Hong, S. "Applications of capacitive deionization: Desalination, softening, selective removal, and energy efficiency". *Desalination* **449,** 118–130 (2019).

28. Gamaethiralalage, J. G. *et al.* "Recent advances in ion selectivity with capacitive deionization". *Energy and Environmental Science* **14,** 1095–1120 (2021).

29. Lado, J. J. *et al.* "Removal of nitrate by asymmetric capacitive deionization". *Separation and Purification Technology* **183,** 145–152 (2017).

30. Oyarzun, D. I., Hemmatifar, A., Palko, J. W., Stadermann, M. & Santiago, J. G. "Ion selectivity in capacitive deionization with functionalized electrode: Theory and experimental validation". *Water Research X* **1,** 100008 (2018).

31. Guyes, E. N., Malka, T. & Suss, M. E. "Enhancing the ion-size-based selectivity of capacitive deionization electrodes". *Environmental Science and Technology* **53,** 8447–8454 (2019).

32. Guyes, E. N., Shocron, A. N., Chen, Y., Diesendruck, C. E. & Suss, M. E. "Long-lasting, monovalent-selective capacitive deionization electrodes". *npj Clean Water* **4** (2021).

33. Uwayid, R. *et al.* "Perfect divalent cation selectivity with capacitive deionization". *Water Research* **210,** 117959 (2022).

34. Eliad, L., Salitra, G., Soffer, A. & Aurbach, D. "Ion Sieving Effects in the Electrical Double Layer of Porous Carbon Electrodes: Estimating Effective Ion Size in Electrolytic Solutions". *The Journal of Physical Chemistry B* **105,** 6880–6887 (2001).

35. Avraham, E., Yaniv, B., Soffer, A. & Aurbach, D. "Developing Ion Electroadsorption Stereoselectivity, by Pore Size Adjustment with Chemical Vapor Deposition onto Active Carbon Fiber Electrodes. Case of Ca2+/Na+ Separation in Water Capacitive Desalination". *The Journal of Physical Chemistry C* **112,** 7385–7389 (2008).

36. Hou, C. H. & Huang, C. Y. "A comparative study of electrosorption selectivity of ions by activated carbon electrodes in capacitive deionization". *Desalination* **314,** 124–129 (2013).

37. Han, L., Karthikeyan, K. G., Anderson, M. A. & Gregory, K. B. "Exploring the impact of pore size distribution on the performance of carbon electrodes for capacitive deionization". *Journal of Colloid and Interface Science* **430,** 93–99 (2014).

38. Tang, W., Kovalsky, P., Cao, B., He, D. & Waite, T. D. "Fluoride Removal from Brackish Groundwaters by Constant Current Capacitive Deionization (CDI)". *Environmental Science and Technology* **50,** 10570–10579 (2016).

39. Suss, M. E. "Size-Based Ion Selectivity of Micropore Electric Double Layers in Capacitive Deionization Electrodes". *Journal of The Electrochemical Society* **164,** E270–E275 (2017).

40. Wang, L. & Lin, S. "Mechanism of Selective Ion Removal in Membrane Capacitive Deionization for Water Softening". *Environmental Science and Technology* **53,** 5797–5804 (2019).

41. He, D., Wong, C. E., Tang, W., Kovalsky, P. & David Waite, T. "Faradaic Reactions in Water Desalination by Batch-Mode Capacitive Deionization". *Environmental Science and Technology Letters* **3,** 222–226 (2016).

42. Holubowitch, N., Omosebi, A., Gao, X., Landon, J. & Liu, K. "Quasi–Steady–State Polarization Reveals the Interplay of Capacitive and Faradaic Processes in Capacitive Deionization". *ChemElectroChem* **4,** 2404–2413 (2017).

43. Tang, W., He, D., Zhang, C., Kovalsky, P. & Waite, T. D. "Comparison of Faradaic reactions in capacitive deionization (CDI) and membrane capacitive deionization (MCDI) water treatment processes". *Water Research* **120,** 229–237 (2017).

44. Dykstra, J. E., Keesman, K. J., Biesheuvel, P. M. & van der Wal, A. "Theory of pH changes in water desalination by capacitive deionization". *Water Research* **119,** 178–186 (2017).

45. Yu, J., Jo, K., Kim, T., Lee, J. & Yoon, J. "Temporal and spatial distribution of pH in flow-mode capacitive deionization and membrane capacitive deionization". *Desalination* **439,** 188–195 (2018).

46. Landon, J., Gao, X., Omosebi, A. & Liu, K. "Emerging investigator series: local pH effects on carbon oxidation in capacitive deionization architectures". *Environmental Science: Water Research and Technology.* **7,** 861–869 (2021).

47. Shocron, A. N. *et al.* "Electrochemical removal of amphoteric ions". *Proceedings of the National Academy of Sciences of the United States of America* **118,** e2108240118 (2021).

48. Kang, J. S. *et al.* "Surface Electrochemistry of Carbon Electrodes and Faradaic Reactions in Capacitive Deionization". *Environmental Science and Technology* **56,** 12602–12612 (2022).

49. Avraham, E., Bouhadana, Y., Soffer, A. & Aurbach, D. "Limitation of Charge Efficiency in Capacitive Deionization". *Journal of The Electrochemical Society* **156,** P95 (2009).

50. Avraham, E., Noked, M., Bouhadana, Y., Soffer, A. & Aurbach, D. "Limitations of Charge Efficiency in Capacitive Deionization". *Journal of The Electrochemical Society* **156,** P157 (2009).

51. Cohen, I., Avraham, E., Noked, M., Soffer, A. & Aurbach, D. "Enhanced charge efficiency in capacitive deionization achieved by surface-treated electrodes and by means of a third electrode". *Journal of Physical Chemistry C* **115,** 19856–19863 (2011).

52. Suss, M. E. *et al.* "Capacitive desalination with flow-through electrodes". *Energy and Environmental Science* **5,** 9511–9519 (2012).

53. Remillard, E. M., Shocron, A. N., Rahill, J., Suss, M. E. & Vecitis, C. D. "A direct comparison of flow-by and flow-through capacitive deionization". *Desalination* **444,** 169–177 (2018).

54. Zhang, C., He, D., Ma, J., Tang, W. & Waite, T. D. "Faradaic reactions in capacitive deionization (CDI) - problems and possibilities: A review". *Water Research* **128,** 314–330 (2018).

55. Bouhadana, Y. *et al.* "Capacitive Deionization of NaCl Solutions at Non-Steady-State Conditions: Inversion Functionality of the Carbon Electrodes". *The Journal of Physical Chemistry C* **115,** 16567–16573 (2011).

56. Cohen, I., Avraham, E., Bouhadana, Y., Soffer, A. & Aurbach, D. "Long term stability of capacitive de-ionization processes for water desalination: The challenge of positive electrodes corrosion". *Electrochimica Acta* **106,** 91–100 (2013).

57. Cohen, I., Avraham, E., Bouhadana, Y., Soffer, A. & Aurbach, D. "The effect of the flow-regime, reversal of polarization, and oxygen on the long term stability in capacitive de-ionization processes". *Electrochimica Acta* **153,** 106–114 (2015).

58. Bayram, E. & Ayranci, E. "A systematic study on the changes in properties of an activated carbon cloth upon polarization". *Electrochimica Acta* **56,** 2184–2189 (2011).

59. Avraham, E., Noked, M., Bouhadana, Y., Soffer, A. & Aurbach, D. "Limitations of charge efficiency in capacitive deionization processes III: The behavior of surface oxidized activated carbon electrodes". *Electrochimica Acta* **56,** 441–447 (2010).

60. Chen, Z. *et al.* "Effects of ageing and incorporation of ion-exchange membrane on the electrosorption performance of activated carbon based electrodes modules". *Desalination and Water Treatment* **51,** 3489–3496 (2013).

61. Gao, X., Omosebi, A., Landon, J. & Liu, K. "Surface charge enhanced carbon electrodes for stable and efficient capacitive deionization using inverted adsorption-desorption behavior". *Energy and Environmental Science* **8,** 897–909 (2015).

62. Gao, X., Omosebi, A., Holubowitch, N., Landon, J. & Liu, K. "Capacitive Deionization Using Alternating Polarization: Effect of Surface Charge on Salt Removal". *Electrochimica Acta* **233,** 249–255 (2017).

63. Lu, D., Cai, W. & Wang, Y. "Optimization of the voltage window for long-term capacitive deionization stability". *Desalination* **424,** 53–61 (2017).

64. De Levie, R. "On porous electrodes in electrolyte solutions: I. Capacitance effects". *Electrochimica Acta* **9,** 1231–1245 (1963).

65. De Levie, R. "On porous electrodes in electrolyte solutions-IV". *Electrochimica Acta* **9,** 1231–1245 (1964).

66. Suss, M. E. *et al.* "Impedance-based study of capacitive porous carbon electrodes with hierarchical and bimodal porosity". *Journal of Power Sources* **241,** 266–273 (2013).

67. Qu, Y., Baumann, T. F., Santiago, J. G. & Stadermann, M. "Characterization of Resistances of a Capacitive Deionization System". *Environmental Science & Technology* **49,** 9699–9706 (2015).

68. Kuo, H. A. *et al.* "Understanding resistances in capacitive deionization devices". *Environmental Science: Water Research and Technology* **6,** 1842–1854 (2020).

69. Biesheuvel, P. M. & Bazant, M. Z. "Nonlinear dynamics of capacitive charging and desalination by porous electrodes". *Physical Review E - Statistical, Nonlinear, and Soft Matter Physics* **81,** 1–12 (2010).

70. Zhao, R., Biesheuvel, P., Miedema, H., Bruning, H. & van der Wal, A. "Charge Efficiency: A Functional Tool to Probe the Double-Layer Structure Inside of Porous Electrodes and Application in the Modeling of Capacitive Deionization". *The Journal of Physical Chemistry Letters* **1,** 205–210 (2010).

71. Biesheuvel, P. M., Fu, Y. & Bazant, M. Z. "Diffuse charge and Faradaic reactions in porous electrodes". *Physical Review E - Statistical, Nonlinear, and Soft Matter Physics* **83** (2011).

72. Biesheuvel, P. M., Zhao, R., Porada, S. & van der Wal, A. "Theory of membrane capacitive deionization including the effect of the electrode pore space". *Journal of Colloid and Interface Science* **360,** 239–248 (2011).

73. Porada, S., Bryjak, M., Van Der Wal, A. & Biesheuvel, P. M. "Effect of electrode thickness variation on operation of capacitive deionization". *Electrochimica Acta* **75,** 148–156 (2012).

74. Zhao, R. *et al.* "Time-dependent ion selectivity in capacitive charging of porous electrodes". *Journal of Colloid and Interface Science* **384,** 38–44 (2012).

75. Biesheuvel, P. M., Fu, Y. & Bazant, M. Z. "Electrochemistry and capacitive charging of porous electrodes in asymmetric multicomponent electrolytes". *Russian Journal of Electrochemistry* **48,** 580–592 (2012).

76. Biesheuvel, P. M., Hamelers, H. V. & Suss, M. E. "Theory of Water Desalination by Porous Electrodes with Immobile Chemical Charge". *Colloids and Interface Science Communications* **9,** 1–5 (2015).

77. Hemmatifar, A. *et al.* "Equilibria model for pH variations and ion adsorption in capacitive deionization electrodes". *Water Research* **122,** 387–397 (2017).

78. He, F., Biesheuvel, P., Bazant, M. Z. & Hatton, T. A. "Theory of water treatment by capacitive deionization with redox active porous electrodes". *Water Research* **132,** 282–291 (2018).

79. Guyes, E. N., Shocron, A. N., Simanovski, A., Biesheuvel, P. M. & Suss, M. E. "A one-dimensional model for water desalination by flow-through electrode capacitive deionization". *Desalination* **415,** 8–13 (2017).

80. Biesheuvel, P. M., Porada, S., Levi, M. & Bazant, M. Z. "Attractive forces in microporous carbon electrodes for capacitive deionization". *Journal of Solid State Electrochemistry* **18,** 1365–1376 (2014).

81. Kim, T. *et al.* "Enhanced charge efficiency and reduced energy use in capacitive deionization by increasing the discharge voltage". *Journal of Colloid and Interface Science* **446,** 317–326 (2015).

82. Biesheuvel, P. M., van Soestbergen, M. & Bazant, M. Z. "Imposed currents in galvanic cells". *Electrochimica Acta* **54,** 4857–4871 (2009).

83. Alfisi, D., Shocron, A. N., Gloukhovski, R., Vermaas, D. A. & Suss, M. E. "Resistance Breakdown of a Membraneless Hydrogen-Bromine Redox Flow Battery". *ACS Sustainable Chemistry and Engineering* **10,** 12985–12992 (2022).

84. Huang, J. & Zhang, J. "Theory of Impedance Response of Porous Electrodes: Simplifications, Inhomogeneities, Non-Stationarities and Applications". *Journal of The Electrochemical Society* **163,** A1983–A2000 (2016).

85. Algurainy, Y. & Call, D. F. "Improving Long-Term Anode Stability in Capacitive Deionization Using Asymmetric Electrode Mass Ratios". *ACS ES&T Engineering* **2,** 129–139 (2022).

86. Lado, J. J., Pérez-Roa, R. E., Wouters, J. J., Isabel Tejedor-Tejedor, M. & Anderson, M. A. "Evaluation of operational parameters for a capacitive deionization reactor employing asymmetric electrodes". *Separation and Purification Technology* **133,** 236–245 (2014).

87. Schiffer, Z. J. & Manthiram, K. "Electrification and Decarbonization of the Chemical Industry". *Joule* **1,** 10–14 (2017).

88. Yan, Z. *et al.* "Renewable electricity storage using electrolysis". *Proceedings of the National Academy of Sciences of the United States of America* **117,** 12558–12563 (2020).

89. De Luna, P. *et al.* "What would it take for renewably powered electrosynthesis to displace petrochemical processes?" *Science* **364,** eaav3506 (2019).

90. Bui, J. C. *et al.* "Continuum Modeling of Porous Electrodes for Electrochemical Synthesis". *Chemical Reviews* **122,** 11022–11084 (2022).

91. Pan, F. & Yang, Y. "Designing CO2 reduction electrode materials by morphology and interface engineering". *Energy and Environmental Science.* **13,** 2275–2309 (2020).

92. Bui, J. C. *et al.* "Engineering Catalyst–Electrolyte Microenvironments to Optimize the Activity and Selectivity for the Electrochemical Reduction of CO2 on Cu and Ag". *Accounts of Chemical Research* **55,** 484–494 (2022).

93. García de Arquer, F. P. *et al.* "CO2 electrolysis to multicarbon products at activities greater than 1 A cm-2". *Science* **367,** 661–666 (2020).

94. Endrdi, B. *et al.* "High carbonate ion conductance of a robust PiperION membrane allows industrial current density and conversion in a zero-gap carbon dioxide electrolyzer cell". *Energy & Environmental Science* **13,** 4098–4105 (2020).

95. Zheng, T. *et al.* "Copper-catalysed exclusive CO2 to pure formic acid conversion via single-atom alloying". *Nature Nanotechnology* **16,** 1386–1393 (2021).

96. Müller, L. J. *et al.* "A Guideline for Life Cycle Assessment of Carbon Capture and Utilization". *Frontiers in Energy Research* **8** (2020).

97. Ramdin, M. *et al.* " Electroreduction of CO 2 /CO to C 2 Products: Process Modeling, Downstream Separation, System Integration, and Economic Analysis ". *Industrial & Engineering Chemistry Research* **60,** 17862–17880 (2021).

98. Hawks, S. A. *et al.* "Analyzing Production Rate and Carbon Utilization Trade-offs in CO2RR Electrolyzers". *ACS Energy Letters* **7,** 2685–2693 (2022).

99. Gawel, A. *et al.* "Electrochemical CO2 reduction - The macroscopic world of electrode design, reactor concepts & economic aspects". *iScience* **25** (2022).

100. Sisler, J. *et al.* "Ethylene Electrosynthesis: A Comparative Techno-economic Analysis of Alkaline vs Membrane Electrode Assembly vs CO2–CO–C2H4 Tandems". *ACS Energy Letters* **6,** 997–1002 (2021).

101. Somoza-Tornos, A., Guerra, O. J., Crow, A. M., Smith, W. A. & Hodge, B. M. "Process modeling, techno–economic assessment, and life cycle assessment of the electrochemical reduction of CO2: a review". *iScience* **24,** 102813 (2021).

102. Sturman, M. & Oelgemöller, M. "Process Parameters in the Electrochemical Reduction of Carbon Dioxide to Ethylene". *ChemBioEng Reviews* **8,** 149–188 (2021).

103. Shin, H., Hansen, K. U. & Jiao, F. "Techno–economic assessment of low–temperature carbon dioxide electrolysis". *Nature Sustainability 2021,* 1–9 (2021).

104. Moore, T. *et al.* "Electrolyzer energy dominates separation costs in state-of-the-art CO2 electrolyzers: Implications for single-pass CO2 utilization". *Joule* **7,** 782–796 (2023).

105. Rabinowitz, J. A. & Kanan, M. W. "The future of low–temperature carbon dioxide electrolysis depends on solving one basic problem". *Nature Communications* **11,** 1–3 (2020).

106. Xie, K. *et al.* "Bipolar membrane electrolyzers enable high single-pass CO2 electroreduction to multicarbon products". *Nature Communications* **13,** 1–12 (2022).

107. Xie, Y. *et al.* "High carbon utilization in CO2 reduction to multi-carbon products in acidic media". *Nature Catalysis* **5,** 564–570 (2022).

108. Huang, J. E. *et al.* "CO2 electrolysis to multicarbon products in strong acid". *Science* **372,** 1074–1078 (2021).

109. Greenblatt, J. B., Miller, D. J., Ager, J. W., Houle, F. A. & Sharp, I. D. "The Technical and Energetic Challenges of Separating (Photo)Electrochemical Carbon Dioxide Reduction Products". *Joule* **2,** 381–420 (2018).

110. Wang, Q. *et al.* "Enhanced performance of gas diffusion electrode for electrochemical reduction of carbon dioxide to formate by adding polytetrafluoroethylene into catalyst layer". *Journal of Power Sources* **279,** 1–5 (2015).

111. Xing, Z. *et al.* "Tuning the Microenvironment in Gas-Diffusion Electrodes Enables High-Rate CO2 Electrolysis to Formate". *ACS Energy Letters* **6,** 1694–1702 (2021).

112. Xing, Z. *et al.* "Enhancing carbon dioxide gas-diffusion electrolysis by creating a hydrophobic catalyst microenvironment". *Nature Communications* **12,** 136 (2021).

113. Rabinowitz, J. A., Ripatti, D. S., Mariano, R. G. & Kanan, M. W. "Improving the Energy Efficiency of CO Electrolysis by Controlling Cu Domain Size in Gas Diffusion Electrodes". *ACS Energy Letters* **7,** 4098–4105 (2022).

114. Ripatti, D. S., Veltman, T. R. & Kanan, M. W. "Carbon Monoxide Gas Diffusion Electrolysis that Produces Concentrated C2 Products with High Single-Pass Conversion". *Joule* **3,** 240–256 (2019).

115. Bazant, M. Z., Kilic, M. S., Storey, B. D. & Ajdari, A. "Towards an understanding of induced–charge electrokinetics at large applied voltages in concentrated solutions". *Advances in Colloid and Interface Science* **152,** 48–88 (2009).

116. Zhang, B. A., Ozel, T., Elias, J. S., Costentin, C. & Nocera, D. G. "Interplay of Homogeneous Reactions, Mass Transport, and Kinetics in Determining Selectivity of the Reduction of CO2 on Gold Electrodes". *ACS Central Science* **5,** 1097–1105 (2019).

117. Strathmann, H. "Electrodialysis, a mature technology with a multitude of new applications". *Desalination* **264,** 268–288 (2010).

118. Campione, A. *et al.* "Electrodialysis for water desalination: A critical assessment of recent developments on process fundamentals, models and applications". *Desalination* **434,** 121–160 (2018).

119. Gurreri, L., Tamburini, A., Cipollina, A. & Micale, G. "Electrodialysis Applications in Wastewater Treatment for Environmental Protection and Resources Recovery: A Systematic Review on Progress and Perspectives". *Membranes* **10,** 146 (2020).

120. Xu, T. & Huang, C. "Electrodialysis-based separation technologies: A critical review". *AIChE Journal* **54,** 3147–3159 (2008).

121. Fidaleo, M. & Moresi, M. "Electrodialysis Applications in The Food Industry". *Advances in Food and Nutrition Research* **51,** 265–360 (2006).

122. Fleury, V., Chazalviel, J. N. & Rosso, M. "Coupling of drift, diffusion, and electroconvection, in the vicinity of growing electrodeposits". *Physical Review E* **48,** 1279–1295 (1993).

123. Huth, J. M., Swinney, H. L., McCormick, W. D., Kuhn, A. & Argoul, F. "Role of convection in thin-layer electrodeposition". *Physical Review E* **51,** 3444–3458 (1995).

124. Tan, J. & Ryan, E. M. "Computational study of electro-convection effects on dendrite growth in batteries". *Journal of Power Sources* **323,** 67–77 (2016).

125. Li, G., Archer, L. A. & Koch, D. L. "Electroconvection in a Viscoelastic Electrolyte". *Physical Review Letters* **122,** 124501 (2019).

126. Zhang, D. *et al.* "Electrodeposition of Zinc in Aqueous Electrolytes Containing High Molecular Weight Polymers". *Macromolecules* **53,** 2694–2701 (2020).

127. Ma, M. C., Li, G., Chen, X., Archer, L. A. & Wan, J. "Suppression of dendrite growth by cross-flow in microfluidics". *Science Advances* **7,** eabf6941 (2021).

128. Melcher, J. R. & Taylor, G. I. "Electrohydrodynamics: A Review of the Role of Interfacial Shear Stresses". *Annual Review of Fluid Mechanics* **1,** 111–146 (1969).

129. Saville, D. A. "ELECTROHYDRODYNAMICS: The Taylor-Melcher Leaky Dielectric Model". *Annual Review of Fluid Mechanics* **29,** 27–64 (1997).

130. Schnitzer, O. & Yariv, E. "The Taylor-Melcher leaky dielectric model as a macroscale electrokinetic description". *Journal of Fluid Mechanics* **773,** 1–33 (2015).

131. Bazant, M. Z. "Electrokinetics meets electrohydrodynamics". *Journal of Fluid Mechanics* **782,** 1–4 (2015).

132. Rubinstein, I. & Shtilman, L. "Voltage against current curves of cation exchange membranes". *Journal of the Chemical Society, Faraday Transactions 2: Molecular and Chemical Physics* **75,** 231–246 (1979).

133. Maletzki, F., Rösler, H. W. & Staude, E. "Ion transfer across electrodialysis membranes in the overlimiting current range: stationary voltage current characteristics and current noise power spectra under different conditions of free convection". *Journal of Membrane Science* **71,** 105–116 (1992).

134. Rubinstein, I. "Electroconvection at an electrically inhomogeneous permselective interface". *Physics of Fluids A* **3,** 2301–2309 (1991).

135. Rubinstein, I. & Maletzki, F. "Electroconvection at an electrically inhomogeneous permselective membrane surface". *Journal of the Chemical Society, Faraday Transactions* **87,** 2079–2087 (1991).

136. Mani, A. & Wang, K. M. "Electroconvection Near Electrochemical Interfaces: Experiments, Modeling, and Computation". *Annual Review of Fluid Mechanics* **52,** 509–529 (2020).

137. Nikonenko, V. V. *et al.* "Effect of electroconvection and its use in intensifying the mass transfer in electrodialysis (Review)". *Russian Journal of Electrochemistry* **53,** 1122–1144 (2017).

138. Nikonenko, V. V. *et al.* "Competition between diffusion and electroconvection at an ion-selective surface in intensive current regimes". *Advances in Colloid and Interface Science* **235,** 233–246 (2016).

139. Nikonenko, V. V. *et al.* "Desalination at overlimiting currents: State-of-the-art and perspectives". *Desalination* **342,** 85–106 (2014).

140. Rubinstein, I. & Zaltzman, B. "Electro-osmotically induced convection at a permselective membrane". *Physical Review E* **62,** 2238–2251 (2000).

141. Rubinstein, I. & Zaltzman, B. "Electro-osmotic slip of the second kind and instability in concentration polarization at electrodialysis membranes". *Mathematical Models and Methods in Applied Sciences* **11,** 263–300 (2001).

142. Zaltzman, B. & Rubinstein, I. "Electro-osmotic slip and electroconvective instability". *Journal of Fluid Mechanics* **579,** 173–226 (2007).

143. Smyrl, W. H. & Newman, J. "Double layer structure at the limiting current". *Transactions of the Faraday Society* **63,** 207–216 (1967).

144. Dukhin, S. S. "Electrokinetic phenomena of the second kind and their applications". *Advances in Colloid and Interface Science* **35,** 173–196 (1991).

145. Dukhin, S. S. & Mishchuk, N. A. "Intensification of electrodialysis based on electroosmosis of the second kind". *Journal of Membrane Science* **79,** 199–210 (1993).

146. Zholkovskij, E. K., Vorotyntsev, M. A. & Staude, E. "Electrokinetic Instability of Solution in a Plane-Parallel Electrochemical Cell". *Journal of Colloid and Interface Science* **181,** 28–33 (1996).

147. Rubinstein, S. M. *et al.* "Direct observation of a nonequilibrium electro-osmotic instability". *Physical Review Letters* **101,** 236101 (2008).

148. Kwak, R., Guan, G., Peng, W. K. & Han, J. "Microscale electrodialysis: Concentration profiling and vortex visualization". *Desalination* **308,** 138–146 (2013).

149. Kwak, R., Pham, V. S., Lim, K. M. & Han, J. "Shear Flow of an Electrically Charged Fluid by Ion Concentration Polarization: Scaling Laws for Electroconvective Vortices". *Physical Review Letters* **110,** 114501 (2013).

150. deValença, J. C., Wagterveld, R. M., Lammertink, R. G. H. & Tsai, P. A. "Dynamics of microvortices induced by ion concentration polarization". *Physical Review E* **92,** 031003(R) (2015).

151. Pham, S. V. *et al.* "Helical vortex formation in three-dimensional electrochemical systems with ion-selective membranes". *Physical Review E* **93,** 033114 (2016).

152. Kang, S. & Kwak, R. "Pattern Formation of Three-Dimensional Electroconvection on a Charge Selective Surface". *Physical Review Letters* **124,** 154502 (2020).

153. Kim, B., Choi, S., Pham, V. S., Kwak, R. & Han, J. "Energy efficiency enhancement of electromembrane desalination systems by local flow redistribution optimized for the asymmetry of cation/anion diffusivity". *Journal of Membrane Science* **524,** 280–287 (2017).

154. Stockmeier, F. *et al.* "On the Interaction of Electroconvection at a Membrane Interface with the Bulk Flow in a Spacer-Filled Feed Channel". *Journal of Membrane Science* **678,** 121589 (2023).

155. Warren, A. J., Sharma, A., Zhang, D., Li, G. & Archer, L. A. "Structure and Dynamics of Electric-Field-Driven Convective Flows at the Interface between Liquid Electrolytes and Ion-Selective Membranes". *Langmuir* **37,** 5895–5901 (2021).

156. Stockmeier, F. *et al.* "Direct 3D observation and unraveling of electroconvection phenomena during concentration polarization at ion-exchange membranes". *Journal of Membrane Science* **640,** 119846 (2021).

157. Stockmeier, F. *et al.* "Measurement of Electrokinetically induced hydrodynamics at Ion-selective interfaces using 3D Micro particle tracking velocimetry (µPTV)". *MethodsX* **9,** 101814 (2022).

158. Demekhin, E. A., Shelistov, V. S. & Polyanskikh, S. V. "Linear and nonlinear evolution and diffusion layer selection in electrokinetic instability". *Physical Review E* **84,** 036318 (2011).

159. Pham, V. S., Li, Z., Lim, K. M., White, J. K. & Han, J. "Direct numerical simulation of electroconvective instability and hysteretic current-voltage response of a permselective membrane". *Physical Review E* **86,** 046310 (2012).

160. Demekhin, E. A., Nikitin, N. V. & Shelistov, V. S. "Direct numerical simulation of electrokinetic instability and transition to chaotic motion". *Physics of Fluids* **25** (2013).

161. Druzgalski, C. L., Andersen, M. B. & Mani, A. "Direct numerical simulation of electroconvective instability and hydrodynamic chaos near an ion-selective surface". *Physics of Fluids* **25** (2013).

162. Urtenov, M. K. *et al.* "Basic mathematical model of overlimiting transfer enhanced by electroconvection in flow-through electrodialysis membrane cells". *Journal of Membrane Science* **447,** 190–202 (2013).

163. Druzgalski, C. L. & Mani, A. "Statistical analysis of electroconvection near an ion-selective membrane in the highly chaotic regime". *Physical Review Fluids* **1,** 073601 (2016).

164. Ristenpart, W. D. *et al.* "Electrohydrodynamic Flow and Colloidal Patterning near Inhomogeneities on Electrodes". *Langmuir* **24,** 12172–12180 (2008).

165. Zabolotsky, V. I. *et al.* "Electroconvection in systems with heterogeneous ion-exchange membranes". *Petroleum Chemistry* **57,** 779–789 (2017).

166. deValença, J. C. *et al.* "Confined Electroconvective Vortices at Structured Ion Exchange Membranes". *Langmuir* **34,** 2455–2463 (2018).

167. Pismenskaya, N. D. *et al.* "Effect of Surface Modification of Heterogeneous Anion-Exchange Membranes on the Intensity of Electroconvection at Their Surfaces". *Russian Journal of Electrochemistry* **55,** 1203–1220 (2019).

168. Roghmans, F. *et al.* "2D Patterned Ion-Exchange Membranes Induce Electroconvection". *Advanced Materials Interfaces* **6,** 1–11 (2019).

169. Seo, M., Kim, W., Lee, H. & Kim, S. J. "Non-negligible effects of reinforcing structures inside ion exchange membrane on stabilization of electroconvective vortices". *Desalination* **538,** 115902 (2022).

170. Karatay, E., Andersen, M. B., Wessling, M. & Mani, A. "Coupling between Buoyancy Forces and Electroconvective Instability near Ion-Selective Surfaces". *Physical Review Letters* **116,** 194501 (2016).

171. deValença, J. C., Kurniawan, A., Wagterveld, R. M., Wood, J. A. & Lammertink, R. G. H. "Influence of Rayleigh-Bénard convection on electrokinetic instability in overlimiting current conditions". *Physical Review Fluids* **2,** 033701 (2017).

172. Demekhin, E. A., Ganchenko, G. S. & Kalaydin, E. N. "Transition to electrokinetic instability near imperfect charge-selective membranes". *Physics of Fluids* **30** (2018).

173. Li, G., Townsend, A., Archer, L. A. & Koch, D. L. "Suppression of electroconvective and morphological instabilities by an imposed cross flow of the electrolyte". *Physical Review Fluids* **6,** 033701 (2021).

174. Rubinstein, I. & Zaltzman, B. "The effects of reaction kinetics upon the instabilities in cathodic electrodeposition". *Current Opinion in Colloid & Interface Science* **60,** 101591 (2022).

175. Kim, S., Khanwale, M. A., Anand, R. K. & Ganapathysubramanian, B. "Computational framework for resolving boundary layers in electrochemical systems using weak imposition of Dirichlet boundary conditions". *Finite Elements in Analysis and Design* **205,** 103749 (2022).

176. Andersen, M. B., Wang, K. M., Schiffbauer, J. & Mani, A. "Confinement effects on electroconvective instability". *Electrophoresis* **38,** 702–711 (2017).

177. Kim, J., Davidson, S. M. & Mani, A. "Characterization of Chaotic Electroconvection near Flat Inert Electrodes under Oscillatory Voltages". *Micromachines* **10,** 161 (2019).

178. Liu, W., Zhou, Y. & Shi, P. "Scaling relations in shear electroconvective vortices". *Physics of Fluids* **32,** 072009 (2020).

179. Liu, W., Zhou, Y. & Shi, P. "Shear electroconvective instability in electrodialysis channel under extreme depletion and its scaling laws". *Physical Review E* **101,** 043105 (2020).

180. Pham, V. S. & Van, D. A. "Numerical modeling for 3D vortices patterns of electroconvective flow developing in shear flow". *Physics of Fluids* **34** (2022).

181. Shi, P. "Direct numerical simulation of electroconvection with thin Debye layer matching canonical experiments". *Physics of Fluids* **33,** 032015 (2021).

182. Karatay, E., Druzgalski, C. L. & Mani, A. "Simulation of chaotic electrokinetic transport: Performance of commercial software versus custom-built direct numerical simulation codes". *Journal of Colloid and Interface Science* **446,** 67–76 (2015).

183. Davidson, S. M., Wessling, M. & Mani, A. "On the Dynamical Regimes of Pattern-Accelerated Electroconvection". *Scientific Reports* **6,** 1–10 (2016).

184. Cai, S., Wang, Z., Lu, L., Zaki, T. A. & Karniadakis, G. E. "DeepM&Mnet: Inferring the electroconvection multiphysics fields based on operator approximation by neural networks". *Journal of Computational Physics* **436,** 1–17 (2021).

185. Guan, Y., Brunton, S. L. & Novosselov, I. "Sparse nonlinear models of chaotic electroconvection". *Royal Society Open Science* **8,** 202367 (2021).

186. Pope, S. B. *Turbulent Flows* (Cambridge University Press, 2000).

187. Kourmatzis, A. & Shrimpton, J. S. "Turbulence closure models for free electroconvection". *International Journal of Heat and Fluid Flow* **71,** 153–159 (2018).

188. Mani, A. & Park, D. "Macroscopic forcing method: A tool for turbulence modeling and analysis of closures". *Physical Review Fluids* **6,** 054607 (2021).

189. Hamba, F. "Nonlocal expression for scalar flux in turbulent shear flow". *Physics of Fluids* **16,** 1493–1508 (2004).

190. Park, D. & Mani, A. *Direct Calculation of the Eddy Viscosity Operator in Turbulent Channel Flow at Re_τ=180.* https://arxiv.org/abs/2108.10898. 2022.

191. Park, D., Liu, J. & Mani, A. *Direct measurement of the eddy viscosity tensor in a canonical separated flow: What is the upper bound of accuracy for local Reynolds stress models?* AIAA SCITECH 2022 Forum. 2022.

192. Liu, J., Williams, H. H. & Mani, A. "Systematic approach for modeling a nonlocal eddy diffusivity". *Physical Review Fluids* **8,** 124501 (2023).

193. Uzdenova, A. "2D Mathematical Modelling of Overlimiting Transfer Enhanced by Electroconvection in Flow-Through Electrodialysis Membrane Cells in Galvanodynamic Mode". *Membranes* **9** (2019).

194. Uzdenova, A., Kovalenko, A. & Urtenov, M. "Theoretical Analysis of Electroconvection in the Electrodialysis Desalination Channel under the Action of Direct Current". *Membranes* **12** (2022).

195. Mattsson, E. & Bockris, J. O. "Galvanostatic studies of the kinetics of deposition and dissolution in the copper + copper sulphate system". *Transactions of the Faraday Society* **55,** 1586 (1959).

196. Brown, O. & Thirsk, H. "The rate-determining step in the electro-deposition of copper on copper from aqueous cupric sulphate solutions". *Electrochimica Acta* **10,** 383–393 (1965).

197. Deng, D. *et al.* "Overlimiting current and shock electrodialysis in porous media". *Langmuir* **29,** 16167–16177 (2013).

198. *CRC handbook of chemistry and physics, 103rd edition (Internet Version 2022)* (ed Rumble, J. R.) (CRC Press/Taylor & Francis, Boca Raton, FL, 2022).